COUPLING BETWEEN PHASE TRANSFORMATION AND VISCOPLASTICITY IN HIGH-TEMPERATURE SHAPE MEMORY ALLOYS

A Dissertation

by

PAWAN SATISH CHAUGULE

Submitted to the Graduate and Professional School of
Texas A&M University
in partial fulfillment of the requirements for the degree of

DOCTOR OF PHILOSOPHY

Chair of Committee,	Jean-Briac le Graverend
Committee Members,	Dimitris C. Lagoudas
	Ibrahim Karaman
	Darren J Hartl
Head of Department,	Ivett Leyva

December 2021

Major Subject: Aerospace Engineering

ABSTRACT

The purpose of this research work is to further the understanding of the coupling between phase transformation and viscoplasticity in high-temperature shape memory alloys (HTSMAs), which are active materials. Fundamental understanding of the coupling is essential to facing the challenge of achieving improved actuation performance from HTSMAs. The improvement involves enhancing the alloy's existing functional properties and work output to endure extremes in stress, strain and temperature. The improvement will eventually aid in moving closer to the overarching goal of reducing the weight of actuation systems required in the aerospace and automotive domains, while maintaining structural adaptability without critically affecting performance or the safety, in all to improve fuel efficiency. Experimental studies on these alloys have carved pathways for the above improvement, and their processing with scalability has also been understood to prepare for an increasing demand in the future. But, for the successful design of these alloys, it is necessary to have a comprehensive understanding of the effect of viscoplasticity on their phase transformation or functional properties and the overall behavior.

The objective of the present study is to investigate the coupling between phase transformation and viscoplasticity in a Ti-rich Ni-Ti-20Hf (at.%) HTSMA. To achieve the objective two approaches are followed. Experimental investigations are conducted on the selected alloy at different thermal cycling rates to vary the amount of viscoplasticity generated, and observe its effect on the phase transformation and response. The results are analyzed and inferences are made based on the interactions between the above two phenomena. Parallelly, a crystal-plasticity model is developed which accounts for the phenomena observed experimentally and the coupling between the two phenomena. The model is calibrated using the experimental results and inferences, and the underlying mechanisms responsible for the coupled response, are brought forward.

The contributions of this study are: (i) new interpretations on the overall functional fatigue of Ni-Ti-Hf alloys; (ii) establishing rate-dependency of the entire macroscopic response and the active phenomena; (iii) revealing a two-way coupling between viscoplasticity and phase transformation;

(iv) developing of a crystal-plasticity model for HTSMAs; and (v) generating anisotropic and isotropic coupled responses.

DEDICATION

To my family, friends, and all my teachers

ACKNOWLEDGMENTS

I would like to take this opportunity to express my gratitude to everyone who made my journey through graduate life at Texas A&M University a memorable experience that I will cherish forever. The experiences that I have had, both academically and otherwise, made me grow as a researcher and person. To this, I sincerely thank my advisor, faculty members of Texas A&M University, and friends.

My aim of pursuing a doctoral degree in Aerospace Engineering was fulfilled by the support and guidance of my advisor Dr. Jean-Briac le Graverend. He had sparked my interest in a field new to me by providing an open-ended dissertation problem. To tackle the problem he provided me with the required time to meet in person, shared his knowledge of modeling, and allocated more than sufficient computational resources. On starting my experimental endeavor he was supportive of me using his lab to conduct experiments at my own time and discuss the results while sharing his experimental wisdom. He endured the repetitive questions I asked him by patiently answering them every time. His participation in every facet of my research work and mentoring has shaped my overall research outlook. The biggest impact he has had on me was to be flexible in dealing with the problems faced in life and to deal with them one at a time. I am extremely grateful to him for being my mentor.

I would also like to thank Dr. O. Benafan from NASA Glenn Research Center for being a mentor and co-advisor to me. Based on just one phone call, he not only provided us with the required raw material to pursue experimental investigations but actively guided me by reviewing the test results and inferences. He has shared his knowledge of the material to a great extent which has given me confidence in my expertise. I am very grateful to have collaborated with him. Dr. O. Benafan acknowledges support from the NASA Transformative Aeronautics Concepts Program (TACP), Transformational Tools & Technologies Project, through which he was able to provide us the raw material provided.

I would like to express sincere thanks to my graduate committee: Dr. D. C. Lagoudas, Dr. I.

Karaman, and Dr. D. J. Hartl, for their service and providing useful criticism, which has served to improve the quality of my dissertation. My special thanks to Dr. Lagoudas and his student Jobin Joy, for understanding my modeling work and providing me feedback and areas to improve the model's capabilities. Some of the results in this thesis are because of their contributions.

I would also like to thank Dr. L. Perez, who helped me and my group with high-performance computations essential for the modeling results of this dissertation. She patiently taught me the basics of computing and operating on Linux machines, which I plan on using for the rest of my research career.

Sincere thanks to Dr. H. Sehitoglu, Dr. P. Anderson, Dr. P. Thamburaja, Dr. P. J. Guruprasad, and Dr. H. H. Hilton, whose works and inputs have directly influenced my research.

I would like to acknowledge the Department of Aerospace Engineering for supporting me with a Teaching Assistantship position and providing lab facilities to conduct my experiments. Helping me with the lab facilities and experiments was Mr. Rodney Inmon, to whom I am grateful for providing help graciously. I would also like to acknowledge the Texas A&M High-Performance Research Computing as the modeling research was conducted with the advanced computing resources provided by the facility.

Thanks to my friends and well-wishers; the time I spent in College Station has been an enjoyable sojourn. I would like to thank firstly my research group member Harikrishnan Rajendran who has been a supportive colleague to discuss professional and personal matters. I would like to thank my roommates, Roshan S Kumar, Sai S Dammati, and John P John for accommodating me. I will always remember the fun-filled exchanges, times spent watching TV series and cooking together. I would also like to thank my close friends Komal Kumari, Rishita Das, and Sualeh Khurshid with whom I started my doctoral program in the same department. Some of the interactions we had during lunchtime in the break room have shaped my mindset and given me purpose, while the rest have provided good humor. I will always look back at this quality and well-spent moments fondly. I also would like to thank my friends Vedang Deshpande, Vigneshwaran Radhakrishnan, Niladri Das, and Sumit Khatri with whom I was gladly able to talk about research and personal activities. I

would also like to thank my closest friends from undergraduate life, Animesh Swain, Anish Gupta, and my hostel mates at IIT Bombay, with whom I shared the best years of my life. I would also like to thank the members of the Coldplay band, who have written songs that are inspiring and soulful to me as I mostly listen to them while doing research.

Finally, I would like to thank my family members for their constant support and encouragement. The importance given to education by my parents Dr. Satish Chaugule and Dr. Manjusha Chaugule has played a large role in my pursuit of a doctoral degree. They made sure that I had a comfortable life without any responsibilities and worries so that I could focus solely on my research and dissertation work. I thank my sister Dr. Akshata Chaugule, for having my back and being a best friend to me.

CONTRIBUTORS AND FUNDING SOURCES

Contributors

This work was supported by a dissertation committee consisting of Professor Jean-Briac le Graverend (advisor), Dimitris C. Lagoudas, Darren J Hartl of the Department of Aerospace Engineering and Professor Ibrahim Karaman of the Department of Material Science and Engineering.

All other work conducted for the dissertation was completed by the student independently under the supervision of Dr. Jean-Briac le Graverend.

Funding Sources

This research did not receive any specific grant from funding agencies in the public, commercial, or not-for-profit sectors. Graduate study was supported by a Teaching Assistantship position from the Department of Aerospace Engineering at Texas A&M University.

NOMENCLATURE

Notation	Definition
TT	Transformation temperatures
TRIP	Transformation-induced plasticity
Thermo-elasticity	
E_{ijkl}	Stiffness coefficients
$\mathbb{C}$	Stiffness tensor
μ	Shear modulus
α_{CTE}	Coefficient of thermal expansion
T_m	Melting temperature
$\boldsymbol{\epsilon}_e$	Elastic strain tensor
$\boldsymbol{\epsilon}_{th}$	Thermal strain tensor
Viscoplasticity	
$\gamma^s_{p/vp}$	Plastic/viscoplastic slip
n	Power law exponent
K	Slip resistance
C_{visco}	Coefficient of viscosity
Q_1	Linear isotropic hardening
Q	Non-linear isotropic hardening
b	Rate of dislocation density
r_0	Initial yield radius

Notation	Definition
Viscoplasticity (Continued)	
C	Kinematic hardening magnitude
D	Rate of kinematic hardening
$h_1..h_7$	Interaction matrix parameters
$\mathbf{n}$	Slip-plane normal
$\mathbf{l}$	Slip-direction
$\mathbf{R}^g$	Rotatin matrix
T^s	Orientatin tensor (for slip)
$\boldsymbol{\sigma_g}$	Resolved stress
Φ^s_{vp}	Viscoplastic driving force
r^s	Yield radius
r_0	Initial radius
r^s_i	Isotropic hardening
q	Plastic/viscoplastic dislocation density variable
x^s	Kinematic hardening variable
α^s	Kinematic scalar variable
τ^s	Resolved shear stress
$\rho_{p/vp}$	Plastic/viscoplastic total dislocation density variable
$\boldsymbol{\epsilon}_{p/vp}$	Plasitc/viscoplastic strain tensor

Notation	Definition
Phase transformation	
M_f, M_s, A_s, A_f	Transformation temperatures (TTs)
C_m	Slope of martensite TTs
C_a	Slope of austenite TTs
g^{tr}	Magnitude of transformation strain
β	Coefficient of latent heat of transformation
m^{tr}	Rate of transformation
T_0	Phase equilibrium temperature at zero stress
$Y_1^0\ Y_2^0$	Transformation resistance (dislocation free state)
$Y_1\ Y_2$	Transformation resistance
g^{det}	Magnitude of detwinning strain
m^{det}	Rate of detwinning
Y_{det}	Detwinning resistance
m	Habit-plane normal
b	Habit-plane shear
t	Detwin plane normal
a	Detwin plane shear
ξ	Total martensite volume fraction
ξ_{re}^{α}	Reversible martensite variant volume fraction
ξ_0	Reference volume fraction rate
Φ_{tr}^{α}	Transformation driving force
$\boldsymbol{\epsilon}_{tr}$	Transformation strain tensor

Notation	Definition
Detwinning	
Φ_{de}^{α}	Detwinning driving force
λ^{α}	LCV volume fraction
λ^{0}	Initial LCV volume fraction
g^{det}	Detwinning magnitude parameter
λ_{ref}	Reference detwinning rate
m^{det}	Detwinning kinetics/exponent
$\boldsymbol{\epsilon}_{de}$	Detwinning strain tensor
Transformation induced plasticity	
Φ_{TRIP}^{α}	TRIP driving force
γ_{tr}^{α}	TRIP slip
τ_p	TRIP hardening
γ_0	Reference slip rate
ΔG_{slip}	Activation energy of dislocation slipping (stress-free configuration)
k_b	Boltzmann's constant
τ_0	RSS to overcome Peierl's obstacles
p, q	Power law exponents
k_1	Hardening parameter
k_2	Dislocation parameter
ρ_{α}	TRIP dislocation density variable
ρ_{TRIP}	TRIP total dislocation density variable
$\boldsymbol{\epsilon}_{TRIP}$	TRIP strain tensor

Notation	Definition
Coupling	
Y_{p1}, Y_{p2}	Resistance to transformation
d_1,c_1,d_2,c_2	Resistance coupling parameters
ξ_{ir}^{α}	Retained martensite
g^{ret}	Retained martensite coupling parameter
Thermodynamic variables	
u	Internal energy
$\mathbf{q}$	Heat energy/flux
q_s	Heat supply
s	Entropy
T	Tempeature
ψ	Helmholtz free energy density
λ_0	Latent heat of transformation
β	Parameter for latent heat

Notation	Definition
a	Scalar
$\mathbf{a}, \mathbf{b}$	First order tensors
$\mathbf{A}, \mathbf{B}$	Second order tensors
$\mathbb{A}, \mathbb{B}$	Fourth order tensors
Operation	**Definition**
$\dot{\mathrm{a}}$	Time rate of variable
$\mathbf{a} \otimes \mathbf{b}$	Dyadic product
$\mathbf{A}.\mathbf{B}$	Simple product
$\mathbf{A} : \mathbf{B}$	Double contraction

TABLE OF CONTENTS

Page

LIST OF FIGURES

FIGURE Page

LIST OF TABLES

1. INTRODUCTION

1.1 Background

Shape memory alloys (SMAs) have been a subject of intense scientific curiosity since the discovery of the thermoelastic martensitic transformation [14]. Their unique capabilities are due to the diffusionless transformation between two solid-state phases: mainly the high temperature phase called austenite, and the lower temperature phase called martensite. Through this transformation phenomenon, two mostly exploited behaviors are (i) superelasticity: regaining initial configuration upon removal of the external load (in Fig. 1.1) within certain temperature limits [15], and (ii) shape memory effect (SME) or actuation: regaining initial configuration by means of thermal cycling under stress-free (or applied stress conditions) [16].

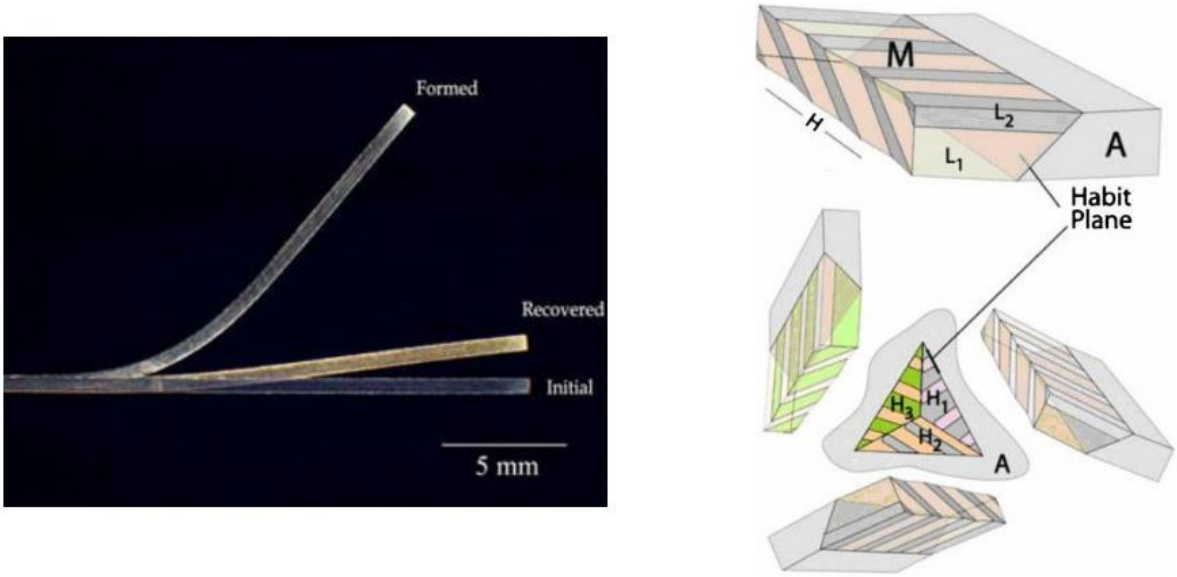

Figure 1.1: Shape memory alloy regaining initial configuration upon removal of external load, due to the phase transformation between martensite and austenite phases (shown on the right part) [1].

1.2 Literature review of experimental investigations

Experimental research on well-known SMAs, such as binary NiTi, is well established, defining their operation (or strain recovery) domain based on limits set by the applied stress and temperature. The above research brought forth advances in engineering applications and helped industries, such as aerospace, medical, microelectronics and automotive, develop interests in these alloys [17, 18]. Additionally, research outside their operation limits, i.e., at high temperatures [19, 20, 21, 22] and under high stresses [23, 24, 5, 25, 2, 26] is also well established. The above studies have observed and concluded that on exceeding the limits, the functionality of these alloys is degraded by phenomena such as plasticity [27] (in rate-independent regime), viscoplasticity [21, 22] (in rate-dependent regime), transformation-induced plasticity (TRIP) (at high stresses) [28], and deformation twinning [29]. These phenomena are observed to individually generate lattice defects such as dislocations, deformation twins, and retained phases [27], all of which have an effect on the reversible martensitic transformation [30].

Apart from experimental evidence of the above phenomena, there is evidence of simultaneous occurrence and interactions between phase transformation and plasticity in SMAs. The role of dislocations on the SME was first observed by Perkins [31]. He later demonstrated that dislocation tangles assist in the nucleation and growth of a preferred martensite plate arrangement and explained the mechanism of two-way SME [32]. The simultaneous occurrence was observed by Gall et al. [33] in polycrystal SMAs, when the grain-to-grain crystal orientation variation, favored plastic slip in some grains while transformation in others. In single crystal SMAs, Hamilton et al. [2] observed dislocations at austenite-martensite interfaces (in Fig. 1.2), in particular some dislocations indexed to austenite slip systems were formed by martensite twin variants. More recently, through TEM investigations, Norfleet et al. [28] and Bowers et al. [34] correlated the formation of stress-induced martensite variants with particular austenite slip systems. These studies, hence, indicated a coupling between transformation and plasticity due to their interactions, and resulted in influencing several theoretical and modeling studies [35, 36, 37, 5, 38].

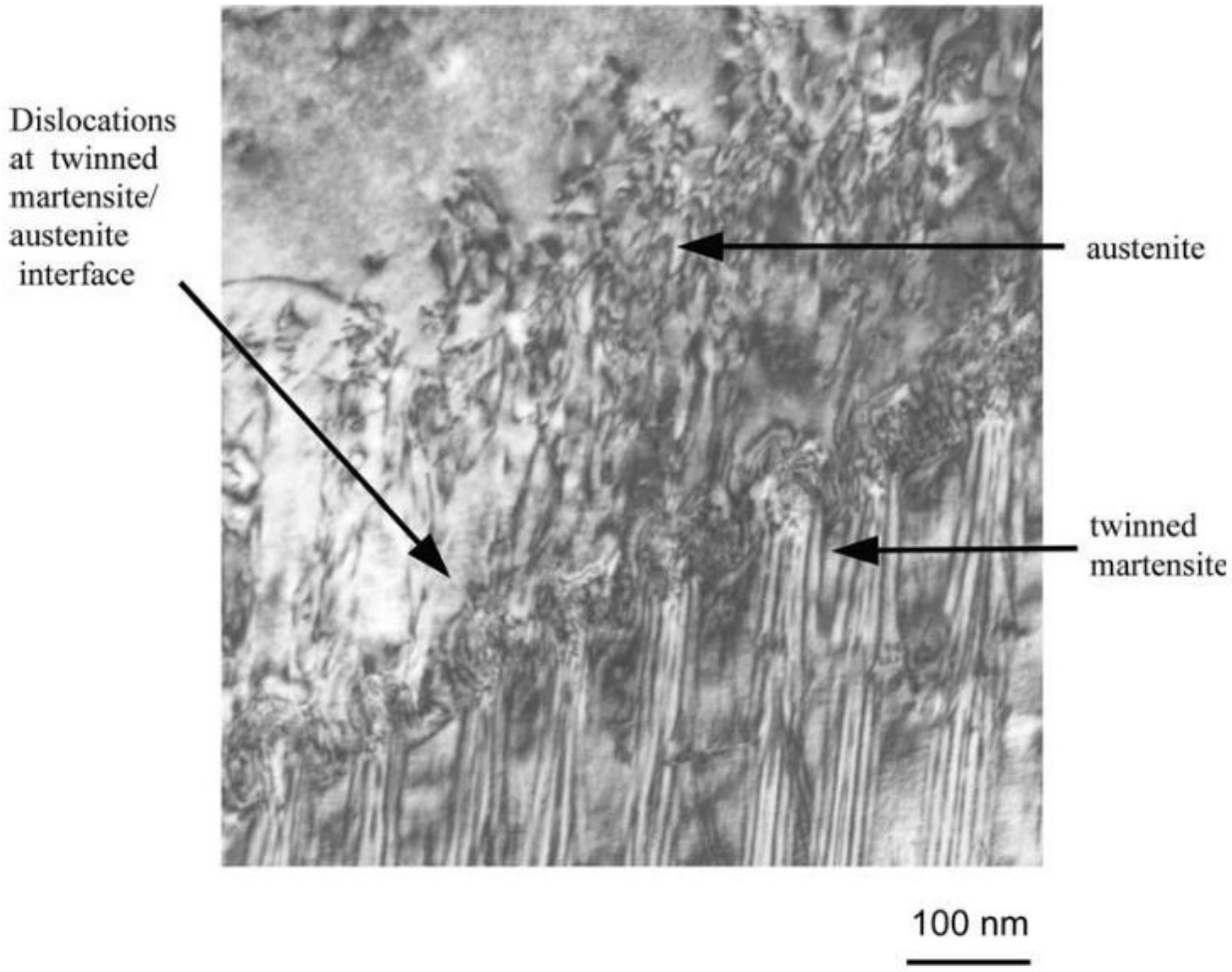

Figure 1.2: Solutionized Ti–50.1 (at.%) Ni single crystal of [111] orientation thermally cycled under constant load with load increased for successive thermal cycles showing dislocations being emitted from martensite-interface at internal twin boundaries. [2].

Given the significance, understanding the transformation-plasticity coupling in SMAs is key to developing: (i) an experimental approach such as "training", or (ii) a computational approach involving materials-by-design in order to obtain their desired functional properties [5]. These properties control the actuation and two-way shape memory effect (actuation under no external stress) of components that need to actuate for extended number of cycles [18, 39, 40]. Hence, these properties have to be efficiently controlled to avoid loss, or even major degradation, due to accumulation of plastic deformation and microstructural evolution, through continuous reorientation of

martensite, or accumulation of retained phases.

On establishing the basis of functionality for SMAs, their acute needs in high-temperature components applications has resulted in the development of high-temperature shape memory alloys (HTSMAs) [41, 1]. These alloys possess the ability to transform at much higher temperatures (> 100 °C) than conventional SMAs, reaching as high as 500 °C transition temperatures. They were developed to expand the operation domain (defined by applied temperature and stress) of SMAs and to design components with high-temperature resistance and functional capabilities. An example of such a development involved adding ternary elements such as Au, Pd, Pt, Zr or Hf in Ni-Ti based SMAs [42, 43, 44, 45, 46]. The resulting HTSMAs have transformation temperatures (TT) in the range of 100 - 300 °C, which is a significant increase (from TT < 100 °C) for SMAs.

The high TT or phase transformation domain, however, poses a challenge to the development of HTSMA systems. The challenge was initially brought forth experimentally by Lagoudas et al. [47] and Kumar et al. [48, 3] in Ni-Ti-Pd HTSMAs. The TT are high enough such that their domain overlaps with the viscoplastic domain, i.e., for temperatures higher than 0.3 - 0.5 of the absolute melting temperature [17, 49]. This overlap results in a coupling between the two phenomena due to their simultaneous occurrence, with viscoplasticity manifesting majorly in the austenite phase through dislocation glide and climb. The effect of viscoplasticity is observed as a reduction in the recoverable strain and a rise in the total strain (in Fig. 1.3) during the reverse transformation (martensite $\rightarrow$ austenite). Furthermore, the actuation performance is degraded as the functional properties such as TT and actuation strain are altered. Apart from the above effects, Kumar et al. [50] also observed (through TEM micrographs) that the random distribution of defects generated by creep, created multiple nucleation sites to form compound twins. This signified an interaction between viscoplasticity and phase transformation, in a manner similar to that observed in SMAs by past studies.

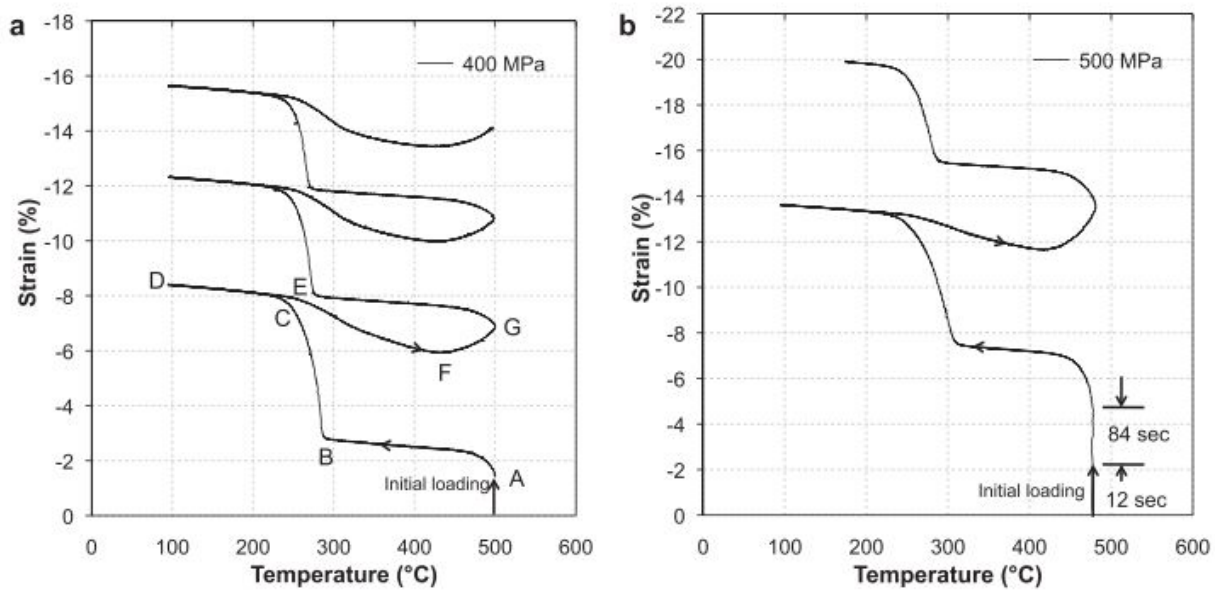

Figure 1.3: Strain–temperature response of Ti50.5Pd30Ni19.5 HTSMA at 5 °C/min showing (a) simultaneous creep and transformation during thermal cycling under a constant 400MPa stress; (b) simultaneous creep and transformation during thermal cycling under a constant 500MPa stress. The deformation during the 2nd thermal cycle exceeded the extensometer strain measurement limit in (b) [3].

1.3 Motivation for experimental investigations

The above facts and inferences motivated the present study to conduct an experimental investigation that can reveal a deeper understanding of the coupling between viscoplasticity and phase transformation in HTSMAs. Prior to conducting the investigation, the state-of-the-art literature on actuation behavior of HTSMAs was studied. A brief summary of the literature is as follows. It includes investigations of factors such as rate of thermal cycling [47], upper cycle temperature (UCT) [51, 52], stress levels [53, 54], and number of cycles [55], on the actuation behavior of HTSMAs. In addition to studying expensive Ni-Ti-Pd/Pt HTSMAs [56, 44], new HTSMA systems of Ni-Ti-Hf and Ni-Ti-Zr have also been explored as cost-effective alternatives. The actuation life of these new alloys was extensively explored [46, 57, 58, 59, 60, 61, 13, 62, 63], which helped quantify their TTs (in Fig.1.4(a)), dimensional stability (via thermal cycling under high stresses), work output, and strength (in Fig.1.4(b)), in comparison to the Ni-Ti and Ni-Ti-Pd/Pt systems. The

interactions between transformation and plasticity were also investigated in a Ni-Ti-Hf SMA by Casalena et al. [64] and it was suggested that the hysteresis of the alloy can be tuned to be small through plasticity.

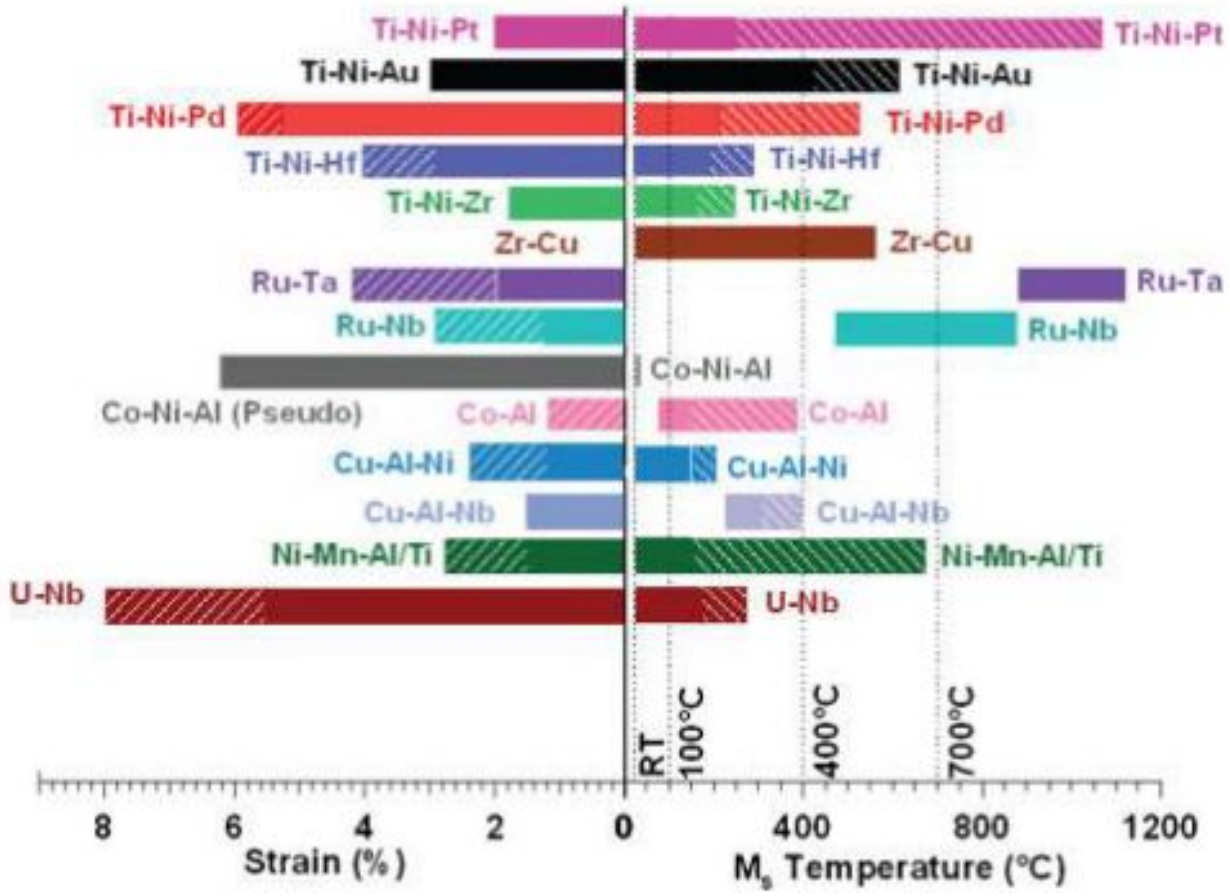

Figure 1.4: A comparison of transformation temperatures, and shape memory strains for all reported HTSMAs (see Ma et al. [1] for details)

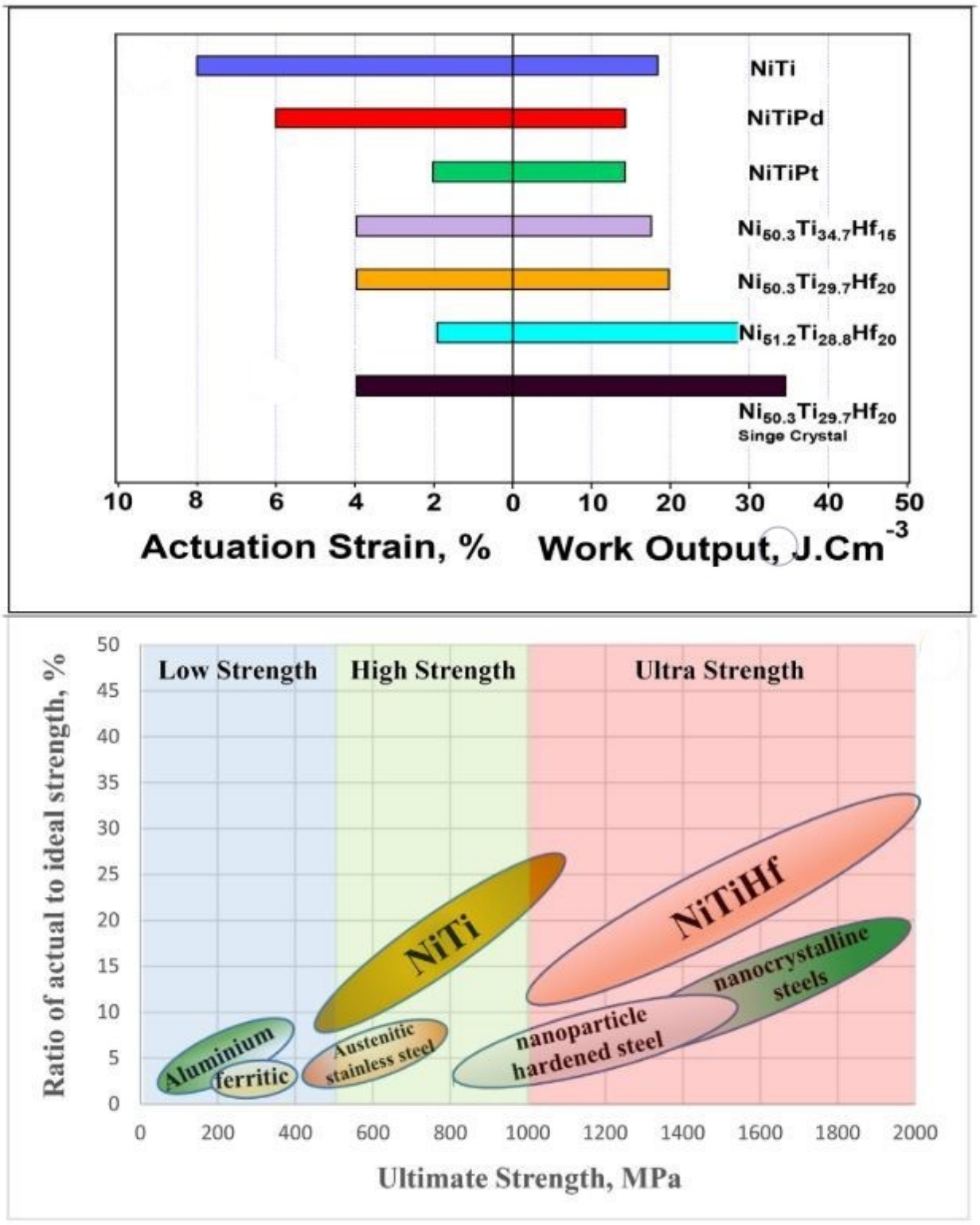

Figure 1.4: (Continued) Actuation strains and work outputs of selected NiTi-based alloys (top) and comparison of the strength of common materials with shape memory alloys (bottom) (see Saghain et al. [4] for details).

However, the role of coupling between phase transformation and viscoplasticity in HTSMAs, for their entire actuation life (until failure), was not examined yet. Recent developments in using HTSMAs as energy dense actuators, particularly Ni-Ti-Hf based HTSMAs, have generated interesting applications such as rock splitters (for extraterrestrial applications) [65] and torque tubes [55]. These applications have stirred the interest in these alloys and encouraged their scalability [6]. The overarching goal in the field of HTSMAs is to ensure these alloys can maintain their functional and structural capabilities at high temperatures, to meet their application demands. The aim of the the present study is to understand the effect of viscoplasticity on the response and functional properties of the above alloys, which can help in achieving part of the overarching goal. Therefore, the present study tries to answer the following important questions:

Q. 1 *How do the interactions or the coupling between phase transformation and viscoplasticity manifest in any HTSMA during actuation?*

Q. 2 *What are the fundamental mechanisms behind the occurrence of the coupling that result in affecting its functionality?*

Q. 3 *Can these mechanisms be predicted (or even controlled) using modeling studies?*

Understanding the fundamental mechanisms will become ever increasingly important for such alloys. The purpose of the present study is, therefore, to identify and decouple the phenomena generating irrecoverable (or permanent) deformations actively involved in degrading the actuation response. The approach followed to achieve this objective involves conducting experimental tests along with post-experimental analyses on a selected Ni-Ti-Hf system. In addition, the present study follows a second approach in parallel. The approach involves formulating a constitutive model that interprets and simulates the fundamental mechanisms of the coupled behavior (observed experimentally) using a set of constitutive equations.

1.4 Literature review on modeling studies

The above experimental studies have been instrumental in developing tools that depend on theoretical frameworks and constitutive modeling to simulate the behavior of these alloys, at the macro, micro, and atomic scale. For instance, at the macro scale, constitutive models were devel-

oped for Ni-Ti-Pd HTSMAs by Lagoudas et al. [66], Hartl et al. [67], Chemisky et al. [68] and Sakahei et al. [69] to simulate the response over multiple thermal cycles and rates. The above models account for the phenomena of phase transformation, TRIP (rate-independent), viscoplasticity (rate-dependent), and the accumulation of retained martensite. The phenomena are accounted in an isotropic manner, and by following a phenomenological approach. Constitutive models developed for the relatively new Ni-Ti-Hf HTSMAs include the ones by Farjam et al. [70] and Xu et al. [71]. They simulate the macroscale response generated by phase transformation, TRIP, and viscoplasticity (but excluding the coupling) using an isotropic formulation developed by following a phenomenological approach.

At the micro scale, studies published on HTSMAs include theoretical predictions for Ni-Ti-Hf. Using theories such as geometrically linearized theory [72] and lattice deformation theory [73], Stebner et al. [53] and Sehitoglu et al. [13], respectively, predict phase transformation strains. They do so using characteristics of the crystal structure (i.e. lattice parameters) and crystal orientation leading to an anisotropic formulation. Whereas, at the atomic scale, Wang et al. [74] establishes the flow stress for plastic slip, also in a theoretical manner. As experimental investigations presented in the earlier sections, and studies on processing and scaling of these alloys [6] surge, the modeling studies will continue to grow and assist in accelerating the commercialization of these alloys.

Modeling the entire behavior of HTSMAs (including the coupling), while accounting for anisotropy, can require resolving/resorting to the micro- or nano-scale and following one of the approaches summarized in Cisse et al. [75] and implemented on SMAs. In case of modeling at the microscale, a crystal-mechanics approach had been adopted to simulate the phase transformation [76, 77, 9, 78, 79]. Building on the previous models, a crystal-plasticity based approach had been adopted to simulate the phase transformation and its associated irrecoverable mechanisms, such as plastic slip in martensite/austenite [80, 34, 81, 82, 83, 84] and accumulation of retained phases [85]. The latter approach is capable of accounting for the evolution of microscopic internal variables (such as martensite variant volume fraction) associated with the above phenomena across crystallographic textures considered in great details. Characterizing all the phenomena is challeng-

ing and accounting for all the variables usually makes crystal-plasticity models computationally expensive. However, these models are known for their robustness (to various thermomechanical conditions), as pointed out by Lagoudas et al.[86]. In addition, since crystal-plasticity models follow a physics based approach, they can provide more accurate simulations compared to the macroscopic ones [75]. Macro-micro models built using the crystal-plasticity approach are even capable for using the atomistic calculations and parameters and bridging the micro to the macro scale response through multiscale methods [75, 87].

Implementing a crystal-plasticity approach that accounts for multiple microscale mechanisms, including their couplings, is a challenge that very few studies have addressed in the field of SMAs. Manchiraju et al. [36] formulated a coupling between plasticity and phase transformation, which occurs when the stress is redistributed grain-to-grain by the two phenomena resulting in affecting each other's driving force. Richard et al. [88] considered an interplay between plasticity and transformation, wherein, plastic slip acts as a bridging mechanism to overcome the incompatibility between non-transforming (misoriented) grains, enabling transformation along the forward path. Paranjape et al. [38] used a finite deformation phase field/crystal-plasticity informed model, to simulate and interpret experimental findings that can be inferred as a two-way coupling. The local incompatibility at the austenite - martensite (A-M) interface drives plasticity in austenite. While in subsequent cycles, the large plasticity developed overall, hinders the A-M transformation, but aids it, in regions of comparatively less plasticity, hence the two-way coupling. More recently, Sittner et al. [5] reviewed all of the above studies with their predictions, and laid down a mathematical theory of coupling between phase transformation and plasticity. The theory claims that the coupling is strong during the reverse transformation, i.e., when the dislocations play a role in achieving strain-compatibility on the habit planes (A-M interfaces), as shown in Fig. 1.5.

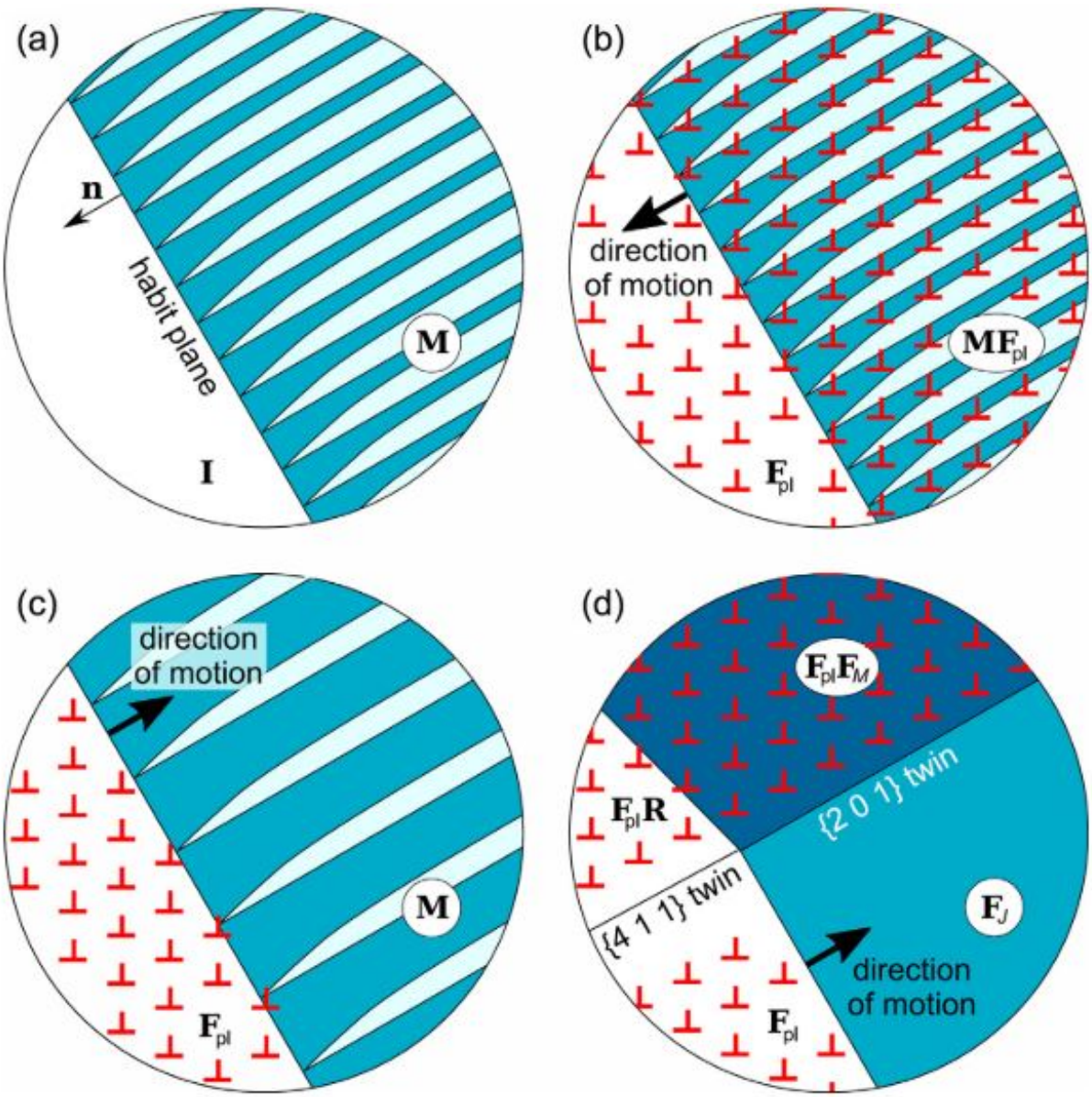

Figure 1.5: Habit plane interface between (a) austenite (I) and a martensitic microstructure (M) satisfying the compatibility condition, (b-d) kinematically admissible couplings between the habit plane motion and plastic slip: (b) austenite is plasticized in front of the moving habit plane in the forward transition, (c) austenite is plasticized behind the moving habit plane in order to achieve compatibility with a microstructure (M) not satisfying the compatibility condition, (d) a $\{20\bar{1}\}$ rigid plastic twin in martensite during the reverse transition, transforming continuously into a $\{114\}$ twin in austenite (analogously to the subplot (b), the austenite phase is plasticized for compatibility reasons) (see Sittner et al. [5] for more details).

1.5 Motivation for constitutive modeling

The previously mentioned studies and approaches motivated the present study to develop a theoretical formulation of the coupling between phase transformation and viscoplasticity in HTSMAs at the microscale. To the best knowledge of the author, such a formulation has never been developed before and, neither has any anisotropic modeling effort been conducted on any HTSMA system, while accounting for the coupling. On identifying this gap in literature, the following important questions were raised.

Q. 4 *How can the fundamental mechanisms behind the coupled behavior (observed experimentally) be interpreted through a set of constitutive equations at the micro scale?*

Q. 5 *What role can the texture (or microtexture) play in the interpretations and the overall functionality? Texture is important to consider because in most crystalline materials there is a preferred orientation or texture present [8], which makes the material properties texture specific.*

Q. 6 *Can the coupling mechanisms be predicted (or even controlled) through modeling?*

To addresses Q. 4 and 5 questions the present study looks towards formulating a crystal-plasticity framework that can take into account the coupled phenomena, by building on the concepts and knowledge presented in the above-described studies on coupling. Adopting a crystal-plasticity framework is, essential and instrumental in investigating the effect of texture on irrecoverable deformations and, therefore, shape memory alloy performance. The primary aim of the modeling effort is to interpret the fundamental mechanisms of the coupled behavior (observed experimentally), instead of giving a precise numerical prediction for a particular HTSMA. To achieve this aim, the present study will implement the model and simulate the qualitative trends of the coupled behavior which modifies the actuation properties of an HTSMA.

1.5.1 Scope of modeling study

The crystal-plasticity framework in the present study is developed to account for plastic (rate-independent) and viscoplastic (rate-dependent) slip in a HTSMA. In addition, a thermodynamic framework is developed to account for the phase transformation and its associated irrecoverable

mechanisms, i.e., TRIP and retained martensite, through the formation of martensite variants at the microscale. The coupling between phase transformation and viscoplasticity is brought about by the dislocation density (generated from plastic/viscoplastic slip) affecting the phase transformation properties and driving force.

1.6 Objectives

1.6.1 Experimental investigations

The following objectives were drafted to aid the investigations and potentially answer Q. 1 and 2. The experimental objectives listed are to:

- Perform a series of thermomechanical tests on a Ti-rich Ni-Ti-20Hf (at.%) HTSMA
- Select:
    1. A high stress value ensuring the sample fails in a reasonable amount of time
    2. A wide temperature range to ensure the transformation paths are completed
    3. Several thermal cycling rates ensuring a good array of rates are studied
- Dissociate the macroscopic response in order to narrow down the phenomena that occured
- Lastly, conduct post experimental analyses such as Differential Scanning Calorimetry (DSC) tests, and X-ray Diffraction (XRD) analyses to understand the effect of the coupling, inside the microstructure

1.6.2 Constitutive modeling

The following objectives were drafted to develop the constitutive model and potentially answer Q. 4 and 5 and address Q. 6. The modeling objectives listed are to:

- Formulate a crystal-plasticity framework similar to one that has been extensively implemented by the past studies on the parent SMA - binary Ni-Ti.

- In the framework account for the following phenomena:

    1. Phase transformation
    2. Plastic slip in martensite
    3. Viscoplastic slip in austenite
    4. Accumulation of retained martensite
    5. Coupling between viscoplasticity and phase transformation

- Conduct finite element analysis using the model on:

    1. single crystals oriented along various random orientations, to study the anisotropy
    2. polycrystals with various number of randomly oriented grains (or single crystals) to study the effects of texture

  of the Ni-Ti-20Hf HTSMA.

- Compare simulated and experimental trends to make inferences on the underlying mechanisms responsible for the coupling.

1.7 Organization of present study

Based on the above objectives the present study is organized into two major chapters. Chapter 2 includes all the experimental details, results and discussions. Chapter 3 includes the formulation of the crystal plasticity framework, finite element analyses and results with discussions. Chapter 4 provides concludes the experimental investigations and modeling effort together, and provides future directions.

2. EXPERIMENTAL INVESTIGATIONS *

2.1 Introduction

In this chapter, the experimental investigations conducted on the chose HTSMA system, followed by inferences made based on the results are presented. In Section 2.2 the HTSMA material properties and experimental details of the tests conducted on the alloy, including data-quantification of the results are presented. The experimental tests are conducted so as to activate viscoplasticity followed by phase transformation while observing their effect on the macroscopic response of the HTSMA. A coupling is assumed to be induced due to the sequential occurrence of the two phenomena. The macroscopic responses are investigated only for the cycles in which the above coupling has an effect on the behavior, and the effect from potential damage mechanisms (including cracks opening and closing) and substantial necking can be neglected. Investigating the effect of potential damage mechanisms on the behavior is out of the scope of this study. In Section 2.3, the test results and the post-experimental analyses, including differential scanning calorimetry (DSC) and X-ray diffraction (XRD), are presented and discussed. The analyses provide evidence of the coupling that occurred based on their signatures left in the microstructure. The effect of viscoplasticity over phase transformation, and vice-versa, is also discussed in the same section. Lastly, in Section 2.4 the entire chapter is summarized.

2.2 Experimental details

2.2.1 Material selection and properties

A Ti-rich $Ni_{49.8}Ti_{30.6}Hf_{19.2}$ (at.%) HTSMA system was chosen to investigate the coupling between phase transformation and viscoplasticity. A Ti-rich alloy was chosen because the effect from precipitation on shape memory properties is minimal [89] and the chosen alloy does not form any H-phase precipitates on aging as shown in Fig. 2.1 taken from Benafan et al. [6]. Hence

*Reprinted with permission from "Phase transformation and viscoplasticity coupling in polycrystalline nickel-titanium-hafnium high-temperature shape memory alloys" by P. S. Chaugule, O. Benafan, J.B. le Graverend, 2021, Acta Materialia, vol. 221, p. 117381, Copyright © 2021 Elsevier B.V.

subjecting them to high temperatures for prolonged periods of time should not introduce an effect from precipitates on the material behavior. The alloy was produced using a vacuum induction skull melting (VISM) method and designated as FS4-H7 [6] according to its material-batch. The cast ingots were homogenized at 1050 °C for 72 h in a vacuum furnace, followed by hot extrusion at 900 °C to a final rod diameter of 1.016 cm. Additional details pertinent to this alloy can be found in Benafan et al. [6], and a summary of the key material properties obtained are listed in Table 2.1.

Figure 2.1: Representative TEM micrograph of Ti-rich Ni-Ti-Hf alloy aged at 550 °C for 3 h and air cooled. The alloy does not show any precipitates formed in the martensite matrix [6].

Table 2.1: Material properties of the $Ni_{49.8}Ti_{30.6}Hf_{19.2}$ HTSMA [6]. Modified with permission from Chaugule et al. [7].

Properties	*Nomenclature*	*Martensite*	*Austenite*
Young's modulus	E (GPa)	60.8	77.6
Shear modulus	μ (GPa)	22.86	29.17
Poisson ratio	ν	0.42	0.41
Coefficient of thermal expansion	α_{CTE} (1/K)	9.56 x 10^{-6}	11.46 x 10^{-6}
Transformation temperatures	M_f, M_s (°C)	259.5, 288	
	A_s, A_f (°C)		306.5, 330.2
Stress influence coefficients	C_M (MPa/ °C)	20.77	
	C_A (MPa/ °C)		15.29
Melting temperature	T_m	1287 °C 1560.15 K	
Theoretical domains	*Nomenclature*		
Phase-transformation domain (at 500 MPa)	M_f - A_f (°C)	283.5 - 362.8	
Viscoplastic domain	(0.3 - 0.5)*T_m	194 - 506 °C 468 - 780 K	

2.2.2 Experimental Setup

The thermomechanical experiments [90] were performed on an ATS lever arm creep testing frame (see Fig. 2.2(a)) with a maximum capacity of 4,535 kgf. The lever arm is configured to support the loading axis on one end and a weight pan on the other, through a 1:3 ratio. Along the loading axis cylindrical dog-bone specimens (in Fig. 2.2(b)) were gripped using attachments. The

test specimens having dimensions adhering to ASTM standard [91] as shown in Fig. 2.2(c), were machined from the as-extruded rod.

The threaded portions of the test specimen were used for grip attachments, and for mounting two flat discs, known as flags (Fig. 2.2(b)). The flags were used to measure the sample's elongation via a Keyence laser extensometer (in Fig.2.3(a)). The load was applied using dead weights placed on the weight pan, and was measured using an Omega load cell (in Fig. 2.3(b)) with a maximum capacity of 11,120 N. The sample was heated in a ChamberIR infrared furnace (in Fig.2.3(c)) using halogen lamps and reflectors operating at 7.8 watt/mm (or 200 watt/inch), capable of reaching temperatures up to 1648 °C. The sample's temperature was measured using two S-type thermocouples inserted into two holes drilled just outside the gauge section. The heating of the furnace was controlled through the input from the thermocouples (Fig. 2.2(b)) and a PID-controlled feedback loop. The thermal gradient across the gauge section of the sample was less than 5 °C on an average. On modeling the heat transfer inside the gauge section (i.e radially) using the thermal conductivity, specific heat and density values of the alloy [6], the sample is assumed to be have been heated uniformly as shown in Section 2.5.1.

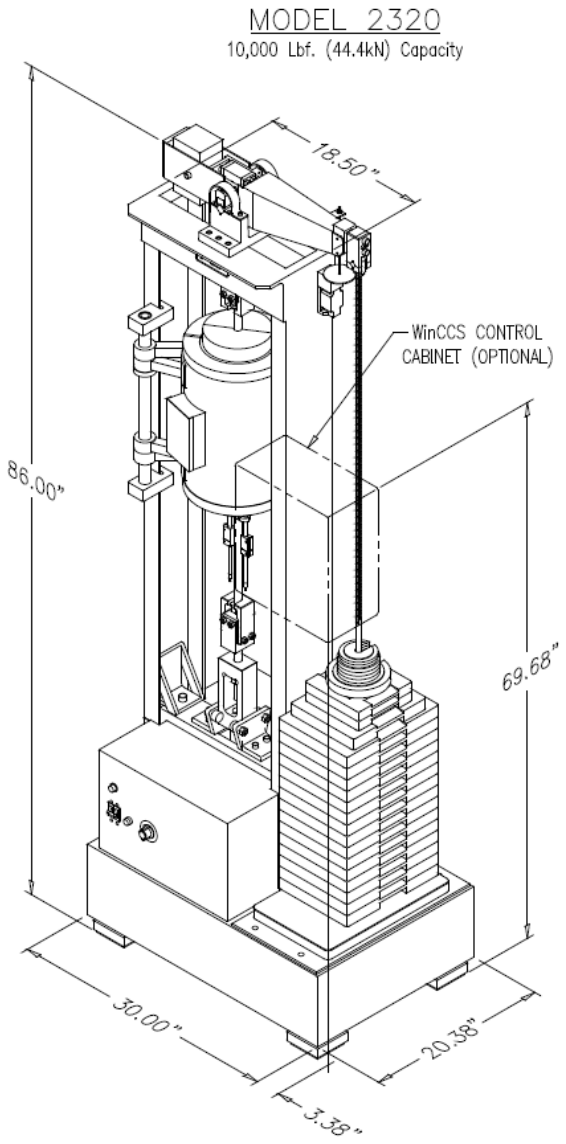

(a)

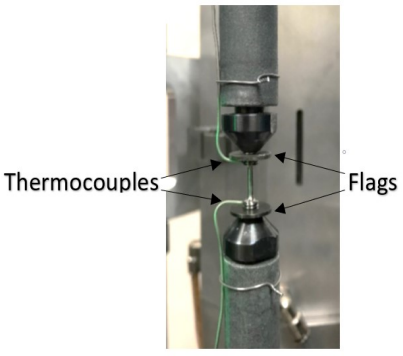

(b)

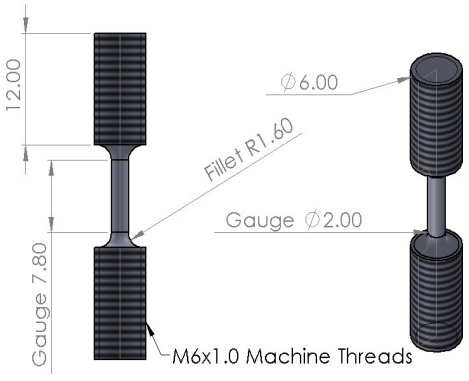

(c)

Figure 2.2: Experimental bench (a) ATS lever arm tester, (b) Sample mounted with flags and thermocouples attached, and (c) Cylindrical dog-bone sample with dimensions in mm. Modified with permission from Chaugule et al. [7].

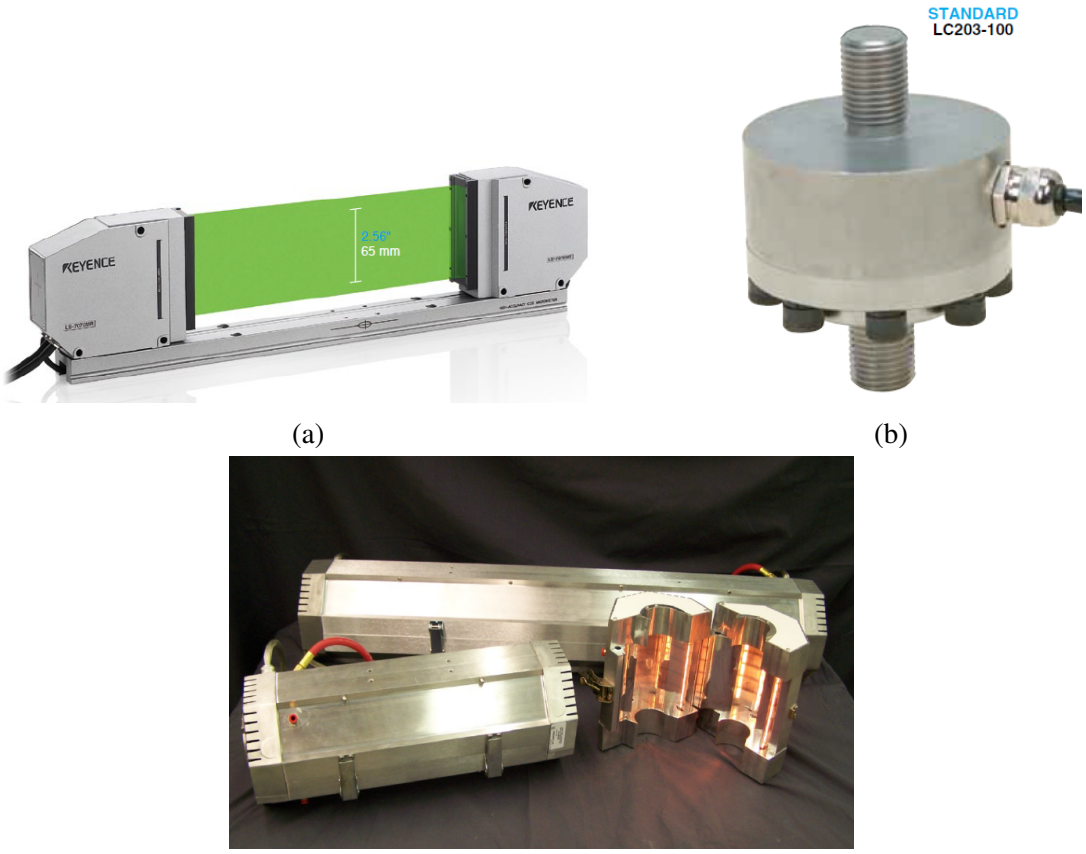

(a) (b)

(c)

Figure 2.3: Experimental bench parts (a) Keyence laser extensometer, (b) Omega load cell, and (c) ChamberIR infrared furnace.

2.2.3 Experimental tests

2.2.3.1 Uniaxial constant force thermal cycling

The uniaxial constant force thermal cycling (UCFTC) tests start with heating the sample to an upper cycle temperature (UCT), under no external load. The sample is then loaded at UCT, cooled to a lower cycle temperature (LCT), and then heated back to the UCT. The thermal cycling is conducted continuously at a fixed rate. A schematic shown in Fig. 2.4 demonstrates this procedure. In the present work each UCFTC test was performed up to failure, to track the strain-temperature response as a function of cycles. The LCT was fixed at 100 °C and the UCT at 500 °C, as it is a potential temperature range yet to be explored for the selected Ni-Ti-Hf alloy. The UCT

of 500 °C was chosen because it lies well within the theoretical viscoplastic domain, ensuring viscoplasticity is activated. Table 2.1 lists the theoretical phase transformation and viscoplastic domains, estimated from the TT and melting point of the alloy, respectively. The constant force (load) applied was based on a stress of 500 MPa, which is beyond the operation limits of this alloy [54]. This stress level was chosen on performing trial tests and ensuring sufficient amount of viscoplastic strain is accumulated through dislocations generated due to glide and/or climb at high temperatures [1], and to attain sample failure in a reasonable amount of time. The behavior of the selected Ni-Ti-Hf alloy at stress levels lower than 500 MPa and for temperature ranges less than 500 °C, is already investigated thoroughly and presented in Benafan et al. [6].

In the case of HTSMAs, the thermal cycling rate is a crucial factor in actuation functions, as it dictates the amount of time spent at high temperatures. The slower the rate, the longer the time spent at high temperatures and, hence, potentially higher contributions from viscoplastic deformations. Therefore, to identify and observe the coupling between phase transformation and viscoplasticity, the present work investigates the effect of heating/cooling rate on the macroscopic response by employing three different rates. The rate effect was investigated earlier by Kumar et al. [3, 50] through similar experiments on Ni-Ti-Pd HTSMAs. The rates considered in the previous studies were 2, 5, and 20 °C/min. The number of thermal cycles conducted at these rates were a maximum of four, under strain-controlled and compression conditions. The strain-temperature responses obtained from the tests helped quantify the actuation and evolution of irrecoverable strains, TT, and work output.

The present study explored an array of thermal cycling rates, viz. 1, 10, and 50 °C/min, under stress-controlled and tension conditions, up till the point of failure. This array represents a change in order of magnitude, while encompassing the thermal cycling rates of the previous studies. Despite being overlooked by many studies, due to the focus on actuating as fast as possible [41, 92, 93], the factor of rate is instrumental in investigating the coupling between phase transformation and viscoplasticity.

Functional properties such as *TT, transformation strain*, and quantifiers, such as *hysteresis,*

cumulative residual strain, cumulative TRIP strain, cumulative viscoplastic strain, and retained phases, are of particular interest in the present study. Data parsing methods based on ASTM standard [90] were used to dissociate the macroscopic response and determine the evolution of functional properties and quantifiers, as shown in the schematic (Fig. 2.4(a)). The schematic accounts for all the mechanisms generating permanent deformations, except for deformation twinning, which can also play an important role during actuation and thermal cycling as demonstrated in Ni-Ti SMAs [94]. In the schematic, the hysteresis width is $A_{50} - M_{50}$, the transformation strain is $\varepsilon_{A_s} - \varepsilon_{A_f}$, and the residual strain for the n^{th} cycle is $\varepsilon_{UCT_n} - \varepsilon_{UCT_{n-1}}$. The residual strain is assumed to be comprised of the TRIP (ε_{TRIP}) and viscoplastic (ε_{vp}) strains, i.e., $\varepsilon_{UCT_n} - \varepsilon_{UCT_{n-1}} = \varepsilon_{TRIP} + \varepsilon_{vp}$. *Note:* The TRIP strain can also have a contribution from retained martensite [3]. However, the magnitude of contribution is not known or straightforwardly determined, hence the above assumption is made.

In order to dissociate ε_{TRIP} and ε_{vp} from the residual strain, the ε_{vp} is first evaluated from a point of minimum. As marked in the schematic, the point occurs roughly at the end of reverse transformation and at the start of a rise in strain. The location of this point is later identified (in Section 2.3.1.2) from the strain-temperature responses. The point is in the theoretical viscoplastic domain, indicating activation of viscoplasticity. Hence, the rise in strain with temperature is assumed to occur due to viscoplasticity and thermal expansion ($\varepsilon_{vp} + \Delta\varepsilon_{th}$). The above assumption is based on the claim that damage can be neglected (see Section 2.1) and that the thermal and viscoplastic strains can be dissociated to be defined from the point of minimum.

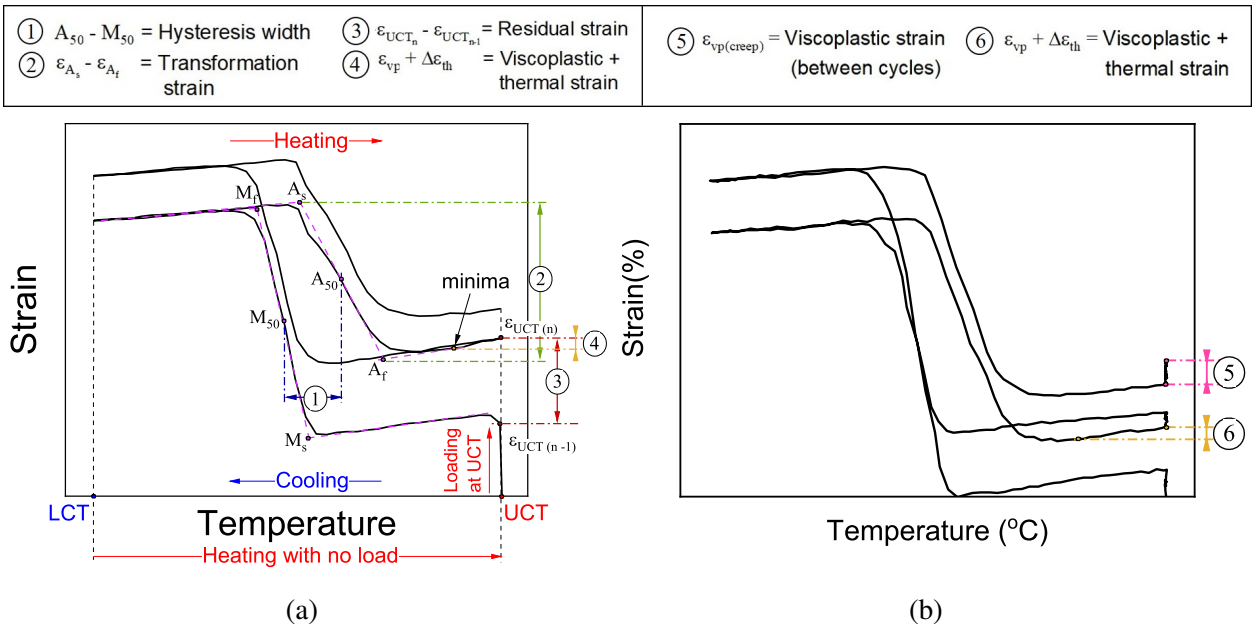

(a) (b)

Figure 2.4: (a) Schematic of a UCFTC test with graphical representation of LCT, UCT, hysteresis width, transformation strain, residual strain and the strain rise (viscoplastic strain + thermal strain). (b) Schematic of an Alternating isothermal creep and UCFTC test with graphical representation of the strain rise (viscoplastic + thermal strain) during a cycle, and viscoplastic strain between cycles while holding at UCT. Reprinted with permission from Chaugule et al. [7].

2.2.3.2 Alternating isothermal creep and UCFTC

An alternating test was conducted by loading and holding the sample at the UCT, giving rise to viscoplastic deformations. After a specific viscoplastic strain was generated, the sample was then subjected to a thermal cycle between the UCT and LCT under the same load. Subsequent to the thermal cycle, the sample was again subjected to the same load at the UCT, and the alternating sequence was continued. The schematic in Fig. 2.4(b) shows a macroscopic response of the above procedure, which is quantified similar to the UCFTC test, with an additional viscoplastic strain generated between each thermal cycle. The LCT, UCT, thermal cycling rate and load were based on the UCFTC tests. A thermal cycling rate of 10 °C/min was chosen for this experiment.

The modified UCFTC test involved sequentially activating isothermal creep and thermal cycling in an alternating manner. The test is similar to the one conducted by Raj et al.[95] on Ni-Ti SMAs, with the exception that the present test was conducted to failure. The aim was to observe an

effect of viscoplasticity over phase transformation at a fast thermal cycling rate. The effect was observed through the evolution of functional properties and quantifiers with respect to the cumulative viscoplastic strain. Since the isothermal creep was active for majority of the time, viscoplasticity became the dominating phenomenon.

2.2.4 Post experimental analysis

2.2.4.1 Differential scanning calorimetry (DSC)

In a DSC analysis, the phase transformation is identified by peaks of enthalpy released or absorbed. A reduction in enthalpy due to a reduction in volume of transformed martensite [55], i.e., accumulation of retained phases, can alter a peak's magnitude. In addition, according to Lagoudas et al. [86], a peak's position can shift due to an increase in internal stresses/energy arising from the nucleation of dislocations or precipitates. Therefore, DSC can be utilized as a tool to observe and study the shift, and change in peaks to prove the presence of internal stresses as well as retained phases.

In the present study, ex situ DSC analyses were conducted in a Labsys DSC analyzer as per ASTM standards [96]. A cylindrical sample was cut out from the sample and polished to remove any oxide layers. It was then placed in an open Alumina crucible held inside the DSC chamber. A constant heat flow was maintained in the chamber, and the temperature was cycled from a LCT (= Room temperature) to UCT (= 400 °C) and back. The rate of thermal cycling was maintained at 10 °C/min.

2.2.4.2 X-ray diffraction (XRD)

Subsequent to the DSC analyses, an ex situ XRD analysis was conducted to identify the retained phases. The XRD tests were conducted at various temperatures to track the phase transformation by analyzing the XRD peaks corresponding to each phase. Therefore, XRD was utilized as a more advanced characterization tool than DSC, in order to dissociate the phases.

An XRD analysis was first conducted at various temperatures on a virgin sample to get a base reference and then on the tested samples. This approach was followed earlier on a Ni-Ti-Hf

HTSMA by Patriarca et al. [60], which confirmed the presence of retained austenite by showing an incomplete phase transformation. Therefore, evidence of retained phases found at certain temperatures give clues about their contribution to the response of the samples at those temperatures [97]. The Rietveld refinement technique was used to analyse the X-ray diffraction data [58]. The list of peaks and their properties, obtained using the technique, corresponded to either one of the phases: B19' martensite, B2 austenite, and $(Ti+Hf)_4Ni_2O_x$ oxides which were present as non-metallic inclusions as shown in Fig. 2.5 taken from Benafan et al. [6]. We note that other secondary phases such as HfO_2 may be present in these Hf-rich alloys, but were not detected in the present study due to potentially very low volume fraction.

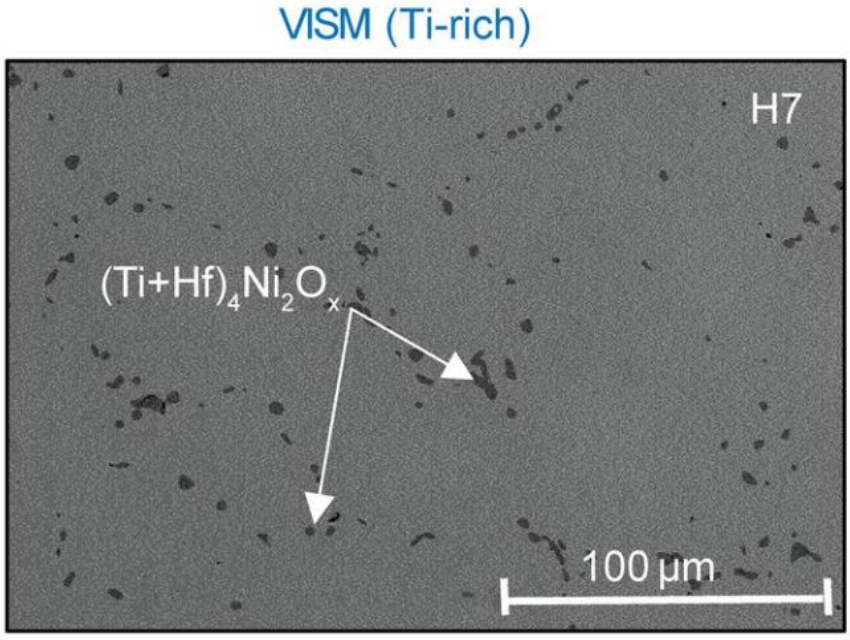

Figure 2.5: Representative SEM micrograph of Ti-rich Ni-Ti-Hf alloy obtained from samples' cross section showing the presence of $(Ti+Hf)_4Ni_2O_x$ oxides present as non-metallic inclusions. VISM: vacuum induction skull melting [6].

2.3 Results and Discussions

2.3.1 Uniaxial constant force thermal cycling

2.3.1.1 Macroscopic responses at different thermal cycling rates

Each UCFTC test was repeated at least twice (in Fig. 2.6(a)) at the three chosen rates of 1, 10 and 50 °C/min, to ensure repeatability in qualitative trends, and hence, the data shown in the following sections are from some of the individual tests. On testing each sample to failure, the position of failure in gauge section and manner of failure was noted. As observed in Fig. 2.6(b),(c), at 10 and 50 °C/min the samples failed close to the middle of the gauge section in a ductile manner. While at 1 °C/min in Fig. 2.6(a) the tested samples failed closed to one end of the gauge section in a brittle-like fashion, and revealed a transgranular crack growth mode through SEM observations (in Fig.2.7), which were also observed by Karakoc et al.[51] for similar UCFTC tests with long fatigue lives.

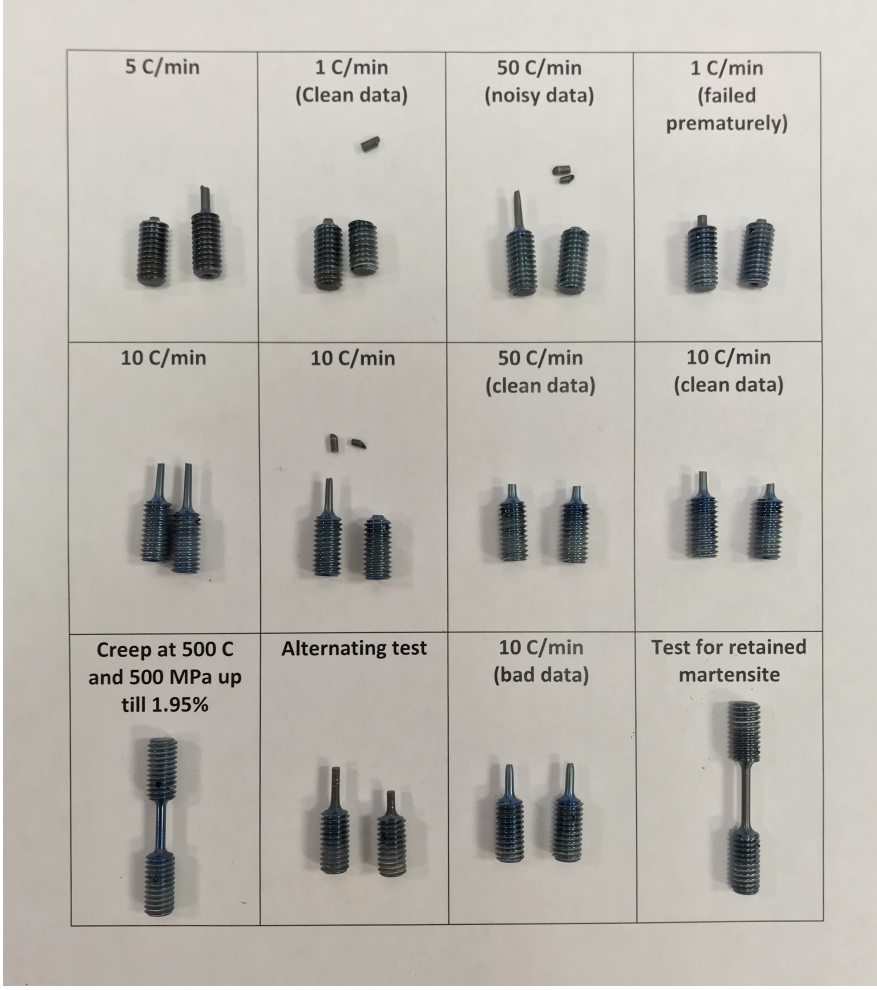

(a)

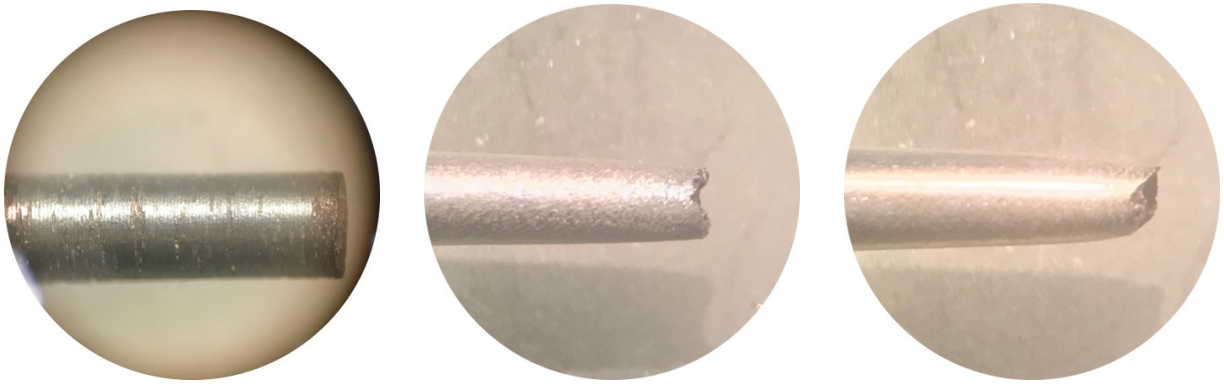

(b) (c) (d)

Figure 2.6: (a) Images of samples taken after each test. Images of gauge section after failure for the (b) 1 °C/min, (c) 10 °C/min, and (d) 50 °C/min.

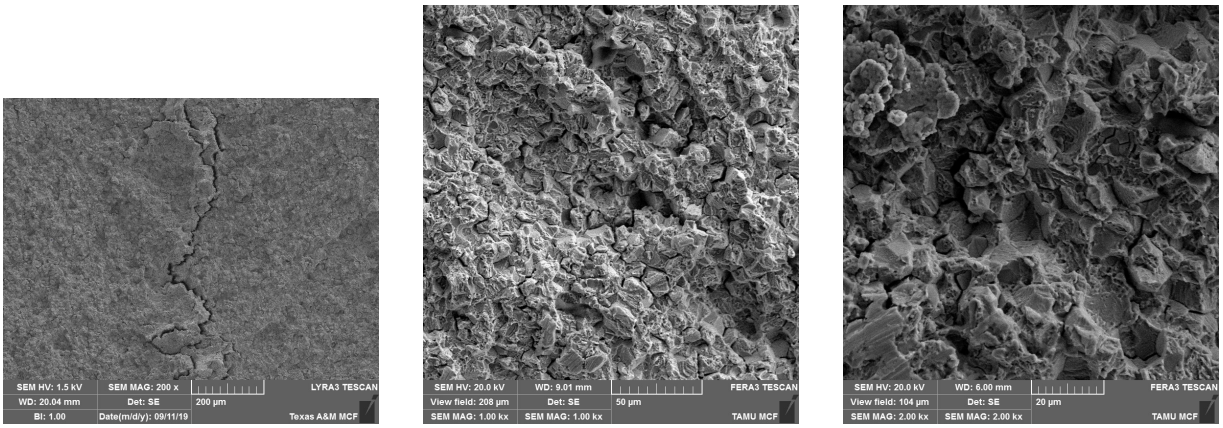

(a) (b) (c)

Figure 2.7: Scanning electron microscope images taken of the fracture surface of the sample tested at 1 °C/min at (a) 200 x, (b) 1000 x, and (c) 2000 x magnification.

The individual strain-temperature responses and strain-time responses generated from the UCFTC tests for each thermal cycling rate, are presented in Fig. 2.8. The strain-temperature and time response at 1 °C/min show a quasi-static trend, while those at 10 and 50 °C/min, show more of a dynamically evolving response. At 1 °C/min the sample is exposed to high temperatures for the most duration. Hence it is assumed to generate more viscoplasticity compared to the faster rates, resulting in a better test configuration for observing a coupling between phase transformation and viscoplasticity.

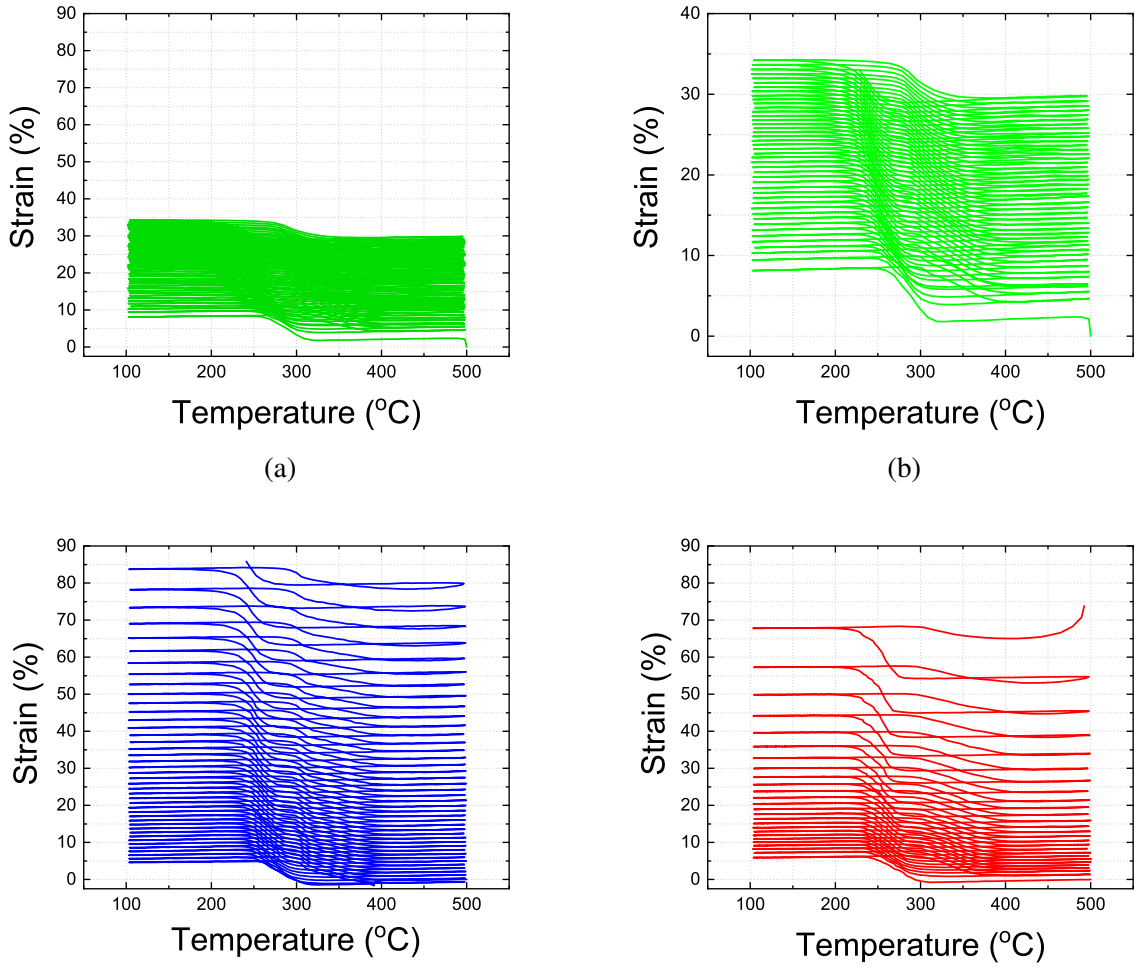

Figure 2.8: Strain-temperature responses at 500 MPa for thermal cycling rates of (a) 1 (scaled), (b) 1, (c) 10, and (d) 50 °C/min, followed by strain-time responses at 500 MPa for the rates of (e) 1 (scaled), (f) 1 °C/min. Reprinted with permission from Chaugule et al. [7].

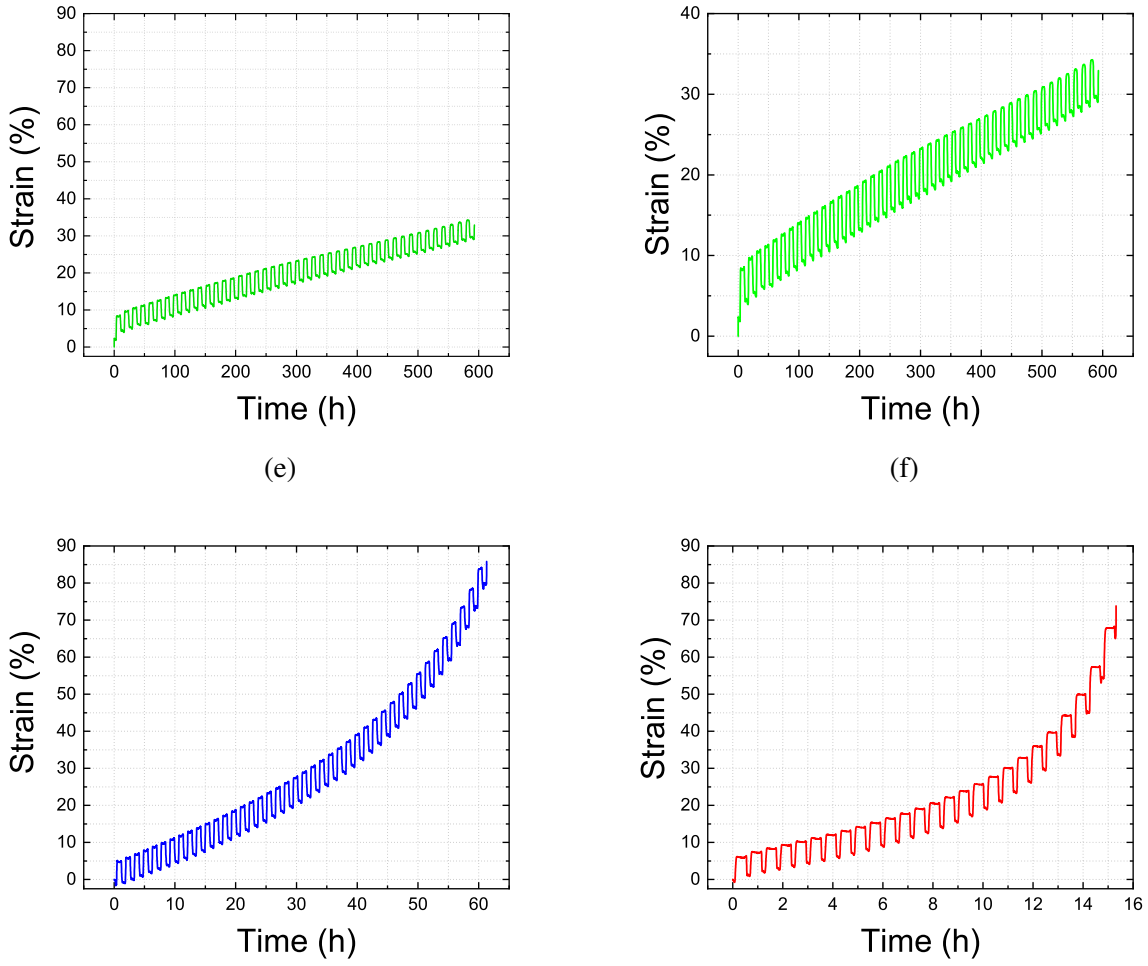

Figure 2.8: (Continued) strain-time responses at 500 MPa for the rates of (g) 10 and (h) 50 °C/min. Reprinted with permission from Chaugule et al. [7].

The strain-time responses generated from the UCFTC tests are presented together in Fig. 2.9 on the same plot to visualize and compare the responses for each thermal cycling rate. The quantities extracted from the curves are summarized in Table 2.2.

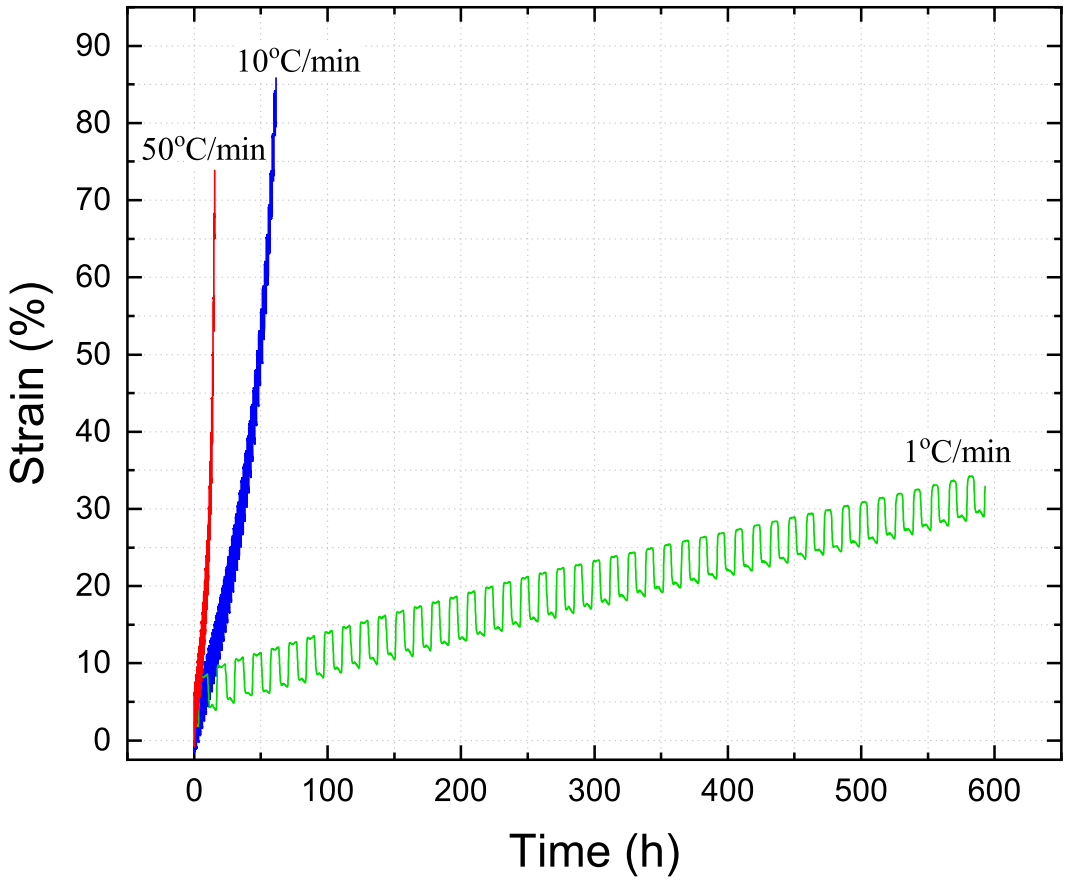

Figure 2.9: Strain-time responses corresponding to the 1, 10 and 50 °C/min thermal cycling rates, cycled between 100 and 500 °C at 500 MPa. Reprinted with permission from Chaugule et al. [7].

Table 2.2: Number of cycles, lifetime and strain to failure obtained from UCFTC at different thermal cycling rates. Reprinted with permission from Chaugule et al. [7].

Thermal cycling rate (°C/min)	*Number of cycles to failure* (N_f)	*Lifetime* (h)	*Strain at failure* (%)
1	44	592	32.9
10	42	61	85.83
50	26	15	73.84

The data indicates that the lifetime and number of cycles to failure reduced with an increase in thermal cycling rate. The lifetime (t_f) data is further used to normalize the time (t) of the respective test and create a strain-time plot, as presented in Fig. 2.10, to better visualize the strain evolution with time for each thermal cycling rate. The curves show that the strain evolution is significantly faster at higher rates, but followed the order: 10 > 50 > 1 °C/min.

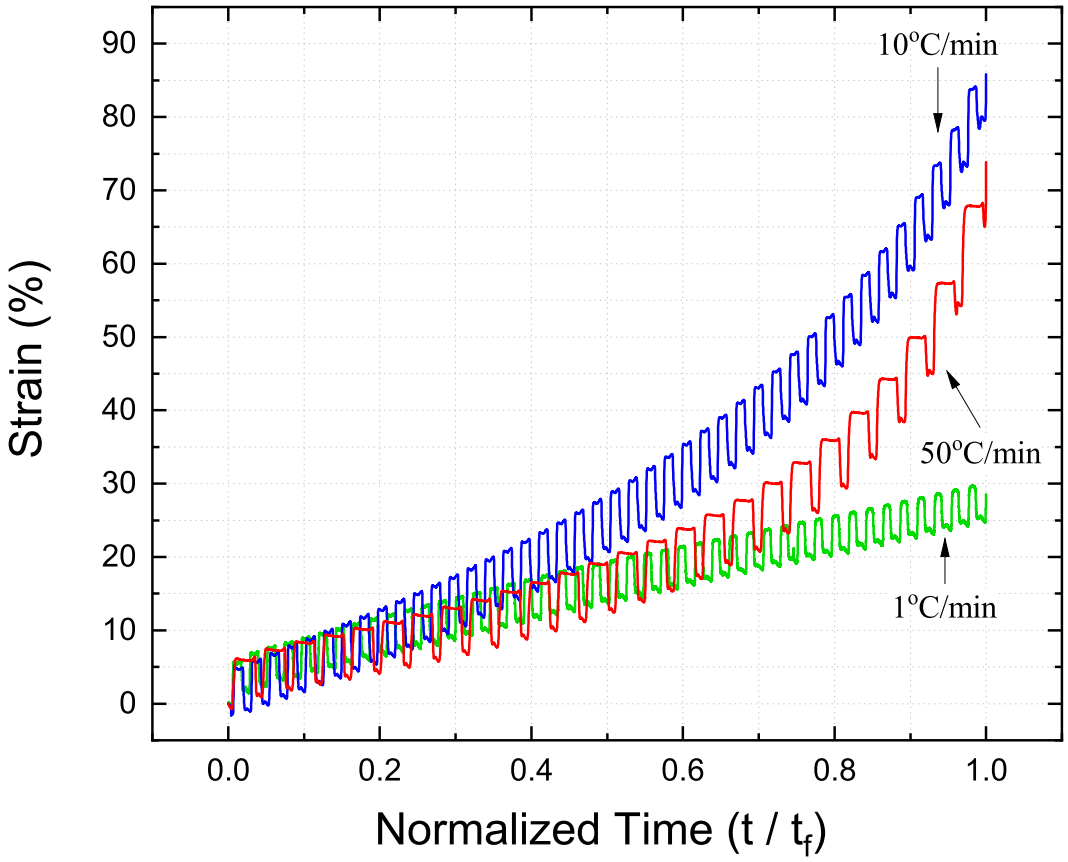

Figure 2.10: Strain-time (normalized) responses corresponding to the 1, 10, and 50 °C/min thermal cycling rates, cycled between 100 and 500 °C at 500 MPa up till failure. Reprinted with permission from Chaugule et al. [7].

Furthermore, the strain at failure data indicates the ductility exhibited also followed the order: 10 > 50 > 1 °C/min. These results can provide insights into the amount of internal stresses generated on following different thermomechanical paths. Making an analogy with isothermal creep,

wherein the ductility sustained before failure is expected to be larger when stress levels are higher and vice-versa [98, 99], it is possible to speculate the amount of internal generated stresses during UCFTC testing. Since the external stress was constant, based on the ductility, it can be speculated the internal stresses in the HTSMA samples also followed the order: 10 > 50 > 1 °C/min.Lastly, to understand the observed continuous increase in strain at each rate we investigate the residual strain in the following section.

2.3.1.2 Dissociating residual strains at different thermal cycling rates

The strain ratcheting observed in the macroscopic responses can be understood from the residual strain accumulated at the end of each thermal cycle, and the irrecoverable mechanisms responsible for it. The residual strain is first dissociated into its thermal and viscoplastic components, as mentioned in Section 2.2.3.1. The thermal strain is evaluated using the linear function, $\alpha_{CTE}.[T - T_{ref}]$, and plotted in Fig. 2.11(a), for the temperature domain 425 °C to 500 °C (in the austenite region). This domain is chosen because the point of minimum (Fig. 2.4), viz. $\approx$ 425 °C $(= 0.44 * T_m)$, lies in the theoretical viscoplastic domain (Table 2.1) for all three rates. Hence the rise in strain ($\varepsilon_{vp} + \Delta\varepsilon_{th}$) is also evaluated from the point of minimum.

The viscoplastic strain (ε_{vp}) is then calculated from the difference between the rise and $\Delta\varepsilon_{th}$ (= 8.595 x 10^{-4}). Its cumulative value is then evaluated and plotted, as shown in Fig. 2.11(b), and is observed to be inversely proportional to the rate overall. The viscoplastic strain arises from the dislocation density generated at high temperatures [1], implying the slower rates will generate more viscoplasticity compared to faster ones, which is consistent with what is observed for all the rates, but for 1 °C/min, its only up till 50%. As from 50 to approximately 80%, the viscoplastic strain at 1 °C/min decreases, whereas for 1 (repeat) 10 and 50 °C/min it keeps increasing. The decrease at 1 °C/min is speculated to occur because of static recovery as the test lasts much longer (at higher temperatures) and is assumed to develop smaller internal stresses than the other rates. Therefore, the production of dislocations becomes slower than their annihilation. These effects were not observed in the repeat test at 1 °C/min, however the test ended prematurely (under 300 h) when the sample failed at one of its ends. On the other hand, at faster rates, static recovery is

reduced and the higher internal stresses generated lead to viscoplastic strains that keeps increasing for 10 and 50 °C/min. Beyond 80%, the strain at 50 °C/min increases sharply compared to 10 °C/min. This can represent an effect of potential damage mechanisms and structural changes such as necking of the sample, and is explained later through the residual strain trends.

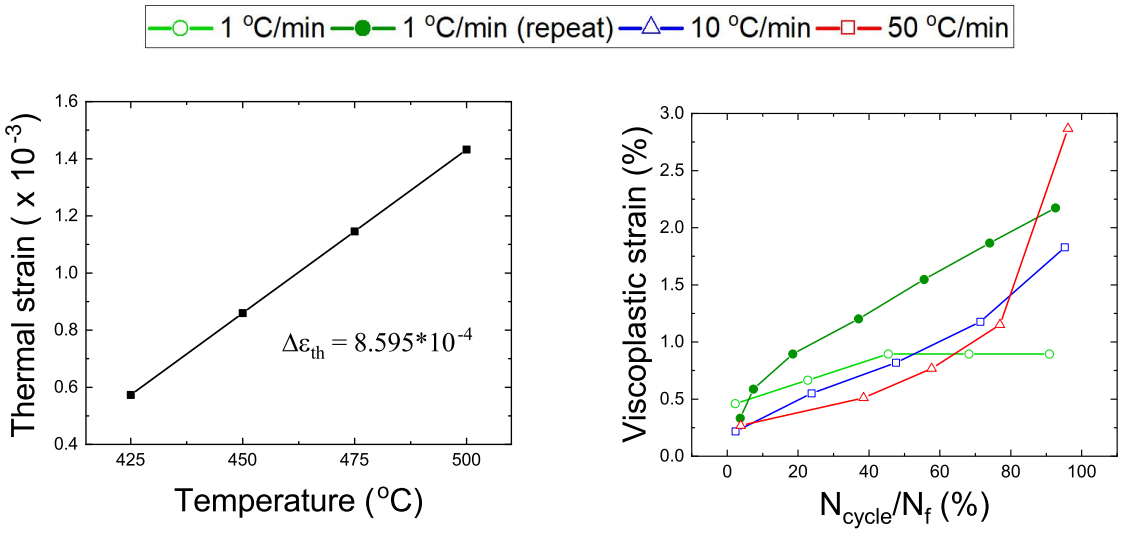

(a) (b)

Figure 2.11: Evolution of (a) thermal strain in austenite, (b) cumulative viscoplastic strains generated during UCFTC at 1, 1 (repeat), 10 and 50 °C/min thermal cycling rates. Modified with permission from Chaugule et al. [7].

The residual strain at the end of each cycle, and its cumulative value is evaluated and plotted, as shown in Fig. 2.12(a). The cumulative strain is observed to increase with cycling and evolve differently for each rate. During the initial thermal cycles, the 1 °C/min condition is observed to produce the largest amount of residual strain followed by 1 (repeat), 50 and 10 °C/min, up until $\approx$ 50%. After that, the 10 and 50 °C/min start to dominate over the 1 °C/min with similar strain magnitudes and evolutions up to $\approx$ 80%. Beyond 80%, they become larger for faster rates (50 > 10 > 1) with increased non-linearity. These trends can be the result of necking of the sample and damage mechanisms (inferred from the transverse cracks in Fig. 2.6). Necking of the samples close to failure (> 80%) increases the true stress significantly, which can result in a non-linear rise of the

residual strain. On the other hand, according to continuum damage mechanics theory [100], higher stresses can be related to increased non-linearity, and hence, the increased non-linear evolution of residual strains can be similarly related to higher internal stresses. Therefore, the internal stresses are inferred to increase with the thermal cycling rate in a monotonic manner (1 < 10 < 50 °C/min) beyond 80%. These trends, hence, indicate an effect of necking and potential damage mechanisms whose contribution cannot be neglected anymore, and dissociating them from the effect of the coupling is out of the scope of this study (Section 1). Therefore, they are not investigated for the residual and the other irrecoverable strains.

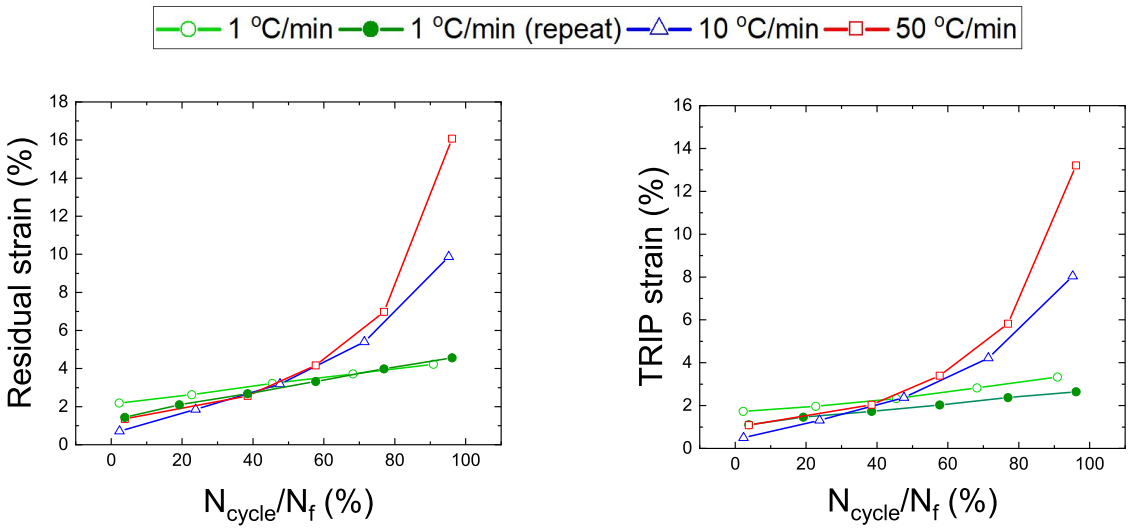

(a) (b)

Figure 2.12: Evolution of (a) cumulative residual strains (b) cumulative TRIP strains, generated during UCFTC at 1, 1 (repeat), 10 and 50 °C/min thermal cycling rates. Modified with permission from Chaugule et al. [7].

Lastly, on dissociating the viscoplastic contribution from the residual strain, the TRIP strain is evaluated for each cycle, and its cumulative value is plotted for each rate in Fig. 2.12(b). Based on the magnitude and trend, it can be reckoned that it is a major component of the residual strain and exhibits rate-dependency. According to Sehitoglu et al. [13], TRIP strain arises from the dislocations generated at the martensite-austenite interfaces during transformation, due to a mismatch

between the two phases resulting in slip. The mismatch creates coherency stresses that can relax depending on the rate of cycling. Slower rates will have more time to relax the coherency stresses than the faster ones. Hence, they result in smaller plastic deformation at the interfaces giving rise to smaller TRIP strains.

As observed in Fig. 2.12(a), the TRIP strain magnitude at 10 and 50 °C/min is consistent with the theory of coherency stresses. However, the order of TRIP strain is 1 > 1 (repeat) ≈ 50 > 10 °C/min in the initial 50% , which is in contradiction with the above theory. The large TRIP strain generated at 1 and 1 (repeat) °C/min, by the end of reverse transformation, can be speculated to have a contribution from retained martensite trapped by dislocations accumulated during TRIP and viscoplasticity, as assumed in Section 2.2.3.1. However, while we acknowledge the effect of such mechanisms, it is not known how much of a contribution exists at this point. In addition, if the above speculation is right, the coherency stresses generated at the slow rate are indeed not small due to the presence of retained martensite.

2.3.1.3 Quantifying contribution of retained martensite

In order to quantify the contribution of retained martensite to the TRIP strain, a separate UCFTC test was performed at 10 °C/min, under 500 MPa for a fixed number of cycles. The 10 °C/min rate as it too showed signs of accumulation of retained martensite (shown later in Section 2.21). The number of cycles were estimated based on the N_f (= 42 in Table 2.2) of the previous UCFTC test at 10 °C/min. The cycles were chosen based on the assumption that it falls between 50 to 80% of N_f, in order to ensure the possibility of accumulation of retained martensite, and to avoid the region affected by potential damage mechanisms. At the end of the thermal cycles, the sample was unloaded to a very small load (≈ 10 MPa) and subjected to a heat treatment, which involved heating the sample to 700 °C at a rate of 50 °C/min. The sample was then cooled and the response is shown in Fig. 2.13.

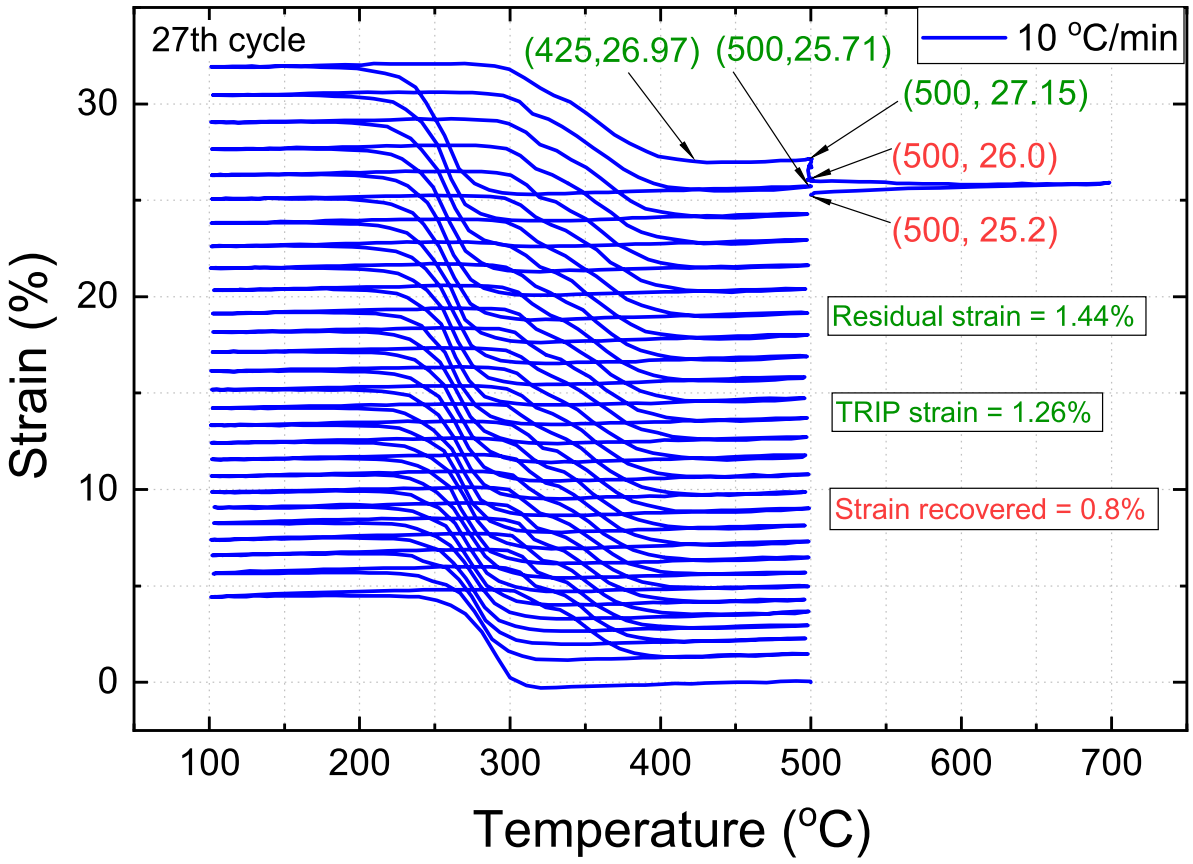

Figure 2.13: UCFTC test performed at 10 °C/min under 500 MPa between 100 and 500 °C for a limited number of cycles, followed by unloading and then a heat treatment up to 700 °C and back to 500 °C to obtain contribution of retained martensite to the residual strain. Reprinted with permission from Chaugule et al. [7].

Based on the values in the plot, in the 27^{th} cycle, the residual strain generated is 1.44%, and corresponding TRIP strain is 1.26%. On unloading at the end of the cycle, and conducting the heat treatment, the strain is observed to decrease by 0.8%. Since the sample is under minimal load during the heat treatment the contribution from elastic and viscoplastic strain is negligible. Therefore, the possible phenomena occurring during the strain recovery are, thermal expansion/contraction, static recovery followed by transformation of retained martensite. The thermal expansion and contraction cancel out at the end of the heat treatment. So the decrease in strain can be mainly due to the recovery and transformation of retained martensite which amounts to 0.8%. Dissociating the

contribution of retained martensite from the recovery in the 0.8% is out of the scope of this study.

Therefore, it can be reckoned that, for the TRIP strain of 1.26% generated in the 27^{th} cycle ($\approx$ 50 - 80% of N_f) the contribution of retained martensite is equal to or less than 0.8%, which is a *63.4%* contribution. This contribution is not a definitive conclusion, as it can vary based on the rate of cycling, the thermomechanical conditions, and the cycle number at which the heat treatment is performed.

2.3.1.4 Transformation temperatures at different thermal cycling rates

The macroscopic responses can be further investigated to understand the phase transformation behavior, by evaluating the characteristic TTs (M_f, M_s, A_s, A_f). The evolution of the TTs are plotted as a function of the normalized number of cycles (N_{cycles}/N_f: where N_f is number of cycles to failure), as presented in Fig. 2.14(a - d), and represented as % hereafter. It helps in comparing responses and trends generated under different conditions, on a common scale. As observed from the plots, the temperatures M_f, M_s and A_s evolve and decrease to lower temperatures with cycling, while the temperature A_f increases with cycling, but only at 10 and 50 °C/min. According to Kumar et al. [3], internal stresses generated during plasticity/viscoplasticity can assist the reverse transformation and oppose the forward transformation resulting in a decrease in A_s and M_f, respectively. This is a trend which is presently observed for all the three rates.

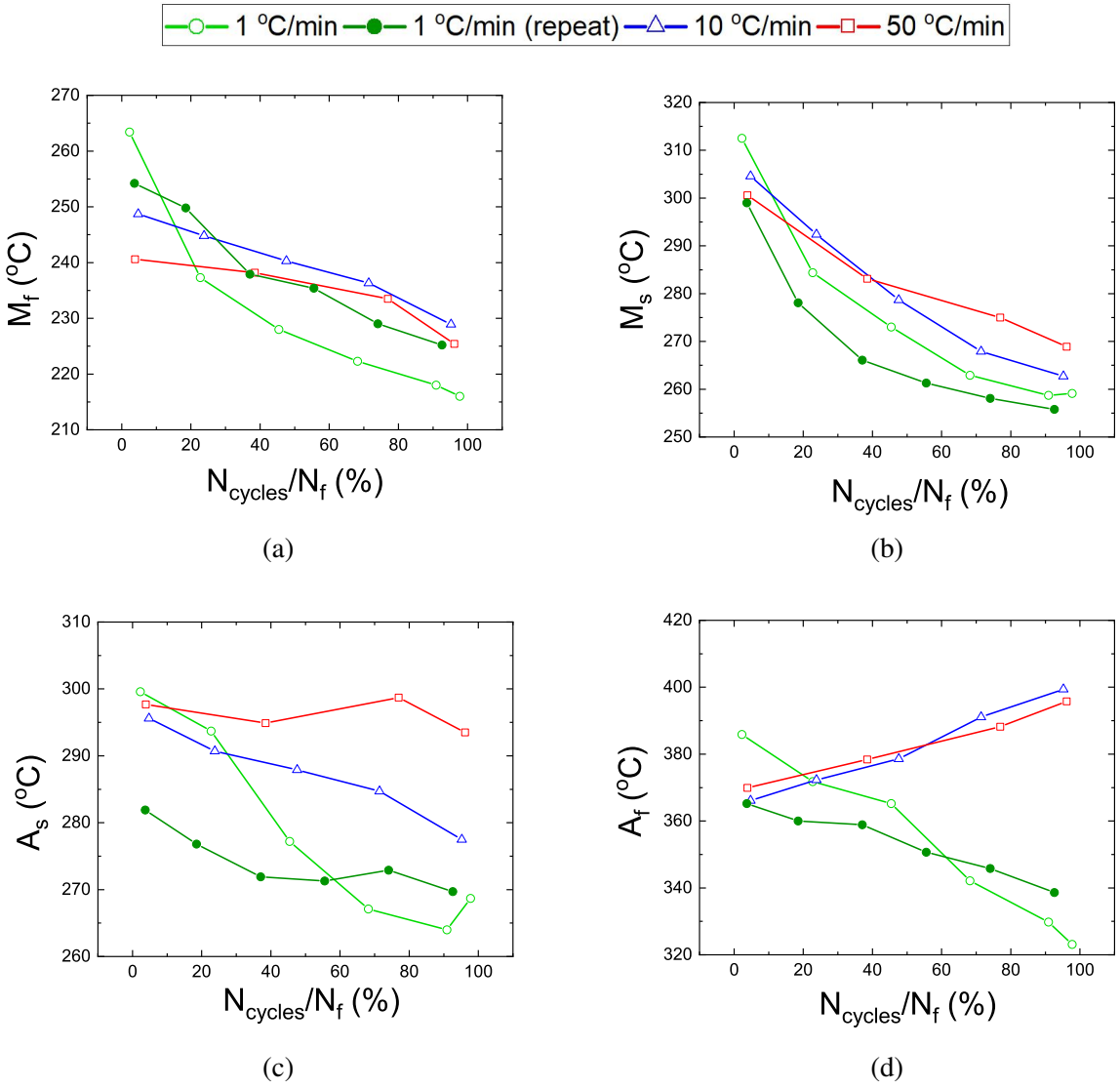

Figure 2.14: Evolution of transformation temperatures (a) M_f, (b) M_s, (c) A_s, and (d) A_f, with respect to the normalized number of cycles (N_{cycles}/N_f) for the 1, 1 (repeat), 10 and 50 °C/min thermal cycling rates. Modified with permission from Chaugule et al. [7].

Based on the TT and the corresponding strains, the slopes of the forward $(\varepsilon_{M_f} - \varepsilon_{M_s})/(M_s - M_f)$ and reverse $(\varepsilon_{A_s} - \varepsilon_{A_f})/(A_f - A_s)$ transformations, are further evaluated and plotted in Fig. 2.15(a),(b). With cycling, an overall increase is observed in the forward slopes for 1 (repeat), 10 and 50 °C/min, and in the reverse slopes for 1 and 1 (repeat) °C/min. Also with cycling, an overall decrease is observed in the forward slope for 1 °C/min, and in the reverse slopes for 10

and 50 °C/min. According to Hamilton et al. [2], an increase in (forward/reverse) slope signifies a dissipation of stored elastic energy coming from plastic (or viscoplastic) accommodation. In case of the forward path, there is a decrease in undercooling (less cooling for transformation), while in case of the reverse path, there is an increase in overheating (more heating for transformation).

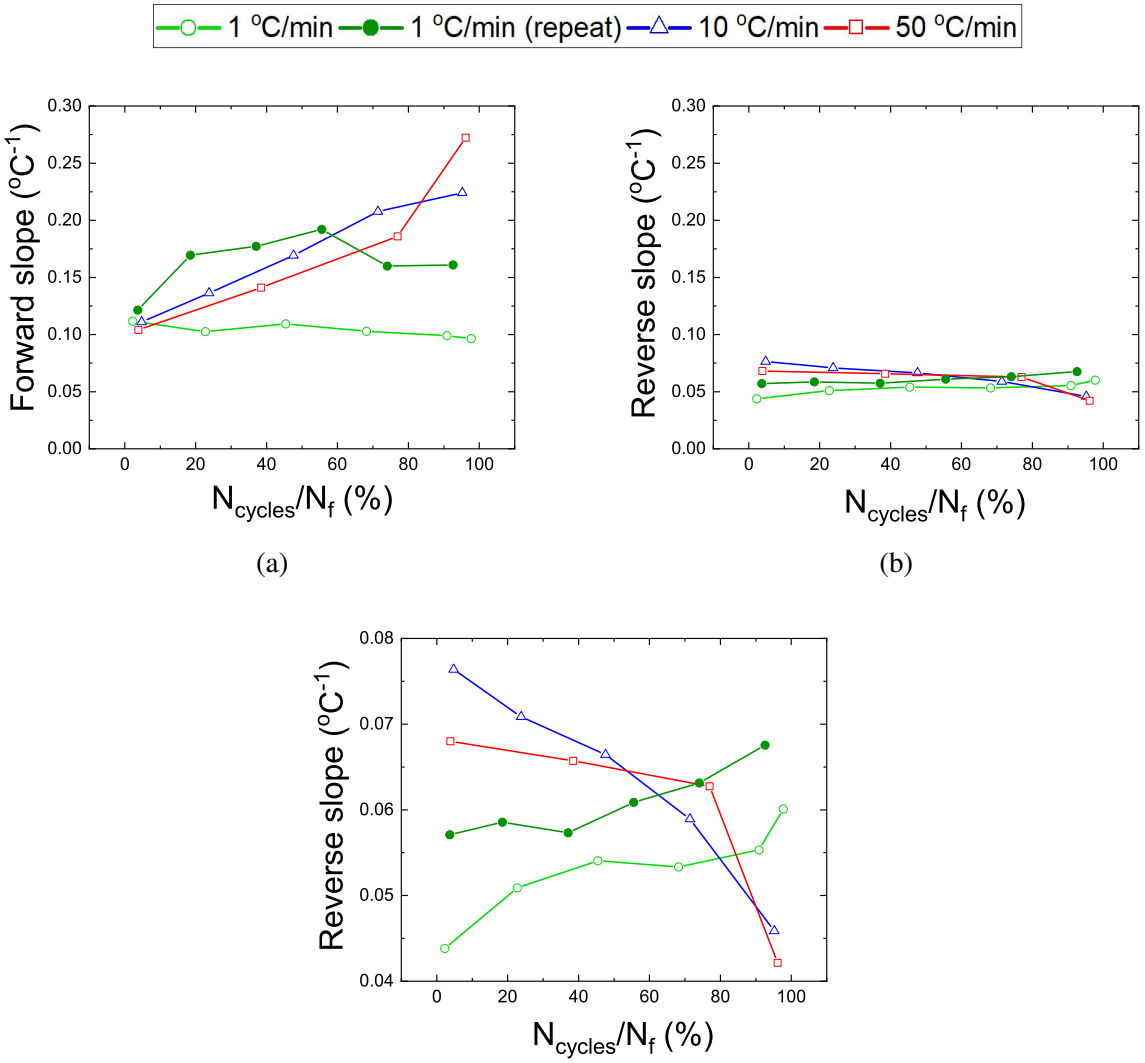

Figure 2.15: Evolution of transformation temperatures slopes of (a) forward ($(\varepsilon_{M_f} - \varepsilon_{M_s})/(M_f - M_s)$), (b) reverse ($(\varepsilon_{A_s} - \varepsilon_{A_f})/(A_s - A_f)$), and (c) scaled reverse transformation paths, with respect to the normalized number of cycles (N_{cycles}/N_f) for the 1, 1 (repeat), 10 and 50 °C/min thermal cycling rates. Modified with permission from Chaugule et al. [7].

In the present study, the dissipation is assumed to be generated majorly by TRIP (elaborated later in Section 2.3.1.2) during the forward path, and by TRIP and viscoplasticity during the reverse path, as viscoplasticity initiates in the reverse path. This assumption can explain the increase in forward slope for the 1 (repeat), 10 and 50 °C/min due to plastic (TRIP) accommodation (see Section 2.3.1.2), and the increase in reverse slope for 1 and 1 (repeat) °C/min due to plastic and viscoplastic accommodations. The accommodations (along reverse path) is also reflected by the decrease in A_f (in Fig. 2.14(d)) for 1 and 1 (repeat) °C/min. As the experimental evidence of accommodations (during martensitic transformation) in other metal alloys, influenced constitutive modeling studies [101, 102, 38], the above indication of plastic (or viscoplastic) accommodations can influence potential modeling studies of HTSMAs.

The decrease in reverse slope for 10 and 50 °C/min signifies a delay in complete transformation, which can be due to an increased resistance to transformation. The increased resistance can stem from either retained martensite or TRIP dislocations which are not accommodated. TRIP dislocations because, at fast rates it is the dominant mechanism (Fig. 2.12(b)). The continuously-increasing internal stresses generated by dislocations from TRIP push (or delay) the Af to higher temperatures while cycling under stressed conditions, which is also observed in the increased A_f (in Fig. 2.14(d)) at 10 and 50 °C/min. Lastly, the (unusual) overall decrease in forward slope at 1 °C/min can be the result of static recovery (as observed later in Fig. 2.11(b)), which reduces the amount of viscoplasticity generated, and its related dissipation.

2.3.1.5 Hysteresis at different thermal cycling rates

The characteristic TT aid in quantifying the hysteresis ($= A_{50} - M_{50}$), whose evolution is plotted in Fig. 2.16, and is observed to constantly increase for each rate (overall) with cycling. Based on the knowledge that phase transformation is an athermal process [103], the transformation fronts can be considered to move at the same speed, irrespective of the thermal cycling rate [104]. However, due to varying cycling rates, each transformation front can interact differently with crystallographic defects, such as dislocations [2] and pockets of phases trapped by them. As a result, the hysteresis generated during this interaction, will exhibit an evolution varying from

rate to rate resulting in a widening (10, 50, and 1 (repeat) °C/min) or narrowing (1 °C/min) with cycling.

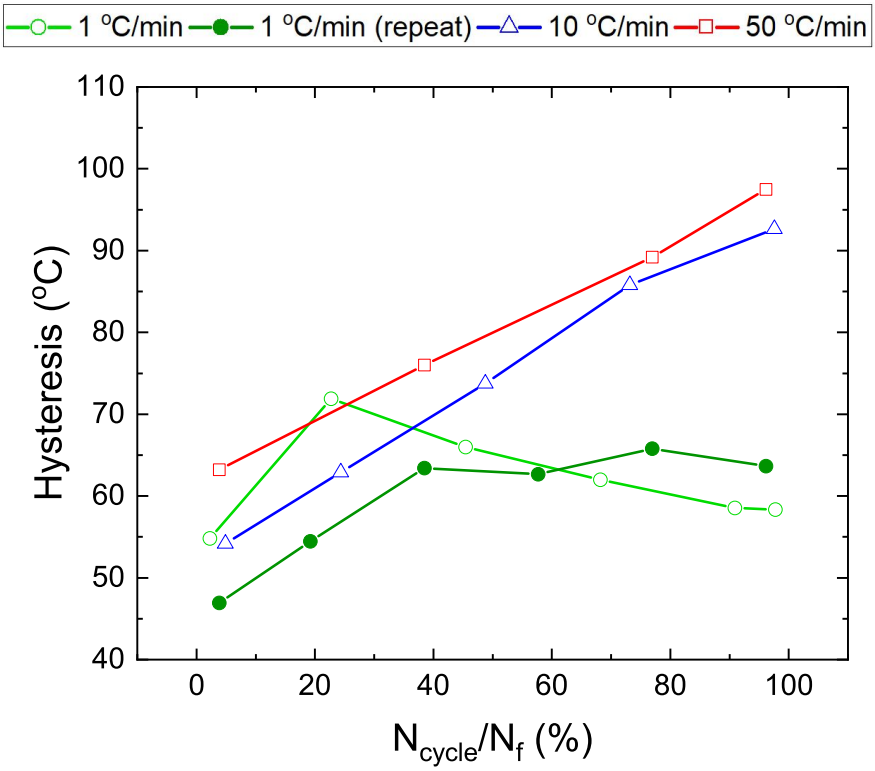

Figure 2.16: Comparison of hysteresis ($= A_{50} - M_{50}$) generated during UCFTC at 1, 1 (repeat) 10 and 50 °C/min thermal cycling rates, as a function of the normalized cycle number. Modified with permission from Chaugule et al. [7].

The widening or increase in hysteresis (with cycling) occurs as defects accumulate [105] and increase the resistance to transformation fronts, causing dissipation of stored energy [2] (also reflected by the TT slopes). The different evolution at each rate, signifies a contrasting amount of defect accumulation with time, and conforms a rate-dependency in the behavior. On the other hand, the narrowing or decrease in hysteresis at 1 °C/min, after 20%, can be due to one of the two reasons: 1) at the slow rate of 1 °C/min the fronts have sufficient time to find alternative routes, instead of overcoming the resistance in their path, or 2) some of the dislocations get annihilated

when the sample is subjected to high temperatures for a longer duration, inducing static recovery (also speculated by [50]), and leading to a decrease in resistance and hysteresis. Since a static recovery was not observed in the 1 (repeat) °C/min test, its hysteresis increased overall.

2.3.1.6 Transformation-strain at different thermal cycling rates

The strains at the characteristic TT can be used to evaluate the recovered strain, i.e., transformation strain ($= \varepsilon_{A_s} - \varepsilon_{A_f}$), and get insights on the martensite phase and its variants. The strain is plotted in Fig. 2.17 and is observed to increase and then decrease for every rate at different % of cycles. According to Kockar et al. [57], internal stress fields generated by dislocations can cause preferred (biased) martensite variants to nucleate and grow, a form of reorientation, leading to an increase in their volume fraction. This results in increasing the transformation strain with cycling. Therefore, based on the magnitude of transformation strain at each cycle, the amount of internal stresses generated with respect to the rate is speculated to follow the order: 10 > 50 > 1 °C/min, which corroborates with the ductilities.

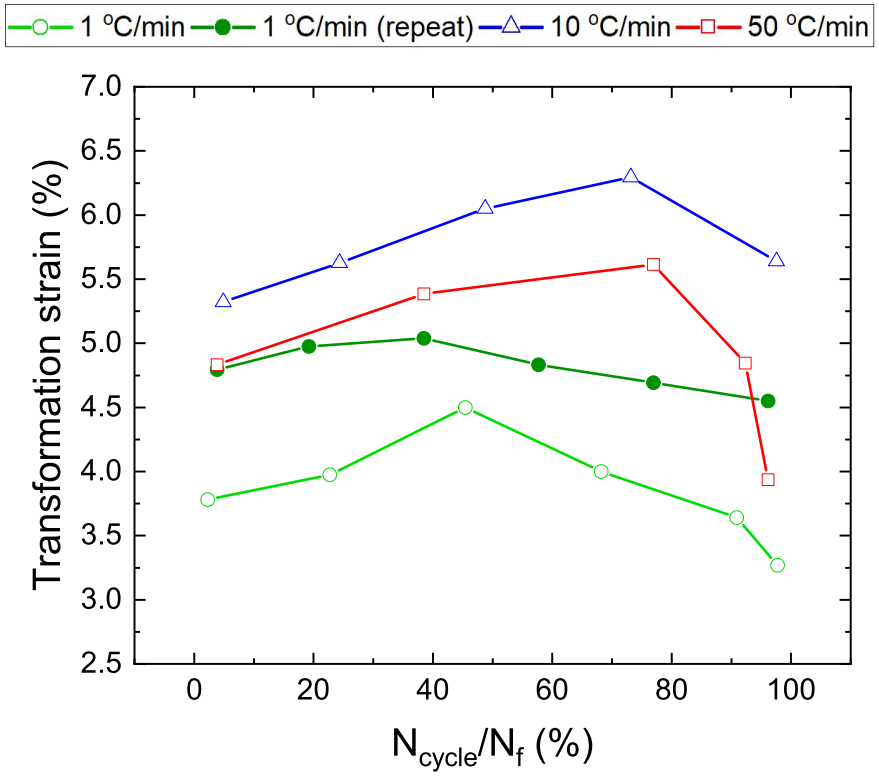

Figure 2.17: Comparison of transformation strain ($= \varepsilon_{A_s} - \varepsilon_{A_f}$) generated during UCFTC at 1, 1 (repeat), 10 and 50 °C/min thermal cycling rates, as a function of the normalized cycle number. Modified with permission from Chaugule et al. [7].

On the other hand, the decrease in transformation strain after so many cycles can imply that either the internal stresses are not favouring the variants of martensite to grow, or there is incomplete transformation due to accumulation of retained martensite by dislocations [52]. Kumar et al. [50] observed the accumulation of retained martensite during an isobaric thermal cycling involving viscoplasticity. The above study reported an identical decrease in transformation strain for two specimens cycled at different rates, while resulting in different irrecoverable strains at the end of the cycling. The present results show no identical decrease in transformation strain for different rates, which contradicts Kumar et al.'s observation. This can be explained by the different amount of retained martensite accumulated based on the rates and the irrecoverable mechanisms.

2.3.2 Post-experimental analyses: Determining retained phases

The responses and interpretations from the UCFTC tests presented earlier lead towards the presence of retained phases contributing to the irrecoverable strains. In order to justify their presence and identify them, post-experimental analysis, such as DSC and XRD, were conducted on the UCFTC tested samples at 1, 10, and 50 °C/min. These analyses can reveal the coupling that occurred between the inelastic phenomena based on their signatures left in the microstructure.

2.3.2.1 Differential scanning calorimetry (DSC)

A DSC analysis was first conducted on a virgin sample of the alloy to obtain a base curve. The curve represents a plot of the normalized heat flow vs. sample temperature. DSC analyses were then conducted on the tested samples and their curves were compared with the base reference, as shown in Fig. 2.18. The data shows, a shift and reduction in size of the peaks (shown by the arrows) with respect to that of a virgin sample. The magnitude of the shift and size reduction with respect to rate followed the order: 10 > 50 > 1 °C/min. Based on this result and the theory in Section 2.2.4.1, it can be speculated that the amount of internal stresses and retained phases generated also followed the same order. This order corroborates with the one inferred from ductility (Fig. 2.9) and transformation strain (Fig. 2.16 (b)) data. In comparison to the virgin sample, the transformation peaks shift to lower temperatures due to internal stresses generated on cycling at the high stress of 500 MPa, and going to a high UCT of 500 °C. This shift corroborates with the trends shown by M_s, M_f, and A_s at all the three rates, and A_f at 1 °C/min in Fig. 2.14. However, the A_f increases at 10 and 50 °C/min, and this increase does not corroborate with the reduced A_f shown by the DSC thermograph. As mentioned in Section 2.3.1.4, it is speculated that the A_f increases with cycling due to the internal stresses created by dislocations and accumulated retained martensite, but that may not be enough to explain why the A_f values show a decreased in the DSC thermographs. In addition, there is no study done on the Ni-Ti-Hf alloy at a stress level of 500 MPa and UCT of 500 °C, and hence, it is difficult to make a judgment on the above discrepancy. To look at DSC thermographs of a (Ni-rich) Ni-Ti-Hf alloy obtained from samples tested at stresses ranging from

200 to 500 MPa, and UCT ranging from 300 to 350 °C, the reader is referred to the works of Karakoc et al. [51, 54].

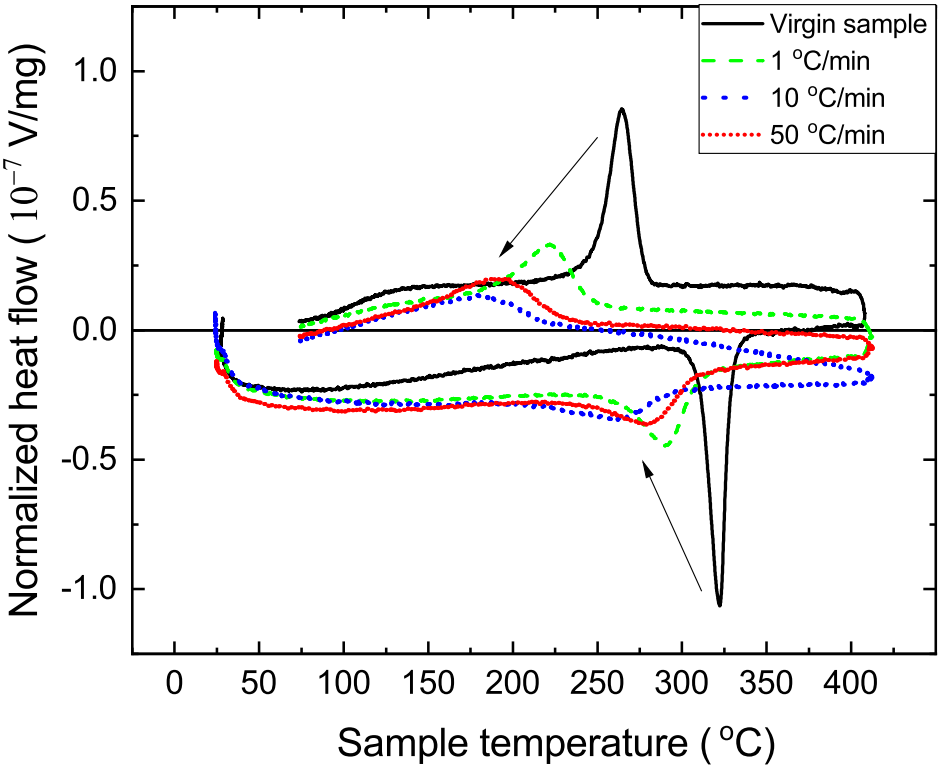

Figure 2.18: Comparison of DSC thermographs conducted on the tested (and failed) samples at 1, 10 and 50 °C/min and a virgin sample. Reprinted with permission from Chaugule et al. [7].

In order to confirm that internal stresses and retained phases were responsible for modifying the peaks, subsequent to performing the DSC analyses, the samples were heat treated to 750°C. This was done in order to annihilate the dislocations present and release the stored internal stresses and trapped phases. Consequently, DSC analyses were performed again on each sample under the same conditions as before, to check for a change in peaks due to the above heat treatment. As observed in Fig. 2.19(a-c), the peaks returned close to that of a virgin sample for all the cases, justifying the presence and effect of internal stresses and retained phases. However, the heights of all the resulting peaks are smaller and their positions are shifted with respect to that of the virgin

sample. *Note:* The DSC analyses on the tested samples were conducted before the XRD analyses, but the heat treatment and post DSC analysis were conducted after the XRD analysis.

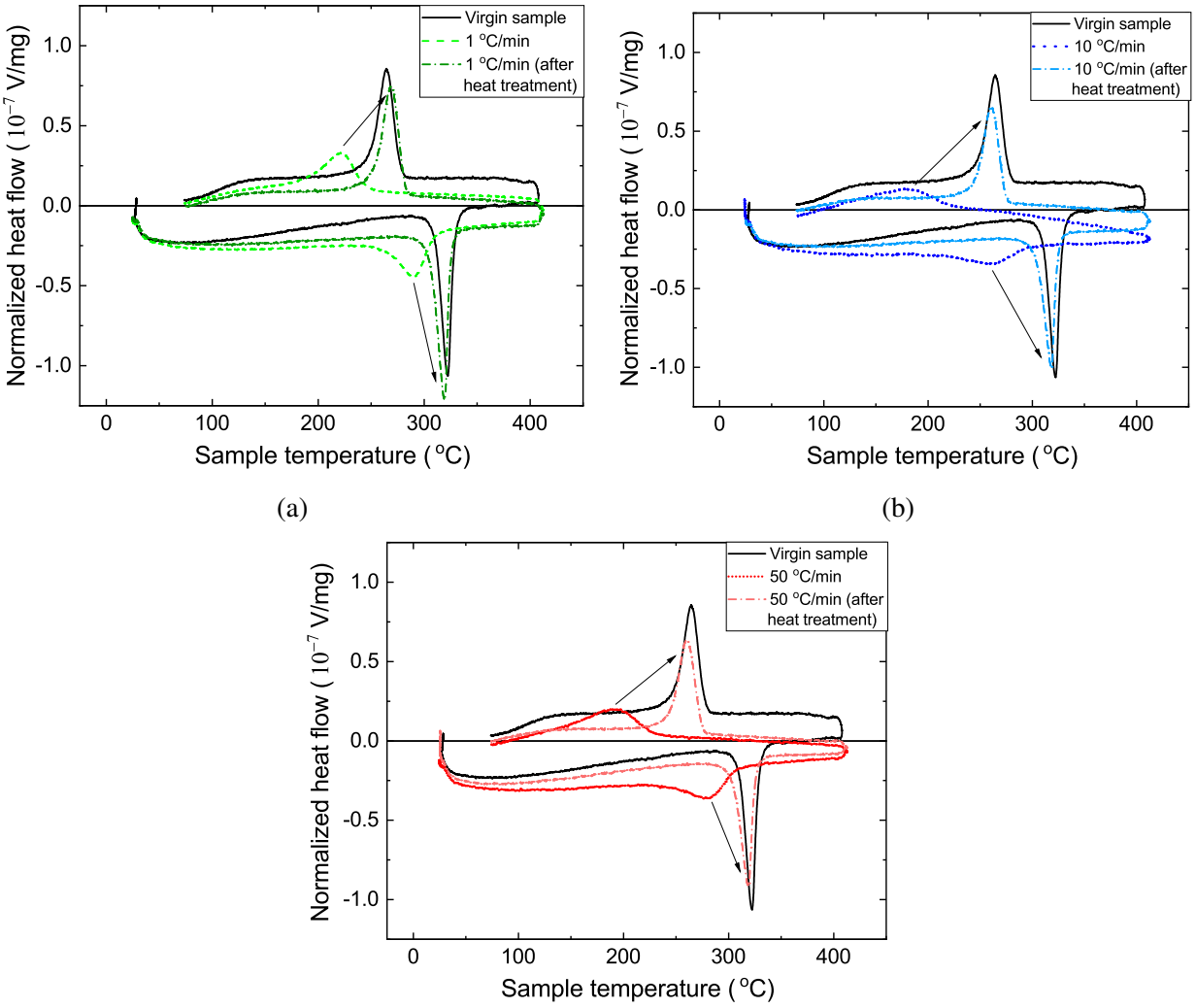

Figure 2.19: Comparison of DSC thermographs after conducting heat treatments on the tested samples for (a) 1 °C/min (b) 10 °C/min and (c) 50 °C/min, with respect to those of a virgin sample. Reprinted with permission from Chaugule et al. [7].

2.3.2.2 X-ray diffraction (XRD)

As described in Section 2.2.4.2 the XRD data (normalized intensity vs. scanning angle) from the virgin sample is shown in Fig. 2.20 with peaks corresponding to phases: B19' martensite, oxide, and B2 austenite labelled as m, o and a, respectively. Most of the peaks present at room temperature (R.T.) are those of B19' with two peaks of oxide. The B19' peaks are consistent with those obtained by Potapov et al. [106]. The oxide phase is present in the form of inclusions that gets introduced during the melting process of this alloy.

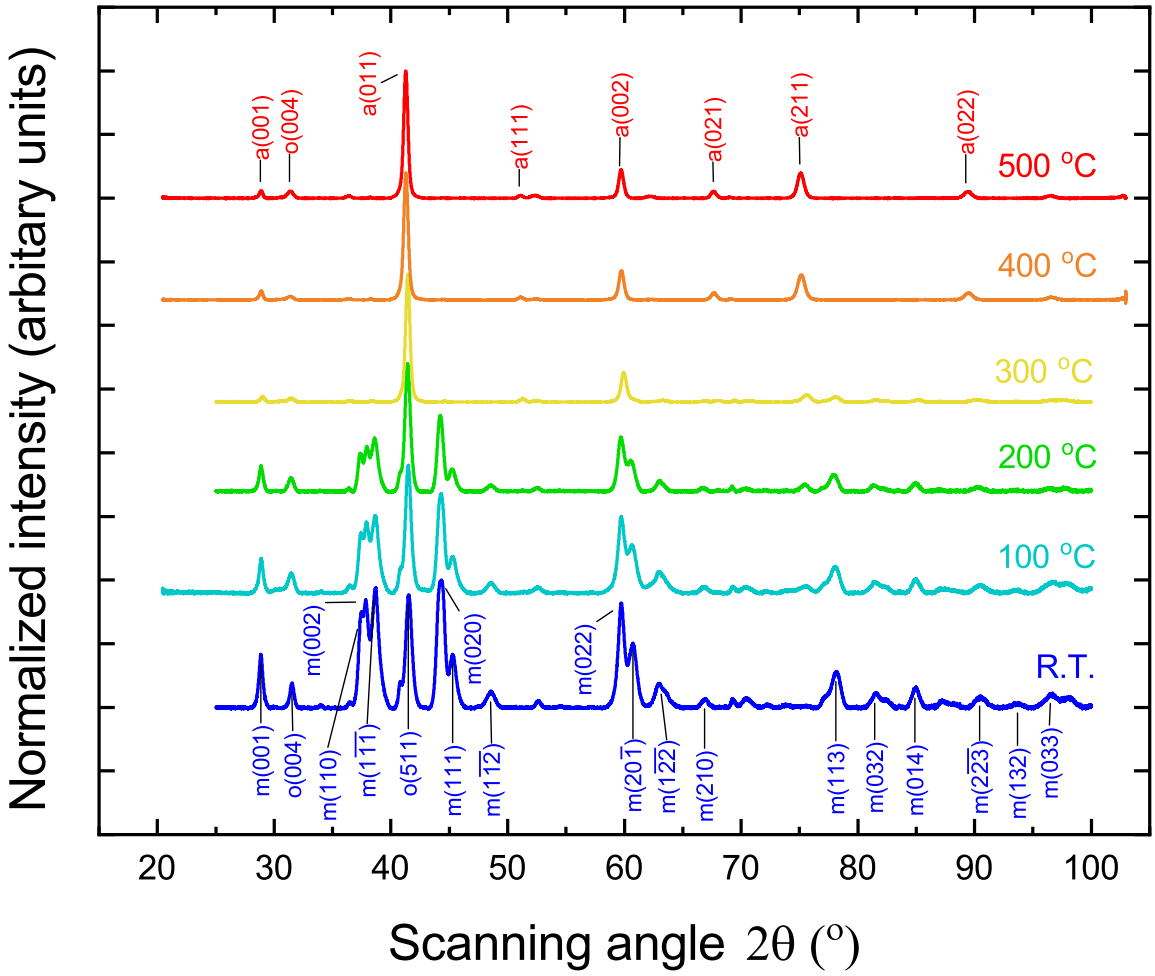

Figure 2.20: XRD data obtained from virgin sample scanned at temperatures from R.T. to 500 °C in increments of 100 °, with peaks of B19', B2 and oxides labelled as m, o and a respectively, at R.T. and 500 °C. Reprinted with permission from Chaugule et al. [7].

As the temperature is raised above R.T., the marked B19' peaks decrease in intensity and disappear by 300 °C, which is close to A_f ($\approx$ 306 °C). The B2 peaks start to appear and their intensity increases as the temperature reaches 500 °C. Therefore, we observe a complete phase transformation of martensite $\rightarrow$ austenite. There are no evidences of retained phases as there are no B2 peaks present at R.T. or B19' peaks present at 500 °C. However, the oxide peak (004) remains as it does not transform. These observations can be used as a base reference for comparing peak locations, intensities, and phases present at specific temperatures, with the data of the tested samples. The entire spectrum of XRD data from individual samples is presented in Section 2.5.2 in the supplementary material.

The XRD data obtained from each tested sample is compared at specific temperatures (see Fig. 2.21(a-d)) to investigate the presence of retained phases. The intensity of each peak is normalized with respect to the maximum intensity in the data set at that temperature, in order to compare with different data sets. The TT: M_f of the virgin sample is 259.5 °C while those of the tested samples falls between 260 - 270 °C (Fig. 2.14(a)). Hence, the XRD data below these temperatures, i.e., at R.T. and 100 °C (Fig. 2.21(a),(b)), was checked for evidence of retained austenite (B2) trapped in the martensite phase. There were no peaks corresponding to B2 found in the tested samples.

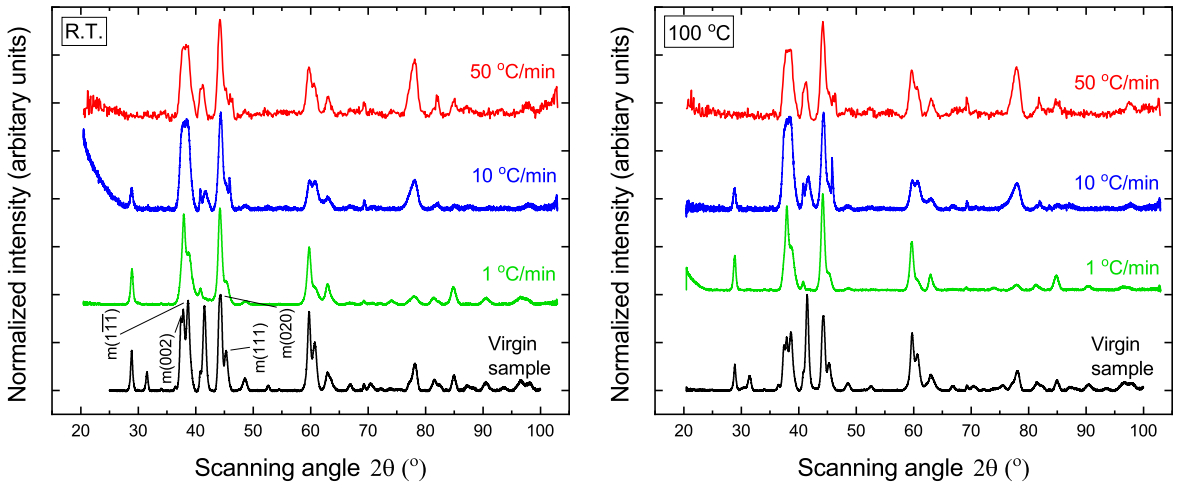

(a) (b)

Figure 2.21: XRD data generated from each UCFTC tested sample is compared with the virgin sample, at (a) R.T., (b) 100 °C. Reprinted with permission from Chaugule et al. [7].

The TT: A_f of the virgin sample is 330 °C and those of the tested samples falls between 320 - 400 °C (Fig. 2.14(d)). Hence, the XRD data above these temperatures i.e. at 400 and 500 °C (Fig. 2.21(c),(d)) was checked for evidence of retained martensite (B19') in the austenite phase. As observed at 400 °C, the labelled peaks of B19', viz. (002), $(1\bar{1}1)$, (020) and (111) for 1 °C/min and the peaks $(1\bar{1}1)$, (020) and (111) for 10 and 50 °C/min, indicate presence of retained martensite. On increasing the temperature to 500 °C the intensity of these peaks diminishes and some of them disappear as they are transformed to austenite completely.

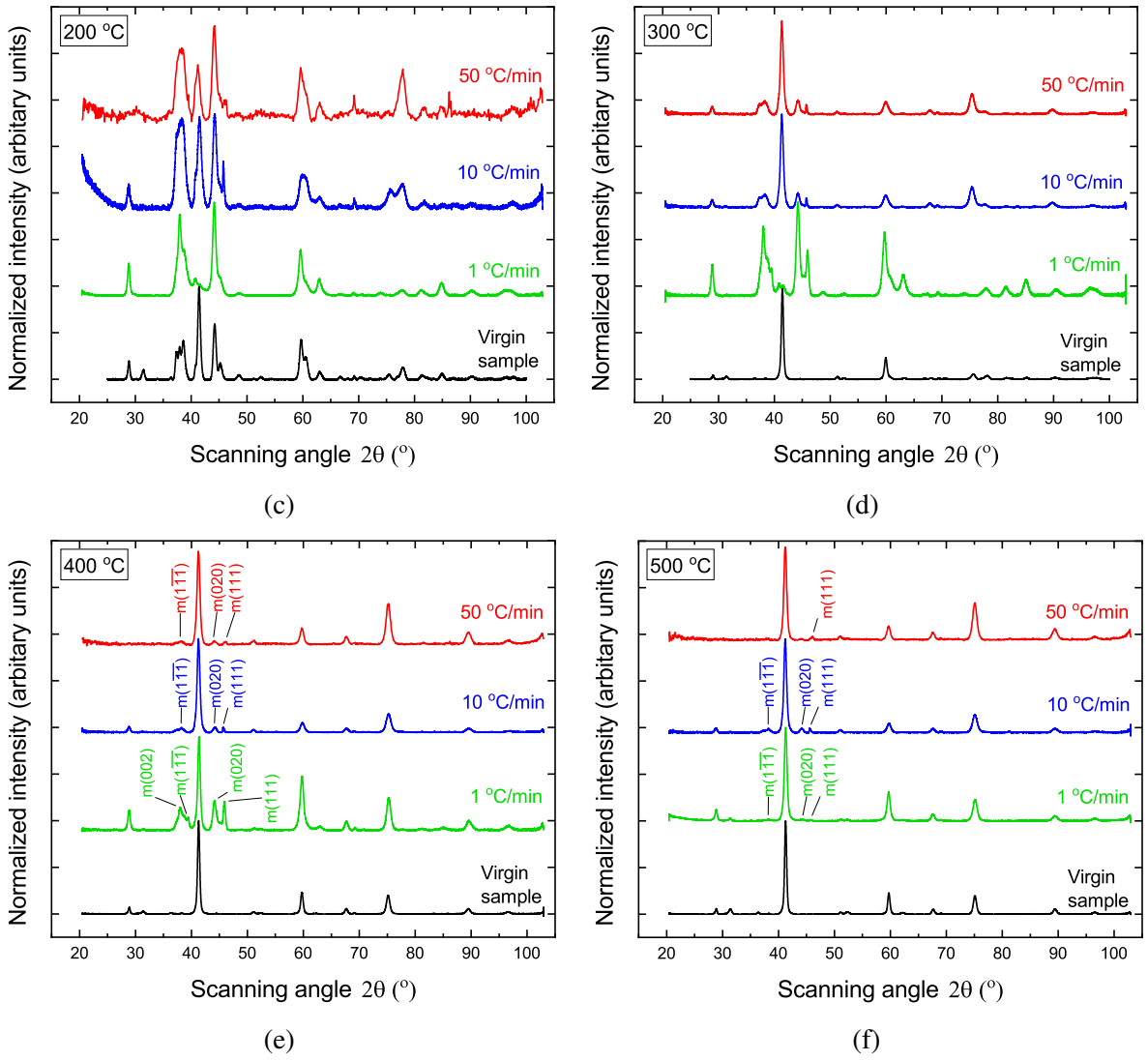

Figure 2.21: (Continued) XRD data generated from each UCFTC tested sample is compared with the virgin sample, at (a) 200 °C, (b) 300 °C, (c) 400 °C, and (d) 500 °C. Reprinted with permission from Chaugule et al. [7].

Based on the number of peaks and peak intensities from the data sets, it can be reckoned that the most and least amount of retained martensite was accumulated at 1 °C/min and 50 °C/min, respectively. This can explain the contribution of retained martensite to the (high) amount of TRIP strain produced at 1 °C/min in the initial 40% cycles (Fig. 2.12(b)). While the data suggests there were sufficiently large amount of dislocations generated which retained the martensite at both 400 and 500 °C at 10 °C/min. This large amount of dislocations can also be interpreted as a large

amount of internal stress, which is consistent with the speculated trends from DSC analyses.

2.3.3 Coupling effects in UCFTC tests

2.3.3.1 Effect of thermal cycling rate over phase transformation

The UCFTC responses (in Fig. 2.9), indicate an effect of thermal cycling rate over the entire behavior, as interpreted from the strain evolution. The evolution of functional properties and quantifiers (Section 2.2.3.1) at different thermal cycling rates brings out an effect of rate over phase transformation and its associated irrecoverable mechanisms. The thermal cycling rate controls the activation and evolution of viscoplasticity, TRIP, and static recovery, in turn controlling the generation of internal stresses and accumulation of defects such as dislocations and retained phases during the entire test. This control is how the thermal cycling rate indirectly affects the phase transformation. It is important to bear in mind that the effect of rate is not classified as monotonic, and the results are explained solely based on their individual magnitudes and trends.

2.3.3.2 Effect of viscoplasticity over phase transformation at all rates

As mentioned earlier, the thermal cycling rate controls the activation of viscoplasticity through the duration of time spent within the viscoplastic domain. The activation of viscoplasticity directly affects the phase transformation for all rates, as evidenced from the functional properties and quantifiers. The effects are created due to an accommodation of viscoplastic dislocations during reverse (phase) transformation, which is observed only at the slow rate (of 1 °C/min). However, exposure to high temperatures at slow rates relieves some of the internal stresses. This unique interplay is observed from the data of 1 °C/min (Fig. 2.16(a),2.11 (b)). To observe an effect of viscoplasticity over phase transformation at a fast cycling rate (10 °C/min), the alternating test is proposed (Section 2.2.3.2) and presented in the next section.

2.3.4 Alternating isothermal creep and UCFTC at 10 °C/min

The alternating test's response with respect to temperature is presented in Fig. 2.22. The test's duration was 241 hrs and a total of 13 thermal cycles were completed until the sample failed in the 14^{th} cycle before achieving a maximum strain of 46.44%. The thermal cycling was conducted

at intervals determined by the magnitude and rate of the viscoplastic strain, generated during an isothermal creep test conducted at the same UCT (500 °C) and stress level (500 MPa), as the alternating test.

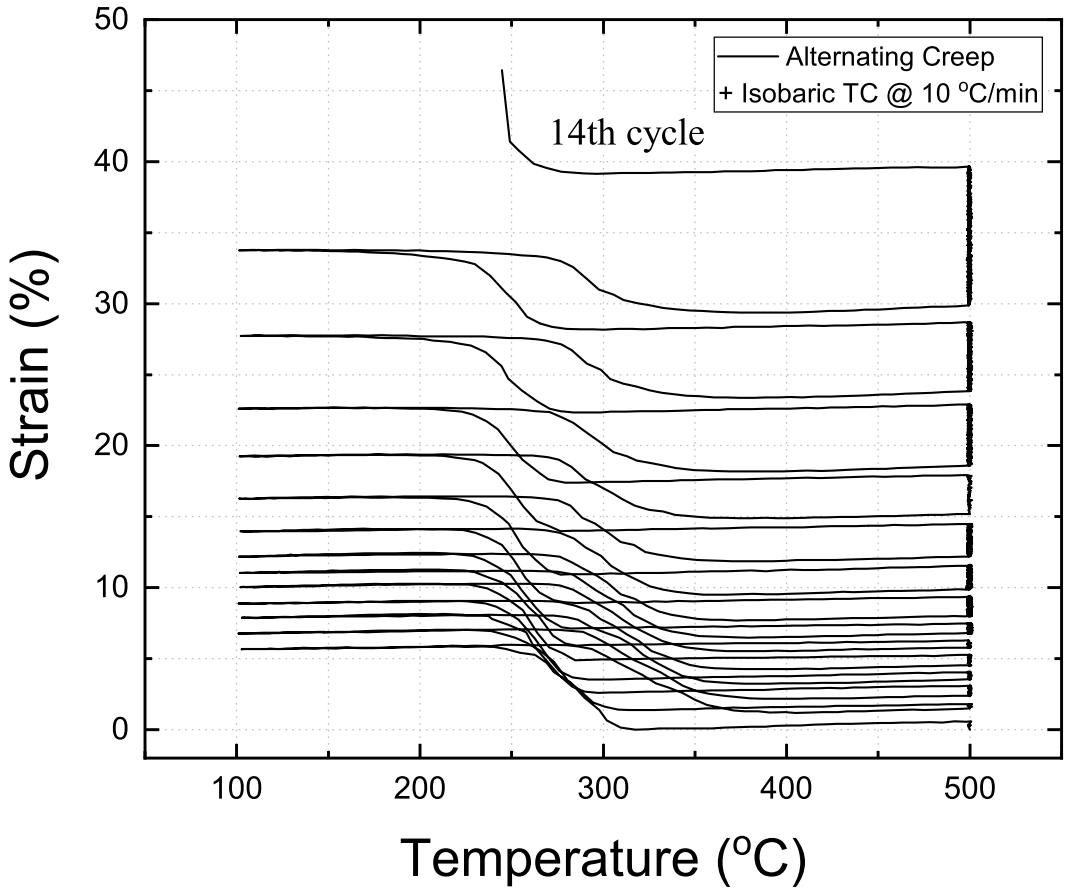

Figure 2.22: Strain-temperature response of alternating isothermal creep and UCFTC (at 10 °C/min) test conducted under a stress of 500 MPa. Reprinted with permission from Chaugule et al. [7].

A comparison is made between the 10 °C/min UCFTC response, the alternating test response, and the creep test response in Fig. 2.23. The comparison highlights (through the yellow dots) the maximum strain at 50 h in the three tests, i.e., 1% in the creep test, 10.2% in the alternating test, and 50.4% in the UCFTC test. As observed, the strain evolution of the alternating test is similar

to that of the creep test, as it is mainly viscoplastic driven. The comparison also shows that, in the alternating and UCFTC test responses, the jump in strain, due to each thermal cycle, varies. The jump or ratcheting of strain can be attributed to the residual strain (with retained phases) generated during cycling. The total strain does not saturate with cycling, contrary to the trend observed by Raj et al. [95] in Ni-Ti, at low temperatures. Therefore, the mechanisms generating the residual strain can be hardenings without a back stress, that would otherwise help in saturating the residual strain.

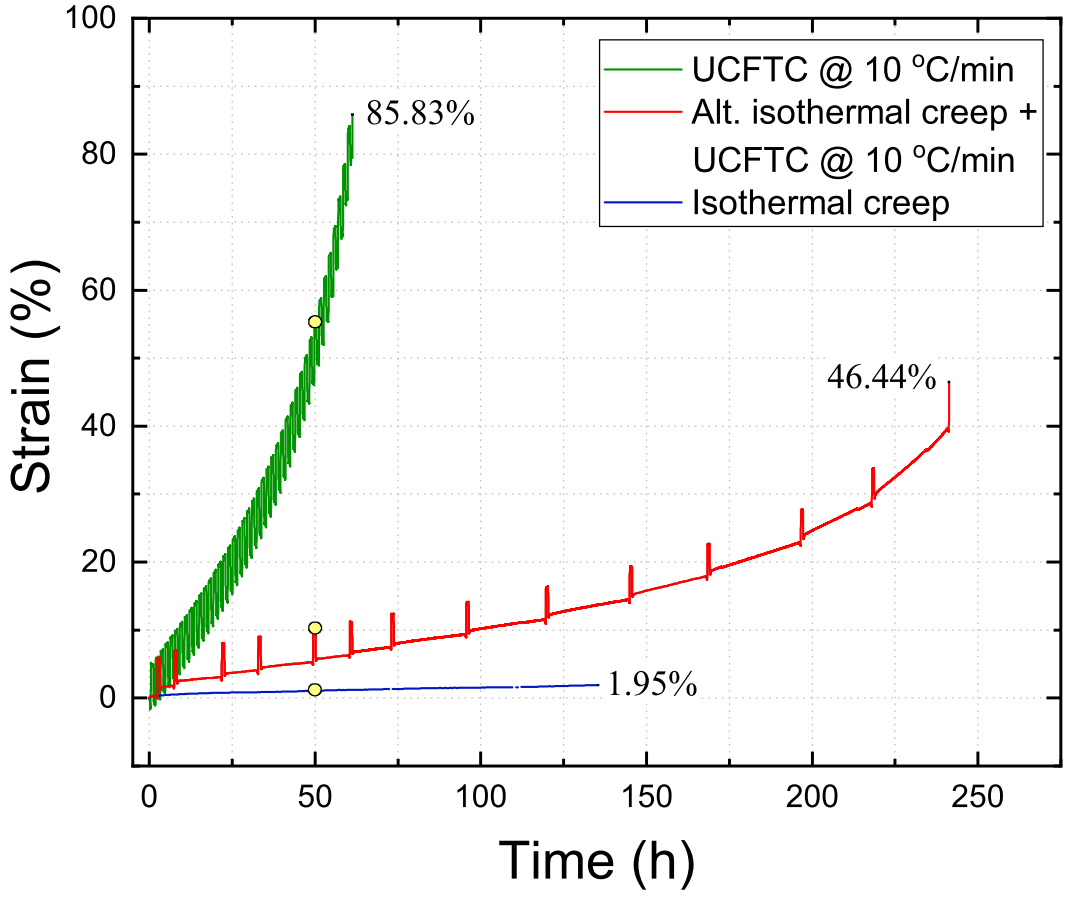

Figure 2.23: Comparison of strain evolution between (i) UCFTC at 10 °C/min, (ii) Alternating isothermal creep and UCFTC at 10 °C/min, and (iii) Isothermal creep at 500 °C, all subjected to a stress of 500 MPa. Reprinted with permission from Chaugule et al. [7].

In the alternating test, viscoplasticity is mainly produced during the isothermal creep loading. To understand its magnitude and evolution, the viscoplastic strain generated between the thermal cycles is plotted with respect to time at the start of each thermal cycle, as shown in Fig. 2.24(a). The cumulative magnitude is evaluated and presented in the same plot. *Note:* The residual strain for each cycle can contain a contribution from retained martensite, but the evaluated viscoplastic strain generated between the cycles does not contain any contribution, as the difference between the end and start points of subsequent cycles eliminates the (retained martensite) contribution. The cumulative viscoplastic strain generated in the entire alternating test is 30.6%. This is quite significant compared to the viscoplastic strain generated in the 1 °C/min $\approx 1\%$ and 10 °C/min $\approx 1.5\%$ (Fig. 2.11(b)), and even the TRIP strain generated in the 10 °C/min $\approx 9\%$ (Fig. 2.12(b)) UCFTC tests. Therefore, the amount of dislocations generated by viscoplasticity in the alternating test dominate over the one from TRIP and, hence, likely control the evolution of the functional properties and the quantifiers.

The constantly evolving magnitude of cumulative viscoplastic strain, as observed in the Fig. 2.24(a), hints to a likely effect of the alternating phase transformation over viscoplasticity. To elucidate this effect, the viscoplastic strain rate from a pure creep test and the alternating test, are plotted with respect to time and compared in Fig. 2.24(b). The primary creep stage of the pure creep test ends after $\approx$ 49 h and is followed by a secondary creep stage up till the last recorded data point. This trend is similar to the one shown by Ni-Ti based SMAs when subjected to creep at high temperatures [21, 107]. The primary-like creep stage of the alternating test finishes after 21 h ($2^{nd}-3^{rd}$ cycle). Past this point, the strain rate remains close to its current value up to 60 h ($5^{th}-6^{th}$ cycle). Beyond 60 h, the strain rate accelerates at a constant rate up till 167 h ($10^{th}-11^{th}$ cycle). Since there is no formation of a plateau between 21 - 167 h, it is difficult to identify a secondary stage. Beyond 167 h, the strain rate begins increase non-linearly up till failure, signifying the onset of tertiary stage (or effect of potential damage mechanisms), at a time between 167 and 196 h (10^{th} and 12^{th} cycle).

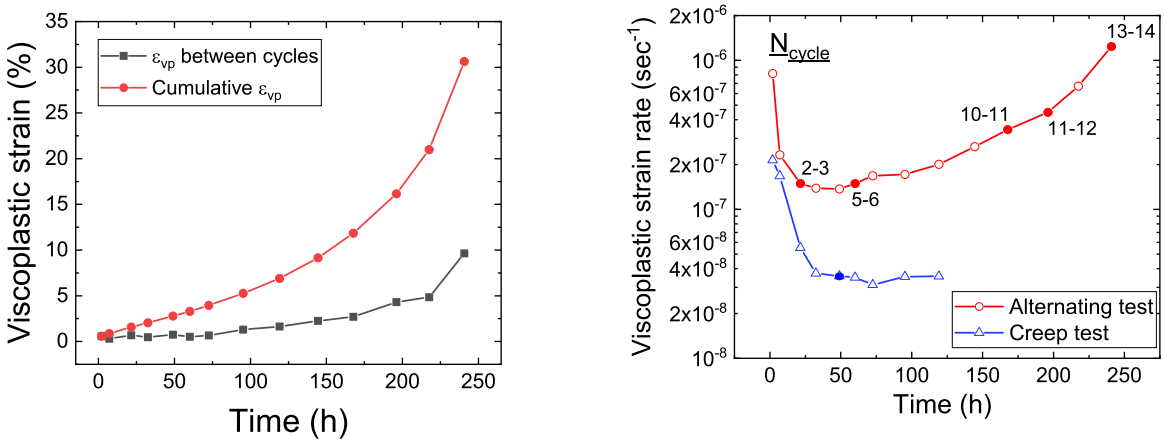

(a) (b)

Figure 2.24: (a) Viscoplastic strain generated between each cycle and its cumulative, obtained from the alternating test. (b) Comparison of viscoplastic strain rate generated during the alternating and isothermal creep test. The numbers next to the alternating test represent the cycle number. Reprinted with permission from Chaugule et al. [7].

On comparing the two tests based on the above observations, it can be inferred that the internal stresses in the alternating test are comparatively higher and they keep evolving leading to a constant increase in strain rate. The comparison also highlights that in the alternating test: the primary stage lasts for a shorter time, a clear secondary stage is hard to identify due to a constantly increasing strain rate, which is overall faster compared to that of the creep test. Based on the above trends the source of increasing internal stress can be the differentiating phenomenon between the two tests, that is the alternating phase transformation and the irrecoverable mechanisms associated with it such as TRIP and accumulation of retained martensite.

As evaluated for the UCFTC tests, the evolution of functional properties such as TT, transformation strain, and quantifiers, such as hysteresis are evaluated for the alternating test and presented as follows. The evolution of TT and their slopes: forward and reverse are plotted with respect to time in Fig. 2.25(a) and (b), respectively. Their slopes show a trend similar to the one from UCFTC at 1 and 1 (repeat) °C/min (Fig. 2.14(e - f)). An increase slope is observed along the forward path up till 50 h (35% N_f) and along the reverse path up till 96 h (57% N_f). As assumed for the UCFTC

tests, the forward slope shows plastic (TRIP) accommodation, whereas the reverse slope shows viscoplastic and plastic (TRIP) accommodations and then resistance to transformation. These trends are different from those shown by 1 and 10 °C/min UCFTC tests. A viscoplastic accommodation is observed in the alternating test at 10 °C/min, and its span is considerably large, because of the long duration in the viscoplastic domain. Beyond 35% N_f (for forward) and 57% N_f (for reverse), the slopes decrease overall indicating either increased transformation resistance or additional heating required to transform the trapped martensite, based on the UCFTC interpretations. The slope trends beyond 167 h are affected by potential damage mechanisms (consistent with the assumed tertiary stage in Fig. 2.24(b)) and are hence, not investigated.

The hysteresis evolution is plotted with respect to time and the cumulative viscoplastic strain, as shown in Fig. 2.25(c) and (d), respectively. The data shows some differences from those of UCFTC (Fig. 2.16) which are as follows. The hysteresis sharply increases in the initial 50 h and 2.78% viscoplastic strain. This can be due to an increase in resistance to transformation, partly from the viscoplastic dislocations generated in the primary stage, and partly from the TRIP dislocations and retained martensite generated in the first five thermal cycles. Beyond 50 h, the hysteresis fluctuates, increasing slightly overall before failure. The fluctuations can be due to a conflict between static recovery (interpreted from UCFTC at 1 °C/min), and nucleation (and growth) of dislocations up till 167 h (11^{th} cycle).

The transformation strain evolution is also plotted with respect to time and the cumulative viscoplastic strain, as shown in Fig. 2.25(e) and (f), respectively. The transformation strain increases at the second cycle, after which it continuously decreases with increasing time and viscoplastic strain. This trend can be explained based on UCFTC responses (Fig. 2.16), i.e., an increase in transformation strain due to variant preference (reorientation) generated by favourable internal stresses, and a decrease due to accumulation of retained martensite. However, the decrease shown in Fig. 2.25(e) is more significant than those from UCFTC. It implies a much larger amount of retained martensite being trapped by viscoplastic dislocations, which can be corroborated with the interpretation from the slopes of the TT (Fig. 2.25(a)) beyond 50 h.

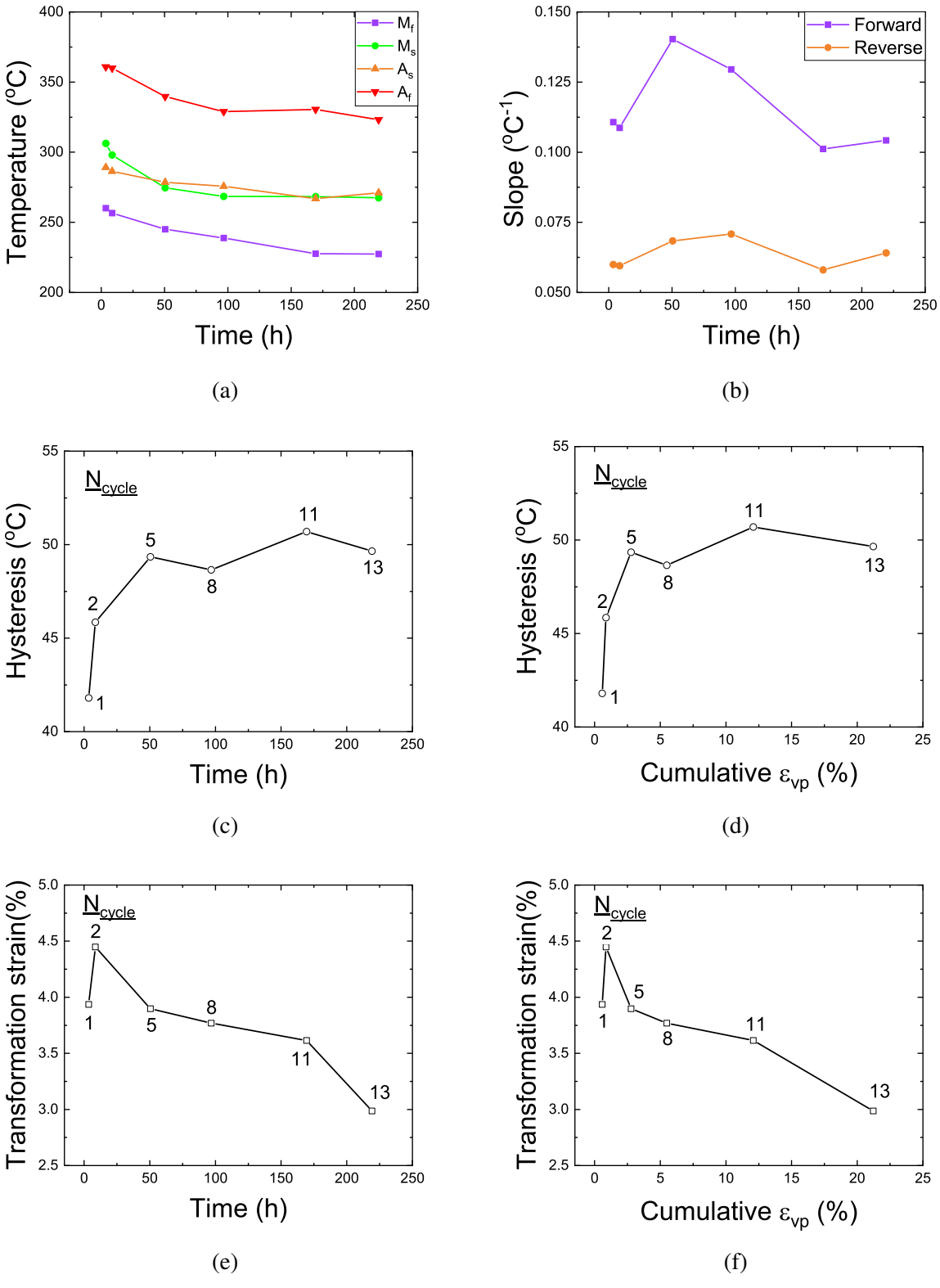

Figure 2.25: Evolution of (a) TT (M_f,M_s,A_s,A_f), (b) slopes of forward ($(\varepsilon_{M_f} - \varepsilon_{M_s})/(M_f - M_s)$) and reverse ($(\varepsilon_{A_s} - \varepsilon_{A_f})/(A_s - A_f)$) transformation, hysteresis, and transformation strain, all generated during the alternating test, and plotted with respect to time in (c),(e) and cumulative viscoplastic strain in (d),(f) respectively. Reprinted with permission from Chaugule et al. [7].

2.3.5 Coupling effects in alternating test

2.3.5.1 Effect of viscoplasticity over phase transformation at 10 °C/min

An effect of viscoplasticity over phase transformation at a rate faster than 1 °C/min was witnessed as a result of generating a larger amount of viscoplastic dislocations. Through the TT plots, it is inferred that the dislocations are partly accommodated during reverse transformation and the rest add to the transformation resistance and internal stresses, resulting in a control over the trends of hysteresis and transformation strain, respectively. The dislocations were also responsible for accumulating retained martensite.

2.3.5.2 Effect of phase transformation over viscoplasticity

The alternating phase transformation and its associated irrecoverable mechanisms added to the internal stress in the microstructure, which fostered the viscoplastic deformation when the sample was held at UCT. This resulted in a constantly evolving viscoplastic strain and strain rate without a visible saturation, giving rise to higher viscoplastic strains compared to those generated from isothermal creep.

All the observations and discussions on the effect of viscoplasticity over phase transformation and vice-versa bring out a two-way coupling between the two phenomena, similar to the two-way coupling between plasticity and phase transformation in SMAs theorized by Paranjape et al. [38]. The degree of coupling, and hence the macroscopic response, is controlled by the internal stresses generated by dislocations and retained martensite.

2.4 Summary

The conclusions from the above experimental investigations are provided in Chapter 4, and a summary of the present chapter is provided as follows. The high temperature behavior of a Ti-rich $Ni_{49.8}Ti_{30.6}Hf_{19.2}$ HTSMA was investigated through two types of experimental tests involving isobaric conditions. The thermomechanical conditions were chosen to activate transformation and viscoplasticity, in order to observe a coupling between these phenomena. The investigations were performed as follows:

1. Series of UCFTC tests were conducted by subjecting the HTSMA to a constant stress of 500 MPa, and thermal cycling, at rates of 1, 10 and 50 °C/min. The macroscopic responses (for each rate) with respect to temperature and time were plotted and compared together.

2. The evolution of functional properties such as TT, transformation strain, and quantifiers, such as hysteresis, cumulative residual, TRIP and viscoplastic strain were investigated. They were compared and discussed for each thermal cycling rate, with respect to cycle progression and prior to the cycles assumed to be affected by necking and potential damage mechanisms.

3. An attempt was made to quantify the contribution of retained martensite to the TRIP strain produced during a UCFTC test (at 10 °C/min). The test was halted and a heat treatment was conducted to free the retained martensite and observe its effect on the strain. The contribution was estimated and inferences were made based on the value.

4. The retained phases generated in the the UCFTC tests, were investigated through several ex situ DSC and XRD analyses. Results from DSC analyses were used as an indirect evidence of the presence of retained phases and internal stresses. While, results from the XRD analyses were used to dissociate the retained phases based on the their peaks and TT.

5. An alternating isothermal creep + UCFTC test was conducted to probe an effect of viscoplasticity on phase transformation at a fast rate of 10 °C/min. Its response was compared to that of an isothermal creep and UCFTC test at 10 °C/min to investigate the rate of strain evolution. The evolution of functional properties and identifiers were also plotted to investigate an effect of viscoplasticity.

6. A two-way coupling between phase transformation and viscoplasticity is revealed from the response of UCFTC at slow rates and the alternating test. The coupling is controlled by the generation and recovery of viscoplastic dislocations and retained phases.

2.5 Supplementary Material

2.5.1 Thermal gradient

2.5.1.1 Across the gauge section

The thermal gradient measured across the gauge section using the temperature values extracted from the thermocouples inserted at the top (T_1) and bottom (T_2) for the 1 °C/min tests are shown in the figure below. The average thermal gradient measured was less than 5 °C, and the maximum was 10 °C.

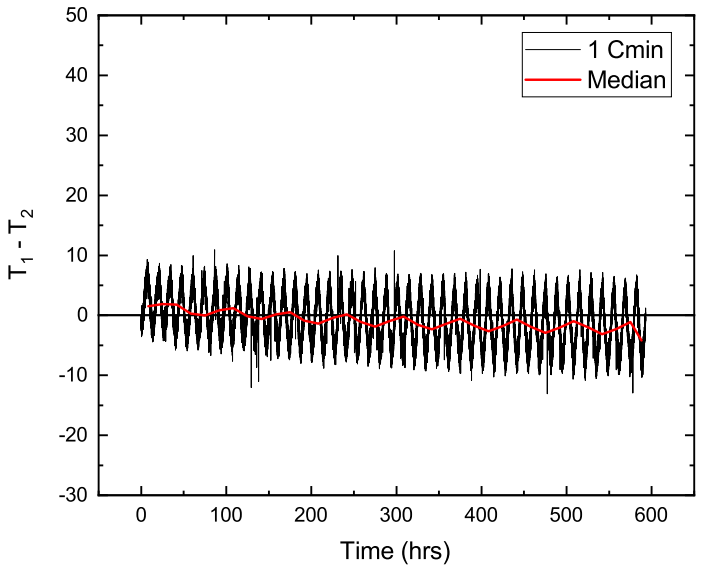

Figure 2.26: Thermal gradient across gauge section for 1 °C/min.

2.5.1.2 Inside the gauge section

To understand the heat transfer inside the gauge section (i.e radially), the Abaqus tool was used to model heating of the sample in a furnace. The thermal conductivity, specific heat and density values of the alloy [6] were implemented in the model. The sample gauge section was subjected

to a constant heat flux (obtained from the furnace specifications) to raise its temperature to 773 K (or 500 °C), and adiabatic conditions were applied at the top and bottom ends. As shown by the temperature distribution in Kelvin, in Fig. 2.27 the sample is assumed to be have been heated uniformly (in the gauge section) in almost 5 seconds. The nodal point marked at the bottom of the gauge section is the location where the thermocouple is inserted in the experimental sample. Through the temperature distribution it is seen that the temperature reaches $\approx$ 773 K at that point in 5 seconds without forming any thermal gradients. This indicates the response and functional properties obtained from the sample data are constitutive.

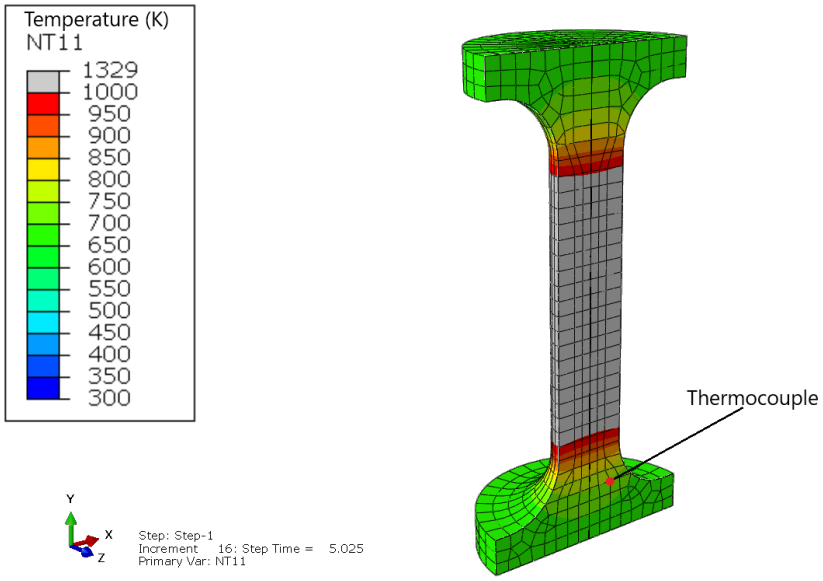

Figure 2.27: Heat transfer show inside the sample through a model created in Abaqus.

2.5.2 Individual XRD data

The XRD data from the tested samples with respect to their scanning temperatures are presented in the following figures Fig. 2.28, 2.29, 2.30. In the data the phase transformation can be tracked as the B19' peaks decrease in intensity while the B2 peaks increase, as the temperature is increased from R.T. to 500 $^{\circ}C$. At R.T. the peaks of B19' are marked, which are eventually

retained at 400 and 500 °C. While at 500 °C the one peak of B2 is marked which is the peak with maximum intensity.

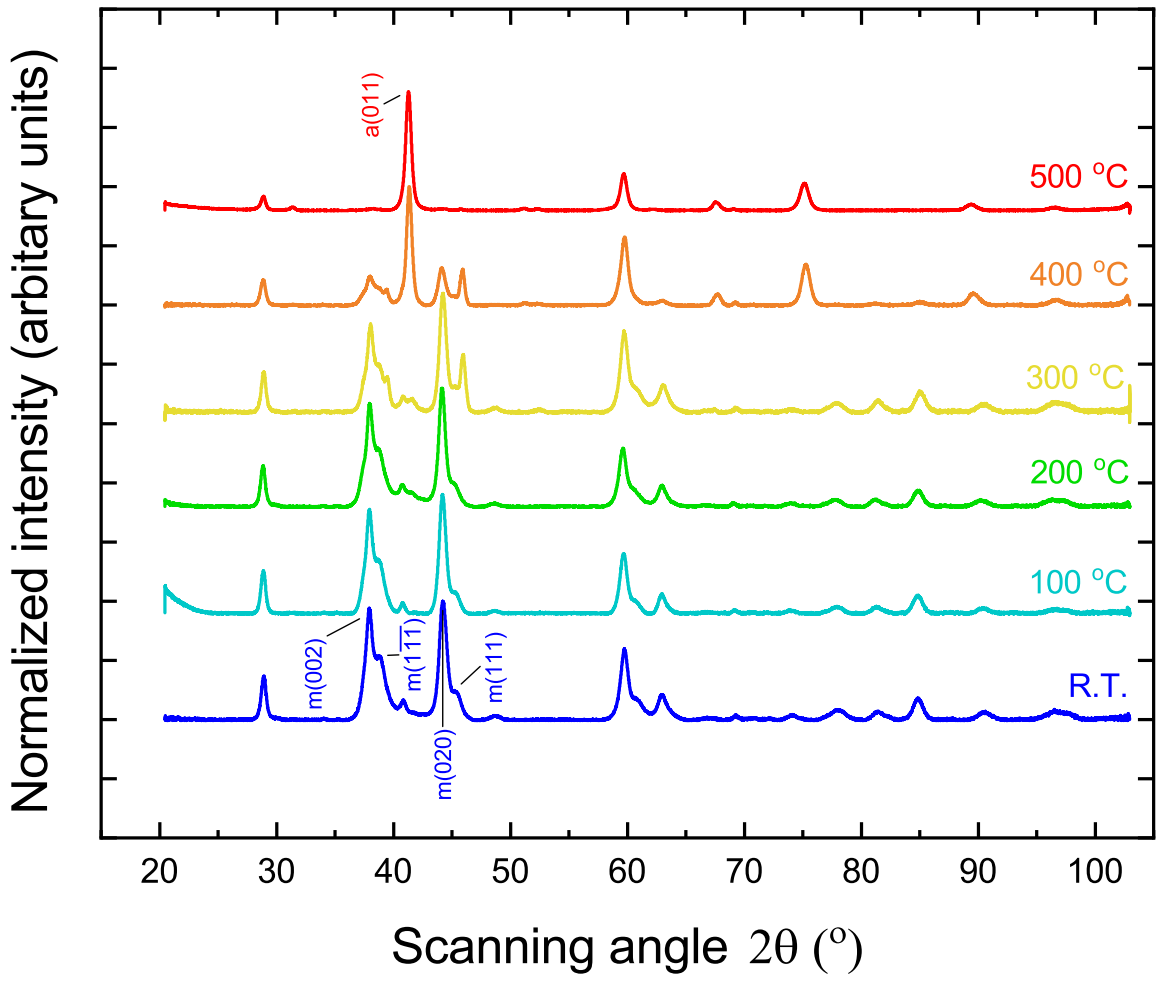

Figure 2.28: XRD data obtained from a tested sample at 1 °C/min scanned at temperatures starting from R.T. to 500 °C in increments of 100°, with peaks of B19' and B2 labelled at respective temperatures. Reprinted with permission from Chaugule et al. [7].

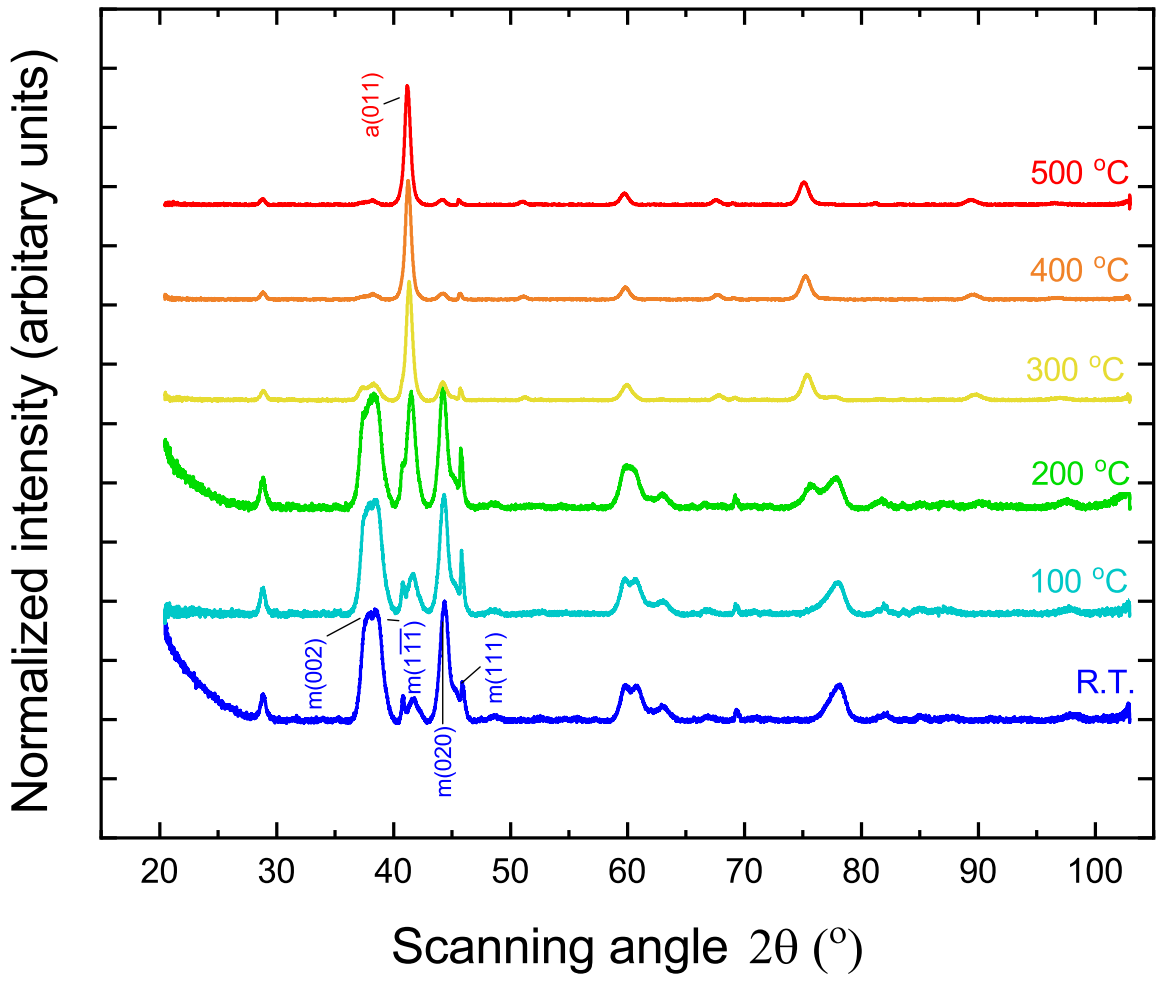

Figure 2.29: XRD data obtained from a tested sample at 10 °C/min scanned at temperatures starting from R.T. to 500 °C in increments of 100°, with peaks of B19' and B2 labelled at respective temperatures. Reprinted with permission from Chaugule et al. [7].

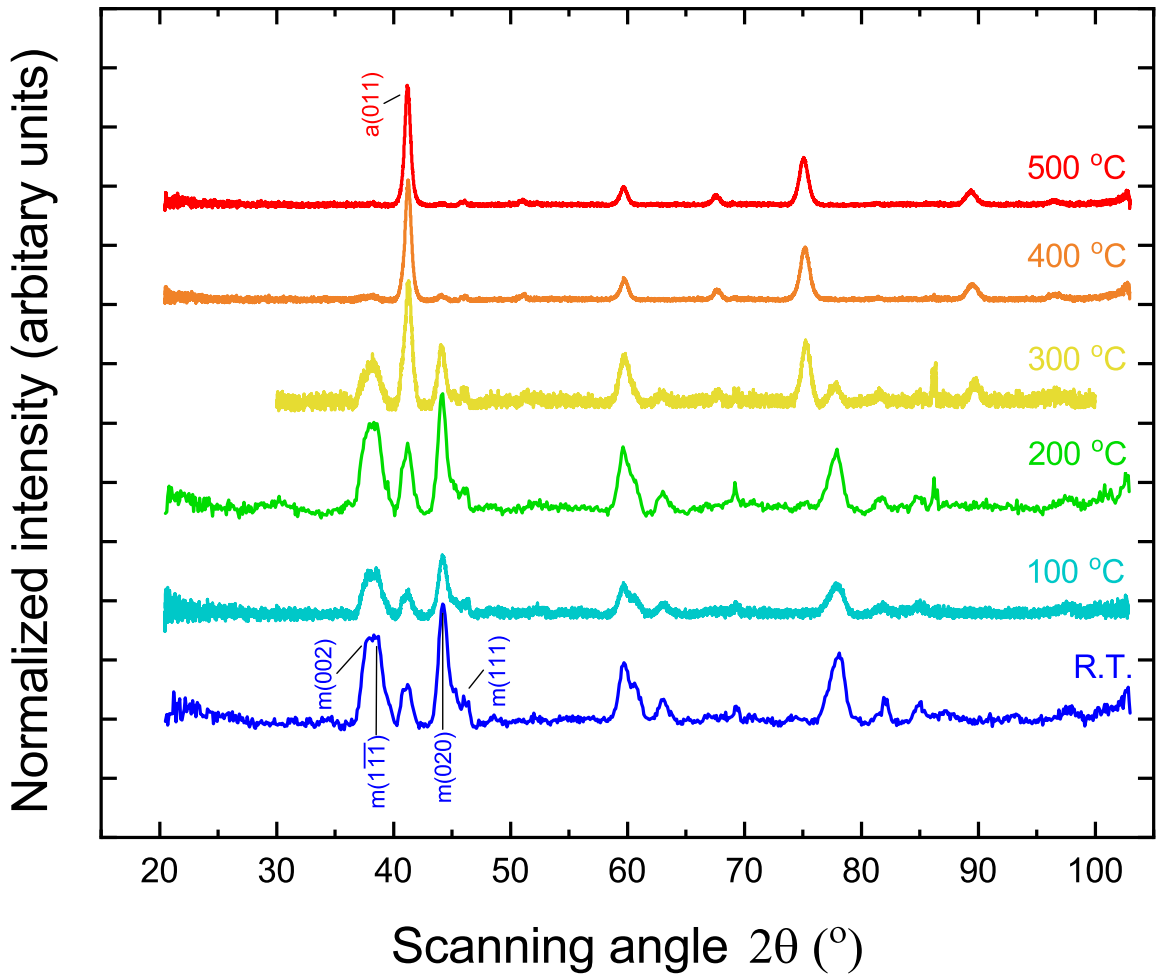

Figure 2.30: XRD data obtained from a tested sample at 50 °C/min scanned at temperatures starting from R.T. to 500 °C in increments of 100°, with peaks of B19' and B2 labelled at respective temperatures. Reprinted with permission from Chaugule et al. [7].

3. CRYSTAL PLASTICITY MODELING

3.1 Introduction

In this chapter, a formulation of the crystal plasticity model is presented, followed by finite element analyses conducted on single crystals and polycrystals of a selected HTSMA system. In Section 3.2 the constitutive equations for the crystal-plasticity and thermodynamic framework are presented. In Section 3.3, the developed crystal-plasticity model is used to conduct a series of finite element analyses conducted of a thermomechanical test. In Section 3.5, the results of the FEA are used to illustrate the model calibration for single crystals and polycrystals using material properties, theoretical values, and experimental trends. Lastly, in Section 3.6 the entire chapter is summarized.

3.2 Theoretical Framework

The mechanisms accounted in the crystal plasticity framework are as follows:

3.2.1 Plastic and viscoplastic slip at the microscale

Micro scale mechanisms, such as plastic/viscoplastic slip, can be defined by considering a unit cell [8]. A unit cell represents the crystal-lattice (e.g. tetragonal, orthorhombic or monoclinic, etc.) and its lattice centering (e.g. BCC, FCC or HCP), as shown in Fig. 3.1. The mechanism of slip occurs on planes and along directions with the highest number of packed atoms, both of which are dependent on the lattice structure, and therefore, the unit cell. The slip also depends on the Schmid factor which is based on the relative orientation of the crystal to the loading axis. The orientations are defined with respect to either the crystal frame of reference at the microscale ([001],[010],[100]) or sample frame of reference at the macroscale (RD,TD,ND). The unit cell along with its associated slip planes **n** and slip directions **l**, belonging to various families, are defined in the crystal frame of reference.

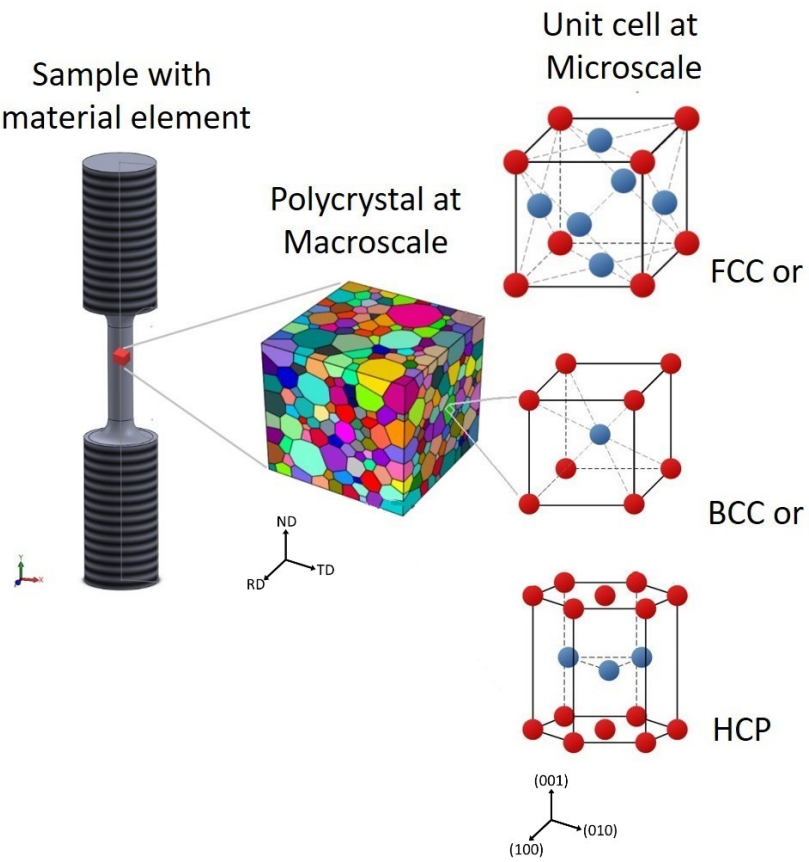

Figure 3.1: Defining the multi-scales from Sample to a Polycrystal (macro) to a Unit Cell (micro). Unit cell/crystal lattice based on arrangement of atoms or lattice centering, which can be either FCC, BCC or HCP [8].

3.2.2 Martensitic transformation at the microscale

Martensitic transformation is known to be a rate-independent, reversible and a crystallographic transition process [79]. The crystallographic transition involves shearing of the austenite (parent) lattice, to form various plates of martensite, which are separated from austenite by interfaces. The plates are called as Habit-Plane Variants (HPVs) [9] or Correspondent Variant Pair [2], and the interfaces are known as Habit Planes [108]. Each martensite HPV consists of two Lattice-Correspondence Variants (LCVs) or twins, separated by an interface called the detwinning plane. Under stress-free conditions, the martensite forms HPVs, which minimizes the macroscopic deformation through self-accommodation and, hence, are called self-accommodating groups (SAGs) or

twinned martensite.

In case of transformation under stressed conditions, the martensite forms oriented variants (or HPVs), which can reorient based on the interaction between them. While inside the HPVs the LCVs can move along their respective interfaces and detwin. The respective movements result in a change in the volume fraction of HPVs and LCVs, and a volumetric growth of variants favored by the principal stresses, as shown in Fig. 3.2 adopted from Thamburaja et al. [9]. In context of this growth, the present study on HTSMAs accounts for the formation of oriented HPVs and de-twinning of LCVs. The interaction between variants during HPV reorientation remains a potential expansion of the present study (elaborated in Section 3.2.3.2).

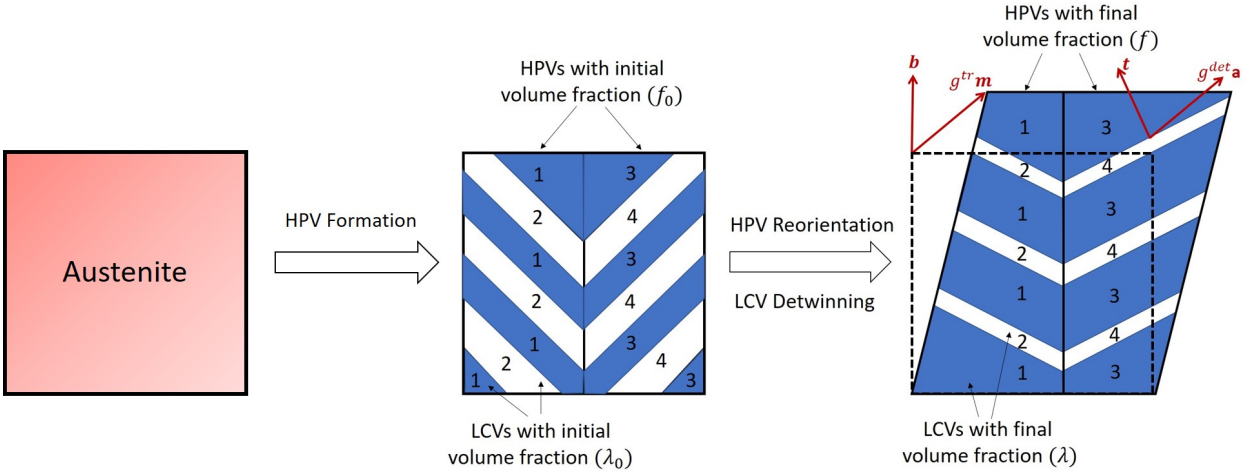

Figure 3.2: Schematic representation of phase transformation from austenite to martensite, through HPV formation. Followed by HPV reorientation and LCV detwinning of martensite variants, shown by a change of initial volume fraction to final volume fraction, adopted from Thamburaja et al. [9]. Marked arrows show the habit plane **b**, shear direction **m**, LCV detwinning plane **t** and detwinning direction **a**.

The martensite variants are formed as a result of (reversible) shearing over the habit-planes **b** along shear-directions **m** (marked arrows in third part of Fig. 3.2), transforming the crystal lattice entirely. Hence, a family of these planes and directions are known as transformation systems. In the formed martensite variants, the LCVs can detwin by shearing along a set of detwinning-planes

t and detwinning-directions **a**, known as the detwinning systems. In case of slip occurring on the A-M interface, resulting in TRIP, the transformation systems are considered [109].

All the above mechanisms give rise to microscale deformations which can be accumulated over the considered systems to obtain macroscopic strains. The macroscopic strains from each phenomenon are combined to give a total strain using a small-strain approximation.

3.2.3 Constitutive equations

3.2.3.1 Total strain

Experimental studies [110, 66, 3, 111, 112, 13, 7] on HTSMAs, provide evidence of the occurrence of: (i) thermal expansion/contraction, (ii) elasticity, (iii) transformation and reorientation (iv) detwinning, (v) TRIP, and (vi) plasticity and viscoplasticity during thermomechanical testing. Therefore, to account for these phenomena, the total strain tensor is defined using a small-strain approximation, as the sum of the $\boldsymbol{\epsilon_{th}}$: thermal, $\boldsymbol{\epsilon_e}$: elastic, $\boldsymbol{\epsilon_{tr}}$: transformation, $\boldsymbol{\epsilon_{de}}$: detwinning, $\boldsymbol{\epsilon_{TRIP}}$: TRIP, $\boldsymbol{\epsilon_{vp}}$: plastic and viscoplastic strain components.

$$\boldsymbol{\epsilon}_{tot} = \underbrace{\boldsymbol{\epsilon}_{th} + \boldsymbol{\epsilon}_{e}}_{elastic} + \underbrace{\boldsymbol{\epsilon}_{tr} + \boldsymbol{\epsilon}_{de} + \boldsymbol{\epsilon}_{TRIP} + \boldsymbol{\epsilon}_{vp}}_{inelastic} \tag{3.1}$$

On heating (or cooling), the thermal strain $\boldsymbol{\epsilon}_{th}$ generated in the alloy is evaluated by the rise (or drop) in temperature T, from the reference temperature T_{ref} (where thermal expansion = 0), and using the coefficient of thermal expansion α_{CTE} (coefficient of thermal expansion) that is different for each phase contrary to past studies on HTSMAs [68, 69, 71].

$$\boldsymbol{\epsilon}_{th} = \alpha_{CTE}(T - T_{ref})\mathbf{I} \tag{3.2}$$

The elastic strain $\boldsymbol{\epsilon_e}$, generated on applying an external load, is evaluated macroscopically using the macroscopic stress $\boldsymbol{\sigma}$, and the effective elastic stiffness tensor $\mathbb{C}$. The effective stiffness is calculated using the stiffness tensor for austenite $\mathbb{C}_A$ and martensite $\mathbb{C}_M$, and martensite volume

fraction ξ using the rule of mixtures.

$$\begin{aligned} \boldsymbol{\epsilon}_e &= [\mathbb{C}]^{-1}.\boldsymbol{\sigma} \\ \mathbb{C} &= \frac{\mathbb{C}_M.\mathbb{C}_A}{\mathbb{C}_M + \xi.(\mathbb{C}_M - \mathbb{C}_A)} \end{aligned} \tag{3.3}$$

Contrary to the elastic strains, the inelastic strains are first evaluated at the microscale for each phenomenon and summed up over their respective systems at the macroscale. During forward transformation (A $\rightarrow$ M), transformation strain $\boldsymbol{\epsilon_{tr}}$ is generated from the formation of every martensite variant α, and is recovered during the reverse transformation (M $\rightarrow$ A). The strain $\boldsymbol{\epsilon_{tr}}$, in Eq. 3.4 [113, 114] is derived from the martensite volume fraction ξ^α of the variant α and its magnitude is controlled by the parameter g^{tr}. The orientation tensor for transformation $\mathbf{P}^\alpha_{tr}$ is evaluated from the habit plane $\mathbf{b}^\alpha$ and shear direction $\mathbf{m}^\alpha$ in a similar fashion as the orientation tensor for slip systems. The tensor is evaluated for each HPV and, hence, represents the transformation systems for all the variants N_v.

$$\begin{aligned} \boldsymbol{\epsilon}_{tr} &= \sum_{\alpha=1}^{N_v} \xi^\alpha g^{tr} \mathbf{P}^\alpha_{tr} \\ \mathbf{P}^\alpha_{tr} &= \frac{1}{2}(\mathbf{b}^\alpha \otimes \mathbf{m}^\alpha + \mathbf{m}^\alpha \otimes \mathbf{b}^\alpha) \end{aligned} \tag{3.4}$$

Upon transforming, detwinning strain $\boldsymbol{\epsilon_{de}}$ is further generated from the detwinning of LVCs formed inside each martensite HPV. The strain $\boldsymbol{\epsilon_{de}}$ in Eq. 3.5 [115, 9] is derived from the amount of detwinning that occurs between the current (λ^α) and the reference (λ^α_0) LCV volume fractions, along with the associated HPV volume fraction ξ^α of the variant α. The orientation tensor $\mathbf{P}^\alpha_{de}$ for detwinning is evaluated using the detwinning plane $\mathbf{t}^\alpha$ and detwinning shear direction $\mathbf{a}^\alpha$ (in Fig. 3.2). The tensor is evaluated for each LCV and, hence, represents the detwinning systems. *Note*: Both the number of HPVs and LCVs, i.e., transformation and detwinning systems, are taken to be N_v.

$$\begin{aligned}\boldsymbol{\epsilon}_{de} &= \sum_{\alpha=1}^{N_v} \xi^{\alpha}(\lambda^{\alpha} - \lambda_0^{\alpha})\mathbf{P}_{de}^{\alpha} \\ \mathbf{P}_{de}^{\alpha} &= \frac{1}{2}(\mathbf{t}^{\alpha} \otimes \mathbf{a}^{\alpha} + \mathbf{a}^{\alpha} \otimes \mathbf{t}^{\alpha})\end{aligned} \tag{3.5}$$

During transformation, internal stresses, known as coherency stresses are generated on the habit planes due to a lattice mismatch between martensite and austenite, as shown in Fig. 3.3. If these stresses are higher than the yield stresses of the corresponding habit planes, plastic slip γ_{tr}^{α} can occur on those planes. The plastic slip, when accumulated over the forward and reverse transformation paths, gives rise to TRIP strain $\boldsymbol{\epsilon_{TRIP}}$ (in Eq. 3.6). The orientation tensor for γ_{tr}^{α} and $\boldsymbol{\epsilon}_{TRIP}$ is taken to be the same as that for transformation.

$$\boldsymbol{\epsilon}_{TRIP} = \sum_{\alpha=1}^{N_v} \gamma_{tr}^{\alpha}\mathbf{P}_{tr}^{\alpha} \tag{3.6}$$

Prior to reverse transformation, the alloy is considered to be in the martensite phase (at low temperatures). Rate-independent [116, 80, 117] plastic slip can occur on the activated slip planes, as illustrated in Fig. 3.3. On the contrary, when the alloy is considered to be in the austenite phase at high temperatures, rate-dependent [38, 69] viscoplastic slip can occur on the activated slip planes. The slip accumulates with time and over families of slip systems giving rise to a macroscopic viscoplastic (or plastic) strain $\boldsymbol{\epsilon}_{vp}$ (or $\boldsymbol{\epsilon}_{p}$) in Eq. 3.7, based on the activated phenomena. *Note:* The $\boldsymbol{\epsilon}_{vp}$ accounts for both plastic strain generated at low temperatures and viscoplastic strain generated at high temperatures, and in the rest of the text only $\boldsymbol{\epsilon}_{vp}$ is used. The strain is derived using the orientation tensor $\mathbf{T}^{s}$ associated with the families of slip systems N_s, evaluated for each slip plane $\mathbf{n}^{s}$ and slip direction $\mathbf{l}^{s}$.

$$\boldsymbol{\epsilon}_{vp}(or\ \boldsymbol{\epsilon}_p) = \sum_{s=1}^{N_s} \gamma_{vp}^s \mathbf{T}^s$$
$$\mathbf{T}^s = \frac{1}{2}(\mathbf{n}^s \otimes \mathbf{l}^s + \mathbf{l}^s \otimes \mathbf{n}^s) \tag{3.7}$$

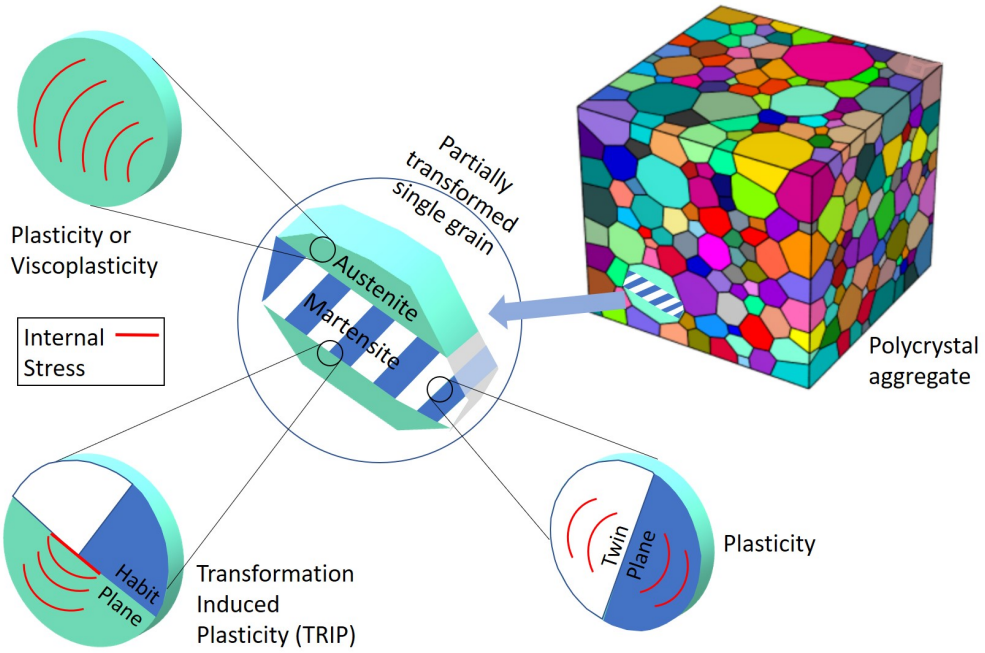

Figure 3.3: Schematic of polcrystalline microstructure of an HTSMA, with a partially transformed grain, enlarged to show the internal stresses causing plasticity in martensite, plasticity/viscoplasticity in austenite, and TRIP at the interface between martensite and austenite. *Note:* all these phenomena do not occur at the same temperature.

The accumulated or equivalent value of each strain tensor $\boldsymbol{\epsilon}_i$ is evaluated as a scalar representative:

$$(\epsilon_{acc})_i = \sqrt{\frac{2}{3}\boldsymbol{\epsilon}_i : \boldsymbol{\epsilon}_i} \tag{3.8}$$

The evolution and description of each inelastic strain component and its associated variables is presented in the following sections.

3.2.3.2 Thermodynamic Framework: Hysteresis and free energy

SMAs and HTSMAs, when subjected to a thermomechanical path of uniaxial constant force thermal cycling (Fig. 3.6(a)), generate a hysteresis curve (Fig. 3.6(b)). The hysteresis is generated as the stored energy dissipates during transformation (A $\leftrightarrow$ M) [118]. To represent this stored energy, the free energy formulation associated with transformation is used, and broken into a chemical and non-chemical part [79, 2] in Eq. A.4. The chemical part (in Eq. A.5) is generated from the difference between the lattice energies of the austenite and martensite phases, due to the nature of bonds making up the lattice. The non-chemical part on the other hand is generated from considered reversible and non-reversible phenomena. The reversible phenomenon is elasticity, which generates elastic strain energy (in Eq. A.6) and, hence, increases the stored elastic energy. Whereas the non-reversible phenomena can be TRIP (in Eq. A.7) and plasticity/viscoplasticity (in Eq. A.8). The stored energy is dissipated through frictional work against transformation resistance and plastic/viscoplastic accommodation (in the phases and interfaces) of dislocations generated by the above non-reversible phenomena. A detailed explanation of the energy dissipation is provided in the work of Hamilton et al. [2].

According to Hamilton et al. [2], an increase in dislocation loops (or density) can cause an increase in slope (forward/reverse) slopes and widening of hysteresis through two respective mechanisms. The first is plastic accommodation (plastic relaxation) of dislocation loops, which dissipates the stored elastic energy and modifies the slopes. The accommodation can further reduce transformation strain and, hence, strain energy during reverse transformation [119]. The second mechanism includes a decrease in effective driving force when the hardening created by dislocation loops increases the transformation (or frictional) resistance. The strain energy is dissipated due to the increased resistance, and more heating is required to transform, which is reflected by a widening in hysteresis. The above two mechanisms basically signify a coupling between phase transformation and plasticity, and the second mechanism is implemented in the present study (and explained below) to define a coupling between phase transformation and viscoplasticity.

Hamilton et al. [2] also presented a model that simulates the reduction of transformation strain

by modifying the TT specified at the mid point during transformation. They do so through a factor which compensates for the energy dissipated and characterises the hysteresis. However, the model does not account for the effect of hardening on the transformation resistance and driving force. In the present work, the effect of hardening (due to plasticity/viscoplasticity) is accounted for through an explicit coupling that affects the transformation resistance (and hysteresis), directly, and the TT and transformation strain evolution, indirectly. Apart from hardening, the hysteresis is also known to evolve due to an interaction energy between martensite variants, defined by the term $\sum_{m,n} H^{mn}\xi^m\xi^n$ [120, 114, 9, 80]. Accounting for it remains a challenging task and sets up paths for potential modeling improvements of the present study as the interaction matrix H^{mn} is not yet defined for any HTSMA, in the open literature.

The constitutive equations for free energy and dissipation used in building the thermodynamic framework are presented in Appendix: A for the sake of brevity. The framework is based on the first and second law of thermodynamics to formulate the dissipation inequality. The inequality employees the free energy expressions, to derive the thermodynamic forces responsible for activating and driving the inelastic phenomena such as transformation, detwinning, TRIP, and viscoplasticity. The force expressions are presented with their conjugate variables in the following sections.

3.2.3.3 Evolution of martensite volume fraction

The martensite volume fraction of each variant generated on transformation is divided into a recoverable ξ_{re} and irrecoverable (retained) ξ_{ir} part: $\xi = \xi_{re} + \xi_{ir}$. The evolution of recoverable martensite is given by Eq. 3.10 and that of retained martensite is introduced later in the Section 3.2.3.6. The retained martensite is accounted because experimental studies [121, 50, 3, 52, 97, 7] on HTSMAs show evidence of its accumulation during thermomechanical testing. The transformation driving force Φ^{α}_{tr} (in Eq. 3.9) for each martensite variant evolves throughout the thermomechanical path as it depends on the temperature and stress. The phase transformation initiates on crossing a threshold based on the critical transformation resistance Y_1 and Y_2 for the forward and reverse paths, respectively. This initiates the evolution of martensite variants (volume fraction), while being constrained by $0 \leq \xi^{\alpha}, \sum_{\alpha=1}^{N_v} \xi^{\alpha} \leq 1$, and depending on the reference rate of

transformation ξ_0.

$$\Phi^{\alpha}_{tr} = g^{tr}(\boldsymbol{\sigma} : \mathbf{P}^{\alpha}_{tr}) + (\lambda^{\alpha} - \lambda^{\alpha}_{0})(\boldsymbol{\sigma} : \mathbf{P}^{\alpha}_{de}) - \beta\,(T - T_0) - \frac{1}{2}\boldsymbol{\epsilon}_e : \Delta\mathbb{C} : \boldsymbol{\epsilon_e} \tag{3.9}$$

$$\dot{\xi}^{\alpha}_{re} = \begin{cases} \xi_0 \left| \dfrac{\Phi^{\alpha}_{tr}}{Y_1} \right|^{m^{tr}} sign(\Phi^{\alpha}_{tr}) & \text{if} \quad Y_1 \leq \Phi^{\alpha}_{tr} \quad \text{and} \quad 0 \leq \xi^{\alpha}, \xi \leq 1 \\ \xi_0 \left| \dfrac{\Phi^{\alpha}_{tr}}{Y_2} \right|^{m^{tr}} sign(\Phi^{\alpha}_{tr}) & \text{if} \quad \Phi^{\alpha}_{tr} \leq -Y_2 \quad \text{and} \quad 0 \leq \xi^{\alpha}, \xi \leq 1 \end{cases} \tag{3.10}$$

where $sign(x) = x/|x|$ with $|x|$ is the absolute value of x.

The evolution of recoverable martensite signifies the formation of HPVs. Under a stressed condition, the LCVs within the HPVs can detwin and the favored variants grow at the expense of the unfavored ones (in Fig. 3.2). The motion of detwinning gives rise to a detwinning strain $\boldsymbol{\epsilon}^{de}$, derived from the LCV volume fraction. The evolution initiates during transformation, only when the driving force for detwinning Φ^{α}_{de} overcomes its resistance Y_{det} that represents $\boldsymbol{\sigma_{DT}}$ i.e. martensite detwinning stress [82, 122] shown schematically in Section 3.3.1.

$$\Phi^{\alpha}_{de} = \xi^{\alpha}(\boldsymbol{\sigma} : \mathbf{P}^{\alpha}_{de}) \tag{3.11}$$

Apart from the detwinning resistance constraint, the activation of detwinning is made to rely on an additional constraint, viz. on the evolution of λ^{α}, in Eq. 3.12, specifically for Ni-Ti-Hf HTSMA. The constraint is adopted from the work of Sehitoglu et al. [13] on Ni-Ti-Hf alloys. It specifies that, the LCV volume fraction will evolve only when $0.5 < \lambda^{\alpha} \leq 1$. The initial values λ^{α}_{0} for each martensite variant have been established mostly for SMAs like Ni-Ti [123, 9]. However, it remains a potential study yet to be conducted in case of HTSMAs. Hence, the above constraint is adopted. In addition, the term $\lambda^{\alpha} - \lambda^{\alpha}_{0}$ in Eq. 3.5 & 3.9 is taken as a constant parameter, i.e. g^{det}, due to the above reason. The parameters that control the detwinning are: g^{det} for magnitude, λ_{ref} for reference detwinning rate, m^{det} for detwinning kinetics. They can be calibrated at best using experimental results from single crystals HTSMAs, as was done in case of SMAs [2, 24].

$$\dot{\lambda}^{\alpha} = \begin{cases} \lambda_{ref} \left| \dfrac{\Phi^{\alpha}_{de}}{Y_{det}(T)} \right|^{m^{det}} sign(\Phi^{\alpha}_{de}) & \text{if} \quad \Phi^{\alpha}_{de} \geq Y_{det}(T) \quad \text{and} \quad 0.5 < \lambda^{\alpha} \leq 1 \\ 0 & \text{otherwise} \end{cases} \tag{3.12}$$

3.2.3.4 Evolution of slip during TRIP

The evolution of slip γ^{α}_{tr} over the habit-planes is activated during transformation when the thermodynamic force Φ^{α}_{TRIP} for TRIP in Eq. 3.13 becomes positive.

$$\Phi^{\alpha}_{TRIP} = (\boldsymbol{\sigma} : \mathbf{P}^{\alpha}_{tr}) - \tau^{\alpha}_{p} \tag{3.13}$$

The evolution of plastic slip γ^{α}_{tr} is adopted as a thermally activated flow rule proposed by Berbenni et al. [124] and implemented by Yu et al. [125] in Ni-Ti. The flow rule in Eq. 3.14 considers the glide of dislocations on overcoming the Peierl's barrier with temperature, resulting in a mean dislocation velocity following an Arrhenius-type law [126]. The ΔG_{slip} is the activation energy for slip, k_b the Boltzmann constant, μ the shear modulus, τ_0 the resolved shear stress required to overcome the Peierl's obstacles, exponents *p* and *q* to define the shape of the curve [124].

$$\dot{\gamma}^{\alpha}_{tr} = \begin{cases} \gamma_0 \left(\dfrac{\boldsymbol{\sigma} : \mathbf{P}^{\alpha}_{tr}}{\mu} \right)^2 exp \left(\dfrac{-\Delta G_{slip}}{k_b T} \left(1 - \left(\dfrac{\Phi^{\alpha}_{TRIP}}{\tau_0} \right)^p \right)^q \right) |\dot{\xi}^{\alpha}_{re}| & \text{if} \quad \Phi^{\alpha}_{TRIP} > 0 \\ 0 & \text{if} \quad \Phi^{\alpha}_{TRIP} \leq 0 \end{cases} \tag{3.14}$$

The dislocations generated by slip create a hardening which increases the resistance τ^{α}_{p} to TRIP. The hardening, in turn, controls the thermodynamic force Φ^{α}_{TRIP} responsible for TRIP and the evolution of $\dot{\gamma}^{\alpha}_{tr}$. The non-linear isotropic hardening is made to evolve phenomenologically in Eq. 3.15 (adopted from Yu et al. [83]), where k_1 controls the magnitude and ρ^{α}_{tr} is a dislocation

density variable:

$$\tau_p^\alpha = k_1 \sqrt{\rho_{tr}^\alpha} \tag{3.15}$$

The dislocation density variable ρ_{tr}^α is derived from an exponential evolution, whose rate is controlled using the parameter k_2 and magnitude by $\dot{\gamma}_{tr}^\alpha$. The total dislocation density represented by the variable ρ_{TRIP} is obtained by considering the dislocations over all the N_v variants.

$$\begin{aligned} \dot{\rho}_{tr}^\alpha &= \dot{\gamma}_{tr}^\alpha \left(1 - k_2 \rho_{tr}^\alpha\right) \\ \rho_{TRIP} &= \sum_{i=1}^{N_v} \rho_{tr}^\alpha \end{aligned} \tag{3.16}$$

3.2.3.5 Crystal plasticity framework

The state-of-the-art literature on crystal plasticity frameworks was influenced by some of the earliest works in the field. These included the works of Asaro [127], Asaro and Needleman [128], Anand and Kothari [129] which developed models accounting for aspects such as rate-dependency, strain hardening and the effects of texture in polycrystals. The current framework is developed to account for the same aspects using a part physics-based and part phenomenological approach. The plastic/viscoplastic slip are derived on the slip systems by a physics-based approach, while their activation and evolution is defined in a phenomenological manner.

Apart from the above two approaches, the current framework also follows a multi-scale approach. To generate the macroscopic response from plasticity/viscoplasticity, their constitutive equations are defined at the macroscale, and then scaled down to the microscale. The scaling is done to account for the response from each family of slip systems considered, by employing a unique macro-micro approach developed by Poubanne and De Bussac [11]. The approach involves comparing the macro- and micro-scale equations of plastic/viscoplastic yielding, hardening, and strain accumulation, to determine scaling coefficients for microscale parameters common to a fam-

ily of slip systems. The macro-micro approach presents a major advantage of tailoring the crystal plasticity model for any possible crystal lattice (through its slip systems), and using experimental macroscale responses (from polycrystals) to calibrate microscale responses (of single crystals). The approach is presented in Appendix: B, for the sake of brevity, while the scaling coefficients are presented in Table 3.1. *Note:* each of these coefficients are temperature dependent.

In SMAs/HTSMAs, the crystal lattice of the martensite variants formed on phase transformation can either be orthorhombic (B19) or monoclinic (B19') depending on the alloy configuration and lattice parameters. The Ni-Ti-Hf HTSMA (considered for the present study) is known to form 12 - B19' martensite variants [13] from the parent cubic (B2) austenite phase. Based on the crystal lattice and arrangement of atoms, there can be several families of slip systems associated to it, with each family differing in generalized stacking fault energy (GSFE). The GSFE is a quantity used to evaluate and compare the strength of slip systems. Chowdhury et al. [30] compares the energy surfaces for several SMAs and HTSMAs, and gives an idea of the family of slip systems that can be considered for the studied alloys.

In case of Ni-Ti-Hf, the slip systems considered in B19' (martensite) belong to the $\{001\}\langle 010\rangle$ family, while in B2 (austenite) belong to the $\{110\}\langle \bar{1}11\rangle$ & $\{110\}\langle 001\rangle$ family [30]. On performing permutations of the miller indices belonging to each family, the possible slip systems for each lattice are obtained (presented later in Section 3.3.2.4). The number of slip systems considered in martensite are 6, belonging to the $\{001\}\langle 010\rangle$ family. Whereas, in austenite, there are 12 belonging to $\{110\}\langle \bar{1}11\rangle$ and 6 belonging to $\{110\}\langle 001\rangle$, which are consistent with those mentioned in Chowdhury et al. [30]. 24 slip systems are, therefore, considered in total.

Table 3.1: Viscoplastic material parameters with their scaling coefficients obtained from the macro-micro approach [11].

		Martensite (B19' Monoclinic)	Austenite (B2 Cubic)	
	Macroscale	$\{001\}\langle 010\rangle$	$\{110\}\langle \bar{1}11\rangle$	$\{110\}\langle 001\rangle$
Power law exponent	n	n	n	n
Slip resistance	K	$\frac{1}{3}K$	$\frac{1}{\sqrt{6}}K$	$\frac{\sqrt{2}}{3}K$
Coefficient of viscosity	C_{visco}	$\frac{1}{2}C_{visco}$	$\frac{\sqrt{6}}{8}C_{visco}$	$\frac{1}{\sqrt{2}}C_{visco}$
Linear isotropic hardening	Q_1	$\frac{2}{3}Q_1$	$\frac{4}{3}Q_1$	$\frac{2}{3}Q_1$
Non-linear isotropic hardening	Q	$\frac{1}{3}Q$	$\frac{1}{\sqrt{6}}Q$	$\frac{\sqrt{2}}{3}Q$
Rate of dislocation density	b	$2b$	$\frac{8}{\sqrt{6}}b$	$\sqrt{2}b$
Initial yield radius	r_0	$\frac{1}{\sqrt{3}}r_0$	$\frac{1}{\sqrt{6}}r_0$	$\frac{\sqrt{2}}{3}r_0$
Kinematic hardening magnitude	C	$\frac{2}{3}C$	$\frac{4}{3}C$	$\frac{2}{3}C$
Rate of kinematic hardening	D	$2D$	$\frac{8}{\sqrt{6}}D$	$\sqrt{2}D$

On defining the slip systems and scaling coefficients, the microscale equations for plasticity/viscoplasticity, adopted from Méric et al. [130], are formulated for the considered slip systems. The macroscopic stress tensor $\boldsymbol{\sigma}$ is resolved as $\boldsymbol{\sigma_g}$ for each crystal/grain g using a rotation matrix $\mathbf{R}^g$ derived from the crystallographic orientation (of the grain) provided by its Euler angles (ϕ_1, Φ, ϕ_2) with respect to the sample frame of reference. $\mathbf{R}^g$ is evaluated according to the Bunge convention [8].

$$\boldsymbol{\sigma_g} = (\mathbf{R}^g)^T.\boldsymbol{\sigma}.\mathbf{R}^g \tag{3.17}$$

The microscopic stress $\boldsymbol{\sigma_g}$ is further resolved over each slip system in the grain, using the orientation tensor $\mathbf{T}^s$, to determine the resolved shear stress (RSS) τ^s. The schematic in Fig. 3.4

shows how the resolving from the sample to macro to micro scale is done.

$$\tau^s = \boldsymbol{\sigma_g} : \mathbf{T}^s \tag{3.18}$$

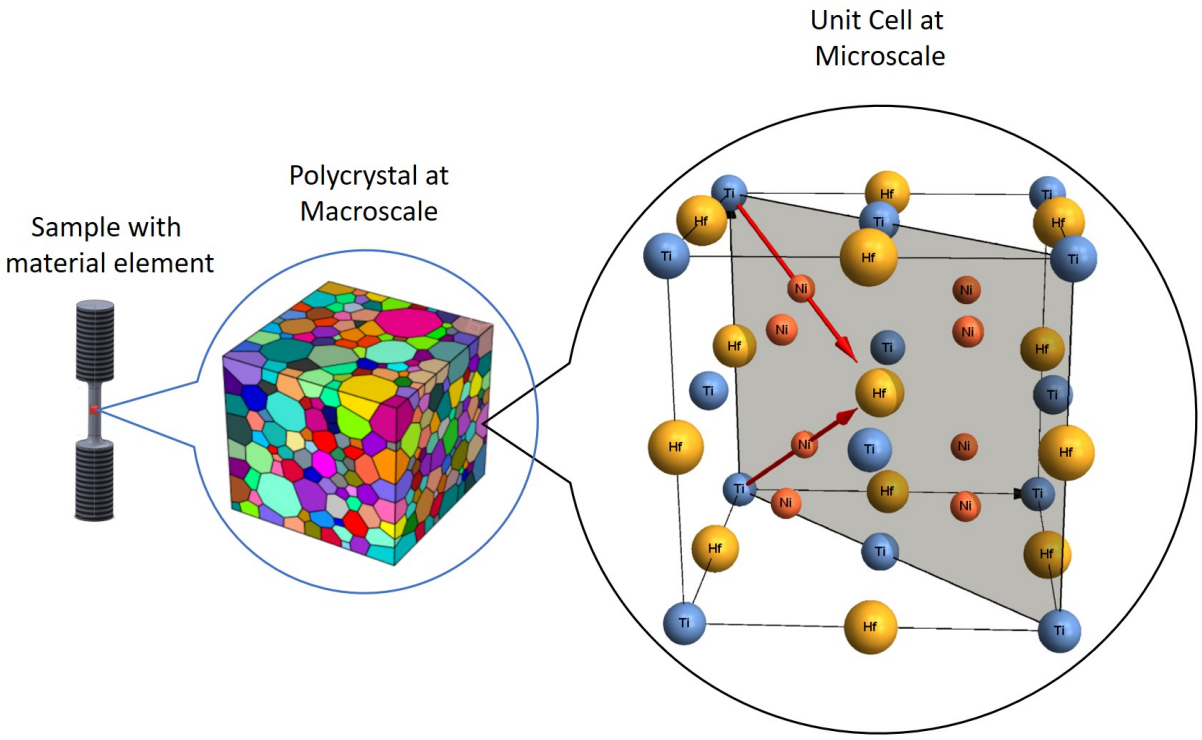

Figure 3.4: Schematic of resolving from the Sample to Macro to Micro scale. The macro scale shows a polycrystalline aggregate, and the micro scale shows a Ni-Ti-Hf crystal lattice with a slip plane and slip directions.

The yield function (or curve) is formulated to depend on an isotropic r^s and a kinematic x^s hardening, and is initially defined by its radius r_0 (in Eq. 3.19). An expansion of the yield curve, when uniform along all directions (isotropic), can be represented by an isotropic hardening variable r_i^s.

$$r^s = r_0 + r_i^s \tag{3.19}$$

The isotropic hardening r_i^s can evolve linearly ($Q_1\gamma_{vp}^s$) and/or non-linearly (Qr_{sum}) (in Eq. 3.20), depending on the plastic/viscoplastic slip γ_{vp}^s as shown in Eq. 3.23. Both linear and non-linear evolutions are considered based on the macroscopic trends seen in the experimental investigations Chapter 2. The parameters Q_1 and Q control the magnitude of the linear and non-linear isotropic hardening, respectively. The variable q^s represents the dislocation density and its evolution is shown by Eq. 3.25. The interaction between slip systems *s* and *j*, in a family of slip systems, is accounted by an interaction matrix hh_{sj}. The effect of the interaction of dislocation densities accumulated over a single family of slip systems N_s, is represented by the variable r_S.

$$\begin{aligned} r_i^s &= Q_1\gamma_{vp}^s + bQr_{sum}^s \\ r_{sum}^s &= \sum_{j=1}^{N_s} hh_{sj}(q^s) \end{aligned} \tag{3.20}$$

Apart from the isotropic hardening a kinematic hardening is also considered in the framework based on the tension-compression asymmetry observed in Fig. 24 of Benafan et al. [6], signifying a Bauschinger like effect. The kinematic hardening generated during a fatigue test results in a shift of the yield curve. It is represented by a kinematic hardening variable x^s which evolves non-linearly based on α^s in Eq. 3.24 and parameter *C* which controls the magnitude. The variable α^s also depends on the slip rate $\dot{\gamma}_{vp}^s$.

$$x^s = C\alpha^s \tag{3.21}$$

The criteria for the onset of slip on each slip system is defined by its driving force Φ_{vp}^s, which is decided by the magnitude of τ^s, r^s and x^s on that slip system. The slip initiates only when $\Phi_{vp}^s > 0$ i.e. when $|\tau^s - x^s| > r^s$ where $|x| = x$.

$$\Phi_{vp}^s = |\tau^s - x^s| - r^s = 0 \tag{3.22}$$

The magnitude of Φ^s_{vp} is then used to determine $\dot{\gamma}^s_{vp}$ (in Eq. 3.23) over the activated slip planes belonging to a family of slip systems N_s. The plastic/viscoplastic slip is then accumulated over the entire family and similarly done for every other activated family present in the grain, to give the plastic/viscoplastic strain tensor (Eq. 3.7) over the entire grain.

$$\dot{\gamma}^s_{vp} = C_{visco}\, sinh \left\langle \frac{\Phi^s_{vp}}{K} \right\rangle^n sign(\tau^s - x^s) \tag{3.23}$$

where $\langle x \rangle$ stands for a Heaviside step function of x: if $x > 0$, then $\langle x \rangle = x$, or else $\langle x \rangle = 0$. The evolution of γ^s_{vp} is predicted using a hyperbolic sine function contrary to the popular Norton's equation used for viscoplastic slip during creep. Chaboche [131] states that although the Norton's equation can very well be used to predict viscoplastic slip, its exponent (*n*) very often varies with varying strain rates. On comparing several viscosity functions, it is observed that the ones used by Miller [132] and Delobelle et al. [133] implement a hyperbolic sine law that works with a constant exponent (contrary to Norton's) in regimes of low and high strain rates (but not impact loading). Therefore, the hyperbolic sine function is justified for varying experimental trends, and implemented in the present study. In addition, to predict the plastic (rate-independent), viscoplastic (rate-dependent) slip, and the transition between them at high temperatures, using a single function, the parameters of the hyperbolic sine law are formulated to be temperature dependent, and calibrated accordingly.

The slip also contributes to an exponential evolution of the scalar variable α^s depending on a material parameter *D*, representing the kinetics of evolution of kinematic hardening, that can be calibrated through cyclic loading tests.

$$\dot{\alpha}^s = (sign(\tau^s - x^s) - D\alpha^s)\dot{\gamma}^s_{vp} \tag{3.24}$$

and the dislocation density variable q^s evolves based on $\dot{\gamma}^s_{vp}$ in an exponential manner depending on *b*, the kinetics of isotropic hardening linked with the increase of dislocation density. The total dislocation density over all families of slip systems is represented by the dislocation density

variable ρ_{vp}

$$\begin{aligned} \dot{q}^s &= \dot{\gamma}^s_{vp}(1 - bq^s) \\ \rho_{p/vp} &= \sum_{s=1}^{N_s} q^s \end{aligned} \tag{3.25}$$

3.2.3.6 Coupling between phase transformation and viscoplasticity

The coupling between phase transformation and viscoplasticity has been interpreted through experimental data, trends and TEM images, obtained after conducting thermomechanical tests on HTSMAs [121, 47, 3, 7]. The coupling is created as a result of nucleation of dislocations during viscoplasticity and TRIP, and subsequently trapping and retaining portions of martensite. The dislocations and retained martensite affect phase transformation properties such as TT, transformation strain, and hysteresis, which depend on quantities such as transformation driving force and recoverable martensite volume fraction. Therefore, to simulate the coupling effect, the total of the dislocation density variables ($\rho_{TRIP} + \rho_{vp}$) has to be accounted as a factor affecting the above quantities. The schematic in Fig. 3.5 shows how the present study produces the coupling by using the dislocation density variables.

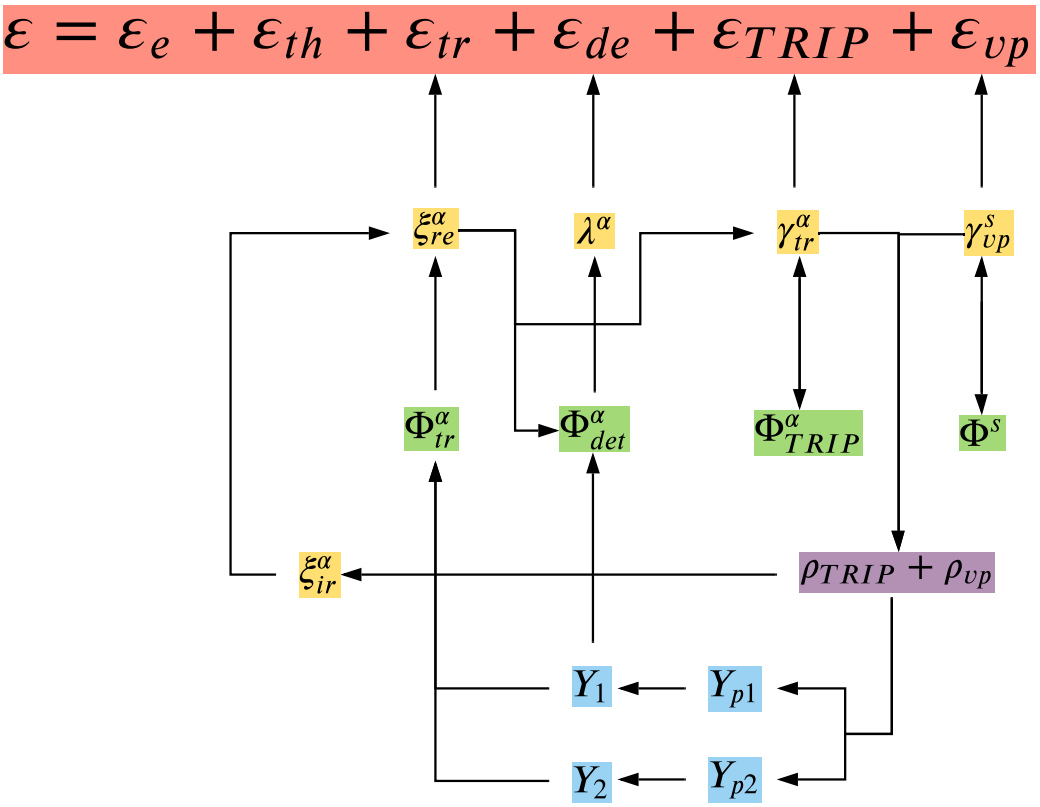

Figure 3.5: Flowchart of coupling between phase transformation and viscoplasticity through the total dislocation density generated during viscoplasticity and TRIP.

The total of the dislocation density variables, is implemented into the evolution of internal variables such as transformation resistance (Y_1, Y_2) and irrecoverable martensite (ξ_{ir}). These affect the driving forces for transformation (Φ_{tr}^{α}) and detwinning (Φ_{det}^{α}) directly, as well as the driving force for TRIP (Φ_{TRIP}^{α}) indirectly, through the recoverable martensite volume fraction (ξ_{re}). The above effects are reflected macroscopically through the modifications of phase transformation properties such as TT, hysteresis width, and transformation strain.

Recalling from 3.2.3.3, the variables Y_1 and Y_2 represent the resistance to transformation for the forward and reverse transformations paths, respectively. They control the hysteresis width in a linear manner and to formulate their evolution with the effect of coupling, the following equations

are proposed:

$$\begin{aligned} Y_1 &= Y_1^0 + Y_{p1} \\ Y_2 &= Y_2^0 + Y_{p1} \end{aligned} \tag{3.26}$$

where, Y^0 represents the resistance in a dislocation free state, and is based on the TT (in Table 3.3). The variables Y_{p1} and Y_{p2} account for the change in transformation resistance caused by the permanent deformations, along the forward and reverse paths, respectively. These variables increase (+) the transformation resistance, to cause a shift in the transformation paths, resulting in an increase or widening of the hysteresis width, and shift of TT. Their evolutions are proposed as an exponential function of the square root [83] of the total of the dislocation density variables, which is controlled though parameters: d_1, d_2 for the asymptotic value and c_1, c_2 for the kinetics:

$$\begin{aligned} Y_{p1} &= \frac{1}{d_1}(1 - e^{-d_1 c_1 \sqrt{\rho_{TRIP}+\rho_{vp}}}) \\ Y_{p2} &= \frac{1}{d_2}(1 - e^{-d_2 c_2 \sqrt{\rho_{TRIP}+\rho_{vp}}}) \end{aligned} \tag{3.27}$$

The evolution of retained martensite has been formulated phenomenologically [68, 85] and simulated for past experimental studies [3]. In the present study, a phenomenological evolution is also formulated, through a direct correlation with the total dislocation density. The retained martensite is predicted by reducing the amount of recoverable martensite, during reverse transformation. This approach falls in line with the transformation-plasticity coupling theory presented by Sittner et al. [5]. Therefore, to formulate the retained martensite, which is a part of the total martensite volume fraction of each variant: $\xi = \xi_{re} + \xi_{ir}$, the following equation is proposed, with a single parameter g^{ret} assuming the role played by the two dislocation density variables is the same:

$$\xi_{ir} = g^{ret}\left(\rho_{TRIP} + \rho_{vp}\right) \tag{3.28}$$

3.3 Finite Element Analysis

3.3.1 Thermomechanical test

The crystal-plasticity framework presented in previous Sections is implemented into a model following an Algorithm presented in Appendix: C. Uniaxial constant force thermal cycling (UC FTC) tests performed in Chapter 2, were simulated. The thermomechanical path followed for simulating the UCFTC test, shown in Fig. 3.6, (a) involves heating (a $\rightarrow$ b) the HTSMA to a upper cycle temperature (UCT) which lies beyond the TT: A_f. The HTSMA is then loaded and subsequently cooled (b $\rightarrow$ c) to a lower cycle temperature (LCT) which lies lower than the TT: M_s. The HTSMA is heated back (c $\rightarrow$ d) to the UCT, while being loaded, and the cycle is repeated, with a constant thermal cycling (heating/cooling) rate. The constant force thermal cycling, hence, results in activation of phase transformation and irrecoverable mechanisms. The activation of phase transformation is based on the TT (M_s, M_f, A_s, A_f) and it involves dissipation of stored elastic energy, which results in hysteresis (ΔT) as observed in the strain-temperature response shown in Fig. 3.6(b).

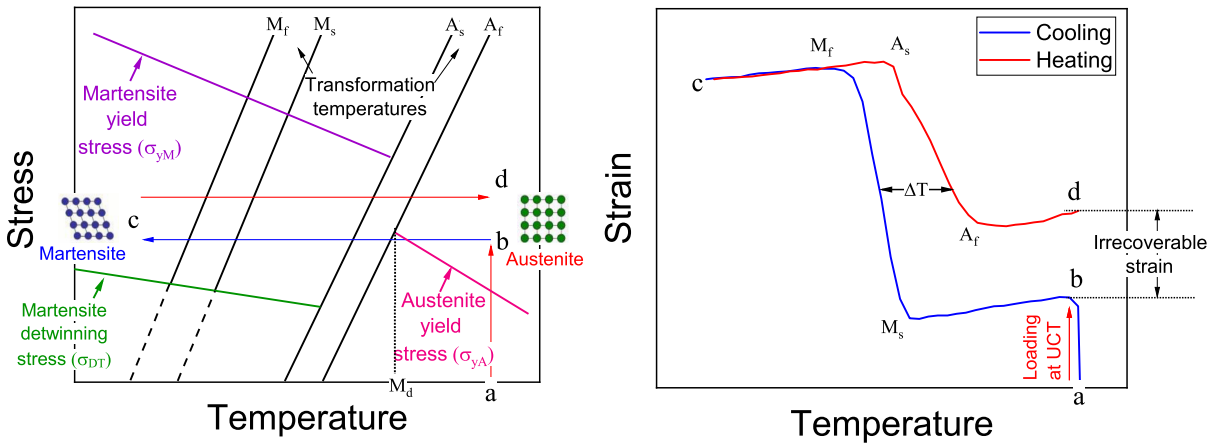

(a) (b)

Figure 3.6: (a) Thermomechanical path followed during a UCFTC test (a → b → c → d) using a $\boldsymbol{\sigma} - T$ phase diagram with material characteristic bounds adopted from Ma et al. [1]. The alloy is initially loaded (a → b) at a certain stress $\boldsymbol{\sigma}$ and temperatures above A_f (in the austenite phase). It is then cooled below M_f until it becomes fully martensite in detwinned state c depending on the $\boldsymbol{\sigma_{DT}}$. During the transformation the specimen actuates by elongating and demonstrating an increase in strain. The alloy is then heated back to the temperature above A_f such that it returns to a fully austenite state and tries to recover the strain generated (state d) (b) Strain-temperature response (actuation) generated during a UCFTC test, showing the marked TT (M_s, M_f, A_s, A_f), hysteresis (ΔT) and the irrecoverable strain in Chapter 2.

The activation of irrecoverable mechanisms is based on the current temperature and stress level (Fig. 3.6(a)). At the UCT, the HTSMA is loaded in the austenite phase and then subsequently cooled at a fixed rate, during which the HTSMA can undergo viscoplastic/plastic deformation, based on the yield stress at the current temperature. On cooling, the austenite phase begins to transform to martensite. In the martensite phase, its variants can exist in either a twinned or de-twinned state based on the stress level compared to the detwinning stress $\boldsymbol{\sigma_{DT}}$. On heating back to the UCT, and completing a cycle, the irrecoverable strain generated by mechanisms of plasticity/viscoplasticity, TRIP, and accumulation of retained martensite results in an opening of the hysteresis loop (Fig. 3.6(b)). Based on the conditions in Chapter 2, the present study simulates UCFTC tests between a LCT of 100 °C and a UCT of 500 °C at a stress level of 500 MPa for thermal cycling rates between 1 and 50 °C/min.

3.3.2 Material Characteristics and parameters

The Ti-rich $Ni_{49.8}Ti_{30.6}Hf_{19.2}$ HTSMA (Chapter 2) is considered in the present study and hence its material properties and parameters are implemented in the constitutive model to simulate the macroscopic response. Required isotropic properties are obtained from Benafan et al. [6]. While required anisotropic material properties and parameters are adopted from past crystal-plasticity studies on Ni-Ti [9, 69, 83], along with theoretical and experimental studies on Ni-Ti-Hf [13, 12]. The adopted parameters are tweaked during calibration for the selected Ni-Ti-Hf HTSMA, as there are no studies in the open literature that list the required parameter values for single crystal Ni-Ti-Hf or any HTSMA.

3.3.2.1 Thermoelastic parameters

The isotropic thermal properties and anisotropic elastic properties used for predicting the thermal and elastic strains in Eq. 3.2 & 3.3 are presented in Table 3.2. A theoretical domain for viscoplasticity is defined based on the melting temperature of the $Ni_{49.8}Ti_{30.6}Hf_{19.2}$ alloy.

Table 3.2: Isotropic material properties of $Ni_{49.8}Ti_{30.6}Hf_{19.2}$ from Benafan et al. [6]. Anisotropic properties from Santamarta et al. [12].

Properties	*Nomenclature*	*Martensite*	*Austenite*
Stiffness coefficients	E_{1111} (GPa)	90.08	200.0
	E_{1122} (GPa)	44.36	136.0
	E_{1212} (GPa)	22.86	29.17
Shear modulus	μ (GPa)	12.78	28.57
Poisson ratio	ν	0.42	0.41
Coefficient of thermal expansion	α_{CTE} (1/K)	9.56 x 10^{-6}	11.46 x 10^{-6}
Melting temperature	T_m	1287 °C	
		1560.15 K	
Theoretical domains			
Viscoplastic domain	(0.3 - 0.5)*T_m	194 - 506 °C	
		468 - 780 K	

3.3.2.2 Phase-transformation parameters

The material properties and calibrated parameters controlling phase-transformation and detwinning in Eq. 3.4 & 3.5, are presented in Table 3.3. The TTs and slopes of TT are standard macroscale properties, which are implemented to evaluate the transformation parameters such as T_0 and transformation resistance (or hysteresis) Y_1, Y_2. The calibration of the parameters $g^{tr}, \beta, m^{tr}, \sigma_0, g^{det}$ and m^{det} for Ni-Ti-Hf is demonstrated later in Section 3.5.1.1.

Table 3.3: Material properties [6] and calibrated parameters controlling phase-transformation and detwinning of $Ni_{49.8}Ti_{30.6}Hf_{19.2}$

Material properties	*Nomenclature*	*Martensite*	*Austenite*
Transformation temperatures (TTs)	M_f, M_s °C	$259.5, 288$	
(at 0 stress)	A_s, A_f °C		$306.5, 330.2$
Slope of martensite TTs	C_m (MPa/°C)	20.77	
Slope of austenite TTs	C_a (MPa/°C)		15.29
Theoretical domains			
Phase-transformation domain	M_f - A_f (°C)	283.5 - 362.8	
(at 500 MPa)			
Transformation parameters			
Magnitude of transformation strain	g^{tr}	0.0965	
Coefficient of latent heat of transformation	β (MPa/°C)	3	
Rate of transformation	m^{tr}	50	
Phase equilibrium temperature at zero stress	T_0 (°C)	296	
Transformation resistance	Y_1^0(MPa)	70	
	Y_2^0(MPa)	70	
Detwinning parameters			
Magnitude of detwinning strain	g^{det}	0.15	
Rate of detwinning	m^{det}	30	
Detwinning resistance	Y_{det}	70	

Recalling from Section 3.2.2, the primary systems accounting for the HPVs and their corresponding LCVs are the family of transformation systems (**m**, **b**) and twinning systems (**t**, **a**),

respectively. The theoretical study by Sehitoglu et al. [13] lists the family of HPVs and LCVs for several Ni-Ti-Hf systems. The study also establishes the theoretical phase transformation (CVP) + detwinning strains for single crystals (oriented along [001], [011] & [111]) of the alloy systems, and validates them through experimental evidence. One of the systems investigated in the study is $Ni_{49.8}Ti_{30.2}Hf_{20}$, which is similar to $Ni_{49.8}Ti_{30.6}Hf_{19.2}$, in terms of being Ti-rich, having close lattice parameters and, hence, forming the same HPV and LCV families. Therefore, the transformation and detwinning strains for single crystals of the $Ni_{49.8}Ti_{30.2}Hf_{20}$ alloy are used to calibrate the transformation and detwinning parameters of the present constitutive model.

As mentioned in Section 3.2.3.5, the above study also mentions that the Ni-Ti-Hf alloy forms 12 B19' martensite variants. To account for all the 12 HPV and LCV variants formed, the entire list of systems (for the family), is required. Hence, the 12 systems were determined by compiling the alloy's lattice parameters [6] (martensite:a, b, c, β; austenite:& a_0) into a FORTRAN code developed by Thamburaja [77] for determining the HPV and LCV systems for a Ni-Ti and Ni-Ti-X system. The code evaluates the systems using the Crystallographic Theory of Martensite (CTM) developed by Ball and James [134] while implementing an algorithm developed by Hane [135]. The systems (**m**,**b**,**t**,**a**) obtained on compiling the code are found to be consistent with the family presented by Sehitoglu et al. [13] and, hence, are implemented into the present study. The 12 systems are as follows:

Table 3.4: Transformation systems (HPVs) of $Ni_{49.8}Ti_{30.2}Hf_{20}$

	Transformation systems (HPVs)	
	Habit plane normal (**m**)	Habit shear direction (**b**)
1	$\{-0.9112, -0.0668, -0.4064\}$	$\langle 0.0118, 0.1677, -0.0650\rangle$
2	$\{-0.9112, -0.4064, -0.0668\}$	$\langle 0.0118, -0.0650, 0.1677\rangle$
3	$\{0.9112, -0.0668, -0.4064\}$	$\langle -0.0118, 0.1677, -0.0650\rangle$
4	$\{-0.9112, 0.4064, 0.0668\}$	$\langle 0.0118, 0.0650, -0.1677\rangle$
5	$\{0.9112, -0.0668, 0.4064\}$	$\langle -0.0118, 0.1677, 0.0650\rangle$
6	$\{-0.9112, 0.4064, -0.0668\}$	$\langle 0.0118, 0.0650, 0.1677\rangle$
7	$\{-0.9112, -0.0668, 0.4064\}$	$\langle 0.0118, 0.1677, 0.0650\rangle$
8	$\{-0.9112, -0.4064, 0.0668\}$	$\langle 0.0118, -0.0650, -0.1677\rangle$
9	$\{-0.0668, -0.9112, -0.4064\}$	$\langle 0.1677, 0.0118, -0.0650\rangle$
10	$\{-0.4064, -0.9112, -0.0668\}$	$\langle -0.0650, 0.0118, 0.1677\rangle$
11	$\{-0.0668, 0.9112, -0.4064\}$	$\langle 0.1677, -0.0118, -0.0650\rangle$
12	$\{-0.4064, 0.9112, -0.0668\}$	$\langle -0.0650, -0.0118, 0.1677\rangle$

Table 3.5: Detwinning systems (LCVs) of $Ni_{49.8}Ti_{30.2}Hf_{20}$

	Detwinning systems (LCVs)	
	Detwin plane normal (**t**)	Detwin shear direction (**a**)
1	$\{0.7071, 0.7071, 0.0000\}$	$\langle 0.0161, 0.1018, 0.4947\rangle$
2	$\{0.7071, 0.0000, 0.7071\}$	$\langle 0.0161, 0.4947, 0.1018\rangle$
3	$\{-0.7071, 0.7071, 0.0000\}$	$\langle -0.0161, 0.1018, 0.4947\rangle$
4	$\{0.7071, 0.0000, -0.7071\}$	$\langle 0.0161, -0.4947, -0.1018\rangle$
5	$\{-0.7071, 0.7071, 0.0000\}$	$\langle -0.0161, 0.1018, -0.4947\rangle$
6	$\{0.7071, 0.0000, 0.7071\}$	$\langle 0.0161, -0.4947, 0.1018\rangle$
7	$\{0.7071, 0.7071, 0.0000\}$	$\langle 0.0161, 0.1018, 0.4947\rangle$
8	$\{0.7071, 0.0000, 0.7071\}$	$\langle 0.0161, 0.4947, 0.1018\rangle$
9	$\{-0.7071, 0.7071, 0.0000\}$	$\langle -0.0161, 0.1018, 0.4947\rangle$
10	$\{0.7071, 0.0000, -0.7071\}$	$\langle 0.0161, -0.4947, -0.1018\rangle$
11	$\{-0.7071, 0.7071, 0.0000\}$	$\langle -0.0161, 0.1018, -0.4947\rangle$
12	$\{0.7071, 0.0000, 0.7071\}$	$\langle 0.0161, -0.4947, 0.1018\rangle$

3.3.2.3 TRIP parameters

The parameters controlling slip during TRIP (Eq. 3.14) and its dislocation density variable (Eq. 3.16) are presented in Table 3.6. The parameters k_1 and k_2 for the TRIP hardening and dislocation density were calibrated for the selected HTSMA based on experimental responses (Chapter 2) over multiple cycles.

Table 3.6: TRIP strain and dislocation parameters calibrated for $Ni_{49.8}Ti_{30.6}Hf_{19.2}$

Slip parameters	*Nomenclature*	*Martensite ↔ Austenite*
Reference slip rate	γ_0	300
Activation energy of dislocation slipping	$\Delta G_{slip}(J^{-1})$	2.5 x 10^{-19}
(stress-free configuration)		
Boltzmann's constant	k_b (J/K)	1.38 x 10^{-23}
RSS to overcome Peierl's obstacles	τ_0 (MPa)	150
Power law exponent	p	0.01
	q	2
Hardening parameter	k_1	0.1
Dislocation parameter	k_2	5000

3.3.2.4 Viscoplastic parameters

Amongst the experimental studies on single crystals for Ni-Ti-Hf HTSMAs in the open literature [60, 136, 53, 137], there is an absence of data generated for a temperature domain that activates viscoplasticity. Therefore, to calibrate the viscoplastic parameters for a Ni-Ti-Hf HTSMA, the only alternative is to rely on viscoplasticity data from polycrystals, as those presented in Chapter 2. Calibrating microscale parameters (for single crystals) from macroscale (or polycrystal) data presents a challenge. To deal with this challenge, the macro-micro approach is implemented, by which the calibration is possible, as reasoned out in Appendix: B. The experimental data and trends in Chapter 2, for multiple cycles, are also used, to calibrate the hardening parameters in (Eq. 3.20 - 3.25) of the crystal-plasticity model. The macroscale parameters are presented in Table 3.1 with their values defined for specific temperature domains in Table 3.9. The slip systems considered are presented in Table 3.7 and 3.8.

Table 3.7: Slip systems in martensite phase of $Ni_{49.8}Ti_{30.2}Hf_{20}$

	Slip systems	
	Slip plane normal (**n**)	Slip direction (**l**)
1	$\{100\}$	$\langle 010 \rangle$
2	$\{100\}$	$\langle 001 \rangle$
3	$\{010\}$	$\langle 001 \rangle$
4	$\{010\}$	$\langle 100 \rangle$
5	$\{001\}$	$\langle 100 \rangle$
6	$\{001\}$	$\langle 010 \rangle$

Table 3.8: Slip systems in austenite phase of $Ni_{49.8}Ti_{30.2}Hf_{20}$

	Slip systems	
	Slip plane normal (**n**)	Slip direction (**l**)
1	$\{110\}$	$\langle\bar{1}11\rangle$
2	$\{110\}$	$\langle\bar{1}11\rangle$
3	$\{1\bar{1}0\}$	$\langle111\rangle$
4	$\{1\bar{1}0\}$	$\langle11\bar{1}\rangle$
5	$\{011\}$	$\langle11\bar{1}\rangle$
6	$\{011\}$	$\langle\bar{1}1\bar{1}\rangle$
7	$\{0\bar{1}1\}$	$\langle1\bar{1}\bar{1}\rangle$
8	$\{0\bar{1}1\}$	$\langle\bar{1}\bar{1}\bar{1}\rangle$
9	$\{101\}$	$\langle11\bar{1}\rangle$
10	$\{101\}$	$\langle1\bar{1}\bar{1}\rangle$
11	$\{\bar{1}01\}$	$\langle\bar{1}1\bar{1}\rangle$
12	$\{\bar{1}01\}$	$\langle\bar{1}\bar{1}\bar{1}\rangle$
13	$\{110\}$	$\langle001\rangle$
14	$\{1\bar{1}0\}$	$\langle001\rangle$
15	$\{011\}$	$\langle100\rangle$
16	$\{0\bar{1}1\}$	$\langle100\rangle$
17	$\{101\}$	$\langle010\rangle$
18	$\{\bar{1}01\}$	$\langle010\rangle$

Table 3.9: Plastic parameters of martensite and viscoplastic parameters of austenite phase calibrated for $Ni_{49.8}Ti_{30.6}Hf_{19.2}$

	Martensite		*Austenite*	
Nomenclature	*Value*	*Temperature* (°C)	*Value*	*Temperature* (°C)
n	100	100 → 250	8	425
			6	500
K (MPa)	10000	100 → 250	500	425
			300	500
C_{visco}	0	100 → 250	2 x 10^{-5}	425
			2 x 10^{-5}	500
Q_1 (MPa)	10000	100 → 250	70	425
			45	500
Q (MPa)	10000	100 → 250	70	425
			45	500
b	1 x 10^{-3}	100 → 250	0.7	425
			0.9	500
r_0 (MPa)	1000	100 → 250	320.9	425
			300	500
C (MPa)	10000	100 → 250	120	425
			100	500
D (MPa)	1000	100 → 250	7	425
			5	500

The experimental investigations (in Chapter 2) reveal, *no* irrecoverable deformations generated in the temperature domain of 100 - 250 °C. Since $M_f \approx 283.5$ °C, the HTSMA is assumed to be

purely martensite in the above domain, signifying no plastic deformations in martensite. Whereas, in the temperature domain of 425 - 500 °C, the irrecoverable deformations generated, increase with temperature. Since $A_f \approx 362.8$ °C, the HTSMA is assumed to be purely austenite in the above domain, signifying viscoplastic deformations in austenite. Therefore, based on this knowledge, and the fact that Eqs. 3.20 - 3.25, mentioned in Section 3.2.3.5 can predict plasticity/viscoplasticity with temperature dependent parameters, the parameters for martensite and austenite, are prescribed accordingly as shown in Table 3.9.

For the intermediary temperature domain of 250 - 425 °C, the HTSMA can be either martensite, austenite or a mixture of the phases depending on the path of transformation (Fig. 3.6). The irrecoverable deformations generated (in the domain) can be due to TRIP or plasticity in the individual phases. Therefore, for plasticity, the parameters are interpolated (by the FE solver) in a linear fashion based on the values defined for the prior and subsequent temperature domains. *Note:* the temperature limits of 100 and 500 °C can be expanded if further experimental investigations are done at those temperatures.

Lastly, the parameters of the interaction matrix hh_{sj} used in Eq. 3.20 and presented in Table 3.10 represents the interactions between a slip system *s* and *j* in a family of slip systems, for each phase. The parameters ($h_1, h_2, h_3, h_4, h_5, h_6$) are prescribed as 1, to create an interaction matrix which defines the interaction between the slip systems within a family, but not between families [130], which is why h_7 = 0. Developing an interaction matrix between families is a potential expansion of the current study.

Table 3.10: Slip systems interaction matrix.

Nomenclature	*Martensite*	*Austenite*
$h_1, h_2, h_3, h_4, h_5, h_6$	1	1
h_7	0	0

3.3.2.5 Transformation-viscoplasticity coupling parameters

The parameters controlling the evolution of the coupling between transformation and viscoplasticity (Section 3.2.3.6) over multiple cycles were also calibrated using experimental trends (in Chapter 2). The parameters in the coupling equations (Eq. 3.27, 3.28), are calibrated as follows:

Table 3.11: Transformation-viscoplasticity coupling parameters calibrated for $Ni_{49.8}Ti_{30.6}Hf_{19.2}$

Variables controlled by parameters	*Nomenclature*	*Martensite ↔ Austenite*
Resistance to transformation	$d_1(MPa)^{-1}$	0.01
(Y_{p1}, Y_{p2})	c_1	60.
	$d_2(MPa)^{-1}$	0.1
	c_2	30.
Retained martensite (ξ_{ir}^{α})	g^{ret}	0.01

3.3.3 Finite Element (FE) solver

The constitutive model with its parameters is implemented using a commercial FE software Zebulon Z-set [138], in order to simulate the thermomechanical test on the selected HTSMA. An implicit integration method is used, with automatic time stepping based on the tolerance specified. In case of single crystals, the integration is performed on one integration node (using Z-sim option in Zebulon) representing a single grain, while in case of polycrystals an entire RVE representing an aggregate of grains is considered.

3.4 Summary of constitutive equations

To summarize the constitutive model a summary of its equations is presented:

Table 3.12: Summary of equations: Part I

Constitutive equations	
1. Small strain	$\boldsymbol{\epsilon}_{tot} = \underbrace{\boldsymbol{\epsilon}_{th} + \boldsymbol{\epsilon}_{e}}_{elastic} + \underbrace{\boldsymbol{\epsilon}_{tr} + \boldsymbol{\epsilon}_{de} + \boldsymbol{\epsilon}_{TRIP} + \boldsymbol{\epsilon}_{vp}}_{inelastic}$
	$\boldsymbol{\epsilon}_{th} = \alpha(T - T_0).\mathbf{I}$
	$\boldsymbol{\epsilon}_{e} = [\mathbb{C}]^{-1} : \boldsymbol{\sigma} \qquad \mathbb{C} = \xi\mathbb{C}_M + (1-\xi)\mathbb{C}_A$
	$\boldsymbol{\epsilon}_{tr} = \sum_{\alpha=1}^{N_v} \xi^{\alpha} g^{tr} \mathbf{P}_{tr}^{\alpha} \qquad \mathbf{P}_{tr}^{\alpha} = \frac{1}{2}(\mathbf{b}^{\alpha} \otimes \mathbf{m}^{\alpha} + \mathbf{m}^{\alpha} \otimes \mathbf{b}^{\alpha})$
	$\boldsymbol{\epsilon}_{de} = \sum_{\alpha=1}^{N_v} \xi^{\alpha} \underbrace{(\lambda^{\alpha} - \lambda_0^{\alpha})}_{g^{det}} \mathbf{P}_{de}^{\alpha} \quad \mathbf{P}_{de}^{\alpha} = \frac{1}{2}(\mathbf{t}^{\alpha} \otimes \mathbf{a}^{\alpha} + \mathbf{a}^{\alpha} \otimes \mathbf{t}^{\alpha})$
	$\boldsymbol{\epsilon}_{TRIP} = \sum_{\alpha=1}^{N_v} \gamma_{tr}^{\alpha} \mathbf{P}_{tr}^{\alpha}$
	$\boldsymbol{\epsilon}_{vp} = \sum_{s=1}^{N_s} \gamma_{vp}^{s} \mathbf{T}^{s} \qquad \mathbf{T}^{s} = \frac{1}{2}(\mathbf{n}^{s} \otimes \mathbf{l}^{s} + \mathbf{l}^{s} \otimes \mathbf{n}^{s})$
	$\dot{\boldsymbol{\epsilon}}_{acc} = \sqrt{\frac{2}{3}\dot{\boldsymbol{\epsilon}} : \dot{\boldsymbol{\epsilon}}}$

Table 3.13: Summary of equations: Part II

Constitutive equations	
2. Thermodynamic framework	$\psi = \psi_e + \psi_{ch} + \psi_h + \psi_{vp}$
	$\psi_e = \frac{1}{2}\boldsymbol{\epsilon}_e : \mathbb{C} : \boldsymbol{\epsilon}_e$
	$\psi_{ch} = \psi_{tr} + \psi_{th}$
	$= \beta(T - T_0)\sum_{\alpha=1}^{N_v} \xi^\alpha + c_v \left[(T - T_0) - T.ln\left(\frac{T}{T_0}\right)\right]$
	$\psi_h = \sum_{\alpha=1}^{N_v} \tau_p \lvert\gamma_{tr}^\alpha\rvert$
	$\psi_{vp} = \sum_{s=1}^{N_s} (x^s + r^s)\lvert\gamma_{vp}^s\rvert$
Dissipation	$\Gamma = \boldsymbol{\sigma} : \dot{\boldsymbol{\epsilon}} - \dot{\psi} - s\dot{T} - \frac{\boldsymbol{q}.\boldsymbol{\nabla} T}{T} \geq 0$
Thermodynamic forces	$\Phi_{tr}^\alpha = g^{tr}(\boldsymbol{\sigma} : \mathbf{P}_{tr}^\alpha) + \underbrace{(\lambda^\alpha - \lambda_0^\alpha)}_{g^{det}}(\boldsymbol{\sigma} : \mathbf{P}_{de}^\alpha) - \beta\,(T - T_0) - \frac{1}{2}\boldsymbol{\epsilon_e} : \Delta\mathbb{C} : \boldsymbol{\epsilon_e}$
	$\Phi_{de}^\alpha = \xi^\alpha(\boldsymbol{\sigma} : \mathbf{P}_{de}^\alpha)$
	$\Phi_{TRIP}^\alpha = (\boldsymbol{\sigma} : \mathbf{P}_{tr}^\alpha) - \tau_p$
	$\Phi_{vp}^s = (\boldsymbol{\sigma} : \mathbf{T}^s) - x^s - r^s$

Table 3.14: Summary of equations: Part III

Constitutive equations (Continued)	
3. Evolution of:	
Martensite volume fraction	$\dot{\xi}^{\alpha}_{re} = \begin{cases} \xi_0 sign(\Phi^{\alpha}_{tr}) \left\lvert \dfrac{\Phi^{\alpha}_{tr}}{Y_1} \right\rvert^{m^{tr}} & if \;\; Y_1 \leq \Phi^{\alpha}_{tr} \quad \& \;\; 0 \leq \xi^{\alpha} \leq 1 \\ \xi_0 sign(\Phi^{\alpha}_{tr}) \left\lvert \dfrac{\Phi^{\alpha}_{tr}}{Y_2} \right\rvert^{m^{tr}} & if \;\; \Phi^{\alpha}_{tr} \leq -Y_2 \;\; \& \;\; 0 \leq \xi^{\alpha} \leq 1 \end{cases}$
LCV volume fraction	$\dot{\lambda}^{\alpha} = \begin{cases} \lambda_{ref} sign(\Phi^{\alpha}_{de}) \left\lvert \dfrac{\Phi^{\alpha}_{de}}{Y_{det}} \right\rvert^{m^{det}} & if \;\; Y_{det} \leq \Phi^{\alpha}_{de} \;\; \& \;\; 0.5 < \lambda^{\alpha} \leq 1 \\ 0 & otherwise \end{cases}$
Slip during TRIP	$\dot{\gamma}^{\alpha}_{tr} = \begin{cases} \gamma_0 \left(\frac{\boldsymbol{\sigma}:\mathbf{P}^{\alpha}_{tr}}{\mu} \right)^2 exp \left(\frac{-\Delta G_{slip}}{k_b T} \left(1 - \left(\frac{\Phi^{\alpha}_{TRIP}}{\tau_0} \right)^p \right)^q \right) \lvert \dot{\xi}^{\alpha}_{re} \rvert & \\ \qquad \ldots if \;\; \Phi^{\alpha}_{TRIP} > 0 & \\ 0 \qquad if \;\; \Phi^{\alpha}_{TRIP} \leq 0 & \end{cases}$
Resistance to TRIP	$\tau^{\alpha}_{p} = k_1 \sqrt{\rho^{\alpha}_{tr}}$
Dislocation density from TRIP	$\dot{\rho}^{\alpha}_{tr} = \dot{\gamma}^{\alpha}_{tr} \left(1 - k_2 \rho^{\alpha}_{tr} \right)$
	$\rho_{TRIP} = \sum_{i=1}^{N_v} \rho^{\alpha}_{tr}$

Table 3.15: Summary of equations: Part IV

Constitutive equations (Continued)	
4. Crystal plasticity framework:	$\boldsymbol{\sigma_g} = (\mathbf{R}^g)^T.\boldsymbol{\sigma}.\mathbf{R}^g$
	$\tau^s = \boldsymbol{\sigma_g} : \mathbf{T}^s$
	$\Phi^s = \lvert\tau^s - x^s\rvert - r^s$
	$r^s = r_0 + r_i^s \quad r_i^s = Q_1\gamma_{vp}^s + bQr_{sum}^s \quad r_{sum}^s = \sum_{j=1}^{N_s} hh_{sj}.q^s$
	$x^s = C\alpha^s$
4. Evolution of:	
Viscoplastic slip	$\dot{\gamma}_{vp}^s = C_{visco}\, sinh \left\langle \dfrac{\Phi_{vp}^s}{K} \right\rangle^n sign(\tau^s - x^s)$
Viscoplastic strain	$\dot{\boldsymbol{\epsilon}}_{vp}(= \dot{\boldsymbol{\epsilon}}_p) = \sum_{s=1}^{N_s} \dot{\gamma}_{vp}^s \mathbf{T}^s$
Kinematic hardening variable	$\dot{\alpha}^s = (sign(\tau^s - x^s) - D\alpha^s)\dot{\gamma}_{vp}^s$
Dislocation density	$\dot{q}^s = \dot{\gamma}_{vp}^s(1 - bq^s)$
from viscoplasticity	$\rho_{vp/p} = \sum_{s=1}^{N_s} q^s$

Table 3.16: Summary of equations: Part V

Constitutive equations (Continued)	
5.Transformation-viscoplasticity coupling	
Resistance to transformation	$Y_1 = Y_1^0 + Y_{p1} \quad Y_2 = Y_2^0 + Y_{p1}$
	$Y_{p1} = \frac{1}{d_1}(1 - e^{-d_1 c_1 \sqrt{\rho_{TRIP}+\rho_{vp}}})$
	$Y_{p2} = \frac{1}{d_2}(1 - e^{-d_2 c_2 \sqrt{\rho_{TRIP}+\rho_{vp}}})$
Retained martensite	$\xi_{ir} = g^{ret}\left(\rho_{TRIP} + \rho_{vp}\right)$

3.5 Results and discussions

The thermomechanical test simulated on a Ti-rich $Ni_{49.8}Ti_{30.6}Hf_{19.2}$ HTSMA is a UCFTC test with thermomechanical conditions prescribed in Section 3.3.1. The HTMSA is considered in single-crystal form for the purpose of calibrating the model parameters. Simulations on a polycrystalline HTSMA were carried out with the calibrated model. Results are generated and presented for a single and multiple cycles of the thermomechanical test in the following sections.

3.5.1 Single cycle: Single-crystal responses

The orientations of single-crystals is defined with respect to the loading direction which is fixed along the z-axis. Therefore, the default orientation of a crystal is along the normal to the [001] plane, which can be rotated using a set of three Euler angles (ϕ_1, Φ, ϕ_2), to generate any randomly oriented crystal. For instance, the Euler angles $(0^o, 45^o, 0^o)$ and $(0^o, 54.74^o, 45^o)$ are used to generate crystals along the [011] and [111] directions, respectively. Along with [001], [011], and

[111], any set of random orientations can be defined. In fact, it is used to calibrate the model, more specifically the sum of transformation and detwinning strains presented in the following section. *Note:* The plane [] will be referred to as direction of the normal, in the rest of the text.

3.5.1.1 Calibration of transformation + detwinning strain

A single cycle of the UCFTC test is simulated for single crystals of the considered HTSMA (Section 3.3.2), at a thermal cycling rate of 1°C/min. The strain-temperature response generated by (only) the sum of transformation and detwinning strains are shown in Fig. 3.7. On inspecting the variants, it is observed that the number of activated variants and their volume fractions control the maximum strain generated along each orientation. Along [001], all the 12 variants are activated, with the 1^{st} variant dominating and reaching a volume fraction of 0.619. Along [011], 3 out of 12 variants are activated, with the 7^{th} variant dominating and reaching a volume fraction of 0.719. While along [111], 2 out of 12 variants are activated with the 8^{th} variant dominating and reaching a volume fraction of 0.999, and it contributes to the entire strain. Hence, the dominant variant changes with the orientation because the variant which is aligned along the loading axis is favored [139] to grow. This results in an increase in the maximum strain, TT, and hysteresis, as shown by the data in Table 3.17.

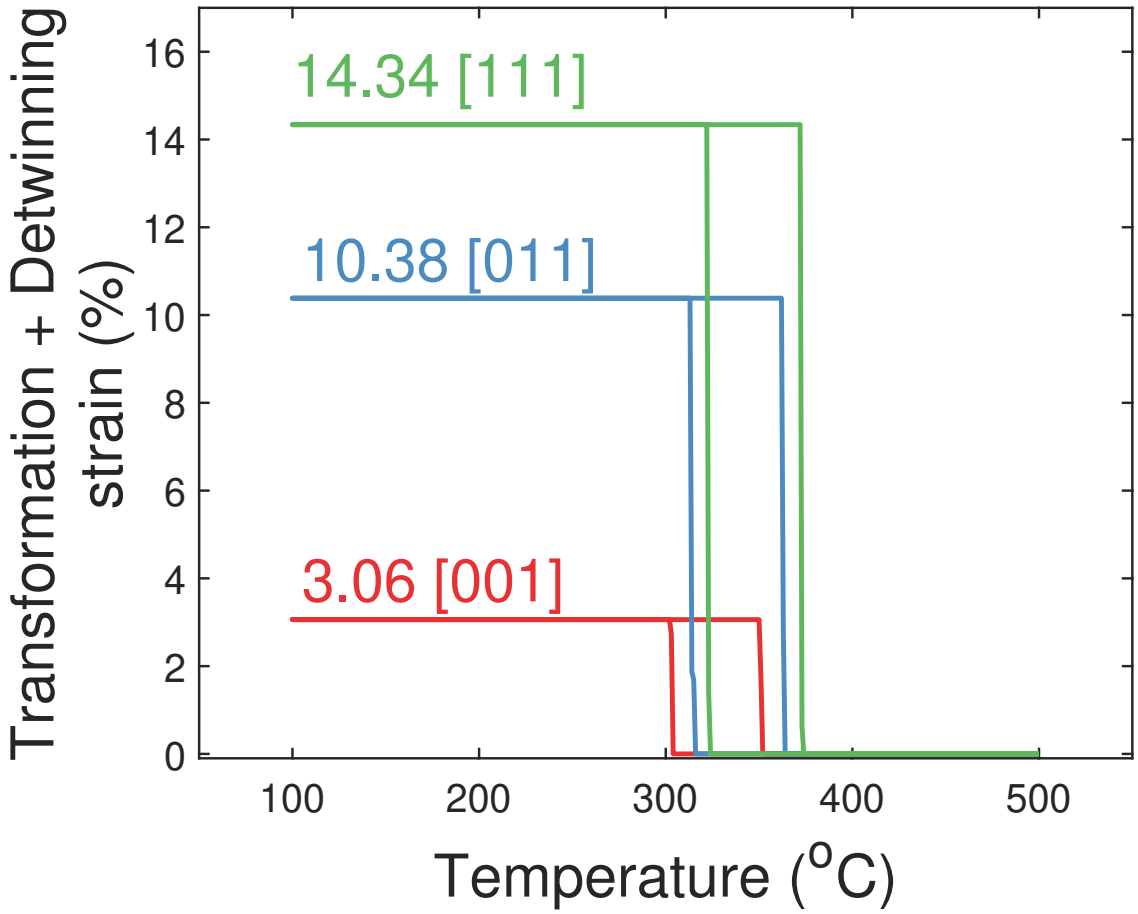

Figure 3.7: Sum of transformation and detwinning strains vs. temperature, simulated from a UCFTC test between 100 - 500 °C at 1 °C/min and 500 MPa, on single crystals of $Ni_{49.8}Ti_{30.6}Hf_{19.2}$

Table 3.17: Comparison of strains obtained from Sehitoglu [13] for $Ni_{49.8}Ti_{30.2}Hf_{20}$ vs. calibrated strains for $Ni_{49.8}Ti_{30.6}Hf_{19.2}$ using crystal plasticity model.

Literature (Sehitoglu et al.[13])	[011]-Type I CVP & detwinning strain (%)			
[001] Single crystal	2.63			
[011] Single crystal	9.60			
[111] Single crystal	19.34			
Calibrated strains	Transformation + Detwinning strain (%)	M_s (°C)	A_f (°C)	Hysteresis (°C)
[001] Single crystal	3.06	304	352	48
[011] Single crystal	10.38	316	364	48
[111] Single crystal	14.34	324	374	50

As observed in Table 3.17, the strains are calibrated very close to the literature values of [001] and [011], but are quite far off from the [111] value. The detwinning strain is expected to fall short of its theoretical value along the [111] orientation, because as mentioned in Section 3.2.3.3, the magnitude of the detwinning strain (Eq. 3.5) is controlled by a constant parameter g^{det}, and not by the more appropriate evolution term $\lambda^{\alpha} - \lambda_0^{\alpha}$. It, therefore, limits the present study from accurately predicting the detwinning strain for orientations close to [111]. In addition, the strains were intentionally calibrated close to the [001] and [011] values, and not the [111] value, to avoid simulating large strain magnitudes ($\geq 14.34\%$) using a small-strain model.

3.5.1.2 Random orientations

As the present study aims to investigate the effect of crystal orientations (and eventually texture) on the entire response (including the irrecoverable deformations), a single cycle of UCFTC (mentioned earlier) is simulated for 500 random orientations as demonstrated by the inverse pole

figure in Fig. 3.8 (a). The random orientations were generated using a software package called Neper [140, 141, 142] and are distributed randomly throughout the stereographic triangle, as shown by their Euler angles (ϕ_1, Φ, ϕ_2) in Fig. 3.8 (b),(c),(d).

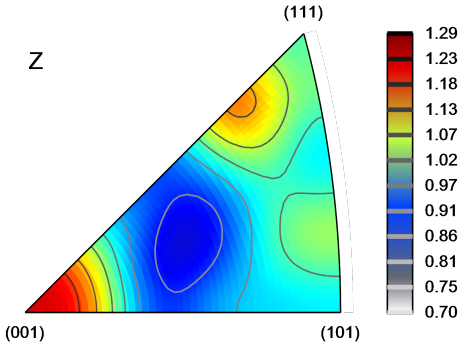

(a)

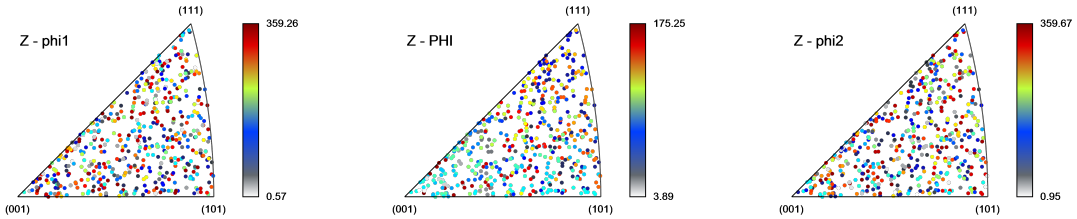

(b) (c) (d)

Figure 3.8: (a) Inverse Pole figure of 500 random grains generated using the tool - ATex [10] to show the resulting texture generated through contours of miller indices. Distribution of 500 sets of random Euler angles along Z axis (b) ϕ_1, (c) Φ, and (d) ϕ_2.

The responses generated from the 500 random orientations are presented by random colors in Fig. 3.9 while those generated from [001], [011] and [111] are marked in black. As observed they random responses are spread out between the responses of [001] and [111], but there are few outliers with responses of strains lower than that of [001] but with higher TT. These responses are from orientations which correspond to high miller indices, presented later in this section. The

observed spread in the plot is due to a variation in activation of distinct martensite variants as the orientations change. Therefore, the activation of variants depends on the orientations and, hence, the crystal frame of reference. The frame of references are not unique, because due to the crystal lattice symmetry they can be related by mutual orientations rotations to form symmetrically equivalent frames. On extending the fact, an equivalent symmetry can be expected in the activation of distinct martensite variants along random orientations. In other words, two different rotations can lead to formation of the same variants and resulting transformation and detwinning strains too. This hypothesis is based on the study by Humbert et al. [143] on determining the number of physically distinct variants.

Data points of maximum: (i) total, (ii) transformation, (iii) detwinning, (iv) TRIP, and (v) viscoplastic strains are extracted from the strain-temperature responses. Data points indicating the TT: M_s and A_s, and their difference indicating the hysteresis are also extracted in a similar manner. All the above quantities are plotted in Fig. 3.10-3.14 with respect to the Euler angles (Φ, ϕ_2) in the form of a combination of scatter and surface plots.

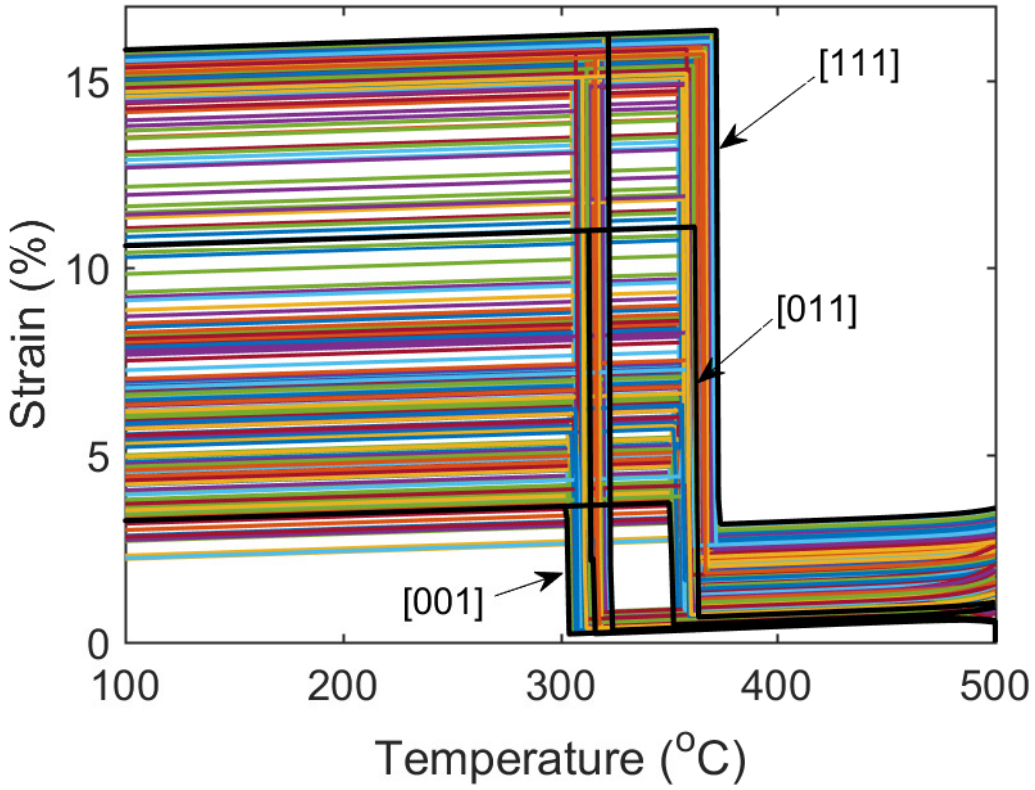

Figure 3.9: Strain-temperature responses generated from the UCFTC tests along 500 individual single crystals defined by their random orientations.

In the scatter + surface plots, periodic structures are visible with respect to the Euler angles. To comprehend their periodicity, a projection of the 3D plot is created on the $\Phi - \phi_2$ (X-Y) plane, and shown on the side. The plot is divided into 4 quarters with a range of $0 \leq \Phi, \phi_2 \leq \pi/2$ and numbered in a clockwise manner. These quarters when compared across the entire plot show periodicity with respect to the Euler angles. For instance, the total, transformation, detwinning and TRIP strains, TT and hysteresis show a similarity between opposite quarters, i.e., $1 \leftrightarrow 3$ and $2 \leftrightarrow 4$. This can imply the planes of $\phi_2 = 0$ and $\Phi = \pi/2$ acts as a mirror planes together. Whereas, the viscoplastic strain shows a similarity between the quarters $1 \leftrightarrow 2$ and $3 \leftrightarrow 4$, which can imply the plane of $\phi_2 = 0$ acts as a mirror plane.

The hypothesis of two different rotations resulting in the activation of same martensite variants,

can explain the symmetry observed in the total (in Fig. 3.10), transformation (in Fig. 3.11(b)), detwinning (in Fig. 3.11(d)) and TRIP (in Fig. 3.12(b)) strains. Since the variants are activated at the TT, the hypothesis can also explain the symmetry observed in the TT (in Fig. 3.13(b),(d)) and derived hysteresis (in Fig. 3.14(b)). On the other hand, the viscoplastic strains, depends on the activation of slip systems which are oriented different to the martensite variants but depend on the same crystal frame of reference. Therefore, the above hypothesis can be extended as two different orientations resulting in the activation of same slip systems. This can explain the observed symmetry in (in Fig. 3.12(d)).

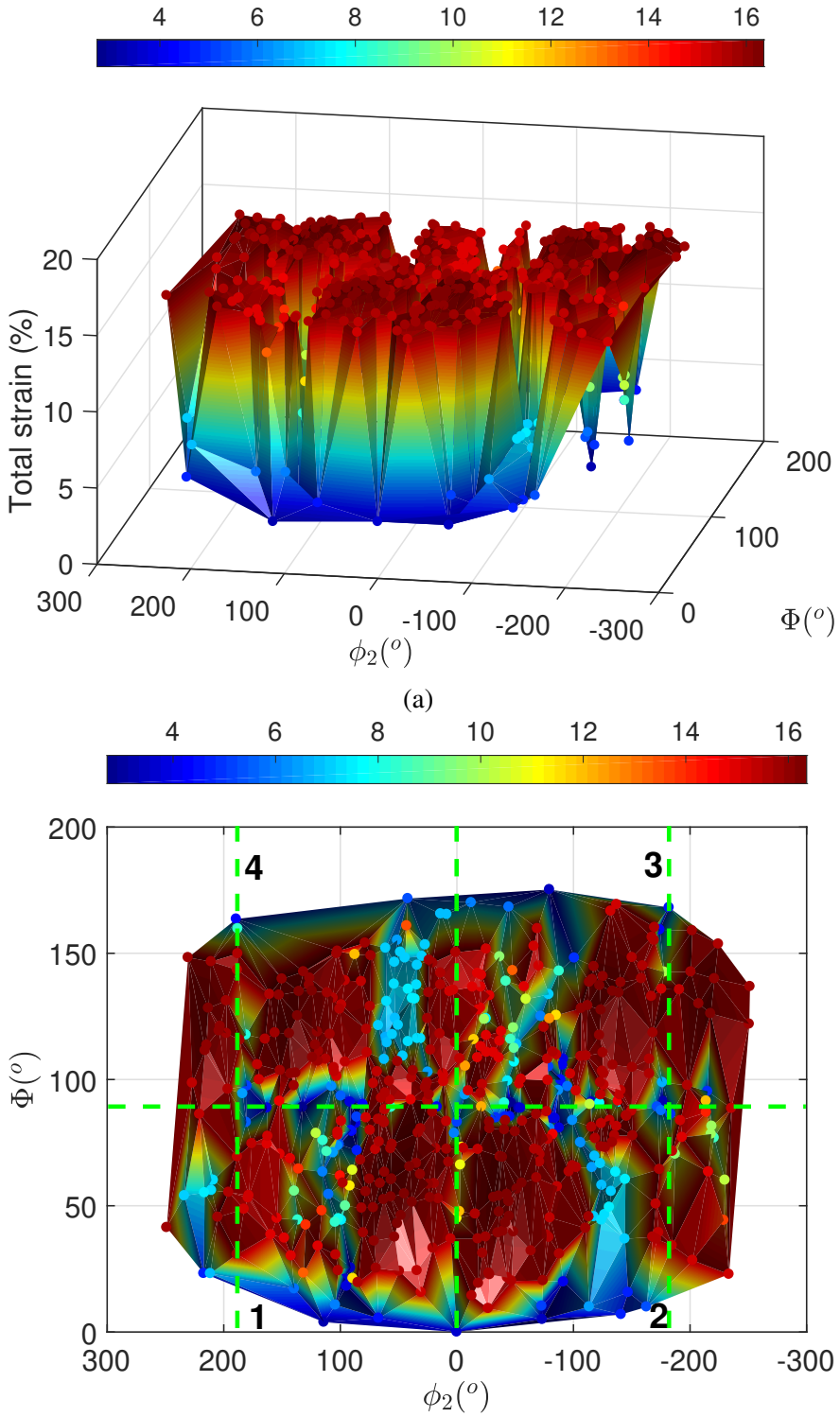

Figure 3.10: (a) 3D scatter+surface plots of total strain data points from 500 randomly oriented single crystals, at 1 °C/min. (b) Projection of 3D plot on Φ - ϕ_2 plane.

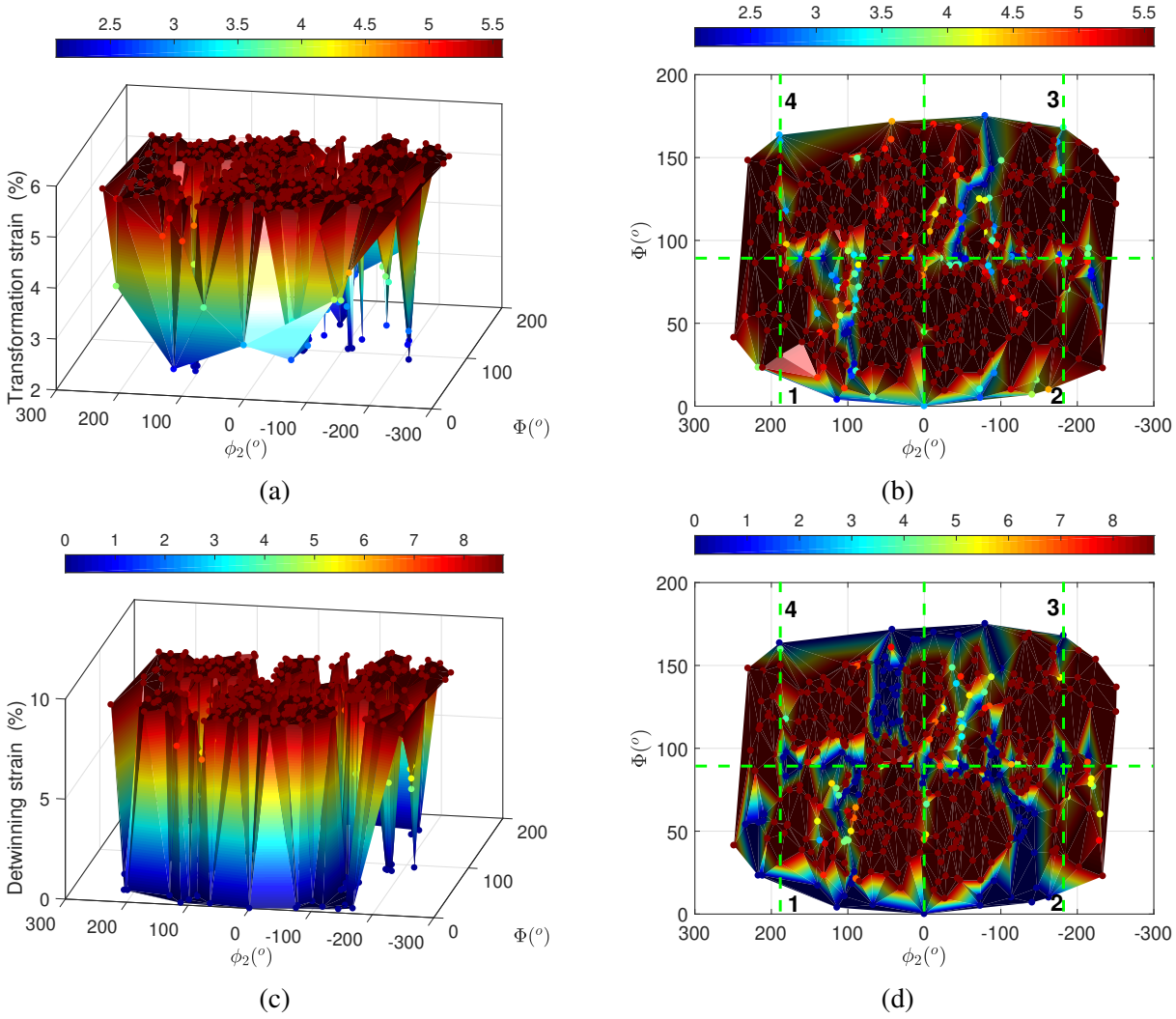

Figure 3.11: 3D scatter+surface plots and projections of transformation strain (a),(b) and detwinning strain (c),(d) data points from 500 randomly oriented single crystals.

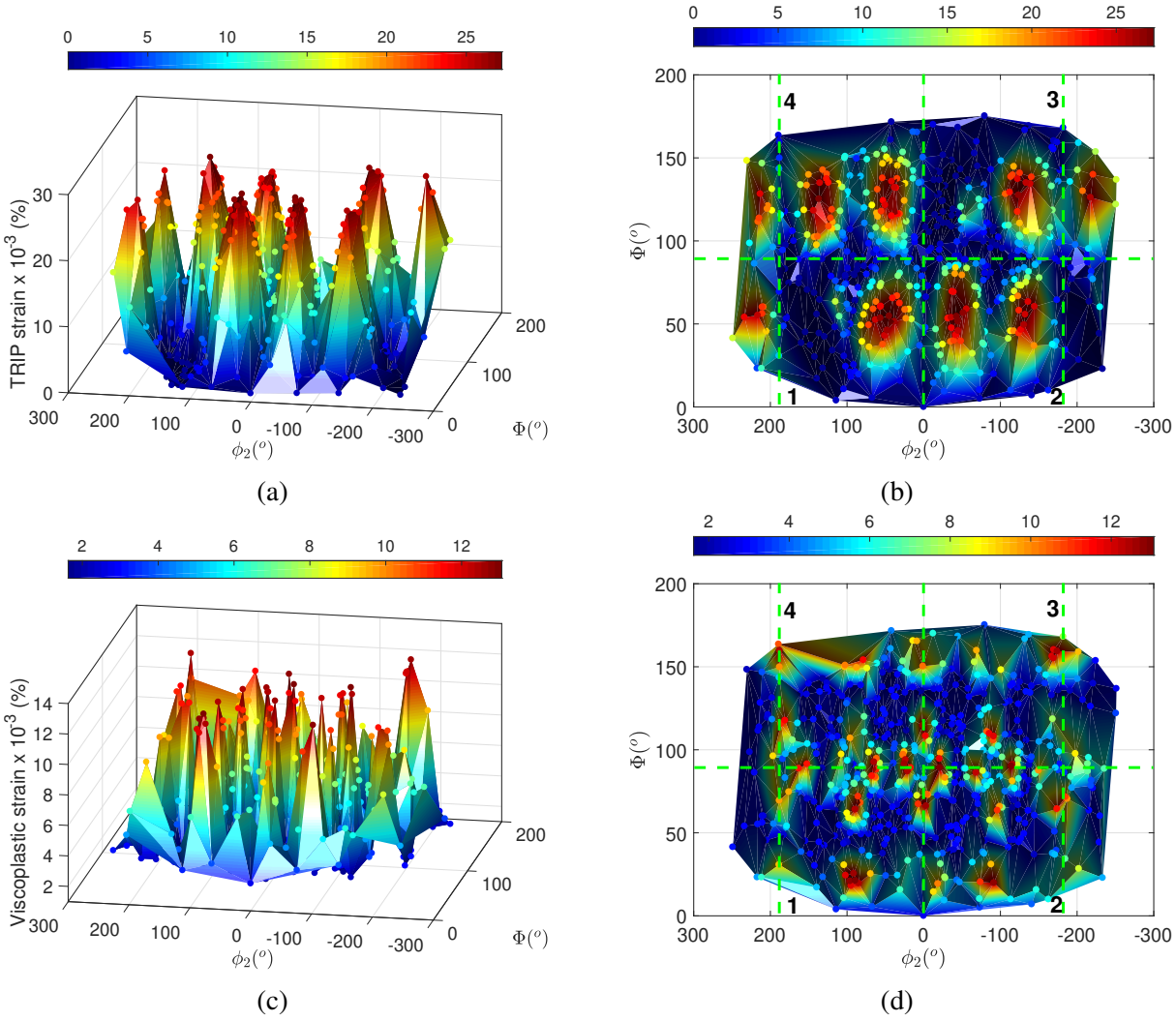

Figure 3.12: 3D scatter+surface plots and projections of TRIP strain (a),(b) and viscoplastic strain (c),(d) data points from 500 randomly oriented single crystals.

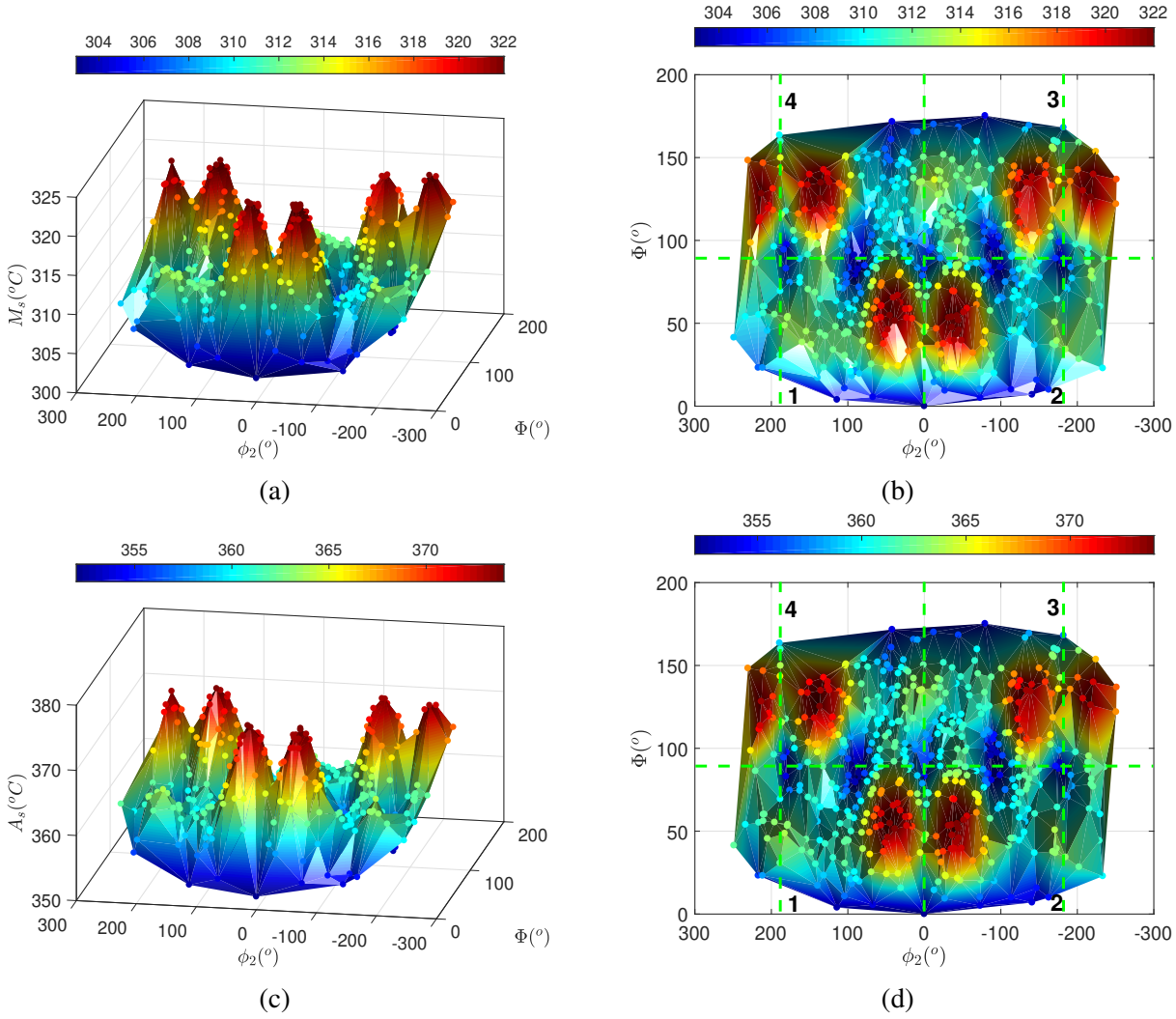

Figure 3.13: 3D scatter+surface plots and projections of TT: M_s (a),(b) and A_f (c),(d) data points from 500 randomly oriented single crystals.

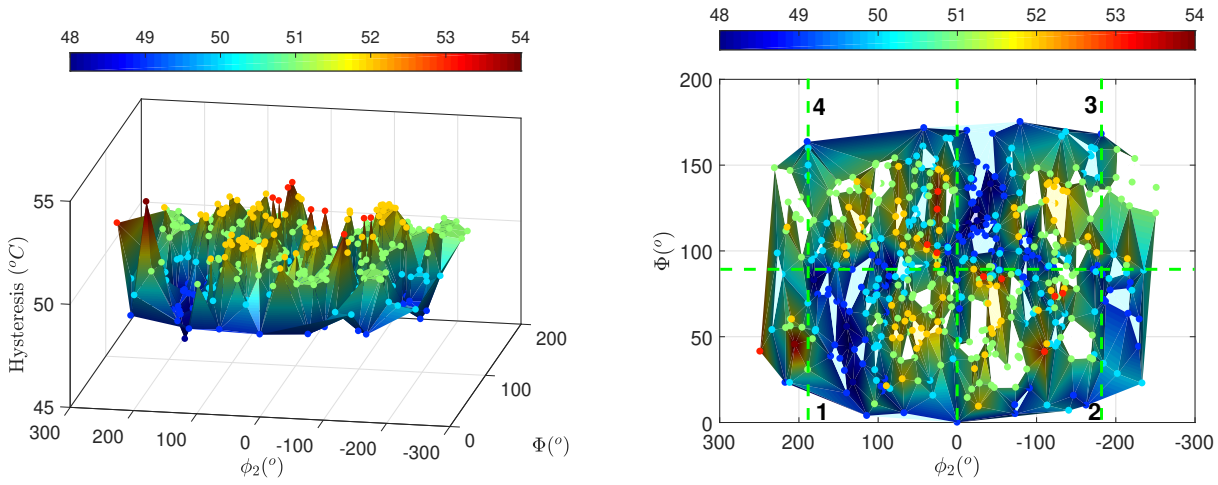

Figure 3.14: 3D scatter+surface plots and projection of hysteresis data points from 500 randomly oriented single crystals.

The data from the 3D plots can be useful to estimate and optimize target properties desired from a HTSMA system, for potential applications. Optimizing the target properties can involve, for instance, (i) maximizing total strain while minimizing irrecoverable strain from TRIP and/or viscoplasticity, or (ii) maximizing the TT while minimizing the viscoplastic strains, or (iii) optimizing the hysteresis etc. The data can also be used to calibrate computationally efficient phenomenological models [144] or train machine learning models [145] which can then mimic and predict the anisotropic responses for various orientations and thermomechanical conditions.

To understand the individual data magnitudes and trends, 7 responses from the above 500 random responses are shown in Fig. 3.15(a) along with the response from [001], [011], and [111]. The 7 responses were chosen in increasing order of maximum total strain. As observed in the plot, all the random responses fall in between the [001] and [111] responses. However, the orientation (2 42 1) with a large miller indices, acts like an outlier as it deforms less compared to [001], but with a higher TT. The [111] orientation produces the largest amount of total and TRIP strains at the highest TT. The random orientation [21$\bar{4}$] produces the largest amount of viscoplastic strain ($\approx$ 0.61%), while [011] produces the least amount of viscoplastic strain ($\approx$ 0.16%).

The sum of transformation and detwinning strain components generated by the random orientations are consistent with the trends in literature [13, 53, 60]. The trends referred to are crystallographic dependent trends shown by theoretical and experimental data, through inverse pole figures (IPF) created for Ni-Ti-Hf HTSMAs. On the other hand, irrecoverable strains generated at the end of the cycle in Fig. 3.15 (b), do not show any trend with respect to the crystallographic orientations. Since the irrecoverable strain depends on a combination of TRIP and viscoplasticity, i.e., on a combined set of transformation and slip systems, their trends will mostly likely result in a random variation. An IPF of all the 10 orientations is provided in the Supplementary Material 3.7.

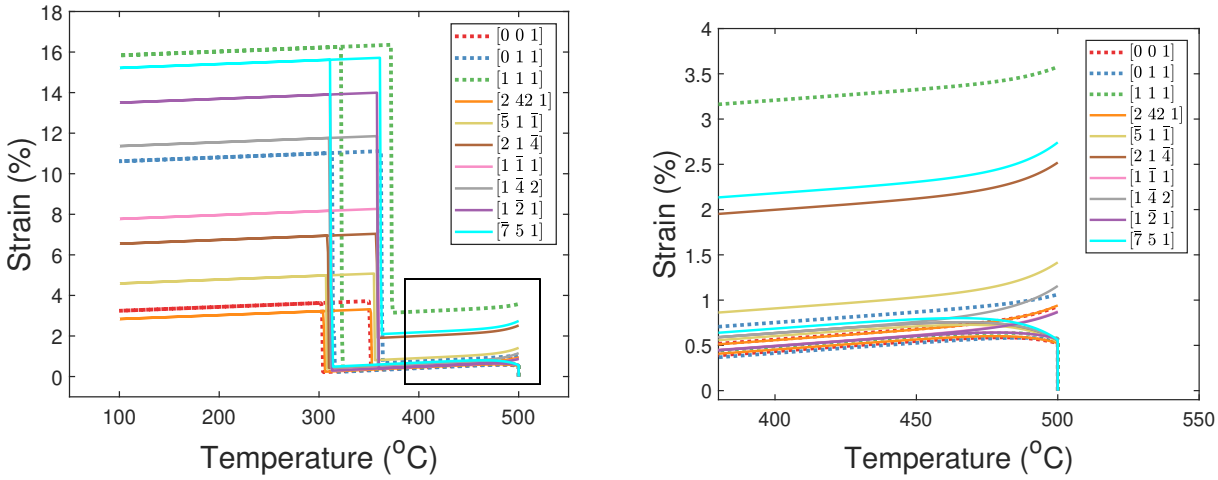

Figure 3.15: Comparison of (a) total strain vs temperature and (b) irrecoverable strain vs temperature, generated for [001], [011], [111] and 7 random orientations, on simulating a single cycle UCFTC at 1 °C/min.

3.5.1.3 Rate-dependency

Experimental studies [47, 50, 7] have established the (entire) experimental response of HTSMAs to be rate-dependent, when thermally cycled at different rates, while being subjected to high temperatures and high stresses. The studies conclude that the main factors responsible for the rate-dependency are (i) viscoplastic deformations, (ii) the coherency (or internal) stresses at the A-M

interfaces, (iii) and the effect of coupling between viscoplasticity and phase transformation. A rate-dependent behavior is simulated by the present study through rate-dependent viscoplastic relations and their coupling with phase transformation. The phase transformation relations considered (in Eq. 3.10), were implemented by Thamburaja et al. [9] and Yu et al. [85] on Ni-Ti SMAs, and by Sakahei et al. [69] on Ni-Ti-Pd HTSMAs. These relations were pointed out to be rate-independent (by Thamburaja et al.) or nearly rate-independent (by Yu et al. and Sakahei et al.) depending on the exponent (m) for the rate of transformation.

In the present study, the rate-dependency is investigated with respect to viscoplasticity and its coupling with the transformation resistance. The coupling effect alters the activation and evolution of variants, which is reflected in the transformation, detwinning and TRIP strains. This effect is observed in the simulated results of a single cycle of UCFTC, on single crystals, at three different rates, viz. 1, 10 and 50 °C/min, which were also investigated experimentally [7]. Based on the responses from random orientations (in Fig. 3.15), single crystals oriented along [001], [$21\bar{4}$], [011], and [111] are chosen. The orientation [$21\bar{4}$] is chosen as it produces the maximum viscoplastic strain amongst all the four orientations.

A comparison of the total strain vs. temperature responses is shown in Fig. 3.16. As observed, the maximum (total) strain decreases with the thermal cycling rate: 1 > 10 > 50 °C/min for each orientation. However, the decrease in strain is not observed to be the same for all orientations as observed in the plots. To observe the difference more closely the total strain and its components (in Eq. 3.1), are presented in Section 3.7.2 of the Supplementary Material 3.7, while some of the responses are inferences are presented and discussed here. The rate-dependency in the total strain along each orientation is due to the rate-dependency of its components and their contribution. The elastic and thermal strains are rate-independent for each orientation. The viscoplastic strain is rate-dependent as it decreases with an increase in rate for each orientation. The transformation, detwinning, and TRIP strains are observed to be rate-independent for the orientations [001], [$21\bar{4}$] and [111], but they show a minor rate-dependency along [011], as shown in Fig. 3.17.

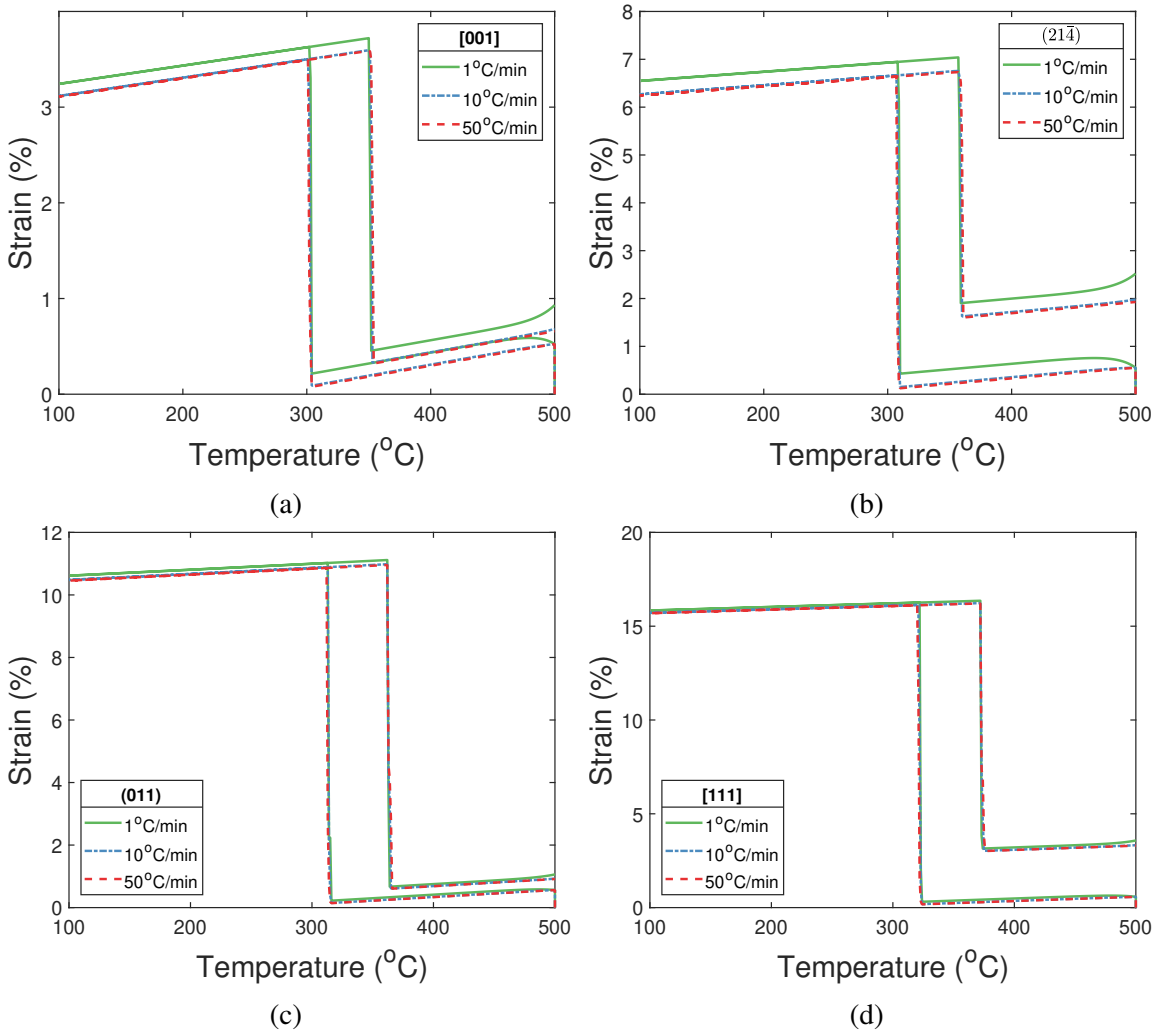

Figure 3.16: Strain-temperature response of total strain at 1, 10 and 50 °C/min along (a) [001], (b) [21$\bar{4}$], (c) [011], and (d) [111].

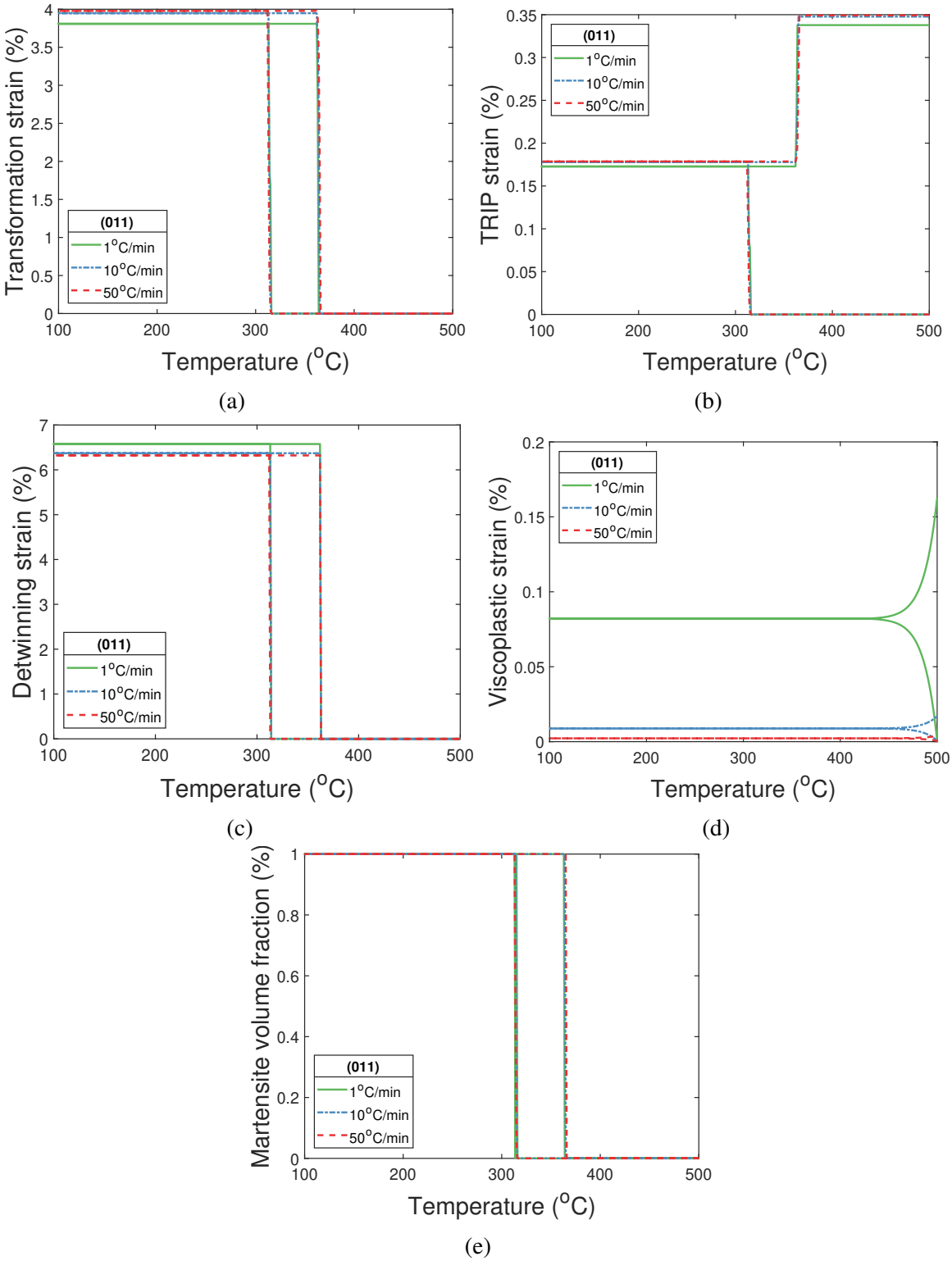

Figure 3.17: Strain-temperature response at 1, 10 and 50 °C/min for [011] (a) Transformation, (b) TRIP, (c) Detwinning, (d) Viscoplastic strains and, (e) Martensite volume fraction.

Along [011], the transformation (in Fig. 3.17 (a)) and TRIP (in Fig. 3.17 (b)) strains increase with the rate, but the detwinning (in Fig. 3.17 (c)) and viscoplastic (in Fig. 3.17 (d)) strains decrease with the rate. The total martensite volume fraction (in Fig. 3.17(e)) evolution is the same for all the rates. But on inspecting the variants, it is observed that only 2 variants are activated at 1 °C/min, and 3 variants get activated at 10 and 50 °C/min. The volume fraction of the dominant variant decreases from 0.749 (at 1 °C/min) to 0.725 (at 10 °C/min) and 0.720 (at 50 °C/min). This change in variant volume fraction or preferential activation of variant, is due to an effect of the coupling on the transformation resistance, which induces a minor rate-dependency in the transformation, TRIP and detwinning strains as observed in the plots.

3.5.2 Single cycle: Polycrystal responses

The experimental responses obtained for (polycrystal) Ni-Ti-Hf [7] motivate the effort to implement the current constitutive model on polycrystals and simulate their responses. These responses are eventually qualitatively and quantitatively (when necessary) compared with single crystal responses and with experimental responses in the following sections.

3.5.2.1 Polycrystal RVE

In the present study, polycrystals are considered in the form of representative volume elements (RVEs) representing an aggregate of several grains (or single crystals) by Voronoi tessellations in 3D space, limited to a cubic domain [140]. The RVE, as illustrated in Fig. 3.18(a), is built using the tool - Neper [141] such that each internal grain (in Fig. 3.18(b)) is assigned a random orientation (in 3D space) and random volume fraction. To perform FE analysis on the RVE, it is meshed using linear C3D8 hexahedral elements, in order to apply periodic boundary conditions. This consists of applying a uniaxial constant force on all the elements of the RVE along the Z direction while satisfying the constraints of displacements and tractions at two homologous points on opposite faces of the RVE [146]. The displacement: $\boldsymbol{u} = \boldsymbol{E} + \boldsymbol{v}$, where $\boldsymbol{v}$ is the periodic field of fluctuation that is equal on opposite faces, and the traction: $\boldsymbol{t} = \boldsymbol{\sigma}.\boldsymbol{n}$ is opposite on opposite faces. The magnitude of the applied force is based on the size of the RVE.

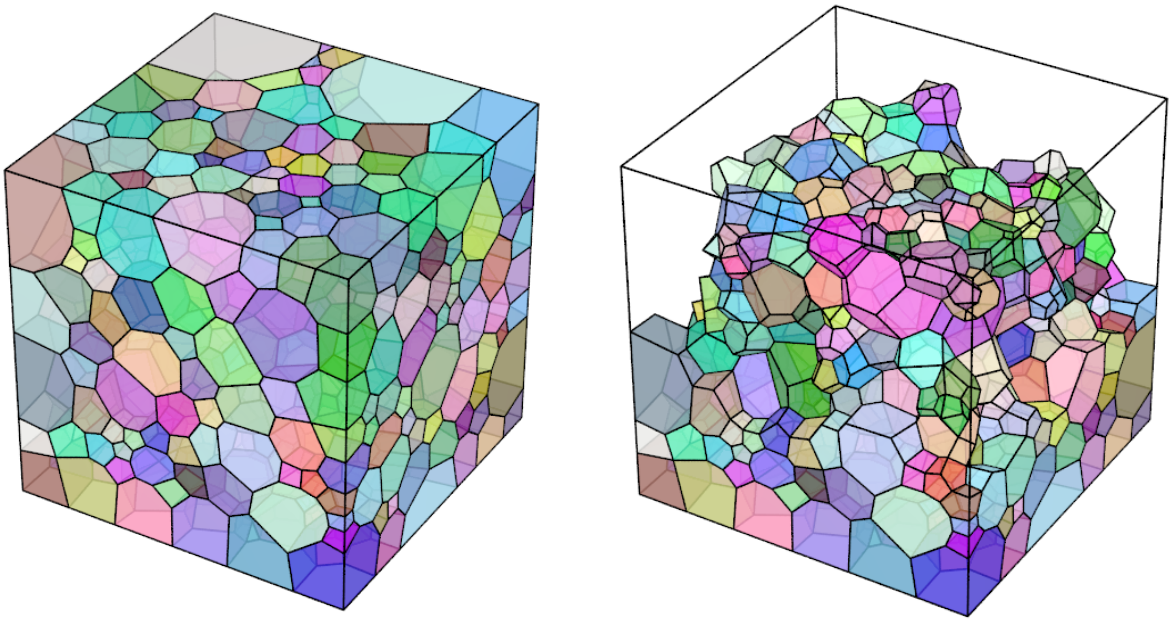

(a) (b)

Figure 3.18: (a) Representative volume element (RVE) of a polycrystal made of several randomly orientated grains (or crystals) and occupying random volume fractions. (b) RVE showing the 3D internal structure of a select few grains.

3.5.2.2 Grain distribution in polycrystal RVE

Deciding the number of grains to be included in the polycrystal RVE depends on how the response changes with the number of grains. The number of grains are increased to essentially obtain a grain-independent response. The size of the (RVE) domain is also increased simultaneously to preserve the grain size distribution, as an increase in number of grains within a fixed domain will reduce the size of each grain. Preserving the grain distribution (while increasing the grains) is essential to avoid size effects on the response. The grain size distribution in each domain is shown through a histogram in Fig. 3.19(a), which plots the relative grain size vs its frequency. The frequency (or number) of small grains is the largest, and the frequency drops as the relative grain size increases. Since this trend is roughly the same for each domain, it can be assumed that the grain size distribution is preserved on increasing the number of grains and domain size.

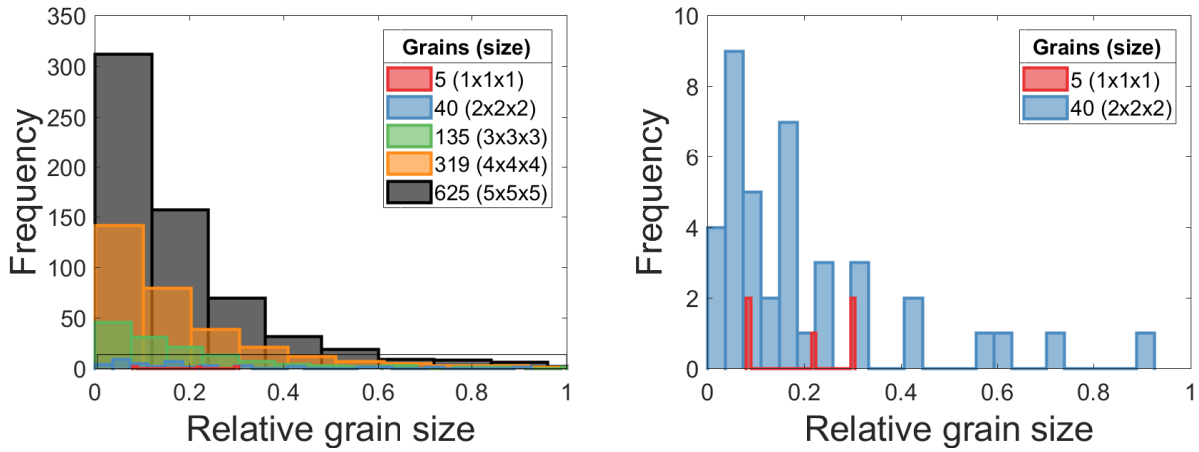

(a) (b)

Figure 3.19: (a) Histogram showing distribution of relative grain size describing the grain distribution (trend) for polycrystals with increasing number of grains and domain size. (b) Blown up histogram of 5 and 40 grain polycrystals.

3.5.2.3 Polycrystal responses

On implementing the constitutive model for each polycrystal domain and simulating a single cycle UCFTC test at 1 °C/min in each case, the total strain obtained is shown in Fig. 3.20. On increasing the number of grains, but preserving the grain distribution, the TT: M_s,M_f,A_s,A_f for each corresponding polycrystal are observed to be very close to each other. The (maximum) total strains, irrecoverable strains, and transformation slopes vary as the number of grains increases from 5 to 625. However, the strains and slopes appear to saturate as the number of grains increase from 319 to 625. To better visualize the saturation of each strain component, they are shown as separate plots in the Supplementary Material 3.7. In addition, Table 3.19 showed in the Supplementary Material 3.7 compares the memory required, and computation time spent on each domain (of polycrystal) for simulating one UCFTC cycle.

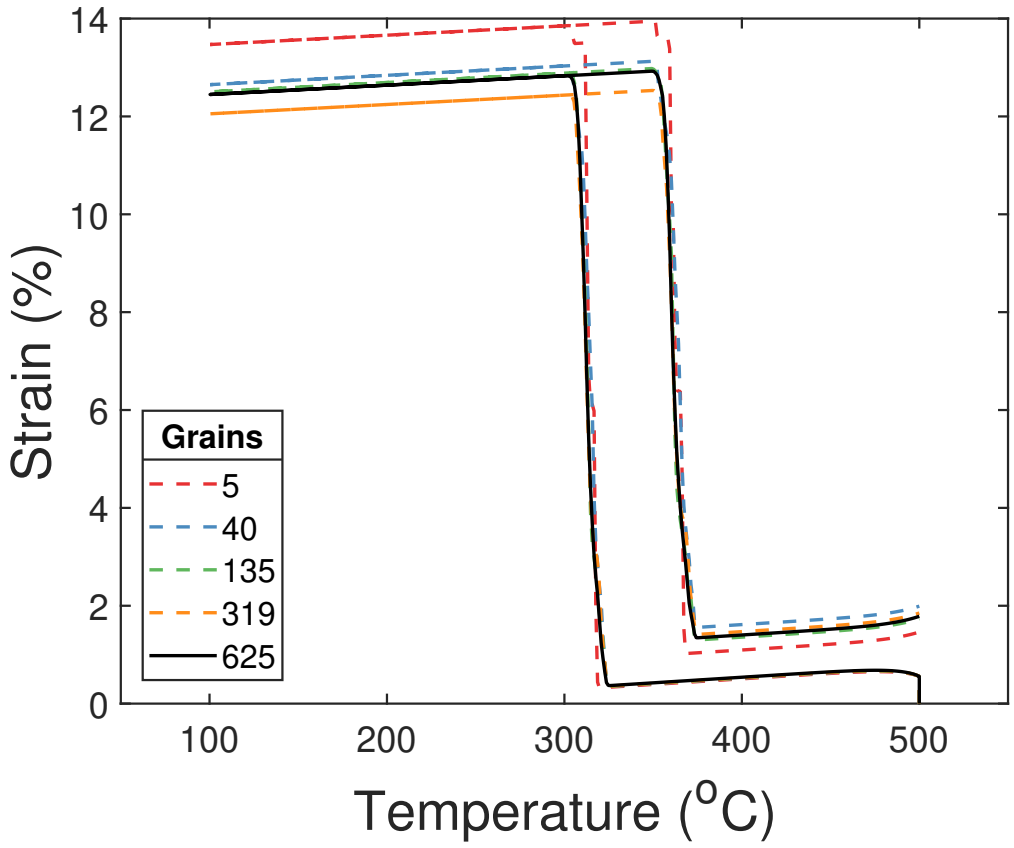

Figure 3.20: Comparison of total strain vs temperature from polycrystal aggregates with increasing number of grains and increasing domain size, for a UCFTC test at 1 °C/min.

3.5.2.4 Degree of anisotropy and isotropy

As the constitutive model accounts for anisotropy, the degree of anisotropy in the polycrystal response is investigated. If the grains in a polycrystal are randomly oriented, as shown by the inverse pole figure for 5 grains (Fig. 3.21 (a) - (c)) and 625 grains (Fig. 3.21 (d) - (f)) polycrystal, a higher number of grains reduces the degree of anisotropy or the effects of any possible texture [147]. To study this effect, the loading direction on each polycrystal is varied and their (anisotropic) responses are compared in Fig. 3.22. As observed, the responses of a 5 grain polycrystal show a high degree of anisotropy, in comparison to the 625 grain responses that are close to being isotropic.

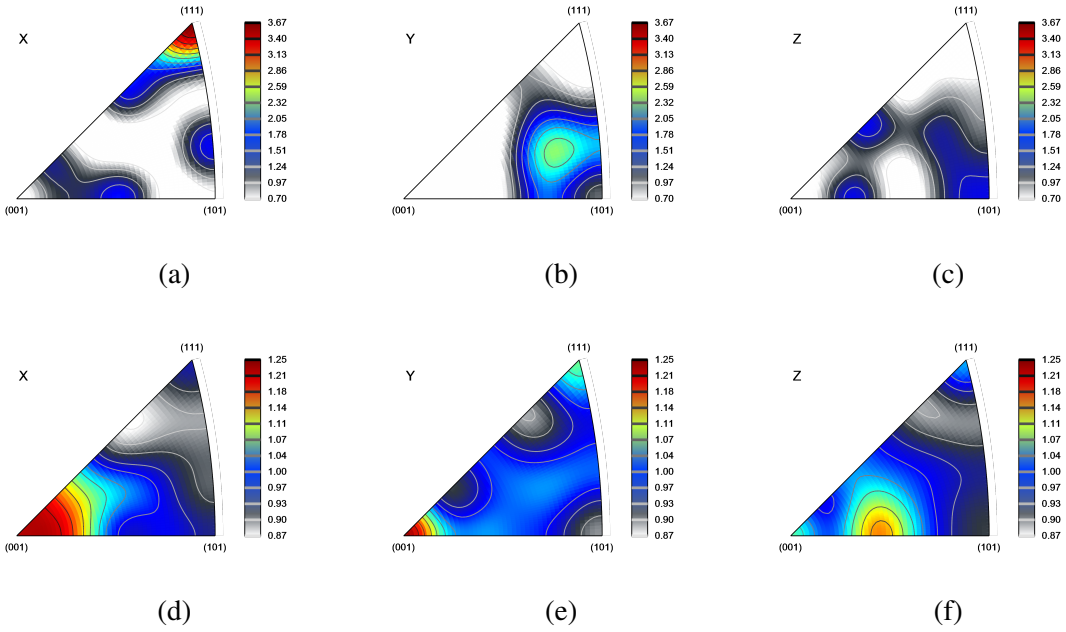

Figure 3.21: Inverse Pole figure of 5 grains in (a) - (c) and 625 grain in (d) - (f) polycrystal along X, Y, and Z directions, respectively generated using the orientations.

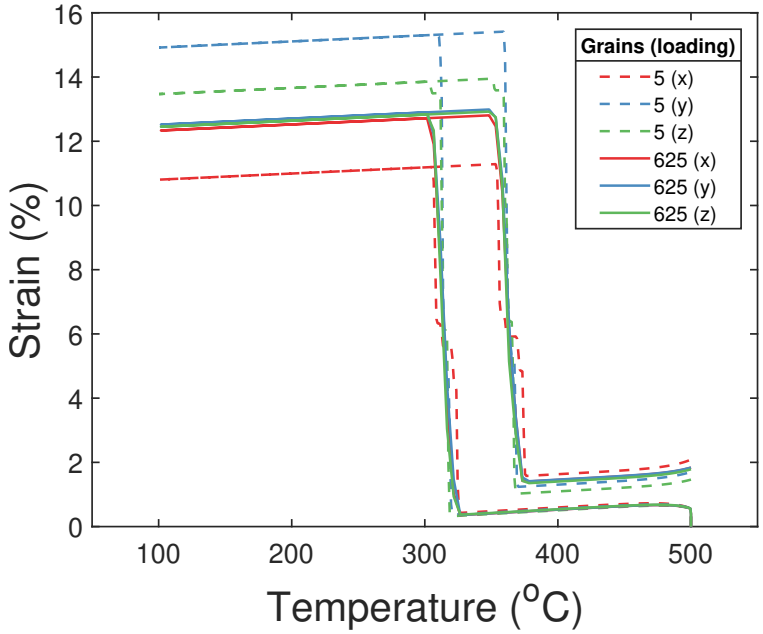

Figure 3.22: Investigating degree of anisotropy and isotropy in polycrsytal by varying loading direction (along x,y, and z) and comparing responses, for polycrystals with 5 and 625 grains.

3.5.2.5 *Relating single crystal and polycrystal responses*

To understand how the single crystal responses relate to the polycrystal response, a comparison is shown between them in Fig. 3.23. The grey dotted lines in the plot mark the TT: M_s, M_f, A_s, and A_f of the polycrystal, and pass through the TT of [001] and [111] single crystals. The data in Table 3.18 shows: (i) the TT: M_s and A_f for the polycrystal are the same as those of [111], and (ii) the TT: M_f and A_s of the polycrystal are the same as those of [001]. Since the TT of different polycrystals were observed to be very close to each other (in Section 3.5.2.3), it can be inferred from Table 3.18, that the TT of the single crystals [001] and [111] decide the TT of the polycrystals.

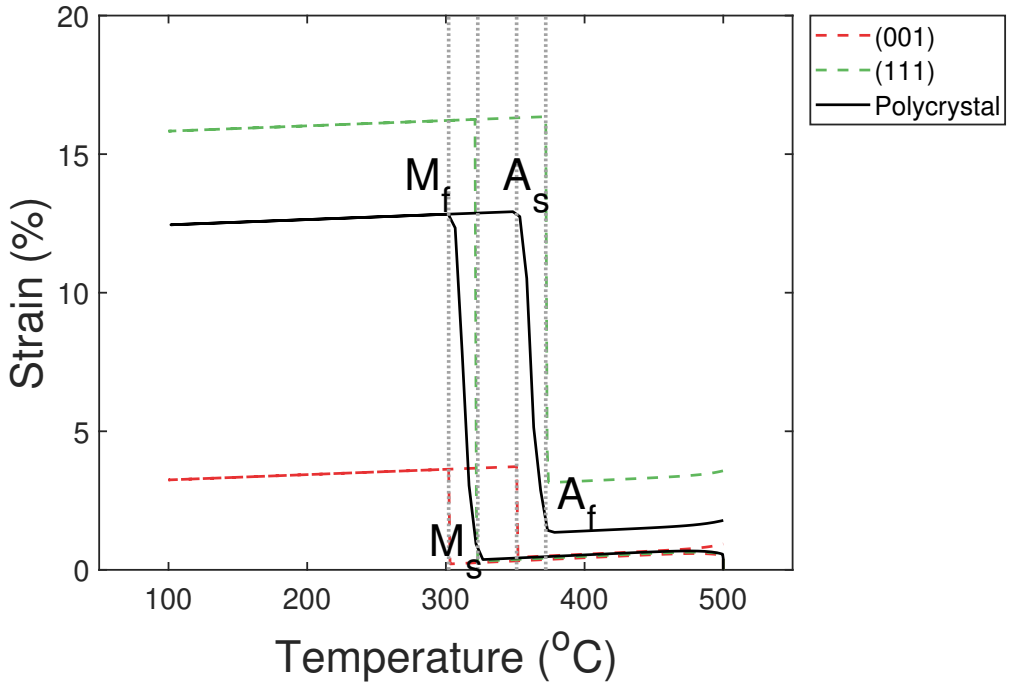

Figure 3.23: Comparison between a polycrystal response from 625 grains, and single crystal responses for [001], [011] and [111], for a single cycle of UCFTC at 1 °C/min.

Table 3.18: Comparison of strains obtained from single crystals vs. polycrystals for a single cycle of UCFTC at 1 °C/min.

Calibrated strains	Maximum total strain (%)	M_s (°C)	M_f (°C)	A_s (°C)	A_f (°C)	Hysteresis (°C)
[001] Single crystal	3.06		304	352		48
[111] Single crystal	14.34	324			374	50
Polycrystal (625 grains)	12.27	324	304	352	374	50.5

3.5.2.6 Comparing experimental and simulated polycrystal responses

The experimental response was obtained from a polycrystal sample of Ni-Ti-Hf HTSMA [7], which most likely contained several thousands of grains. In order to fairly compare the simulated (polycrystal) response with the experimental one, the 625 grain polycrystal is a suitable choice as its response is grain-independent. The comparison is shown in Fig. 3.24. It is observed that the magnitude of the maximum strain simulated (from 625 grains) is almost twice the magnitude obtained experimentally.

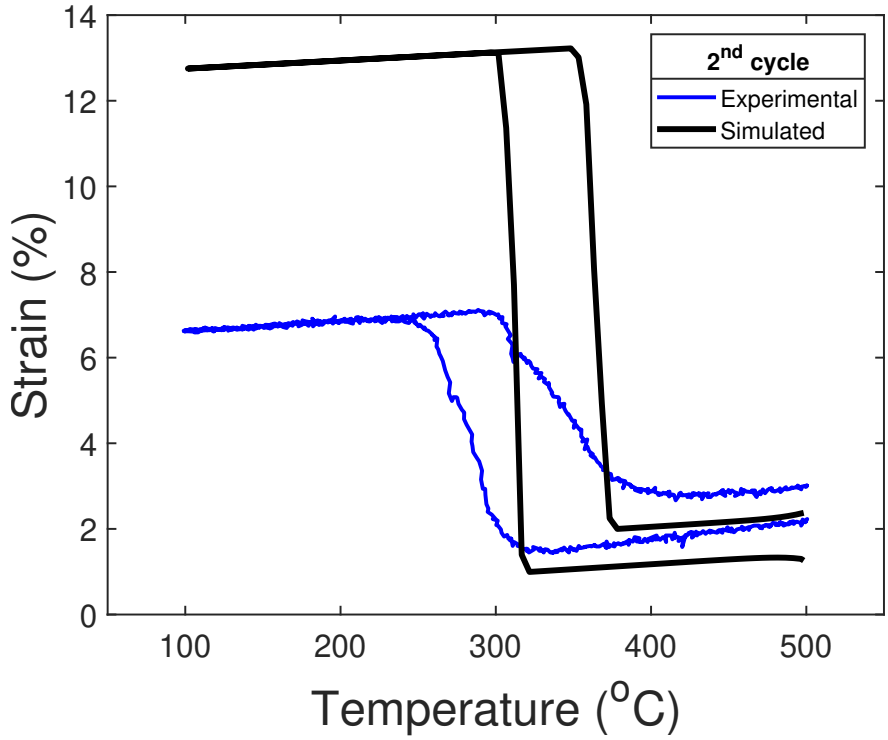

Figure 3.24: Comparison of experimental and simulated (625 grains) strain-time response (2^{nd} cycle) from polycrystals for a UCFTC test at 1 °C/min.

When binary NiTi polycrystals [148] are subjected to a uniaxial tensile test, the stress level saturate, as a plateau is macroscopically visible, indicating an occurrence of reorientation/detwinning. A similar plateau is observed in a [111] oriented Ni-Ti-Hf single crystal [13] response at very high stress values (> 1000 MPa) due to reorientation/detwinning. While from the response of a UCFTC test (on the same single crystal) conducted at 450 MPa, the above study infers an occurrence of detwinning and shows it to be dependent on the loading direction.

On the other hand, experimental studies conducted on Ni-Ti-Hf polycrystals [6, 112, 105] do not show a clear plateau from their macroscopic response, even at stresses greater than 500 MPa. The low energetics of reorientation/detwinning [58] in polycrystals makes them difficult to be discerned macroscopically. Hence, it can be inferred that the likely hood of at least detwinning occurring in polycrystals is very less or limited. Thereby, the response of the polycrystal is re-simulated without activating or including detwinning in the model and the 2^{nd} cycle is compared

in Fig. 3.25.

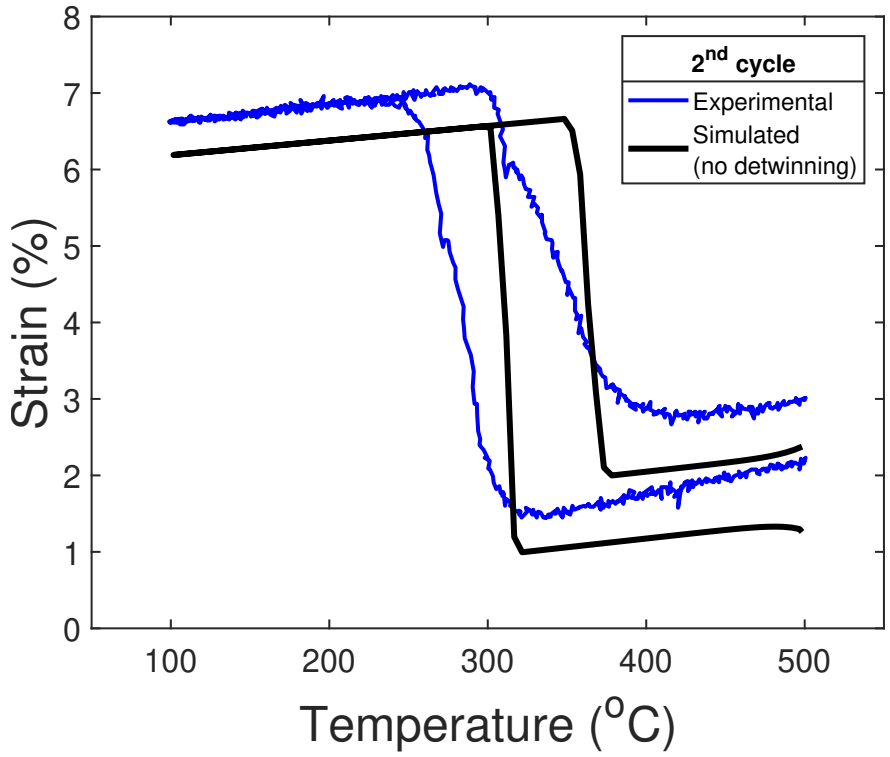

Figure 3.25: Comparison of experimental and simulated (625 grain) strain-temperature response (2^{nd} cycle) without activating detwinning, for a UCFTC test at 1 °C/min

As observed the in Fig. 3.25, the magnitude of (maximum) strain, TRIP and viscoplastic strains are consistent and comparable with the experimental response. To simulate more accurate responses the:

i. The experimental (sample) texture is not currently available and needs to be accounted to improve the response of the (625 grain) polycrystal [149]. Currently the polycrystal includes grains randomly oriented, as shown through an IPF in Fig. 3.21.

ii. The experimental anisotropic elastic constants, which are known to change with temperature for Ni-Ti-Hf (see Fig.25 in [6] and Fig. 8 in [112]), are not currently available and need to be accounted to predict the viscoplastic strains more accurately for the polycrystal.

iii. As mentioned in Section 3.2.3.2 the interaction matrix H^{mn} is not yet defined for any HTSMA yet, and therefore the interaction energy between martensite variants, $\sum_{m,n} H^{mn}\xi^m\xi^n$ is not accounted for in the presented study. Accounting for it will aid in simulating a more accurate (and smoother) response, as demonstrated by Manchiraju et al. [36].

iv. Lastly, to generate the different slopes of forward and reverse transformation paths observed experimentally, the transformation resistances can be made temperature dependent, and formulated in an increasing order as the (forward/reverse) transformation proceeds. The slope of transformation in polycrystals depend on, the number of activated variants [118], orientation of the grains or texture [53], and transformation resistance [2]. Hamilton et al. [2], in particular, states that "the evolution of stored elastic strain energy and variable frictional dissipation give rise to the slope of the curve". Therefore, on formulating a temperature dependent frictional resistance, the simulated responses are obtained and compared just for the slopes in Fig. 3.26. The comparison indicates different slopes for the forward and reverse paths consistent with those from experiments, but the reverse path shows an abrupt change in slope. This is because the resistance is formulated to increase temperature which forces some of the variants to (reverse) transform at higher temperatures. The temperature dependent resistances are implemented solely to mimic the experimental trends and, therefore, are phenomenological. Since they cannot be physically explained for now, they are not used in the remaining of the study.

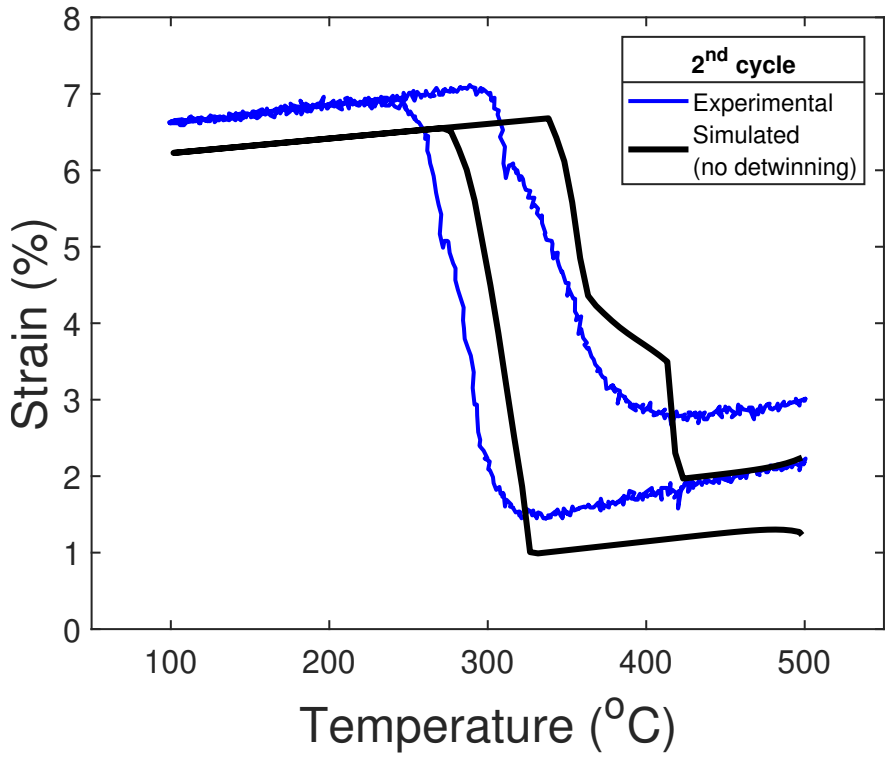

Figure 3.26: Comparison of experimental and simulated (625 grain) with temperature varying resistance strain-temperature (2^{nd} cycle) without activating detwinning, for a UCFTC test at 1 °C/min.

3.5.2.7 Rate-dependency

In Section 3.5.1.3, the rate-dependency in experimental responses of HTSMAs, and variation in single crystal responses with rate, simulated in the present study was discussed. In the present section, the polycrystal responses for a single cycle of UCFTC, are simulated on a 625 grain polycrystal, at three different rates of 1, 10 and 50 °C/min [7]. The responses in Fig. 3.27(a) show a rate-dependent behavior overall. The (maximum) total strain, and transformation strain (in Fig. 3.27(a),(b)) decrease as the rate increases from 1 to 50 °C/min. The TRIP strain (in Fig. 3.27(c)) shows a minor variation with the rate. The viscoplastic strain (in Fig. 3.27(d)) decreases with an increase in rate, and the martensite volume fraction (in Fig. 3.27(e)), shows a slight variation in its evolution of variants at the start of the forward and reverse paths. The TT: M_s decreases slightly with the rate from 323 °C (at 1 °C/min) to 322 °C (at 10 °C/min) to 321 °C (at 50 °C/min), and A_s

increases slightly with the rate from 350 °C (at 1 °C/min) to 351 °C (at 10 °C/min) to 352 °C (at 50 °C/min). The TT: M_f and A_f do not change with the rate.

Given the large number of grains (in the polycrystal), and their associated internal variables, inspecting the individual variant evolutions to explain the trends is not feasible. Hence, inferences based from single crystal results are extended to the polycrystal results, and are as follows: (i) the transformation strain (in Fig. 3.27(b)) can increase as the rate of thermal cycling decreases, due to a preferential growth of the dominant variant at slower rates. This is an effect of the coupling on the transformation resistance, and (iii) the TRIP strain magnitude (in Fig. 3.27(c)) can be explained by the same argument. The (iv) the viscoplastic strain (in Fig. 3.27(d)) is consistent with the trends observed for single crystals, and remains unaffected by the evolution of the martensite volume fraction. Lastly, a decrease in the TT: M_s and increase in A_s with an increase in rate, indicates preferential activation of variants at lower temperatures along the forward path, and at higher temperatures along the reverse path, respectively.

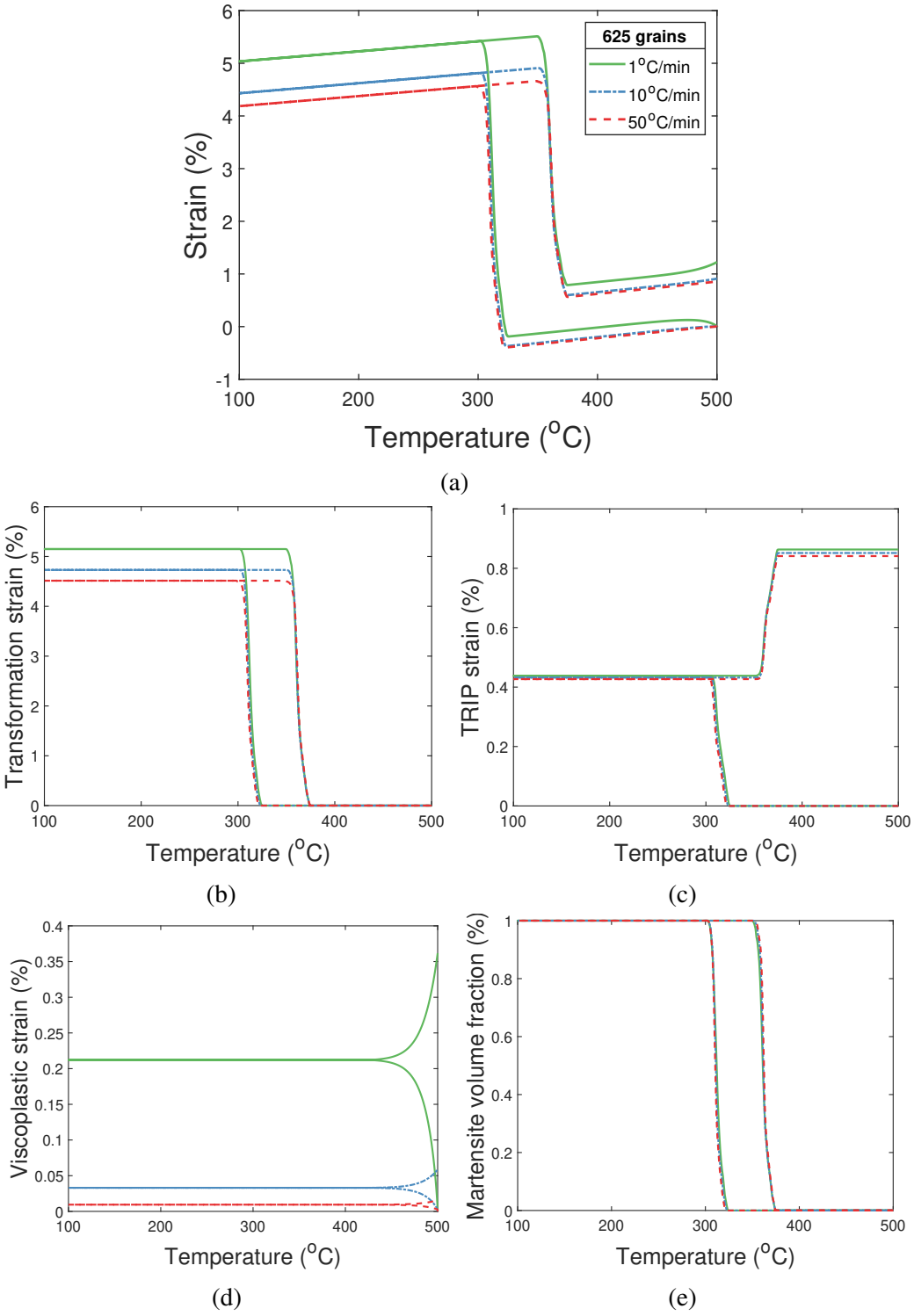

Figure 3.27: Rate-dependent responses obtained from a single cycle of UCFTC at 1, 10 and 50 °C/min for a 625 grain polycrystal: (a) Total strain (without detwinning), (b) Transformation strain, (c) TRIP strain, (d) Viscoplastic strain, and (f) Martensite volume fraction (legends are the same in the sub figures).

3.5.3 Multiple cycles

In order to calibrate the parameters controlling the phase-transformation and viscoplasticity coupling (in Section 3.2.3.6) a 10-cycle UCFTC test is simulated at 1 °C/min. The multiple cycle test activates the coupling and its affects the entire behavior, which is observed to evolve with each cycle and time. The test is simulated on the single crystals and 625 grain polycrystal, chosen in the previous sections. As experimental data on single-crystal HTSMAs for multiple cycles is not available in the open literature, the calibration is done to generate trends similar to those observed experimentally for polycrystals.

3.5.3.1 Total strain vs temperature and time

Shown in Fig. 3.28 is the experimental data of strain vs. temperature and strain vs. time for 10 cycles, obtained from Ni-Ti-Hf polycrystal experiments [7]. The plot in Fig. 3.28(a) shows the hysteresis loops evolving with cycling and the evolution of irrecoverable strain (generated at the end of each cycle) saturating with cycling. While the plot in Fig. 3.28(b) shows the strain ratchetting with time. As explained in Chaugule et al. [7], the hysteresis and strain evolve due to the irrecoverable mechanisms (of TRIP & viscoplasticity), accumulation of retained martensite and the coupling between phase transformation and viscoplasticity. This knowledge is used to calibrate the coupling parameters to obtain similar trends for single crystals.

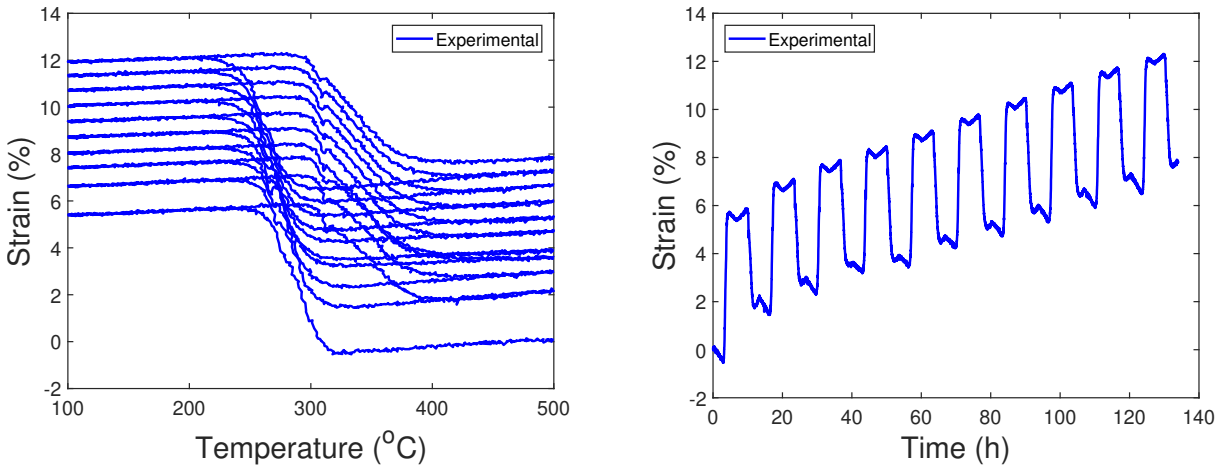

(a) (b)

Figure 3.28: Experimental response of a Ni-Ti-Hf polycrystal [7] when subjected to UCFTC at 1 °C/min (a) strain-temperature and (b) strain-time response (from Chapter 2).

The multiple cycle responses from chosen single crystals are shown with respect to temperature and time in the following figures. The total strain (excluding detwinning) generated from each crystal and the polycrystal shows trends similar to those observed experimentally. These trends are discussed briefly here, and the individual strain components are discussed later.

1. Along [001]: the hysteresis loop shifts to lower temperatures with cycling, while the strain ratchets with time (in Fig. 3.29 (a),(b)). The TT: M_s and A_f are observed to evolve differently with cycling.

2. Along [011]: the hysteresis and strain (in Fig. 3.29 (c),(d)) evolves similar to [001], but there is a minor drop in total strain after 6 cycles.

3. Along [21$\bar{4}$]: the hysteresis and strain (in Fig. 3.29 (e),(f)) evolve similar to [001], but the total strain reaches a higher value due to the accumulation of higher irrecoverable (viscoplastic) strains.

4. Along [111]: the hysteresis and strain (in Fig. 3.29 (g),(h)) evolve similar to the previous orientations, but the total strain reaches the highest values due to the accumulation of higher

irrecoverable (TRIP) strains.

5. For the polycrystal: the hysteresis and strain (in Fig. 3.29 (i),(j)) show trends similar to the single crystal trends, with a visible increase in hysteresis (width) and saturation in the irrecoverable strain at the end of the cycles.

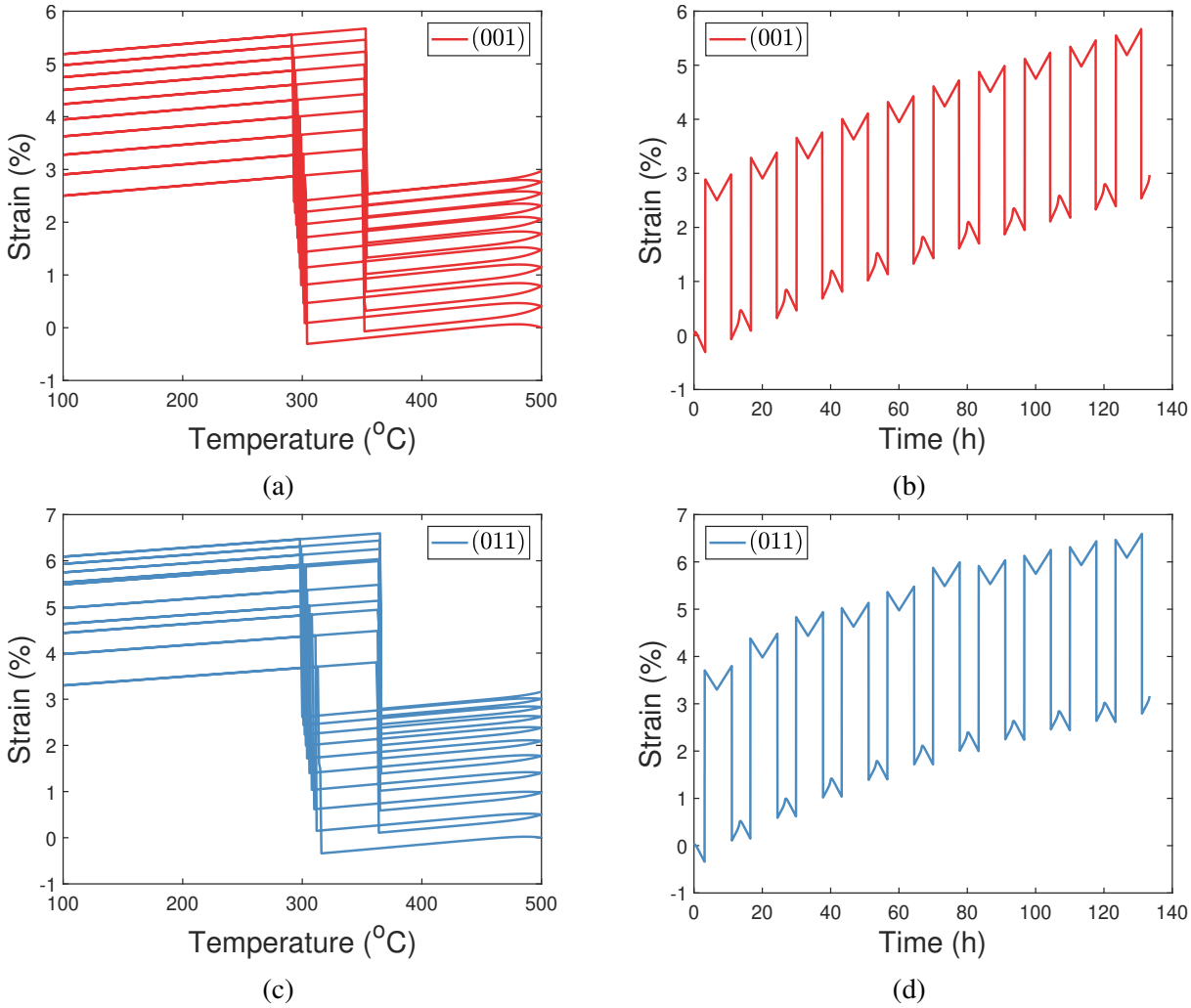

Figure 3.29: (a) Strain vs temperature and strain vs time (simulated) response of a Ni-Ti-Hf single crystal oriented along [001] in (a),(b) and along [011] in (c),(d) when subjected to a 10-cycle uniaxial constant force thermal cycling at 1 °C/min.

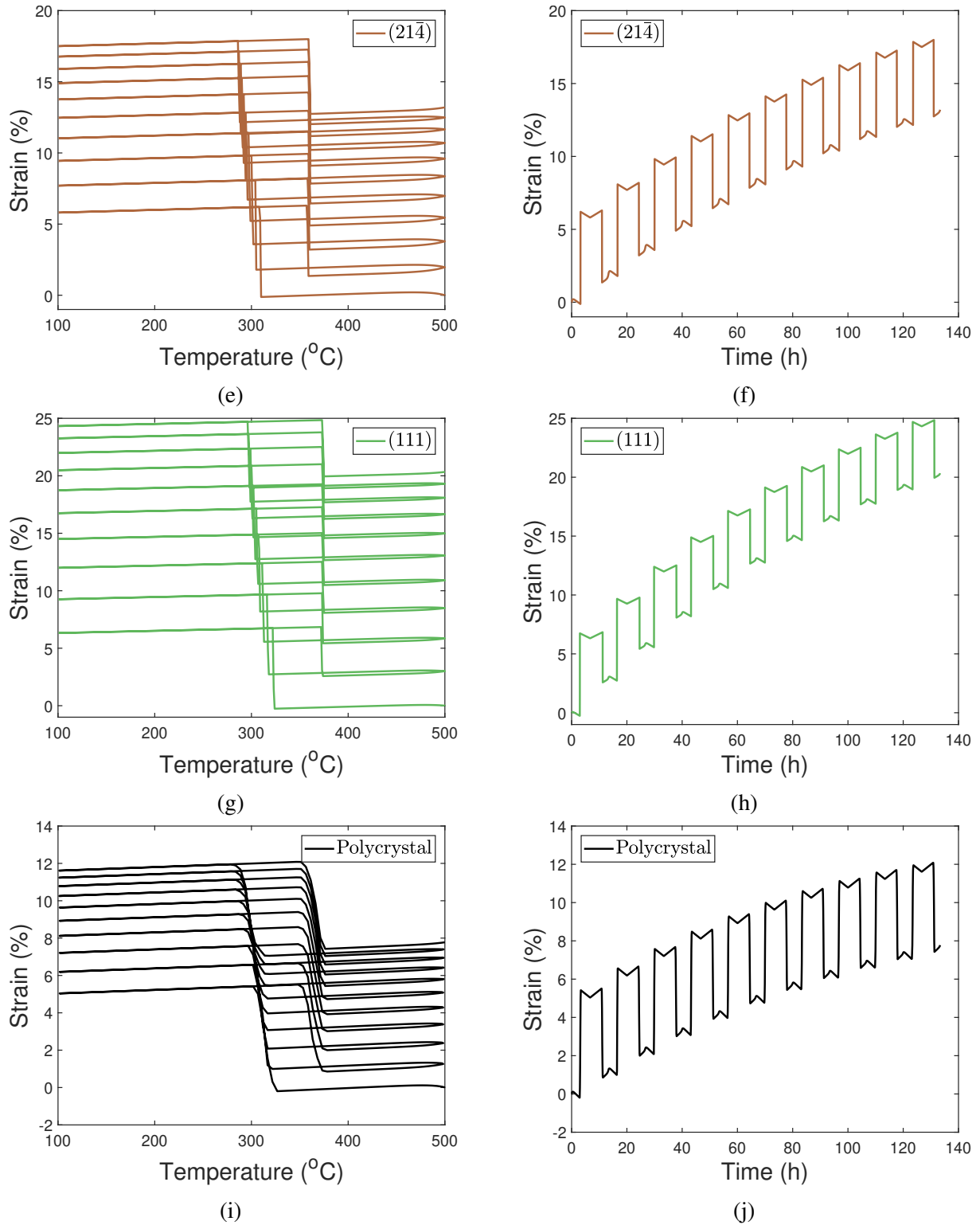

Figure 3.29: (Continued) Strain vs temperature and strain vs time (simulated) response of a Ni-Ti-Hf single crystal oriented along along [21$\bar{4}$] in (e),(f), along [111] in (g),(h), and for polycrystal (625 grains) in (i),(j), when subjected to a 10-cycle uniaxial constant force thermal cycling at 1 °C/min.

To investigate the total strain further, its irrecoverable components (of TRIP and viscoplasticity), recoverable component (of transformation), TT (M_f and A_f), hysteresis, and accumulation of retained martensite, are plotted separately and compared.

3.5.3.2 TRIP strain vs. time

The TRIP strain (in Fig. 3.30) from simulated single crystals, polycrystal, and experimental polycrystals, initiates with a distinct value and evolves differently in each case. As observed, the TRIP strain generated along [001] is the least, while it is the largest along [111]. The amount of slip (during TRIP), corresponding to each martensite variant, depends on the volume fraction of the variant (Eq. 3.14). On inspecting the variants, it is observed that the order of volume fraction reached by the (dominant) martensite variants is: [001] < [011] < [$21\overline{4}$] < [111]. This order is reflected on the TRIP strain magnitude, as observed in the plot. A difference in kinetics of evolution in the TRIP strain generated by the polycrystal and the experimental values is also observed. The kinetics vary because of the way in which the coupling parameters are calibrated. A better calibration can be performed if experimental values from single crystals over multiple cycles is available.

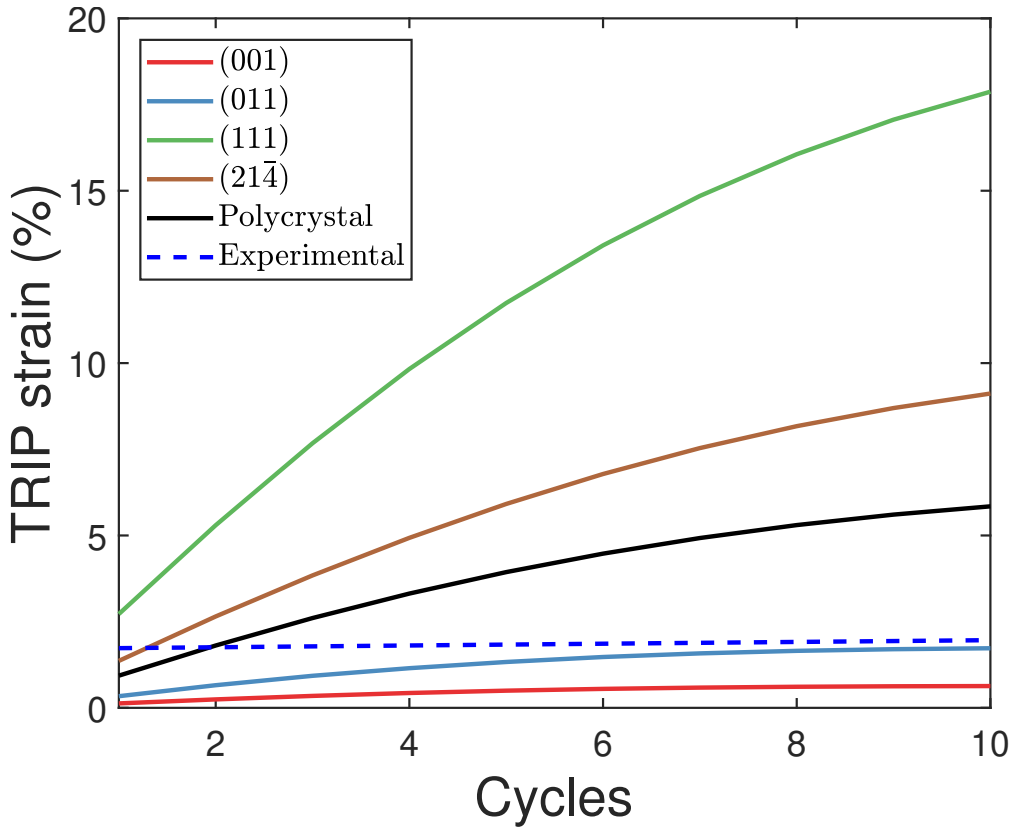

Figure 3.30: TRIP strain generated during a 10-cycle UCFTC at 1 °C/min along [001], [011], [111], [21$\bar{4}$], and in a 625 grain polycrystal, is compared with experimental trend and values, from Ni-Ti-Hf (polycrystal from Chapter 2).

3.5.3.3 Viscoplastic strain vs. time

The viscoplastic strain (in Fig. 3.31) generated from single crystals, polycrystal, and from experiments, can be observed to be nearly homologic, as they initiate with very close values ([21$\bar{4}$] $\approx$ polycrystal and [001]$\approx$[111]), but evolve differently for each orientation. The order of plastic/viscoplastic strain generated from monotonic tensile tests on single crystal FCC metals can be [111] < [011] < [001] [130], while for BCC metals it can be [011] < [001] < [111] [150]. However, the trends for single-crystal HTSMAs are unknown as their lattice arrangement is not classified as BCC and/or FCC in literature, mainly because martensite is a sub-group of austenite [1].

The viscoplastic strain along [001] and [111] starts with the same value and evolve very closely because the contribution of the $\{110\}\langle\bar{1}11\rangle$ family is not accounted along the [111] direction.

Based on the Schmid factor and number of activated slip systems, there are 6 slip systems of the above family activated along the [111] direction for the above family in addition to the 3 activated for the $\{110\}\langle 001\rangle$ family, as shown in Appendix B. The macro-micro parameters are derived using the later family of slip systems and not the former ones in order to simplify the equations, and because they produce a higher Schmid factor. If both families were accounted to derive the macro-micro parameters, two separate equations for slip (Eq. 3.23) at the micro-scale would have to be compared with one equation of strain at the macro-scale. In order to simplify the comparison only one family of slip systems was considered and therefore the accumulated magnitude of viscoplastic strain along [111] is underestimated, even after 10 cycles.

The random orientation $[21\bar{4}]$ produces the largest amount of viscoplastic strain, as recalled from Fig. 3.15(b), which justifies its magnitude (in Fig. 3.31). While along [011] the least amount of viscoplastic strain ($\approx 0.08\%$) is generated in comparison to all the above orientations. Similar to the TRIP strains, a difference in kinetics of evolution in the viscoplastic strain generated by the polycrystal and the experimental values is also observed.

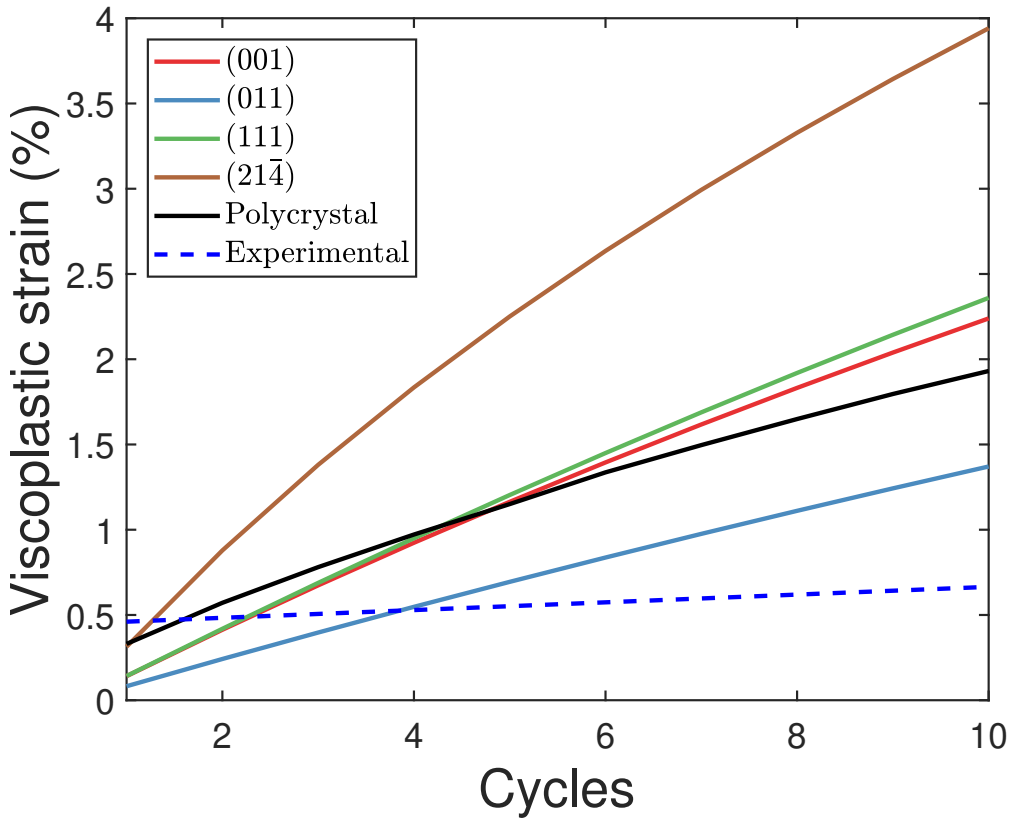

Figure 3.31: Viscoplastic strain generated during a 10-cycle UCFTC at 1 °C/min along [001], [011], [111], [21$\bar{4}$], and in a 625 grain polycrystal, is compared with experimental trend and values, from Ni-Ti-Hf (polycrystal from Chapter 2).

3.5.3.4 Transformation temperatures and hysteresis vs. number of cycles

The TT: M_f and A_f (in Fig. 3.32(a),(b)) are extracted from the total strain vs. temperature plots at points corresponding to the start and end of phase transformation along the forward and reverse paths, respectively. The transformation resistances (in Eq. 3.26) were formulated to increase with cycling due to the coupling, which resulted in a shift in the TT. As observed, the TT A_f increases while M_f decreases with cycling for every orientation and the polycrystal. However, the slopes (or rate of decrease) of each TT are observed to be different for each orientation. This is because of the varying evolution of total dislocation density ($\rho_{TRIP} + \rho_{vp}$) along each orientation (as reflected by their strains).The TT: A_f (in Fig. 3.32(a)) increases slowly with cycling and is not consistent qualitatively with the experimental trend of 1 °C/min. The TT: M_f (in Fig. 3.32(b))

decreases gradually for each orientation and the polycrystal, and is consistent qualitatively with the experimental trend. The hysteresis width (in Fig. 3.32(c)) is evaluated as the difference between the TT: $A_f - M_f$ widens (or increases) for all the orientations, and the polycrystal, which is also consistent qualitatively with the experimental trend.

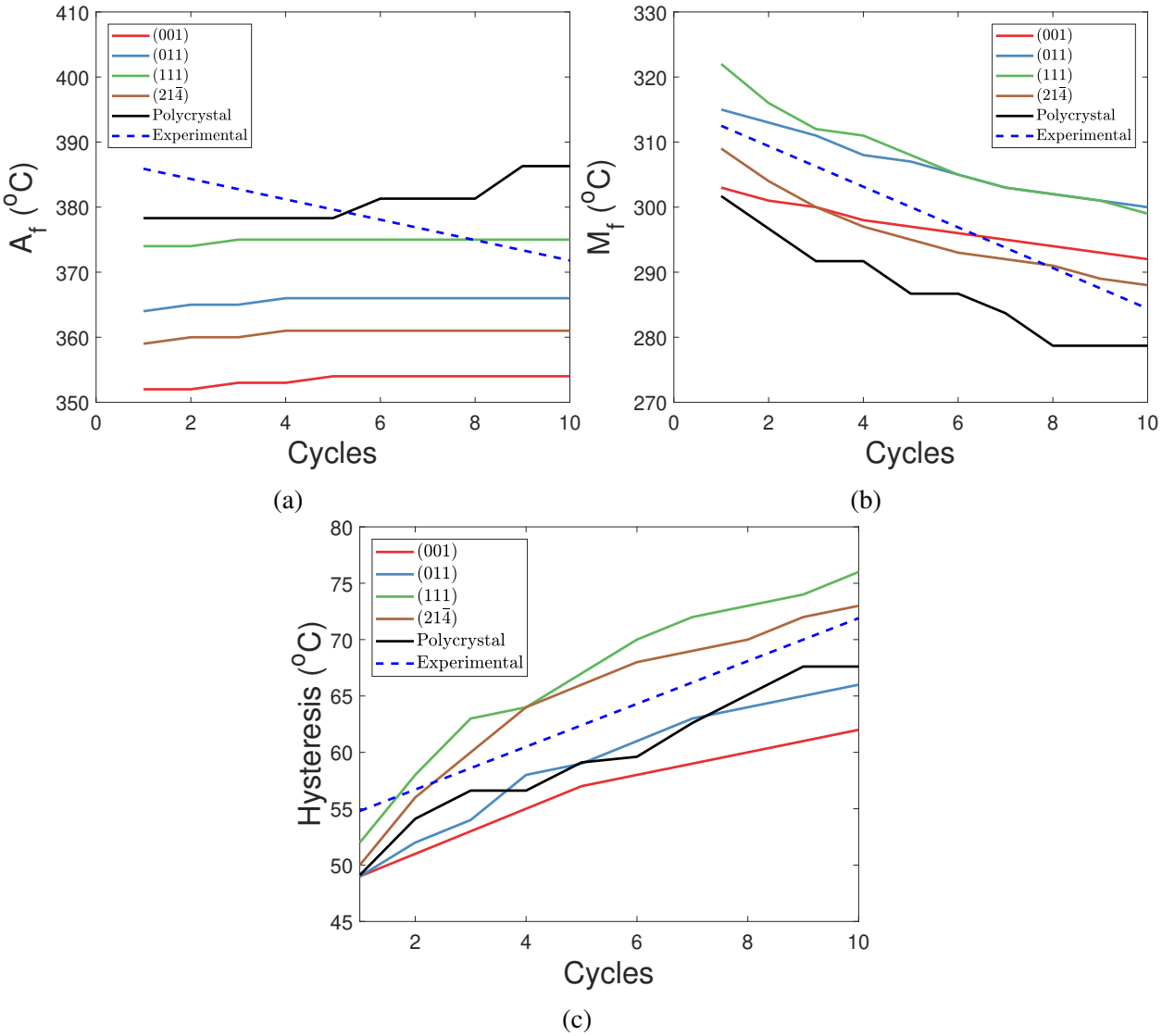

Figure 3.32: Evolution of TT and hysteresis generated during a 10-cycle UCFTC at 1 °C/min along [001], [011], [111], [21$\bar{4}$], and in a 625 grain polycrystal, is compared with experimental trend (polycrystal from Chapter 2).

3.5.3.5 Transformation strain vs. number of cycles

In comparison to the viscoplastic and TRIP strains, the transformation strain (Eq. 3.4) (in Fig. 3.33(a)) does not change significantly for each single crystal and the polycrystal. In 10 cycles, the value decreases by: 0.05% for [011], 0.35% for [111], 0.19% for $[21\bar{4}]$, and 0.35% for the polycrystal. In case of [001], the value increases by 0.02%.

The decrease is due to accumulation of retained martensite (trapped) by the total dislocation density (Eq. 3.28). The retained martensite reduces the amount of recoverable martensite (Eq. 3.10) and, hence, transformation strain (Eq. 3.4). On inspecting the total martensite volume fraction, it is found that the amount of retained martensite follows the order: [001] < polycrystal < [011] < $[21\bar{4}]$ < [111]. It is also found that the volume fraction of the dominant variant reduces with cycling in each single crystal, but other minor variants grow with each cycle. Hence, if the retained martensite overcomes the contribution from minor variants, the transformation strain will reduce.

Whereas in the opposite case, the contribution from the minor variants will lead to an increase in transformation strain, as observed along [001]. The largest amount of retained martensite ($\approx$5%) is accumulated along [111] (in Fig. 3.33(b)). On the other hand, the least amount of retained martensite ($\approx$0.5%) is accumulated along [001] (in Fig. 3.33(c)) and, hence, the preferential (minor) variant activation increases its transformation strain. Such an increase is qualitatively consistent with what is observed experimentally [57, 7]. According to Kockar et al. [57], internal stress fields generated by dislocations can increase the transformation strain with each cycle. The reason mentioned by the study is that when some preferred (biased) martensite variants nucleate and grow, an increase in volume fraction of those variants is observed resulting in an increase in transformation strain.

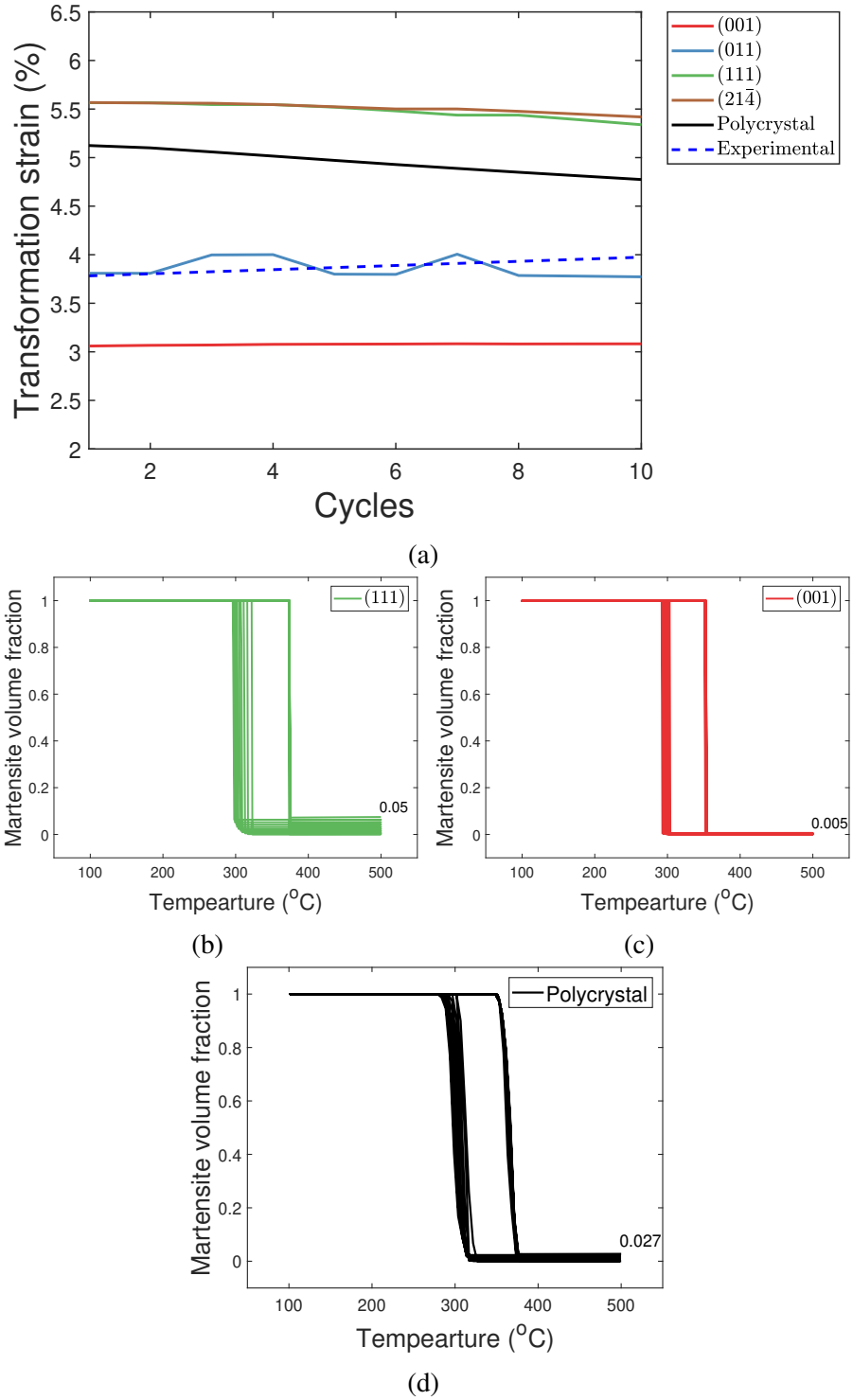

Figure 3.33: (a) Transformation strain generated during a 10-cycle UCFTC at 1 °C/min along [001], [011], [111], [21$\bar{4}$], and polycrystal is compared with the experimental trend (polycrystal from Chapter 2), (b) Evolution of martensite volume fraction for [111], [001], and polycrystal, with accumulated retained martensite at the end of 10 cycles being ≈5%, ≈0.5%, and ≈2.76% respectively.

3.6 Summary

The conclusions from the above constitutive modeling effort are provided in Chapter 4, and a summary of the present chapter is provided as follows:

1. In the present chapter, a crystal plasticity model was developed to account for the phenomena of phase transformation, detwinning, TRIP, plasticity/viscoplasticity, and a coupling between viscoplasticity and phase-transformation in Ni-Ti-Hf HTSMAs.

2. Formulating the model involved following a physics based approach to predict the slip and transformation phenomena, and following a phenomenological approach to simulate the coupling using the dislocation density variables from viscoplasticity and TRIP.

3. Calibrating the model involved simulating a UCFTC thermomechanical test at 1 °C/min along [001], [011], and [111] and comparing the responses with those of literature [13].

4. The model was then implemented on single crystals of 500 random orientations to generate their total response. Some of these responses were compared and dissociated to study their irrecoverable components and functional properties such as TT and hysteresis.

5. The model was also tested for its rate-dependent responses on single crystals of the above three orientations and a random orientation $[21\bar{4}]$.

6. The model was then implemented on a polycrystal to simulate its response with increasing number of grains to obtain a grain-independent response. The polycrystal response of 625 grains was then compared with the experimental response to make inferences about the active phenomena. Subsequently, the rate-dependency in the polycrystal responses was also investigated.

7. Lastly, a multiple cycle thermomechanical test was then simulated using the model for single crystals and their responses were compared with the experimental trends. The effect of coupling on the overall responses and the evolution of their components was investigated.

3.7 Supplementary material

The orientations of the 7 single crystals and the [001], [011] and [111] generating the random responses in Fig. 3.15 are shown on a stereographic triangle in Fig. 3.34 (a) - (c) and an Inverse Pole Figure is created using the orientations in Fig. 3.34(d).

3.7.1 IPF of 10 random orientations

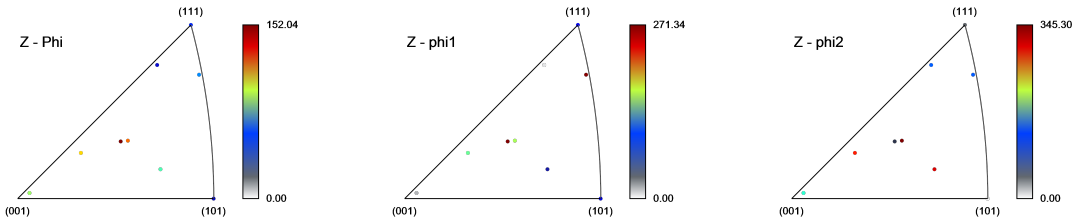

(a) (b) (c)

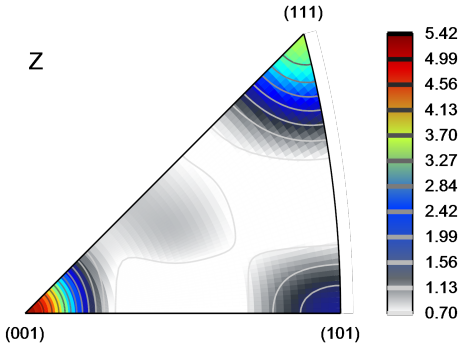

(d)

Figure 3.34: Distribution of random Euler angles (ϕ_1,Φ,ϕ_2) along Z axis for 10 random orientations in (a) - (c), (d) Inverse Pole figure generated using the orientations.

3.7.2 Rate-dependency

The rate-dependency in single crystal responses through their strain components are presented as follows:

In case of [001], the maximum strain (in Fig. 3.35(a)) decreases with the thermal cycling rate: 1 > 10 > 50 °C/min, with a relatively minor difference between the 10 and 50 °C/min responses. This decrease is reflected from the trends of viscoplastic strain (in Fig. 3.35(e)) which decreases with an increase in rate. The transformation and TRIP strain (in Fig. 3.35(b) and (d)), both of which depend on the martensite variant volume fraction, do not vary with the rate. The evolution of the total volume fraction (in Fig. 3.35(f)) is the same for all the three rates, and on inspecting the variants it is observed that all the 12 variants are activated at all rates. The volume fraction of the dominant (1^{st}) variant is also the same at all rates ≈ 0.619. This is eventually reflected in the trend in transformation and TRIP strain.

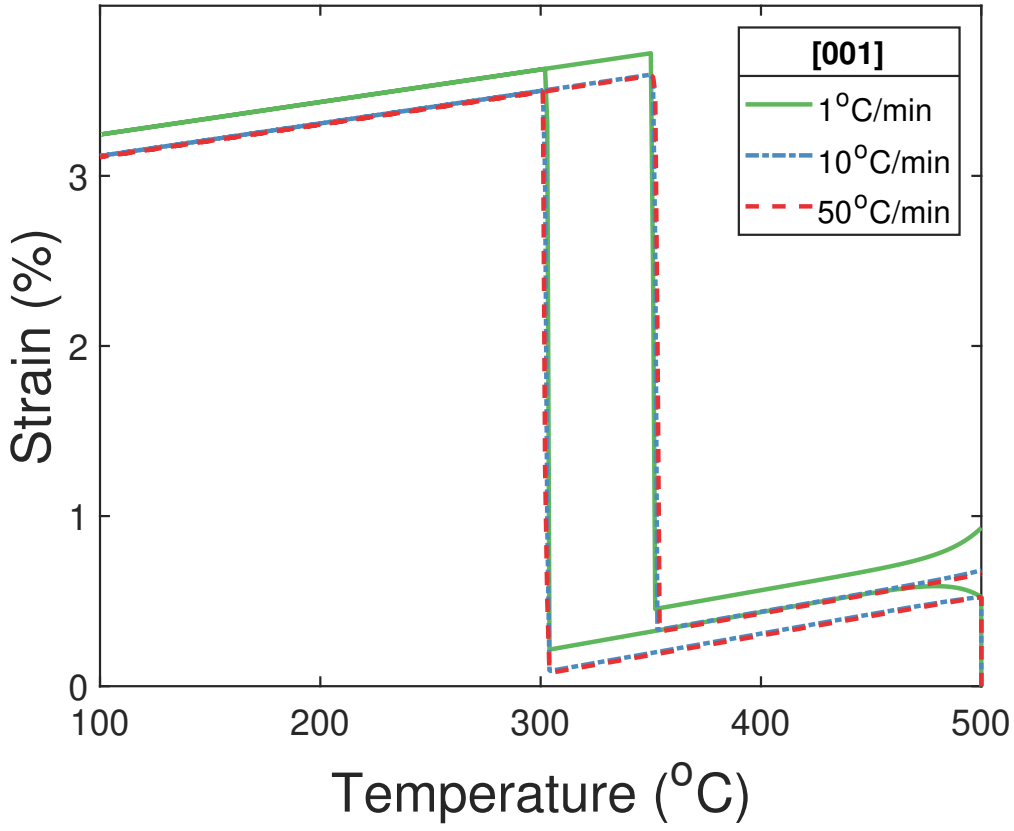

(a)

Figure 3.35: (a) Total strain-temperature response at 1, 10, and 50 °C/min for [001].

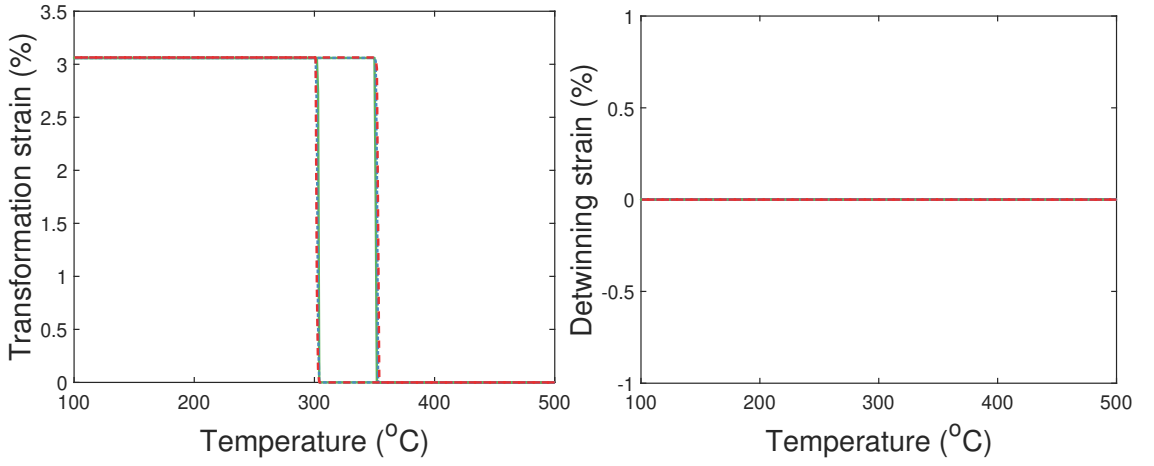

(b)

(c)

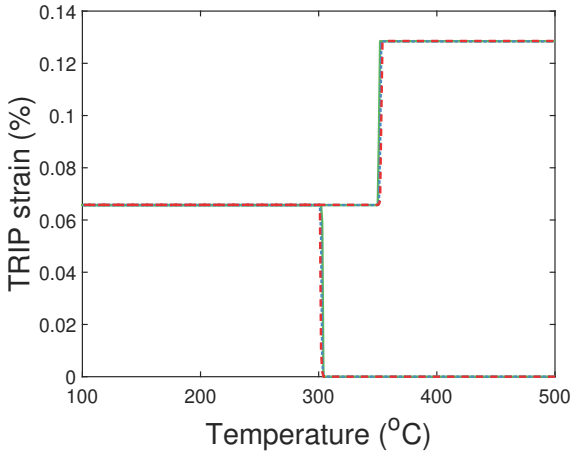

(d)

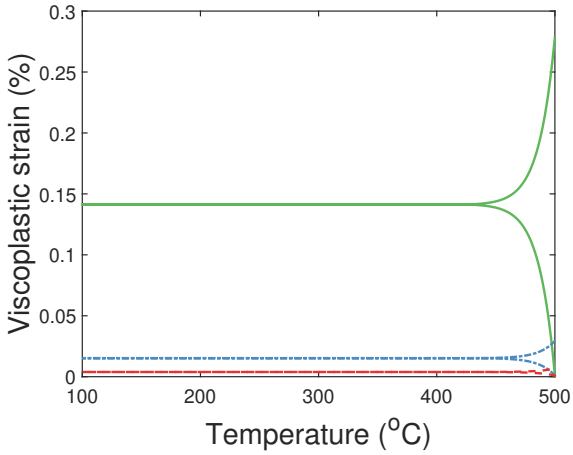

(e)

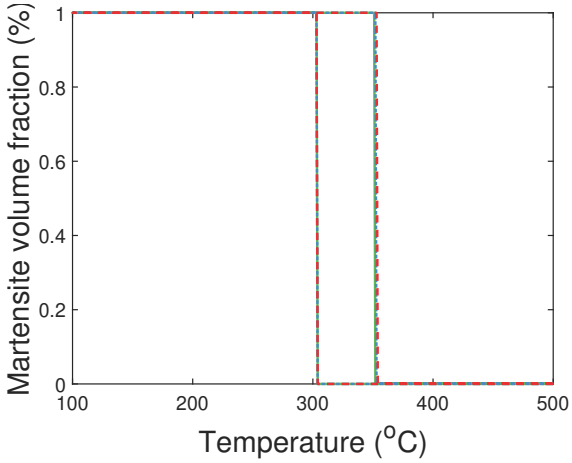

(f)

Figure 3.35: (Continued) Strain-temperature response at 1, 10, and 50 °C/min for [001] (b) Transformation, (c) Detwinning, (d) TRIP, (e) Viscoplastic strain, and (f) Martensite volume fraction evolution (legends are the same in the sub figures).

In case of [011] too the total strain (in Fig. 3.36(a)) decreases with an increase in rate but, the decrease is minor in comparison to that observed for [001]. However, the decrease is a combination of trends shown by the transformation (in Fig. 3.36(b)), detwinning (in Fig. 3.36(c)), TRIP (in Fig. 3.36(d)) and viscoplastic (in Fig. 3.36(e)) strains. The total martensite volume fraction (in Fig. 3.36(f)) evolution is the same for all the rates. But on inspecting the variants, it is observed that only 2 variants are activated at 1 °C/min, and 3 variants get activated at 10 and 50 °C/min. The volume fraction of the dominant variant also decreases from 0.749 (at 1 °C/min) to 0.725 (at 10 °C/min) and 0.720 (at 50 °C/min). This change in variant volume fraction or preferential activation of variant, is due to an effect of the coupling on the transformation resistance, which induces a minor rate-dependency in the transformation and TRIP strain.

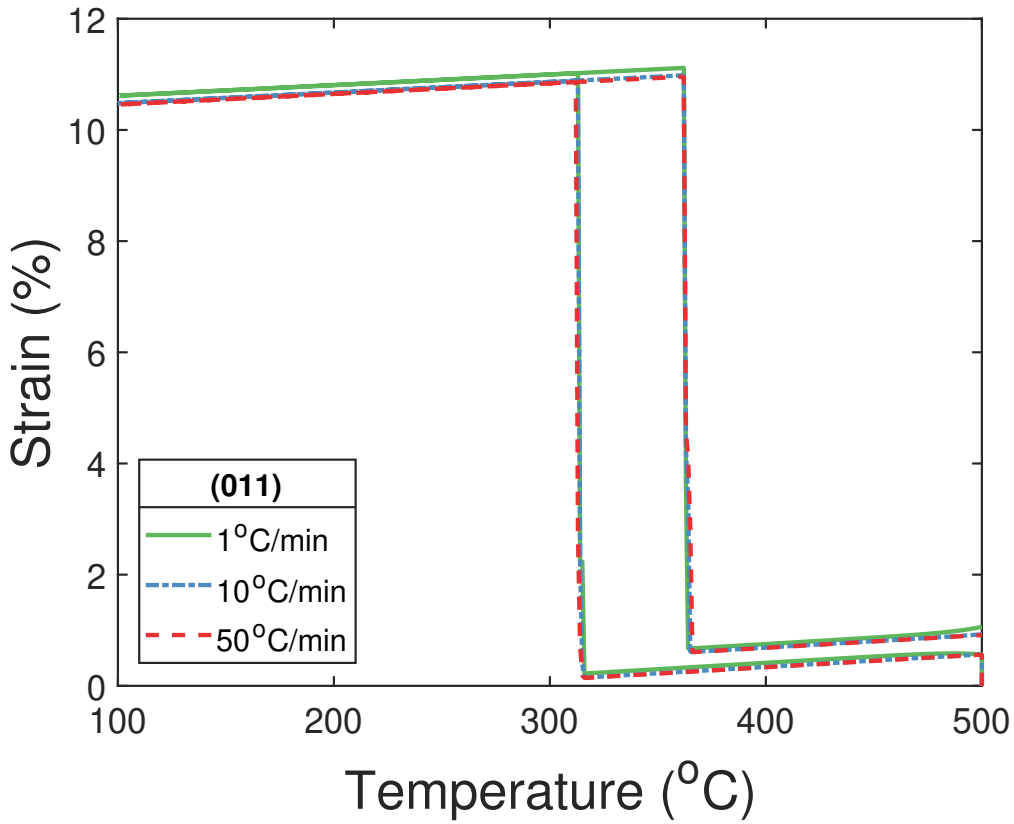

(a)

Figure 3.36: (a) Total strain-temperature response at 1, 10, and 50 °C/min for [011].

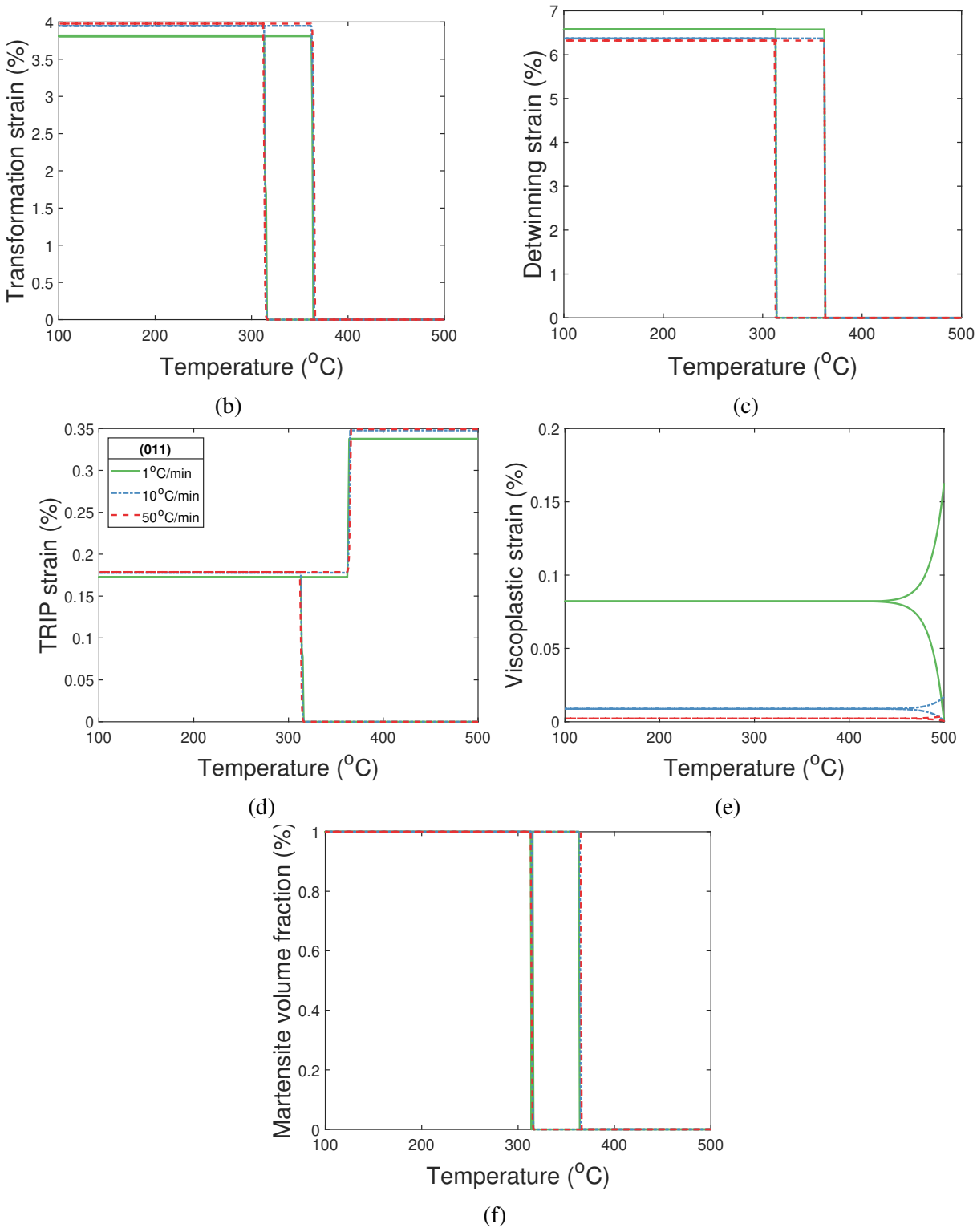

Figure 3.36: (Continued) Strain-temperature response at 1, 10 and 50 °C/min for [011] (b) Transformation, (c) Detwinning, (d) TRIP, (e) Viscoplastic strain, and (f) Martensite volume fraction evolution (legends are the same in the sub figures).

In case of [21$\bar{4}$], the total strain (in Fig. 3.37(a)) decreases with the rate overall, similar to the [001] trend. This transformation (in Fig. 3.37(b)), detwinning (in Fig. 3.37(c)) and TRIP (in Fig. 3.37(d)) strains do not vary with the rate, but the viscoplastic strain (in Fig. 3.37(e)) decreases with rate as expected. The total martensite volume fraction (in Fig. 3.37(f)) evolution is almost the same for all the rates. On inspecting the variants, it is observed that the only 2 variants are activated at all the three rates, and the volume fraction of the dominant variant is: 0.999 for all the three rates. This reflects as a rate-independency in transformation and TRIP strain, and, hence, the total strain decreases with the rate only due to the viscoplastic strain.

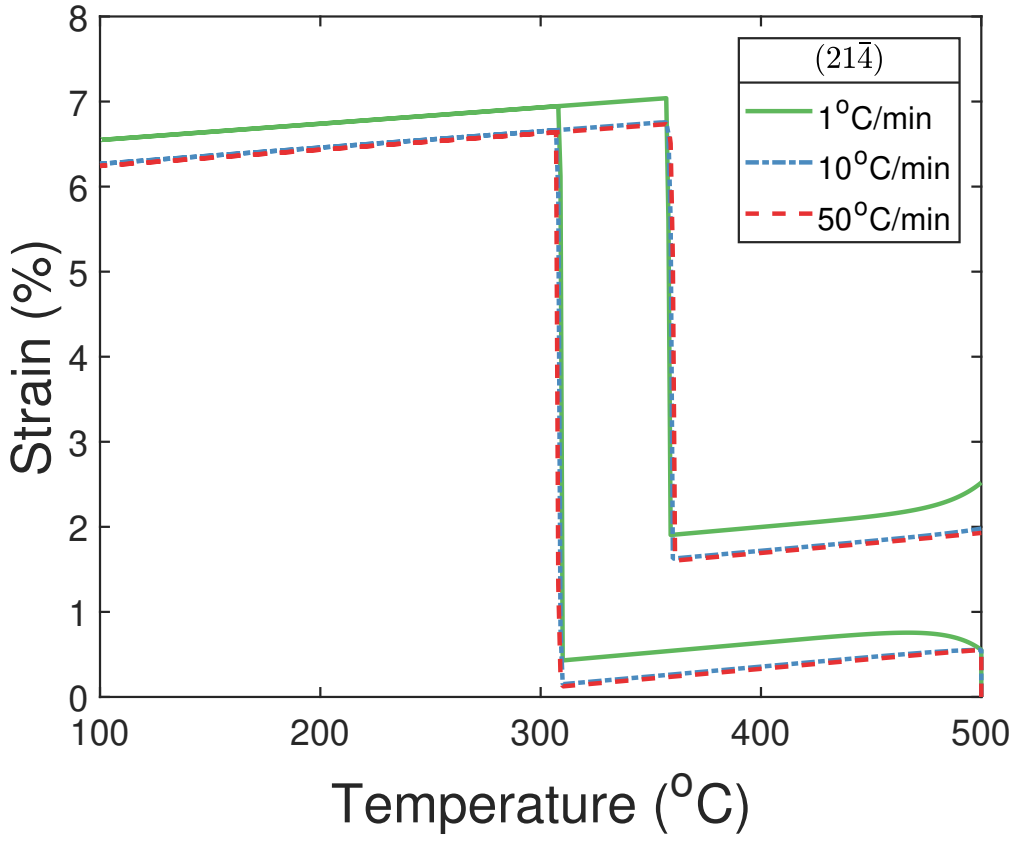

(a)

Figure 3.37: (a) Total strain-temperature response at 1, 10 and 50 °C/min for [21$\bar{4}$].

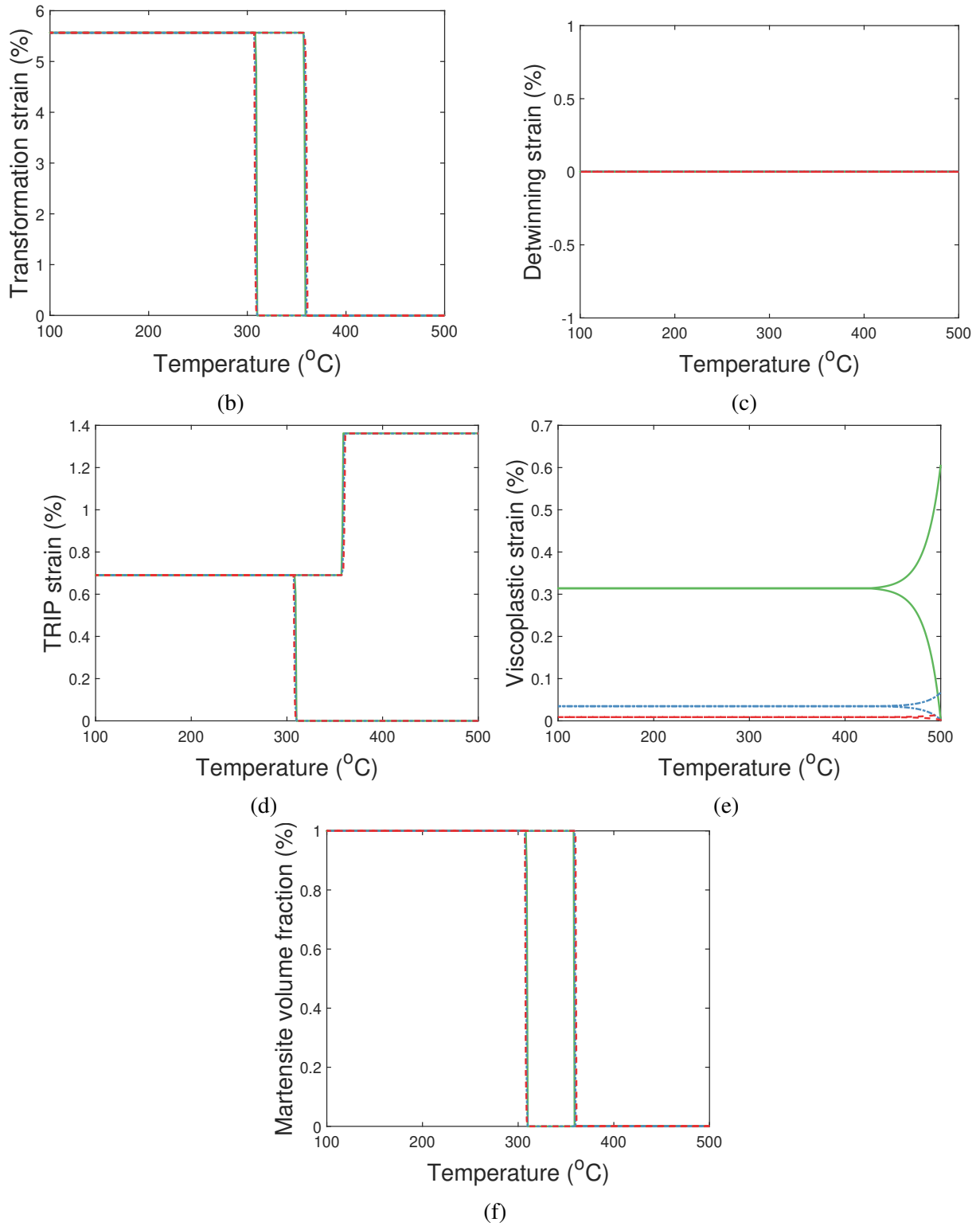

Figure 3.37: Strain-temperature response at 1, 10, and 50 °C/min for $[21\bar{4}]$ (b) Transformation, (c) Detwinning, (d) TRIP, (e) Viscoplastic, and (f) Martensite volume fraction evolution (legends are the same in the sub figures).

Lastly, in case of [111], the total strain shows a minor decrease with rate (in Fig. 3.38(a)) which is due to the viscoplastic strain (in Fig. 3.38(c)) only as the response of each strain component (in Fig. 3.38(b - f)), is the same for all rates. On inspecting the variants, its is observed that the same two variants are activated, and the dominant variant reaches the same volume fraction of 0.999 at all three rates, similar to the [011] case.

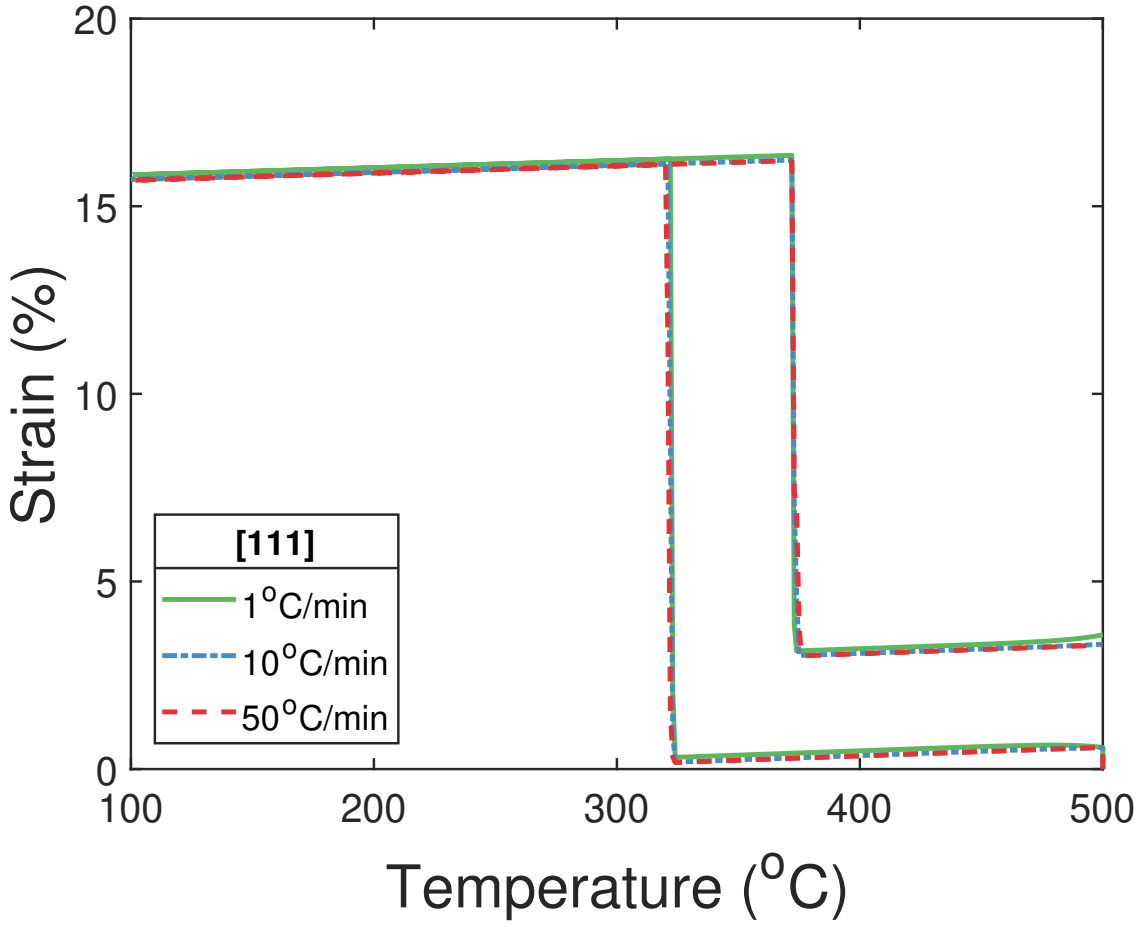

(a)

Figure 3.38: (a) Total strain-temperature response at 1, 10 and 50 °C/min for [111].

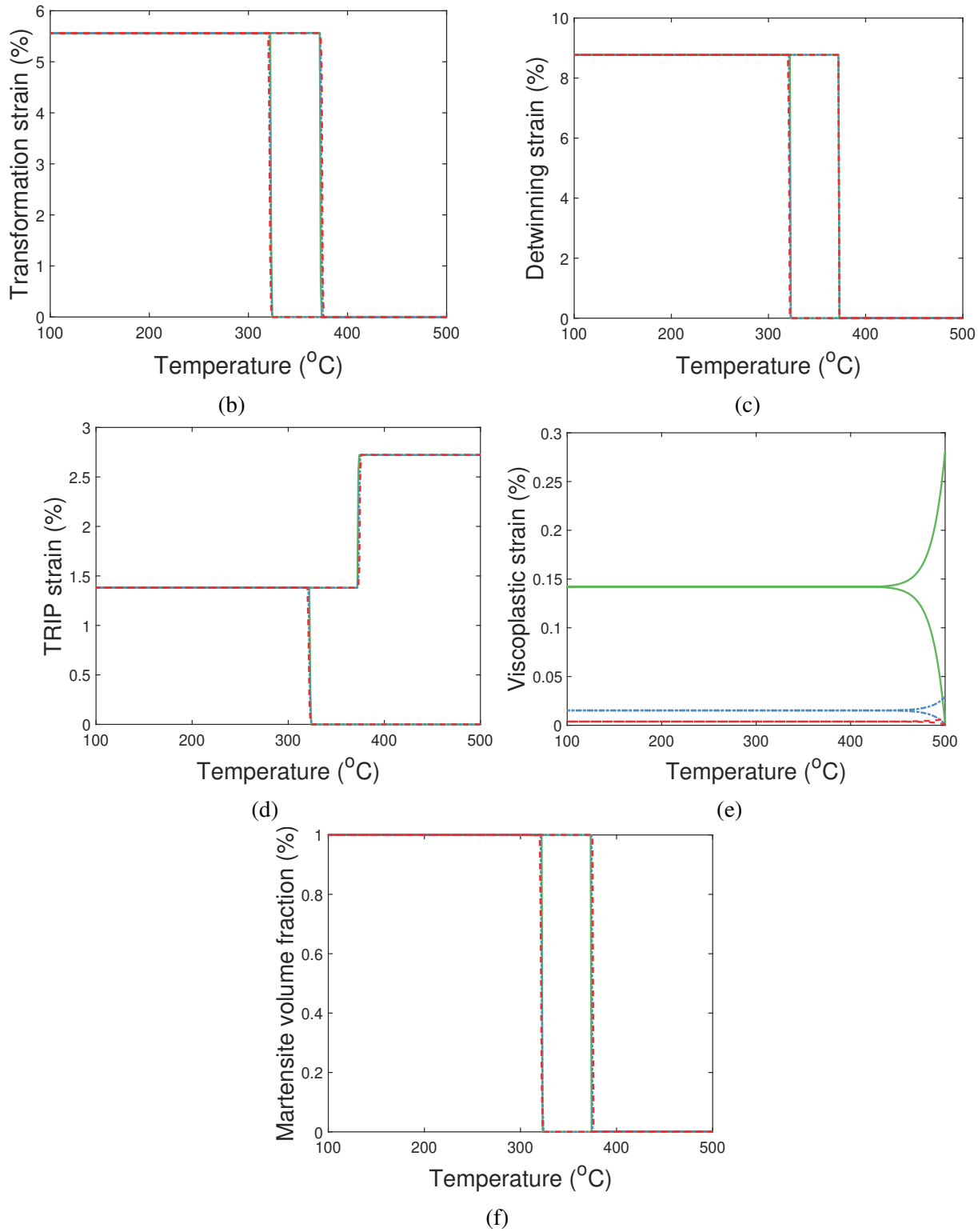

Figure 3.38: (Continued) Strain-temperature response at 1, 10 and 50 °C/min for [111] (b) Transformation, (c) Detwinning, (d) TRIP, (e) Viscoplastic strain, and (f) Martensite volume fraction (legends are the same in the sub figures).

3.7.3 Comparison of polycrystal domains

A single cycle of UCFTC was simulated at 1 °C/min for each of the following domains listed in Table 3.19. The computation time listed below is for a thermal segment of 1 °C. As observed in the table, the computation time increases as the domain of the polycrystal and number of grains increases. Hence the simulations were limited and shown only for the polycrystals with grains ranging from 5 to 625. The response does not change in trends on increasing the grains from 625 to 1080 grains, and hence, it is not included in the comparisons in the next section.

Table 3.19: Domain size of polycrystal RVEs with their file size and computation time spent.

Domain size	Number of grains	File size (kB)	Computation time (h)
1 x 1 x 1	5	85	0.5
2 x 2 x 2	40	613	4
3 x 3 x 3	135	2024	13
4 x 4 x 4	319	4798	32
5 x 5 x 5	625	9292	65
6 x 6 x 6	1080	16,107	182

3.7.4 Comparison of polycrystal responses

As mentioned in Section 3.5.2.2 the number of grains and the size of domain is increased to obtain a grain-independent response, the saturation of responses is demonstrated in this Section. Shown in Fig. 3.39 is the convergence of the entire response, while shown in Fig. 3.40, are each of its components, and the martensite volume fraction in Fig. 3.41.

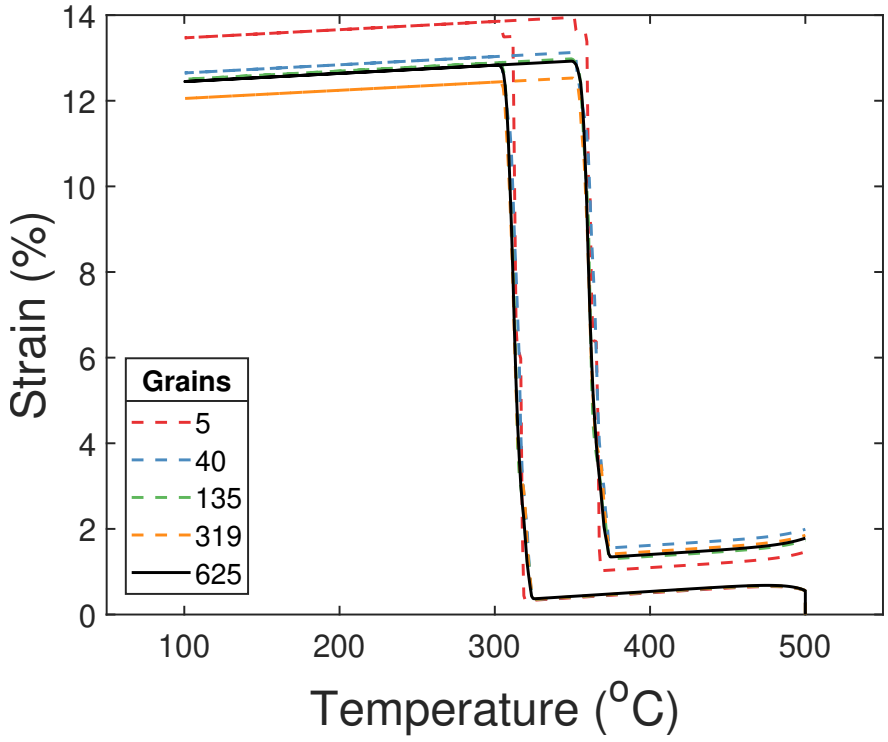

(a)

Figure 3.39: Comparison of total strain vs temperature from polycrystal aggregates with increasing number of grains and increasing domain size, for a UCFTC test at 1 °C/min.

As observed in Fig. 3.20(a),(b), the magnitude of maximum detwinning and transformation strains, and the paths of forward and reverse transformation, seem to saturate with an increase in number of grains. Their trends reflect the trends of the martensite volume fraction in Fig. 3.40. The TRIP strain in Fig. 3.20(c) seems to saturate from 5 to 319 grains, but then increases from 319 to 625 signifying an increase in grains increases the slip during TRIP. The viscoplastic strain in Fig. 3.20(d) which also arises from slip at high temperatures, saturates overall with an increase in grains.

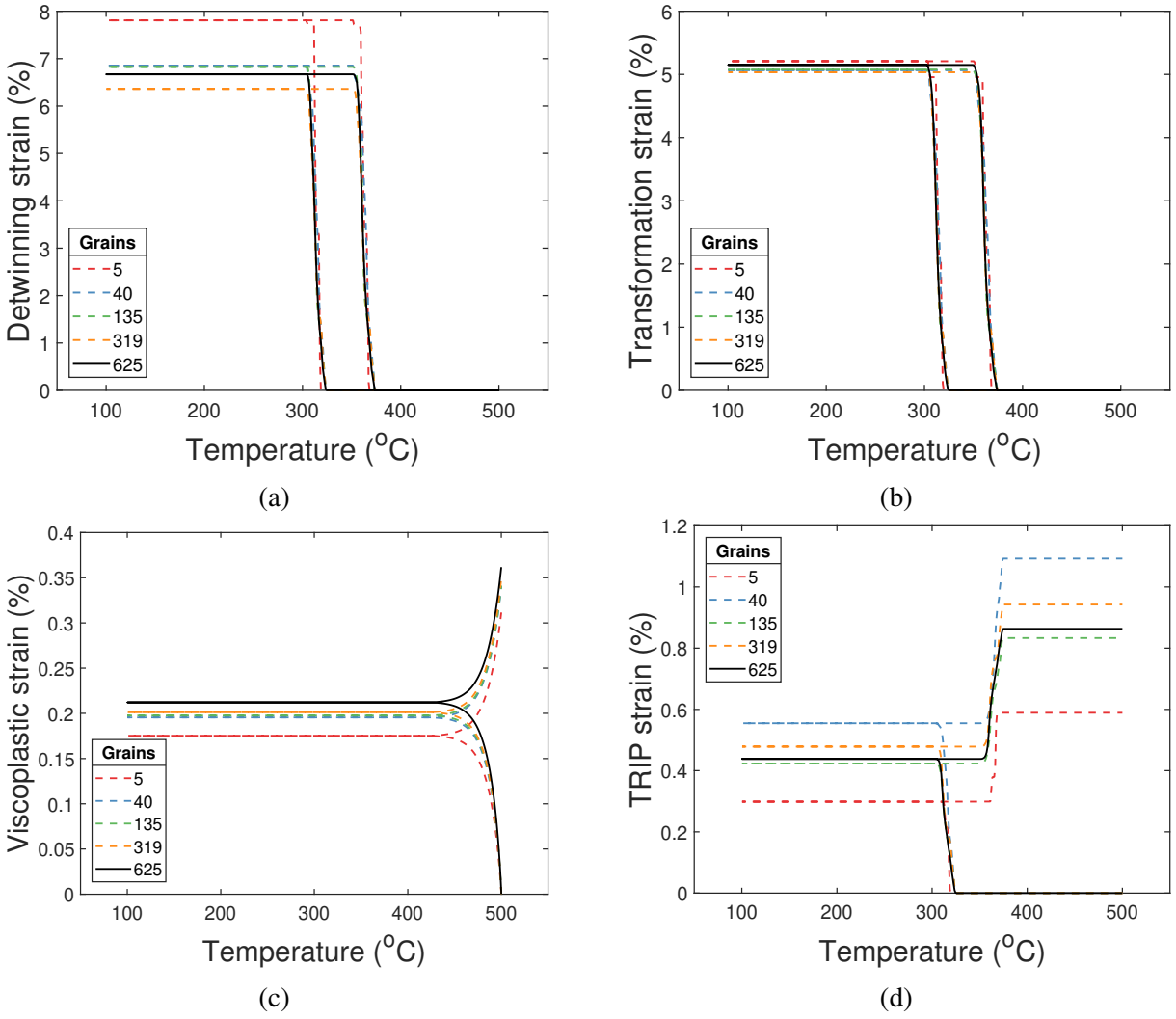

Figure 3.40: Comparison of (a) detwinning, (b) transformation, (c) viscoplastic, and (d) TRIP strain vs temperature from polycrystal aggregates with increasing number of grains and increasing domain size, for a UCFTC test at 1 °C/min.

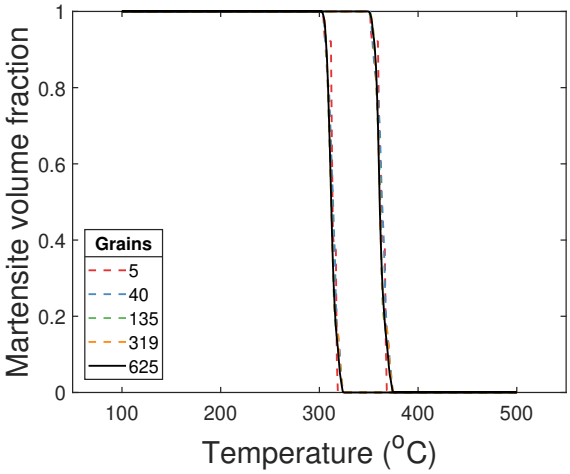

Figure 3.41: Comparison of martensite volume fraction vs temperature from polycrystal aggregates with increasing number of grains and increasing domain size, for a UCFTC test at 1 °C/min.

3.7.5 Polycrystal responses: Different Stresses

The behavior of the selected Ni-Ti-Hf alloy at stress levels lower than 500 MPa and for temperature domains less than 500 °C, was experimentally investigated and presented in Benafan et al. [6]. Using the crystal-plasticity model the response of polycrystals is simulated for the same temperature domain and stresses selected experimentally. The responses at increasing stress levels from 100 to 500 MPa are shown in Fig. 3.42. As the stress increases the amount of total strain, TT, and irrecoverable strain is observed to increase, which is qualitatively consistent with the experiment trends. However, the total strain obtained for each stress level is not consistent quantitatively, and this is primarily because the interaction between the variants is not accounted for in the model and is a potential expansion of the model to simulate accurate results.

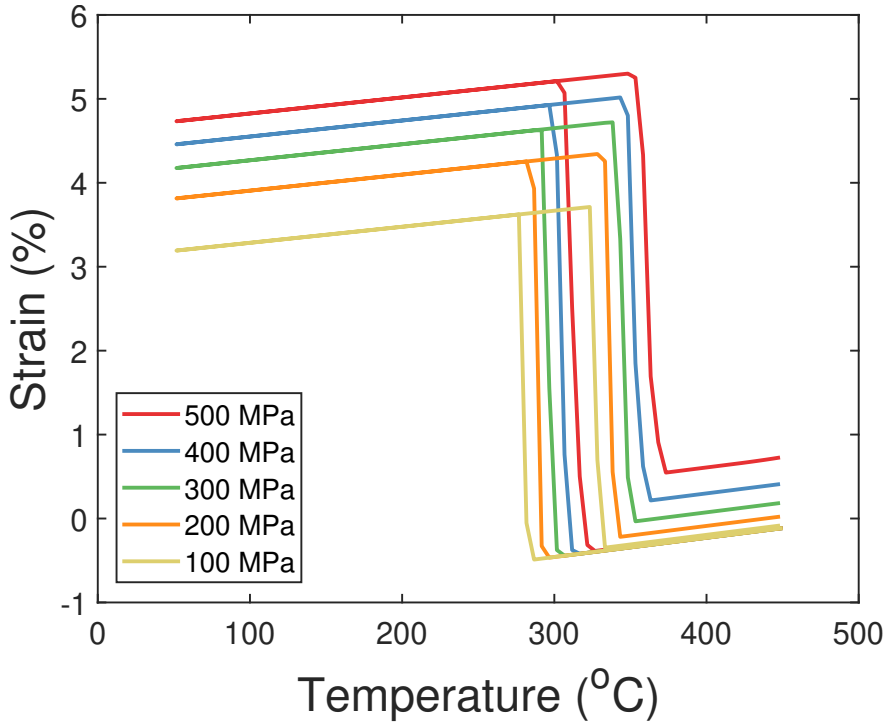

Figure 3.42: Polycrystal (625 grain) responses simulated at increasing stress levels from 100 to 500 MPa for a temperature domain from 50 to 450 °C as experimentally studied in Benafan et al. [6].

4. CONCLUSIONS AND FUTURE DIRECTIONS

The questions raised in Chapter 1 are recalled in this chapter, and an attempt is made to answer them through concluding remarks made from the experimental investigations and crystal-plasticity modeling.

4.1 Experimental investigations

The high temperature behavior of a Ti-rich $Ni_{49.8}Ti_{30.6}Hf_{19.2}$ (at.%) HTSMA was investigated through thermomechanical tests involving isobaric conditions and thermal cycling at different rates. The thermomechanical conditions were chosen to activate transformation and viscoplasticity, in order to observe a coupling between these phenomena. From the results obtained, the following conclusions can be drawn:

1. The entire macroscopic response of the HTSMA, is observed to be rate-dependent. The response changes drastically on increasing the rate from 1 to 10 °C/min, but remains fairly the same in terms of magnitudes and trends from 10 to 50 °C/min. Hence, the thermal cycling rate is an important factor to consider during UCFTC testing and training of these alloys.

2. The thermal cycling rate controls the activation of viscoplasticity and TRIP, which affects phase transformation. Viscoplastic deformation has a major effect at slow rates (of 1 °C/min), but its effects get overshadowed by TRIP at faster rates (i.e., 10 and 50 °C/min). The effect of retained martensite is seen at all three thermal cycling rates.

3. The evolution of transformation temperatures and their slopes at each rate indicated plastic (TRIP) and viscoplastic accommodation of dislocations, which indicate an effect of the two mechanisms on phase transformation. The evolution of hysteresis and transformation strain at each rate indicated a varying accumulation of dislocations and retained phases (with cycling) contributing to an increase in internal stress. The trends and magnitudes of the above

functional properties and quantifiers can act as guide to potential constitutive modeling studies on SMAs and/or HTSMAs, aiming to simulate and predict the degradation of phase transformation behavior.

4. The irrecoverable strains of viscoplasticity and TRIP were observed to evolve faster with the rate of thermal cycling and number of cycles. The TRIP strain was also shown to have a contribution from retained martensite. An attempt was made to quantify the contribution during a UCFTC at 10 °C/min. The contribution obtained was equal to (or less than) 63.4%, and can vary based on the thermomechanical conditions and cycle number. The above facts give insights into underlying mechanisms such as slip and accumulation of phases, which can aid to develop the physics behind potential constitutive modeling.

5. A series of *ex situ* DSC analyses on the tested samples provided an indirect evidence of the presence of retained phases and internal stresses, through the modified transformation peaks. Subsequently, a series of ex situ XRD analyses dissociated the retained phases based on the their peaks and TT. The 1 °C/min and 50 °C/min conditions resulted in accumulating the largest and least amount of martensite respectively, while the 10 °C/min condition resulted in generating the largest amount of internal stresses through dislocations.

6. An alternating isothermal creep/UCFTC test was conducted and its response on comparing to that of an isothermal creep brought forth an effect of phase transformation over viscoplasticity. The effect was identified through the constantly evolving viscoplastic strain rate, due to an increase in internal stresses from the alternating phase transformation and associated irrecoverable mechanisms. The alternating test was also used to observe an effect of viscoplasticity over phase transformation during a fast thermal cycling (10 °C/min). The dominating phenomenon of viscoplasticity affected the functional properties and quantifiers in a manner different from the UCFTC responses.

7. A two-way coupling between phase transformation and viscoplasticity is revealed from the response of UCFTC at slow rates and the alternating test. The coupling is controlled by the

generation and recovery of viscoplastic dislocations and retained phases.

The concluding remarks 1, 2, and 5, answer "Q. 1 *How do the interactions or the coupling between phase transformation and viscoplasticity manifest in any HTSMA during actuation?*", by signifying that the slow rate of 1 °C/min is responsible for manifesting the coupling. Whereas the concluding remarks 3, 6 and 7, are able to answer "Q. 2 *What are the fundamental mechanisms behind the occurrence of the coupling that result in affecting its functionality?*".

4.2 Crystal-plasticity modeling

The experimental responses in Chapter 2 influenced the modeling study by guiding it to account for the relevant phenomena (including the coupling) and calibrating the responses and parameters of the crystal-plasticity model. The entire thermomechanical behavior of a Ni-Ti-Hf HTSMA was simulated by implementing the crystal-plasticity model on single crystals for various random orientations as well as on polycrystals. From the results obtained, the following conclusions can be drawn:

1. The single crystal responses bring forth an effect of their orientation on the entire response, primarily on the TT, maximum strain and irrecoverable strains of TRIP and viscoplasticity. As the orientation changes from [001] $\rightarrow$ [011] $\rightarrow$ [111] the above quantities are observed to increase in magnitude following the same order, except for the viscoplastic strain which follows the order of [011] $<$ [001] $\approx$ [111]. The responses along various random orientations show a symmetry in the values of each of the above quantities with respect to the Euler angles.

2. The TRIP strain magnitude in the responses depends on the activation (and evolution) of dominant martensite variants. Whereas, the viscoplastic strain depends on the Schmid factor and number of activated slip systems, along the chosen crystallographic orientation.

3. The single crystal responses show rate-dependency along all the orientations, which is reflected primarily due to a decrease in viscoplastic strain with the rate of thermal cycling.

However, the [011] orientation shows rate-dependency in the activation of variants due to a preferential activation, which creates a rate-dependent transformation and TRIP strain. This observation was concluded to be an effect of the coupling on the transformation resistance (or driving force).

4. The single crystal behavior over multiple cycles is controlled by the coupling between phase transformation and viscoplasticity, in addition to the factors mentioned earlier. The coupling results in increasing the hysteresis (width), which is reflected as an increase in both the TT (M_s and A_f) with cycling and the transformation strains, are modified based on the orientation.

5. The polycrystal results for a single cycle at a fixed rate bring forth an effect of the number of grains and size of domain, on the entire response. The degree of anisotropy in their response decreases with an increase in number of randomly oriented grains, as the effects of texture fade away.

6. A comparison between the simulated response from 625 grains and the experimental one brings out two inferences: (i) even though detwinning in Ni-Ti-Hf single crystals is observed experimentally and is dependent on the loading direction, (ii) the likely hood of detwinning in Ni-Ti-Hf polycrystals (at stresses of $\approx$ 500 MPa) is very less or limited. Hence, the detwinning phenomena was deactivated for polycrystals, which resulted in simulated responses showing consistency with experimental ones.

7. The rate-dependency in the polycrystal responses for a single cycle show an increase in transformation strain as the rate decreases and is inferred to be due to a preferential (or biased) activation of variants. This trend is consistent with the explanation given for the experimental increase in transformation strain due to internal stresses.

8. Lastly, the polycrystal results over multiple cycles show a trend overall consistent with the experimental responses, with regards to the hysteresis and TT evolution (with cycling), and

strain ratcheting with time.

The crystal-plasticity model was developed on the basis of the constitutive equations pertaining to most of the phenomena observed experimentally. The model answers "Q. 4 *How can the fundamental mechanisms behind the coupled behavior (observed experimentally) be interpreted through a set of constitutive equations at the micro scale?*", by listing the equations behind the mechanisms. Whereas the concluding remarks 1 - 5 are able to answer "Q. 5 *What role can the texture (or microtexture) play in the interpretations and the overall functionality?*", bringing out the effect of texture on the response.

4.3 Present study's applications, limitations and future directions

4.3.1 Applications

The crystal-plasticity model developed in the present study is able to simulate anisotropic and isotropic results for HTSMAs. Therefore, the model can be used to generate responses for textured or un-textured microstructures. For example, the model can be used to predict responses of HTSMAs, which need to be implemented in engineering components, and meet certain functionalities through textured microstructures. To predict the response of the engineering components/structures, the model has to be extended to account for boundary tractions and the geometric stiffness of the structure, which are potential future directions.

The data from random orientations in Fig. 3.9 can be useful for predicting not only the maximum total strain but also the maximum irrecoverable strain that may not be desired in engineering single crystal components, as it can be detrimental to their functionality. The data can be used to understand the hardness/softness of grains with respect to the plasticity/viscoplasticity and TRIP generated by them, that depends on their orientations relative to the loading axis. Once understood, polycrystal configurations of the HTSMA can be rolled in particular directions to orient the grains along the direction of the hard grains. These are some of the applications of the model which address "Q. 3 *Can these mechanisms be predicted (or even controlled) using modeling studies?*".

As mentioned in Section: 3.5.1.2, the data from random orientations can also be used to cali-

brate computationally efficient phenomenological models or train machine learning models using the large number of responses, and thermomechanical conditions, to be able to accurately predict single crystal responses for any orientation. Lastly, the model can also be implemented to predict the responses of precipitated microstructures, wherein a single/multiple precipitate/s are embedded inside a HTSMA matrix. Similar to the polycrystal RVE, the precipitated microstructure can be considered as a single crystal RVE along any random orientation, with the precipitate(s) embedded in it. The application would allow investigating the effect of precipitation and aging on the response of the HTSMA matrix, as done experimentally through aging techniques [57, 151, 61].

Lastly, the macro-micro approach implemented in the present study to account for deformations from various slip systems at the macro scale, can be implemented on other metal alloys which possess multiple slip systems.

4.3.2 Limitations and future directions

Prior to applying the model for the above applications, it is necessary to realize some limitations of the present study while keeping in mind the aim of the study. Recalling the primary aim, which was to interpret the fundamental mechanisms of the coupled behavior (observed experimentally), and simulate the qualitative trends, instead of giving a precise numerical prediction for a particular HTSMA.

- The first and foremost limitation is the small-strain approximation made in the current study, which is not appropriate to simulate/predict the large strains generated by the single-crystal, especially over multiple cycles. A finite deformation formulation is necessary to accurately account for the large strains and rotations, and is hence a strong motive for improving and implementing the model in the future.

- In addition the assumption of deactivating detwinning for polycrystals may not work for single crystals, as they do show a detwinning (experimentally) which is dependent on the loading direction [13]. Implementing a finite deformation formulation may help in dealing with this assumption in the future.

- Formulating a physics based coupling instead of using the present phenomenological coupling, would be more appropriate to accurately account for the underlying mechanisms, such as viscoplastic accommodation. In addition, developing an interaction tensor to account for the interaction between variants during reorientation (as elaborated in Section 3.2.3.2) is an important potential expansion for the future, as justified in Section 3.7.5.

- Meshing of the polycrystal RVEs using tetrahedral elements instead of hexahedral elements, would be a more appropriate meshing technique, especially to mesh the grain boundaries. However, generating periodic boundary conditions for a RVE with tetrahedral elements is a challenge, which the present study was not able to overcome, and is another motive to improve the accuracy of the results in the future.

- Finally, after all the above improvements are made, the calibration of the model will benefit immensely from (potential) experiments conducted on single crystals of the alloy, or relevant data extracted from new literature. As elaborated in Section 3.3.2 the calibration will be a definitive step in improving the model's capabilities.

REFERENCES

[1] G. S. Firstov, J. Van Humbeeck, Y. N. Koval, J.Ma, I.Karaman, and R.D.Noebe, "High-temperature shape memory alloys Some recent developments," *Materials Science and Engineering A*, vol. 378, no. 1-2 SPEC. ISS., pp. 2–10, 2010.

[2] R. F. Hamilton, H. Sehitoglu, Y. Chumlyakov, and H. J. Maier, "Stress dependence of the hysteresis in single crystal NiTi alloys," *Acta Materialia*, vol. 52, no. 11, pp. 3383–3402, 2004.

[3] P. K. Kumar, U. Desai, J. A. Monroe, D. C. Lagoudas, I. Karaman, G. Bigelow, and R. D. Noebe, "Experimental investigation of simultaneous creep, plasticity and transformation of Ti50.5Pd30Ni19.5 high temperature shape memory alloy during cyclic actuation," *Materials Science and Engineering A*, vol. 530, no. 1, pp. 117–127, 2011.

[4] S. M. Saghaian, H. E. Karaca, H. Tobe, A. S. Turabi, S. Saedi, S. E. Saghaian, Y. I. Chumlyakov, and R. D. Noebe, "High strength NiTiHf shape memory alloys with tailorable properties," *Acta Materialia*, vol. 134, no. December, pp. 211–220, 2017.

[5] P. Šittner, P. Sedlák, H. Seiner, P. Sedmák, J. Pilch, R. Delville, L. Heller, and L. Kadeřávek, "On the coupling between martensitic transformation and plasticity in NiTi: Experiments and continuum based modelling," *Progress in Materials Science*, vol. 98, no. February, pp. 249–298, 2018.

[6] O. Benafan, G. S. Bigelow, A. Garg, R. D. Noebe, D. J. Gaydosh, and R. B. Rogers, "Processing and Scalability of NiTiHf High-Temperature Shape Memory Alloys," *Shape Memory and Superelasticity*, vol. 7, no. 1, pp. 109–165, 2021.

[7] P. S. Chaugule, O. Benafan, and J.-B. l. Graverend, "Phase transformation and viscoplasticity coupling in polycrystalline nickel-titanium-hafnium high-temperature shape memory alloys," *Acta Materialia*, vol. 221, p. 117381, 2021.

[8] O. Engler and V. Randle, "Introduction to Texture Analysis," *Introduction to Texture Analysis*, 2009.

[9] P. Thamburaja, H. Pan, and F. S. Chau, "Martensitic reorientation and shape-memory effect in initially textured polycrystalline Ti-Ni sheet," *Acta Materialia*, vol. 53, no. 14, pp. 3821–3831, 2005.

[10] B. Beausir and J.-J. Fundenberger, "ATEX - software (2021-10-28)," 2021.

[11] P. Poubanne and A. De Bussac, "Loi de comportement anisotrope de l'AM1 de 20°C à 1100°C," tech. rep., ENSMA, 1992.

[12] R. Santamarta, R. Arróyave, J. Pons, A. Evirgen, I. Karaman, H. E. Karaca, and R. D. Noebe, "TEM study of structural and microstructural characteristics of a precipitate phase in Ni-rich Ni-Ti-Hf and Ni-Ti-Zr shape memory alloys," *Acta Materialia*, vol. 61, no. 16, pp. 6191–6206, 2013.

[13] H. Sehitoglu, Y. Wu, L. Patriarca, G. Li, A. Ojha, S. Zhang, Y. Chumlyakov, and M. Nishida, "Superelasticity and Shape Memory Behavior of NiTiHf Alloys," *Shape Memory and Superelasticity*, vol. 3, no. 2, pp. 168–187, 2017.

[14] G. Kurdyumov and L. Khandros, "First reports of the thermoelastic behaviour of the martensitic phase of Au-Cd alloys," *Dokl. Akad. Nauk SSSR*, vol. 66, no. 2, pp. 211–214, 1949.

[15] C. Wayman and H. Bhadeshia, "Phase transformations, nondiffusive," in *Physical Metallurgy*, pp. 1031–1075, North-Holland Physics Publishing, New York, 1983.

[16] K. Otsuka and C. Wayman, "Introduction," in *Shape Memory Materials*, ch. 1, pp. 1–26, Cambridge University Press, 1999.

[17] P.K.Kumar, *Influence of inelastic phenomena on the actuation characteristics of high temperature shape memory alloys*. PhD thesis, Texas A&M University, 2009.

[18] J. Mohd Jani, M. Leary, A. Subic, and M. A. Gibson, "A review of shape memory alloy research, applications and opportunities," *Materials and Design*, vol. 56, pp. 1078–1113, 2014.

[19] L. Qian, Q. Sun, and X. Xiao, "Role of phase transition in the unusual microwear behavior of superelastic NiTi shape memory alloy," *Wear*, vol. 260, no. 4-5, pp. 509–522, 2006.

[20] C. Lexcellent, P. Robinet, J. Bernardini, D. L. Beke, and P. Olier, "High temperature creep measurements in equiatomic Ni-Ti shape memory alloy," *Materialwissenschaft und Werkstofftechnik*, vol. 36, no. 10, pp. 509–512, 2005.

[21] G. F. Eggeler, K. Neuking, A. Dlouhy, and E. Kobus, "Creep behavior of NiTi shape memory alloys and the effect of pre-creep on the martensitic phase transformation," 2000.

[22] S. M. Oppenheimer, A. R. Yung, and D. C. Dunand, "Power-law creep in near-equiatomic nickel-titanium alloys," *Scripta Materialia*, vol. 57, no. 5, pp. 377–380, 2007.

[23] G. Kang, Q. Kan, L. Qian, and Y. Liu, "Ratchetting deformation of super-elastic and shape-memory NiTi alloys," *Mechanics of Materials*, vol. 41, no. 2, pp. 139–153, 2009.

[24] T. Ezaz, J. Wang, H. Sehitoglu, and H. J. Maier, "Plastic deformation of NiTi shape memory alloys," *Acta Materialia*, vol. 61, no. 1, pp. 67–78, 2013.

[25] H. Sehitoglu, I. Karaman, R. Anderson, X. Zhang, K. Gall, H. J. Maier, and Y. Chumlyakov, "Compressive response of NiTi single crystals," *Acta Materialia*, vol. 48, no. 13, pp. 3311–3326, 2000.

[26] J. Wang, H. Sehitoglu, and H. J. Maier, "Dislocation slip stress prediction in shape memory alloys," *International Journal of Plasticity*, vol. 54, pp. 247–266, 2014.

[27] D. A. Miller and D. C. Lagoudas, "Thermomechanical characterization of NiTiCu and NiTi SMA actuators: Influence of plastic strains," *Smart Materials and Structures*, vol. 9, no. 5, pp. 640–652, 2000.

[28] D. M. Norfleet, P. M. Sarosi, S. Manchiraju, M. F. Wagner, M. D. Uchic, P. M. Anderson, and M. J. Mills, "Transformation-induced plasticity during pseudoelastic deformation in Ni-Ti microcrystals," *Acta Materialia*, vol. 57, no. 12, pp. 3549–3561, 2009.

[29] P. Šittner, O. Molnárová, L. Kadeřávek, O. Tyc, and L. Heller, "Deformation twinning in martensite affecting functional behavior of NiTi shape memory alloys," *Materialia*, vol. 9, no. October 2019, 2020.

[30] P. Chowdhury and H. Sehitoglu, "A revisit to atomistic rationale for slip in shape memory alloys," *Progress in Materials Science*, vol. 85, pp. 1–42, 2017.

[31] J. Perkins, "Lattice transformations related to unique mechanical effects," *Metallurgical Transactions*, vol. 4, no. 12, pp. 2709–2721, 1973.

[32] J. Perkins and R. O. Sponholz, "STRESS-INDUCED MARTENSITIC TRANSFORMATION CYCLING AND TWO-WAY SHAPE MEMORY TRAINING IN Cu-Zn-Al ALLOYS.," *Metallurgical transactions. A, Physical metallurgy and materials science*, vol. 15 A, no. 2, pp. 313–321, 1984.

[33] K. Gall and H. J. Maier, "Cyclic deformation mechanisms in precipitated NiTi shape memory alloys," *Acta Materialia*, vol. 50, no. 18, pp. 4643–4657, 2002.

[34] M. L. Bowers, X. Chen, M. De Graef, P. M. Anderson, and M. J. Mills, "Characterization and modeling of defects generated in pseudoelastically deformed NiTi microcrystals," *Scripta Materialia*, vol. 78-79, pp. 69–72, 2014.

[35] M. Ahlers, "Martensitic transformation and plastic deformation: A comparison," *Smart Materials and Structures*, vol. 16, no. 1, 2007.

[36] S. Manchiraju and P. M. Anderson, "Coupling between martensitic phase transformations and plasticity: A microstructure-based finite element model," *International Journal of Plasticity*, vol. 26, no. 10, pp. 1508–1526, 2010.

[37] S. Manchiraju, D. Gaydosh, O. Benafan, R. Noebe, R. Vaidyanathan, and P. M. Anderson, "Thermal cycling and isothermal deformation response of polycrystalline NiTi: Simulations vs. experiment," *Acta Materialia*, vol. 59, no. 13, pp. 5238–5249, 2011.

[38] H. M. Paranjape, S. Manchiraju, and P. M. Anderson, "A phase field - Finite element approach to model the interaction between phase transformations and plasticity in shape memory alloys," *International Journal of Plasticity*, vol. 80, pp. 1–18, 2016.

[39] F. Niccoli, C. Garion, C. Maletta, E. Sgambitterra, F. Furgiuele, and P. Chiggiato, "Beam-pipe coupling in particle accelerators by shape memory alloy rings," *Materials and Design*, vol. 114, pp. 603–611, 2017.

[40] K. C. Atli, I. Karaman, R. D. Noebe, G. Bigelow, and D. Gaydosh, "Work production using the two-way shape memory effect in NiTi and a Ni-rich NiTiHf high-temperature shape memory alloy," *Smart Materials and Structures*, vol. 24, no. 12, 2015.

[41] Y. Liu, Z. Xie, J. Van Humbeeck, and L. Delaey, "Some results on the detwinning process in NiTi shape memory alloys," *Scripta Materialia*, vol. 41, no. 12, pp. 1273–1281, 1999.

[42] H. C. Donkersloot and J. H. Van Vucht, "Martensitic transformations in gold-titanium, palladium-titanium and platinum-titanium alloys near the equiatomic composition," *Journal of The Less-Common Metals*, vol. 20, no. 2, pp. 83–91, 1970.

[43] K. H. Eckelmeyer, "The effect of alloying on the shape memory phenomenon in nitinol," *Scripta Metallurgica*, vol. 10, no. 8, pp. 667–672, 1976.

[44] R. Noebe, S. Draper, D. Gaydosh, A. Garg, B. Lerch, N. Penney, G. Bigelow, S. Padula, and J. Brown, "Effect of thermomechanical processing on the microstructure, properties, and work behavior of a Ti50.5Ni29.5Pt20 High-temperature shape memory alloy," *SMST-2006 - Proceedings of the International Conference on Shape Memory and Superelastic Technologies*, pp. 409–426, 2008.

[45] J. Mulder, *Investigation of high temperature shape memory alloys from the Ni-Ti-Zr and Ni-Ti-Hf systems*. PhD thesis, University of Twente, 1995.

[46] H. E. Karaca, E. Acar, H. Tobe, and S. M. Saghaian, "NiTiHf-based shape memory alloys," *Materials Science and Technology (United Kingdom)*, vol. 30, no. 13, pp. 1530–1544, 2014.

[47] D. C. Lagoudas, G. Chatzigeorgiou, D. J. Hartl, and P. K. Kumar, "Coexistence of creep and transformation in high temperature shape memory alloys," *ASME International Mechanical Engineering Congress and Exposition, Proceedings*, vol. 12, no. PART A, pp. 45–51, 2010.

[48] P. K. Kumar and D. C. Lagoudas, "Thermomechanical characterization of a TiPdNi high temperature SMA under tension," *Behavior and Mechanics of Multifunctional and Composite Materials 2007*, vol. 6526, no. April 2007, p. 65262E, 2007.

[49] D. J. Hartl, *Modeling of Shape Memory Alloys Considering Rate-Independent and Rate-Dependent Irrecoverable Strains.* PhD thesis, Texas A&M University, 2009.

[50] P. K. Kumar and D. C. Lagoudas, "Experimental and microstructural characterization of simultaneous creep, plasticity and phase transformation in Ti50 Pd40 Ni10 high-temperature shape memory alloy," *Acta Materialia*, vol. 58, no. 5, pp. 1618–1628, 2010.

[51] O. Karakoc, C. Hayrettin, M. Bass, S. J. Wang, D. Canadinc, J. H. Mabe, D. C. Lagoudas, and I. Karaman, "Effects of upper cycle temperature on the actuation fatigue response of NiTiHf high temperature shape memory alloys," *Acta Materialia*, vol. 138, pp. 185–197, 2017.

[52] S. Padula, S. Qiu, D. Gaydosh, R. Noebe, G. Bigelow, A. Garg, and R. Vaidyanathan, "Effect of upper-cycle temperature on the load-biased, strain-temperature response of NiTi," *Metallurgical and Materials Transactions A: Physical Metallurgy and Materials Science*, vol. 43, no. 12, pp. 4610–4621, 2012.

[53] A. P. Stebner, G. S. Bigelow, J. Yang, D. P. Shukla, S. M. Saghaian, R. Rogers, A. Garg, H. E. Karaca, Y. Chumlyakov, K. Bhattacharya, and R. D. Noebe, "Transformation strains and temperatures of a nickel-titanium-hafnium high temperature shape memory alloy," *Acta Materialia*, vol. 76, pp. 40–53, 2014.

[54] O. Karakoc, C. Hayrettin, D. Canadinc, and I. Karaman, "Role of applied stress level on the actuation fatigue behavior of NiTiHf high temperature shape memory alloys," *Acta Materialia*, vol. 153, pp. 156–168, 2018.

[55] C. Hayrettin, O. Karakoc, I. Karaman, J. H. Mabe, R. Santamarta, and J. Pons, "Two way shape memory effect in NiTiHf high temperature shape memory alloy tubes," *Acta Materialia*, vol. 163, pp. 1–13, 2019.

[56] O. Rios, R. Noebe, T. Biles, A. Garg, A. Palczer, D. Scheiman, H. J. Seifert, and M. Kaufman, "Characterization of ternary NiTiPt high-temperature shape memory alloys," *Smart Structures and Materials 2005: Active Materials: Behavior and Mechanics*, vol. 5761, no. May 2005, p. 376, 2005.

[57] B. Kockar, I. Karaman, J. I. Kim, and Y. Chumlyakov, "A method to enhance cyclic reversibility of NiTiHf high temperature shape memory alloys," *Scripta Materialia*, vol. 54, no. 12, pp. 2203–2208, 2006.

[58] O. Benafan, R. D. Noebe, S. A. Padula, and R. Vaidyanathan, "Microstructural response during isothermal and isobaric loading of a precipitation-strengthened Ni-29.7Ti-20Hf high-temperature shape memory alloy," *Metallurgical and Materials Transactions A: Physical Metallurgy and Materials Science*, vol. 43, no. 12, pp. 4539–4552, 2012.

[59] O. Benafan, "Deformation and phase transformation processes in polycrystalline n," *PhD Dissertation: University of Central Florida*, 2012.

[60] L. Patriarca, H. Sehitoglu, E. Y. Panchenko, and Y. I. Chumlyakov, "High-temperature functional behavior of single crystal Ni51.2Ti23.4Hf25.4 shape memory alloy," *Acta Materialia*, vol. 106, pp. 333–343, 2016.

[61] A. Evirgen, I. Karaman, R. Santamarta, J. Pons, C. Hayrettin, and R. D. Noebe, "Relationship between crystallographic compatibility and thermal hysteresis in Ni-rich NiTiHf and NiTiZr high temperature shape memory alloys," *Acta Materialia*, vol. 121, pp. 374–383, 2016.

[62] O. Karakoc, K. C. Atli, A. Evirgen, J. Pons, R. Santamarta, O. Benafan, R. D. Noebe, and I. Karaman, "Effects of training on the thermomechanical behavior of NiTiHf and NiTiZr high temperature shape memory alloys," *Materials Science and Engineering A*, vol. 794, no. April, p. 139857, 2020.

[63] Karakoc, O., K. C. Atli, O. Benafan, R. D. Noebe, and I. Karaman, "Actuation Fatigue Performance of NiTiZr and Comparison to NiTiHf High Temperature Shape Memory Alloys (in review)," *Material Science & Engineering A*, 2021.

[64] L. Casalena, A. N. Bucsek, D. C. Pagan, G. M. Hommer, G. S. Bigelow, M. Obstalecki, R. D. Noebe, M. J. Mills, and A. P. Stebner, "Structure-Property Relationships of a High Strength Superelastic NiTi–1Hf Alloy," *Advanced Engineering Materials*, vol. 20, no. 9, pp. 1–10, 2018.

[65] O. Benafan, R. D. Noebe, and T. J. Halsmer, "Shape Memory Alloy Rock Splitters (SMARS)— A Non-Explosive Method for Fracturing Planetary Rocklike Materials and Minerals," *Nasa*, vol. 218832, no. July, p. 35, 2015.

[66] D. C. Lagoudas, G. Chatzigeorgiou, and P. K. Kumar, "Modeling and experimental study of simultaneous creep and transformation in polycrystalline high-temperature shape memory alloys," *Journal of Intelligent Material Systems and Structures*, vol. 20, no. 18, pp. 2257–2267, 2009.

[67] D. J. Hartl, G. Chatzigeorgiou, and D. C. Lagoudas, "Three-dimensional modeling and numerical analysis of rate-dependent irrecoverable deformation in shape memory alloys," *International Journal of Plasticity*, vol. 26, no. 10, pp. 1485–1507, 2010.

[68] Y. Chemisky, G. Chatzigeorgiou, P. Kumar, and D. C. Lagoudas, "A constitutive model for cyclic actuation of high-temperature shape memory alloys," *Mechanics of Materials*, vol. 68, pp. 120–136, 2014.

[69] A. H. Sakhaei and P. Thamburaja, "A finite-deformation-based constitutive model for high-temperature shape-memory alloys," *Mechanics of Materials*, vol. 109, pp. 114–134, 2017.

[70] N. Farjam, R. Mehrabi, M. Elahinia, H. Karaca, and R. Mirzaeifar, "Modeling of NiTiHf using finite difference method," in *SPIE*, vol. 1059613, p. 34, 2018.

[71] L. Xu, A. Solomou, T. Baxevanis, and D. Lagoudas, "Finite strain constitutive modeling for shape memory alloys considering transformation-induced plasticity and two-way shape memory effect," *International Journal of Solids and Structures*, vol. 221, no. March, pp. 42–59, 2021.

[72] K. Bhattacharya, *Microstructure of martensite: why it forms and how it gives rise to the shape-memory effect*, vol. 41. 2004.

[73] N. S. Saburi T, "The shape memory effect and related phenomena.," *Solid to solid phase transformations*, p. 1455–1479, 1981.

[74] J. Wang and H. Sehitoglu, "Modelling of martensite slip and twinning in NiTiHf shape memory alloys," *Philosophical Magazine*, vol. 94, no. 20, pp. 2297–2317, 2014.

[75] C. Cisse, W. Zaki, and T. Ben Zineb, "A review of constitutive models and modeling techniques for shape memory alloys," *International Journal of Plasticity*, vol. 76, pp. 244–284, 2016.

[76] P. Thamburaja and L. Anand, "Polycrystalline shape-memory materials: Effect of crystallographic texture," *Journal of the Mechanics and Physics of Solids*, vol. 49, no. 4, pp. 709–737, 2001.

[77] P. Thamburaja, "Constitutive Equations for Superelasticity in Crystalline Shape-Memory Materials," 2002.

[78] L. Anand and M. E. Gurtin, "Thermal effects in the superelasticity of crystalline shape-memory materials," *Journal of the Mechanics and Physics of Solids*, vol. 51, no. 6, pp. 1015–1058, 2003.

[79] E. Patoor, D. C. Lagoudas, P. B. Entchev, L. C. Brinson, and X. Gao, "Shape memory alloys, Part I: General properties and modeling of single crystals," *Mechanics of Materials*, vol. 38, no. 5-6, pp. 391–429, 2006.

[80] X. M. Wang, B. X. Xu, and Z. F. Yue, "Micromechanical modelling of the effect of plastic deformation on the mechanical behaviour in pseudoelastic shape memory alloys," *International Journal of Plasticity*, vol. 24, no. 8, pp. 1307–1332, 2008.

[81] S. Amirhosein, *Modeling of interaction between plasticity and martensitic phase transformations in shape memory alloys*. PhD thesis, National University of Singapore, 2014.

[82] C. Yu, G. Kang, and Q. Kan, "Crystal plasticity based constitutive model of NiTi shape memory alloy considering different mechanisms of inelastic deformation," *International Journal of Plasticity*, vol. 54, pp. 132–162, 2014.

[83] C. Yu, G. Kang, Q. Kan, and X. Xu, "Physical mechanism based crystal plasticity model of NiTi shape memory alloys addressing the thermo-mechanical cyclic degeneration of shape memory effect," *Mechanics of Materials*, vol. 112, pp. 1–17, 2017.

[84] L. Heller, P. Šittner, P. Sedlák, H. Seiner, O. Tyc, L. Kadeřávek, P. Sedmák, and M. Vronka, "Beyond the strain recoverability of martensitic transformation in NiTi," *International Journal of Plasticity*, vol. 116, no. July 2018, pp. 232–264, 2019.

[85] C. Yu, G. Kang, D. Song, and Q. Kan, "Effect of martensite reorientation and reorientation-induced plasticity on multiaxial transformation ratchetting of super-elastic NiTi shape memory alloy: New consideration in constitutive model," *International Journal of Plasticity*, vol. 67, pp. 69–101, 2015.

[86] L. G. Machado and D. C. Lagoudas, *Modeling of SMAs book*, vol. 1. Boston, MA: Springer US, 2008.

[87] L. Hu, S. Jiang, Y. Zhang, X. Zhu, Y. Zhao, and D. Sun, "Influence of slip system combination models on crystal plasticity finite element simulation of NiTi shape memory alloy undergoing uniaxial compression," *Progress in Natural Science: Materials International*, vol. 27, no. 5, pp. 598–605, 2017.

[88] A. W. Richards, R. A. Lebensohn, and K. Bhattacharya, "Interplay of martensitic phase transformation and plastic slip in polycrystals," *Acta Materialia*, vol. 61, no. 12, pp. 4384–4397, 2013.

[89] X. L. Meng, W. Cai, Y. F. Zheng, and L. C. Zhao, "Phase transformation and precipitation in aged Ti-Ni-Hf high-temperature shape memory alloys," *Materials Science and Engineering A*, vol. 438-440, no. SPEC. ISS., pp. 666–670, 2006.

[90] ASTM International, "ASTM 3097:Standard Test Method for Mechanical Uniaxial Constant Force Thermal Cycling of Shape Memory Alloys," tech. rep., 2017.

[91] ASTM E8, "ASTM E8/E8M standard test methods for tension testing of metallic materials 1," Tech. Rep. C, 2010.

[92] D. Jonathan, K. Melcher, and R. Noebe, "Development for active clearance control: Progress on Shape Memory Alloy Actuator Development for Active Clearance," tech. rep., QSS Group, 2006.

[93] M. A. Qidwai, A. Bhattacharyya, I. Vahhi, and S. Pulnev, "Initial investigation in actuator design using high-temperature shape memory alloy," *Smart Structures and Materials 2003: Active Materials: Behavior and Mechanics*, vol. 5053, no. August 2003, p. 81, 2003.

[94] A. N. Bucsek, L. Casalena, D. C. Pagan, P. P. Paul, Y. Chumlyakov, M. J. Mills, and A. P. Stebner, "Three-dimensional in situ characterization of phase transformation induced austenite grain refinement in nickel-titanium," *Scripta Materialia*, vol. 162, pp. 361–366, 2019.

[95] S. V. Raj and R. D. Noebe, "Low temperature creep of hot-extruded near-stoichiometric NiTi shape memory alloy part II: Effect of thermal cycling," *Materials Science and Engineering A*, vol. 581, pp. 145–153, 2013.

[96] ASTM International, "ASTM Standard: F2004-17, Standard Test Method for Transformation Temperature of Nickel-Titanium Alloys by," tech. rep., 2004.

[97] O. Benafan, R. D. Noebe, S. A. Padula, A. Garg, B. Clausen, S. Vogel, and R. Vaidyanathan, "Temperature dependent deformation of the B2 austenite phase of a NiTi shape memory alloy," *International Journal of Plasticity*, vol. 51, pp. 103–121, 2013.

[98] S. Holdsworth, "The European Creep Collaborative Committee (ECCC) approach to creep data assessment," *Journal of Pressure Vessel Technology, Transactions of the ASME*, vol. 130, no. 2, pp. 0240011–0240016, 2008.

[99] A. Mehmanparast, C. M. Davies, G. A. Webster, and K. M. Nikbin, "Creep crack growth rate predictions in 316H steel using stress dependent creep ductility," *Materials at High Temperatures*, vol. 31, no. 1, pp. 84–94, 2014.

[100] J. L. Chaboche, "Continuum Damage Mechanics: Part I - General Concepts.," *Journal of Applied Mechanics, Transactions ASME*, vol. 55, no. 1, pp. 59–64, 1988.

[101] A. Yamanaka, T. Takaki, and Y. Tomita, "Elastoplastic phase-field simulation of self- and plastic accommodations in Cubic $\rightarrow$ tetragonal martensitic transformation," *Materials Science and Engineering A*, vol. 491, no. 1-2, pp. 378–384, 2008.

[102] J. Kundin, D. Raabe, and H. Emmerich, "A phase-field model for incoherent martensitic transformations including plastic accommodation processes in the austenite," *Journal of the Mechanics and Physics of Solids*, vol. 59, no. 10, pp. 2082–2102, 2011.

[103] G. D. Sandrock, A. J. Perkins, and R. F. Hehemann, "The premartensitic instability in near-equiatomic TiNi," *Metallurgical Transactions*, vol. 2, no. 10, pp. 2769–2781, 1971.

[104] Wayman, C.M. and H. Bhadeshia, *Phase Transformations.* Elsevier B.V., fourth, re ed., 1996.

[105] A. Evirgen, I. Karaman, R. Santamarta, J. Pons, and R. D. Noebe, "Microstructural characterization and shape memory characteristics of the Ni50.3Ti34.7Hf15 shape memory alloy," *Acta Materialia*, vol. 83, pp. 48–60, 2015.

[106] P. L. Potapov, A. V. Shelyakov, A. A. Gulyaev, E. L. Svistunova, N. M. Matveeva, and D. Hodgson, "Effect of Hf on the structure of Ni-Ti martensitic alloys," *Materials Letters*, vol. 32, no. 4, pp. 247–250, 1997.

[107] H. Kato, T. Yamamoto, S. Hashimoto, and S. Miura, "High-temperature plasticity of the β-phase in nearly-equiatomic nickel-titanium alloys," *Materials Transactions, JIM*, vol. 40, no. 4, pp. 343–350, 1999.

[108] J. S. Bowles and J. K. Mackenzie, "The crystallography of martensite transformations I," *Acta Metallurgica*, vol. 2, no. 1, pp. 129–137, 1954.

[109] P. Chowdhury and H. Sehitoglu, "Significance of slip propensity determination in shape memory alloys," *Scripta Materialia*, vol. 119, pp. 82–87, 2016.

[110] Y. Q. Wang, Y. F. Zheng, W. Cai, and L. C. Zhao, "Tensile behavior of Ti36Ni49Hf15 high temperature shape memory alloy," *Scripta Materialia*, vol. 40, no. 12, pp. 1327–1331, 1999.

[111] G. S. Bigelow, A. Garg, S. A. Padula, D. J. Gaydosh, and R. D. Noebe, "Load-biased shape-memory and superelastic properties of a precipitation strengthened high-temperature Ni50.3Ti29.7Hf20 alloy," *Scripta Materialia*, vol. 64, no. 8, pp. 725–728, 2011.

[112] O. Benafan, A. Garg, R. D. Noebe, G. S. Bigelow, S. A. Padula, D. J. Gaydosh, N. Schell, J. H. Mabe, and R. Vaidyanathan, "Mechanical and functional behavior of a Ni-rich Ni50.3Ti 29.7Hf20 high temperature shape memory alloy," *Intermetallics*, vol. 50, pp. 94–107, 2014.

[113] E. Patoor, A. Eberhardt, and M. Berveiller, "Micromechanical modeling of SMA behavior," 1994.

[114] X. Gao and L. C. Brinson, "A Simplified Multivariant SMA Model Based on," *Journal of Intelligent Material Systems and Structures*, vol. 13, no. December, pp. 795–808, 2002.

[115] Y. Liu, Z. Xie, J. Van Humbeeck, and L. Delaey, "Asymmetry of stress-strain curves under tension and compression for NiTi shape memory alloys," *Acta Materialia*, vol. 46, no. 12, pp. 4325–4338, 1998.

[116] J. L. Chaboche, "Time-independent constitutive theories for cyclic plasticity," *International Journal of Plasticity*, vol. 2, no. 2, pp. 149–188, 1986.

[117] D. J. Hartl and D. C. Lagoudas, "Constitutive modeling and structural analysis considering simultaneous phase transformation and plastic yield in shape memory alloys," *Smart Materials and Structures*, vol. 18, no. 10, 2009.

[118] J. Ortín and L. Delaey, "Hysteresis in shape-memory alloys," *International Journal of Non-Linear Mechanics*, vol. 37, no. 8, pp. 1275–1281, 2002.

[119] W. C. Johnson and J. K. Lee, "A dislocation model for the plastic relaxation of the transformation strain energy of a misfitting spherical particle," *Acta Metallurgica*, vol. 31, no. 7, pp. 1033–1045, 1983.

[120] N. Siredey, E. Patoor, M. Berveiller, and A. Eberhardt, "Constitutive equations for polycrystalline thermoelastic shape memory alloys. : Part I. Intragranular interactions and behavior of the grain," *International Journal of Solids and Structures*, vol. 36, no. 28, pp. 4289–4315, 1999.

[121] D. C. Lagoudas and P. K. Kumar, "Interaction of creep with the martensitic transformation in TiPdNi High Temp erature Shape Memory Alloys," vol. 06020, pp. 3–6, 2009.

[122] H. Pan, P. Thamburaja, and F. S. Chau, "Multi-axial behavior of shape-memory alloys undergoing martensitic reorientation and detwinning," *International Journal of Plasticity*, vol. 23, no. 4, pp. 711–732, 2007.

[123] P. Thamburaja, "Constitutive equations for martensitic reorientation and detwinning in shape-memory alloys," *Journal of the Mechanics and Physics of Solids*, vol. 53, no. 4, pp. 825–856, 2005.

[124] S. Berbenni, V. Favier, X. Lemoine, and M. Berveiller, "Micromechanical modeling of the elastic-viscoplastic behavior of polycrystalline steels having different microstructures," *Materials Science and Engineering A*, vol. 372, no. 1-2, pp. 128–136, 2004.

[125] C. Yu, G. Kang, Q. Kan, and Y. Zhu, "Rate-dependent cyclic deformation of super-elastic NiTi shape memory alloy: Thermo-mechanical coupled and physical mechanism-based constitutive model," *International Journal of Plasticity*, vol. 72, pp. 60–90, 2015.

[126] M. Tang, L. P. Kubin, and G. R. Canova, "Dislocation mobility and the mechanical response of B.C.C. single crystals: A mesoscopic approach," *Acta Materialia*, vol. 46, no. 9, pp. 3221–3235, 1998.

[127] R. J. Asaro, "Crystal plasticity," *Journal of Applied Mechanics, Transactions ASME*, vol. 50, no. 4, pp. 921–934, 1983.

[128] R. J. Asaro and A. Needleman, "Overview no. 42 Texture development and strain hardening in rate dependent polycrystals," *Acta Metallurgica*, vol. 33, no. 6, pp. 923–953, 1985.

[129] L. Anand and M. Kothari, "A computational procedure for rate-independent crystal plasticity," *Journal of the Mechanics and Physics of Solids*, vol. 44, no. 4, pp. 525–558, 1996.

[130] L. Méric, P. Poubanne, and G. Cailletaud, "Single crystal modeling for structural calculations: Part 1-model presentation," *Journal of Engineering Materials and Technology, Transactions of the ASME*, vol. 113, no. 1, pp. 162–170, 1991.

[131] J. L. Chaboche, "A review of some plasticity and viscoplasticity constitutive theories," *International Journal of Plasticity*, vol. 24, no. 10, pp. 1642–1693, 2008.

[132] A. Miller, "An inelastic constitutive model for monotonic, cyclic, and creep deformation: Part I-equations development and analytical procedures," *Journal of Engineering Materials and Technology, Transactions of the ASME*, vol. 98, no. 2, pp. 97–105, 1976.

[133] P. Delobelle, P. Robinet, and L. Bocher, "Experimental study and phenomenological modelization of ratchet under uniaxial and biaxial loading on an austenitic stainless steel," *International Journal of Plasticity*, vol. 11, no. 4, pp. 295–330, 1995.

[134] J. M. Ball and R. D. James, "Fine phase mixtures as minimizers of energy," *Archive for Rational Mechanics and Analysis*, vol. 100, no. 1, pp. 13–52, 1987.

[135] K. F. Hane, "Martensitic Transformations and Shape-," *Acta Materialia*, vol. 48, pp. 197–222, 2000.

[136] H. E. Karaca, S. M. Saghaian, B. Basaran, G. S. Bigelow, R. D. Noebe, and Y. I. Chumlyakov, "Compressive response of nickel-rich NiTiHf high-temperature shape memory single crystals along the [1 1 1] orientation," *Scripta Materialia*, vol. 65, no. 7, pp. 577–580, 2011.

[137] H. Sehitoglu, Y. Wu, and L. Patriarca, "Shape memory functionality under multi-cycles in NiTiHf," *Scripta Materialia*, vol. 129, pp. 11–15, 2017.

[138] Transvalor/ENSMP, "Z-set user commands," p. 301, 2013.

[139] X. Gao, M. Huang, and L. C. Brinson, "Multivariant micromechanical model for SMAs. Part 1. Crystallographic issues for single crystal model," *International journal of plasticity*, vol. 16, no. 10, pp. 1345–1369, 2000.

[140] R. Quey, P. R. Dawson, and F. Barbe, "Large-scale 3D random polycrystals for the finite element method: Generation, meshing and remeshing," *Computer Methods in Applied Mechanics and Engineering*, vol. 200, no. 17-20, pp. 1729–1745, 2011.

[141] R. Quey and L. Renversade, "Optimal polyhedral description of 3D polycrystals: Method and application to statistical and synchrotron X-ray diffraction data," *Computer Methods in Applied Mechanics and Engineering*, vol. 330, pp. 308–333, 2018.

[142] R. Quey, *Neper reference manual*. No. November, 2019.

[143] M. Humbert, F. Wagner, and C. Esling, "Numbering the Crystallographic variants in phase transformation," *Journal of Applied Crystallography*, vol. 25, no. pt 6, pp. 724–730, 1992.

[144] D. J. Hartl, B. Kiefer, R. Schulte, and A. Menzel, "Computationally-efficient modeling of inelastic single crystal responses via anisotropic yield surfaces: Applications to shape memory alloys," *International Journal of Solids and Structures*, vol. 136-137, pp. 38–59, 2018.

[145] A. Solomou, G. Zhao, S. Boluki, J. K. Joy, X. Qian, I. Karaman, R. Arróyave, and D. C. Lagoudas, "Multi-objective Bayesian materials discovery: Application on the discovery of precipitation strengthened NiTi shape memory alloys through micromechanical modeling," *Materials and Design*, vol. 160, pp. 810–827, 2018.

[146] T. Kanit, S. Forest, I. Galliet, V. Mounoury, and D. Jeulin, "Determination of the size of the representative volume element for random composites: Statistical and numerical approach," *International Journal of Solids and Structures*, vol. 40, no. 13-14, pp. 3647–3679, 2003.

[147] R. Mirzaeifar, R. Desroches, A. Yavari, and K. Gall, "A micromechanical analysis of the coupled thermomechanical superelastic response of textured and untextured polycrystalline NiTi shape memory alloys," *Acta Materialia*, vol. 61, no. 12, pp. 4542–4558, 2013.

[148] O. Benafan, S. A. Padula, R. D. Noebe, T. A. Sisneros, and R. Vaidyanathan, "Role of B19 martensite deformation in stabilizing two-way shape memory behavior in NiTi," *Journal of Applied Physics*, vol. 112, no. 9, pp. 1–11, 2012.

[149] K. Gall and H. Sehitoglu, "Role of texture in tension-compression asymmetry in polycrystalline NiTi," *International journal of plasticity*, vol. 15, no. 1, pp. 69–92, 1999.

[150] H. Lim, J. D. Carroll, J. R. Michael, C. C. Battaile, S. R. Chen, and J. M. D. Lane, "Investigating active slip planes in tantalum under compressive load: Crystal plasticity and slip trace analyses of single crystals," *Acta Materialia*, vol. 185, pp. 1–12, 2020.

[151] H. E. Karaca, S. M. Saghaian, G. Ded, H. Tobe, B. Basaran, H. J. Maier, R. D. Noebe, and Y. I. Chumlyakov, "Effects of nanoprecipitation on the shape memory and material properties of an Ni-rich NiTiHf high temperature shape memory alloy," *Acta Materialia*, vol. 61, no. 19, pp. 7422–7431, 2013.

[152] C. Yu, G. Kang, and Q. Kan, "A physical mechanism based constitutive model for temperature-dependent transformation ratchetting of NiTi shape memory alloy: One-dimensional model," *Mechanics of Materials*, vol. 78, pp. 1–10, 2014.

[153] J. L. Chaboche and G. Rousselier, “On the plastic and viscoplastic constitutive equations-part I: Rules developed with internal variable concept,” *Journal of Pressure Vessel Technology, Transactions of the ASME*, vol. 105, no. 2, pp. 153–158, 1983.

APPENDIX A

THERMODYNAMIC FRAMEWORK

Conservation of Energy

The first law of thermodynamics is based on the conservation of energy, i.e., rate of change of internal energy *u*, due to the rate of work done by surface forces, interpreted as applied stress $\boldsymbol{\sigma}$, the heat energy/flux $\boldsymbol{q}$ entering through the surface, and the heat supply q_s inside the reference volume. Its differential form is:

$$\rho\dot{u} = \boldsymbol{\sigma} : \dot{\boldsymbol{\varepsilon}} - \boldsymbol{\nabla}.\boldsymbol{q} + \rho q_s \tag{A.1}$$

Clausius-Duhem inequality

The Clausius-Duhem inequality or the second law of continuum thermodynamics is based on an entropy inequality. The rate of change of entropy *s* is greater than or equal to the influx of entropy due to the heat flux in the reference configuration, and the entropy increase within the volume due to the heat supply. Its differential form with all terms on one side is:

$$\rho\dot{s} + \frac{\boldsymbol{\nabla}.\boldsymbol{q}}{T} - \frac{1}{T^2}\boldsymbol{q}.\boldsymbol{\nabla}T - \frac{\rho q_s}{T} \geq 0 \tag{A.2}$$

Free energy density

The Helmholtz free energy density ψ (per unit reference volume) is chosen as the thermodynamic potential, as the response of its independent variables such as strain $\boldsymbol{\varepsilon}$, temperature T, and additional internal variables ζ, that can help characterize the material [86]. The free energy density can be defined as:

$$\psi = u - sT \rightarrow \dot{\psi} = \dot{u} - \dot{s}T - s\dot{T} \tag{A.3}$$

The total free energy is broken into its components [79, 9, 83, 69, 152] based on the associated

phenomena :

$$\psi = \underbrace{\psi_{ch}}_{chemical} + \underbrace{\psi_e + \psi_h + \psi_{vp}}_{non-chemical} \tag{A.4}$$

ψ_{ch} is the chemical free energy which is further broken down into a transformation ψ_{tr} and thermal ψ_{th} free energy. As mentioned in Section 3.2.3.2, the ψ_{tr} is generated due to the lattice energy difference between the austenite and martensite phases during transformation. The energy difference generates a latent heat of transformation λ_0 which is implemented using the parameter β where $\lambda_0 = \beta T_0$ in the first term of Eq. A.5. The term also includes T which is the test temperature, and T_0 which is the phase equilibrium temperature based on the TTs; $T_0 = \frac{1}{2}\{\frac{(M_s+M_f)}{2} + \frac{(A_s+A_f)}{2}\}$. The second term in Eq. A.5 represents the ψ_{th} that is derived using the change in temperature and heat capacity c_v.

$$\psi_{ch} = \psi_{tr} + \psi_{th} = \beta(T - T_0)\sum_{\alpha=1}^{N_v} \xi^\alpha + c_v \left[(T - T_0) - T.ln\left(\frac{T}{T_0}\right)\right] \tag{A.5}$$

ψ_e is the elastic free energy defined as:

$$\psi_e = \frac{1}{2}\boldsymbol{\varepsilon_e} : \mathbb{C} : \boldsymbol{\varepsilon_e} \tag{A.6}$$

The transformation hardening free energy ψ_h is associated with the hardening generated by plastic slip during transformation (TRIP). It is derived using the resistance τ_p and slip γ_{tr}^α on the habit-planes while forming the variant α.

$$\psi_h = \sum_{\alpha=1}^{N_v} \tau_p |\gamma_{tr}^\alpha| \tag{A.7}$$

Lastly, ψ_{vp} is the viscoplastic free energy [130] associated with the hardenings generated during viscoplastic slip γ^s in the slip systems. The hardenings considered are: kinematic x^s and isotropic r^s.

$$\psi_{vp} = \sum_{s=1}^{N_s} (x^s + r^s)|\gamma_{vp}^s| \tag{A.8}$$

Dissipation

On rearranging the terms of the First law (Eq. A.1) and Second law (Eq. A.2), expressions for $\dot{u}$ and $\dot{s}$ are obtained which can be plugged into the free energy (Eq. A.3) to get the dissipation Γ inequality for a phase transformation process:

$$\Gamma = \boldsymbol{\sigma} : \dot{\boldsymbol{\varepsilon}} - \dot{\psi} - s\dot{T} - \frac{\boldsymbol{q}.\boldsymbol{\nabla} T}{T} \geq 0 \tag{A.9}$$

Based on the independent variables (T, $\boldsymbol{\varepsilon}$) and internal variables (ξ, γ) on which ψ depends, the dissipation inequality can be rewritten as:

$$\begin{aligned} \Gamma &= \boldsymbol{\sigma} : \dot{\boldsymbol{\varepsilon}} - \dot{\psi}(\boldsymbol{\varepsilon}, T, \xi, \gamma) - s\dot{T} - \frac{\boldsymbol{q}.\boldsymbol{\nabla} T}{T} \geq 0 \\ &= \boldsymbol{\sigma} : \dot{\boldsymbol{\varepsilon}} - \left(\frac{\partial \psi}{\partial \boldsymbol{\varepsilon}} : \dot{\boldsymbol{\varepsilon}} + \frac{\partial \psi}{\partial T}\dot{T} + \frac{\partial \psi}{\partial \xi}\dot{\xi} + \frac{\partial \psi}{\partial \gamma}\dot{\gamma} \right) - s\dot{T} - \frac{\boldsymbol{q}.\boldsymbol{\nabla} T}{T} \geq 0 \end{aligned} \tag{A.10}$$

Substituting the rate form of Eq. 3.1:

$$\dot{\boldsymbol{\varepsilon}} = \dot{\boldsymbol{\varepsilon}}_{th} + \dot{\boldsymbol{\varepsilon}}_{e} + \dot{\boldsymbol{\varepsilon}}_{tr} + \dot{\boldsymbol{\varepsilon}}_{de} + \dot{\boldsymbol{\varepsilon}}_{TRIP} + \dot{\boldsymbol{\varepsilon}}_{vp} \tag{A.11}$$

into the free energy terms (Eq. A.6-A.8), the dissipation inequality (Eq. A.10) can be written as:

$$\begin{aligned} \Gamma &= \boldsymbol{\sigma} : \dot{\boldsymbol{\varepsilon}} - \dot{\psi} - s\dot{T} - \frac{\boldsymbol{q}.\boldsymbol{\nabla} T}{T} \geq 0 \\ &= \boldsymbol{\sigma} : \left(\dot{\boldsymbol{\varepsilon}}_{th} + \dot{\boldsymbol{\varepsilon}}_{e} + \dot{\boldsymbol{\varepsilon}}_{tr} + \dot{\boldsymbol{\varepsilon}}_{de} + \dot{\boldsymbol{\varepsilon}}_{TRIP} + \dot{\boldsymbol{\varepsilon}}_{vp}\right) - \left(\dot{\psi}_{e} + \dot{\psi}_{ch} + \dot{\psi}_{h} + \dot{\psi}_{vp}\right) - s\dot{T} - \frac{\boldsymbol{q}.\boldsymbol{\nabla} T}{T} \geq 0 \\ &= \boldsymbol{\sigma} : \left(\dot{\boldsymbol{\varepsilon}}_{th} + \dot{\boldsymbol{\varepsilon}}_{e} + \dot{\boldsymbol{\varepsilon}}_{tr} + \dot{\boldsymbol{\varepsilon}}_{de} + \dot{\boldsymbol{\varepsilon}}_{TRIP} + \dot{\boldsymbol{\varepsilon}}_{vp}\right) - \left(\left(\frac{\partial \psi_e}{\partial \boldsymbol{\varepsilon}_e} : \dot{\boldsymbol{\varepsilon}}_e + \frac{\partial \psi_e}{\partial \xi}\dot{\xi} + \frac{\partial \psi_e}{\partial T}\dot{T} \right) \right. \\ &\left. + \left(\frac{\partial \psi_{ch}}{\partial \xi}\dot{\xi} + \frac{\partial \psi_{ch}}{\partial T}\dot{T} \right) + \left(\frac{\partial \psi_h}{\partial \gamma}\dot{\gamma} \right) + \left(\frac{\partial \psi_{vp}}{\partial \gamma}\dot{\gamma} \right) \right) - s\dot{T} - \frac{\boldsymbol{q}.\boldsymbol{\nabla} T}{T} \geq 0 \end{aligned} \tag{A.12}$$

Substituting for the total martensitic volume fraction over all the variants and splitting the slip

rate $\dot{\gamma}$ into the contribution from TRIP $\dot{\gamma}^{\alpha}_{tr}$ and viscoplasticity $\dot{\gamma}^{s}_{vp}$.

$$= \boldsymbol{\sigma} : \left(\dot{\boldsymbol{\varepsilon}}_{th} + \dot{\boldsymbol{\varepsilon}}_{e} + \dot{\boldsymbol{\varepsilon}}_{tr} + \dot{\boldsymbol{\varepsilon}}_{de} + \dot{\boldsymbol{\varepsilon}}_{TRIP} + \dot{\boldsymbol{\varepsilon}}_{vp}\right) - \left(\left(\frac{\partial \psi_e}{\partial \boldsymbol{\varepsilon}_e} : \dot{\boldsymbol{\varepsilon}}_e + \frac{\partial \psi_e}{\partial \xi^{\alpha}} \sum_{\alpha=1}^{N_v} \dot{\xi}^{\alpha} + \frac{\partial \psi_e}{\partial T} \dot{T} \right) \right.$$
$$\left. + \left(\frac{\partial \psi_{ch}}{\partial \xi^{\alpha}} \sum_{\alpha=1}^{N_v} \dot{\xi}^{\alpha} + \frac{\partial \psi_{ch}}{\partial T} \dot{T} \right) + \left(\frac{\partial \psi_h}{\partial \gamma^{\alpha}_{tr}} \sum_{\alpha=1}^{N_v} \dot{\gamma}^{\alpha}_{tr} \right) + \left(\frac{\partial \psi_{vp}}{\partial \gamma^{s}_{vp}} \sum_{s=1}^{N_s} \dot{\gamma}^{s}_{vp} \right) \right) - s\dot{T} - \frac{\boldsymbol{q}.\boldsymbol{\nabla} T}{T} \geq 0 \tag{A.13}$$

Gathering the terms with common independent and internal variables.

$$= \left(\boldsymbol{\sigma} - \frac{\partial \psi_e}{\partial \boldsymbol{\varepsilon}_e} \right) : \dot{\boldsymbol{\varepsilon}}_e - \left(\alpha(\boldsymbol{\sigma} : \mathbf{I}) + s + \frac{\partial \psi_e}{\partial T} + \frac{\partial \psi_{ch}}{\partial T} \right) \dot{T} + \boldsymbol{\sigma} : \dot{\boldsymbol{\varepsilon}}_{de} + \boldsymbol{\sigma} : \dot{\boldsymbol{\varepsilon}}_{TRIP} + \boldsymbol{\sigma} : \dot{\boldsymbol{\varepsilon}}_{vp}$$
$$- \left(\frac{\partial \psi_e}{\partial \xi^{\alpha}} + \frac{\partial \psi_{ch}}{\partial \xi^{\alpha}} \right) \sum_{\alpha=1}^{N_v} \dot{\xi}^{\alpha} - \left(\frac{\partial \psi_h}{\partial \gamma^{\alpha}_{tr}} \sum_{\alpha=1}^{N_v} \dot{\gamma}^{\alpha}_{tr} \right) - \left(\frac{\partial \psi_{vp}}{\partial \gamma^{s}_{vp}} \sum_{s=1}^{N_s} \dot{\gamma}^{s}_{vp} \right) - \frac{\boldsymbol{q}.\boldsymbol{\nabla} T}{T} \geq 0 \tag{A.14}$$

Substituting for the strain terms from Eqs. (3.4 - 3.7)

$$= \left(\boldsymbol{\sigma} - \frac{\partial \psi_e}{\partial \boldsymbol{\varepsilon}_e} \right) : \dot{\boldsymbol{\varepsilon}}_e - \left(\alpha(\boldsymbol{\sigma} : \mathbf{I}) + s + \frac{\partial \psi_e}{\partial T} + \frac{\partial \psi_{ch}}{\partial T} \right) \dot{T} + \boldsymbol{\sigma} : \sum_{\alpha=1}^{N_v} \dot{\xi}^{\alpha} g^{tr} \mathbf{P}^{\alpha}_{tr}$$
$$+ \boldsymbol{\sigma} : \sum_{\alpha=1}^{N_v} \left(\dot{\xi}^{\alpha} (\lambda^{\alpha} - \lambda^{\alpha}_0) + \xi^{\alpha} \dot{\lambda^{\alpha}} \right) \mathbf{P}^{\alpha}_{de} + \boldsymbol{\sigma} : \sum_{\alpha=1}^{N_v} \dot{\gamma}^{\alpha}_{tr} \mathbf{P}^{\alpha}_{tr} + \boldsymbol{\sigma} : \sum_{s=1}^{N_s} \dot{\gamma}^{s}_{vp} \mathbf{T}^{s} \tag{A.15}$$
$$- \left(\frac{\partial \psi_e}{\partial \xi^{\alpha}} + \frac{\partial \psi_{ch}}{\partial \xi^{\alpha}} \right) \sum_{\alpha=1}^{N_v} \dot{\xi}^{\alpha} - \left(\frac{\partial \psi_h}{\partial \gamma^{\alpha}_{tr}} \sum_{\alpha=1}^{N_v} \dot{\gamma}^{\alpha}_{tr} \right) - \left(\frac{\partial \psi_{vp}}{\partial \gamma^{s}_{vp}} \sum_{s=1}^{N_s} \dot{\gamma}^{s}_{vp} \right) - \frac{\boldsymbol{q}.\boldsymbol{\nabla} T}{T} \geq 0$$

Once again gathering the terms with common independent and internal variables.

$$
\begin{aligned}
&= \left(\boldsymbol{\sigma} - \frac{\partial \psi_e}{\partial \boldsymbol{\varepsilon}_e}\right) : \dot{\boldsymbol{\varepsilon}}_e - \left(\alpha(\boldsymbol{\sigma} : \mathbf{I}) + s + \frac{\partial \psi_e}{\partial T} + \frac{\partial \psi_{ch}}{\partial T}\right) \dot{T} \\
&+ \sum_{\alpha=1}^{N_v} \left(g^{tr} \boldsymbol{\sigma} : \mathbf{P}_{tr}^{\alpha} + \boldsymbol{\sigma} : (\lambda^{\alpha} - \lambda_0^{\alpha}) \mathbf{P}_{de}^{\alpha} - \frac{\partial \psi_e}{\partial \xi^{\alpha}} - \frac{\partial \psi_{ch}}{\partial \xi^{\alpha}}\right) \dot{\xi^{\alpha}} \\
&+ \sum_{\alpha=1}^{N_v} (\boldsymbol{\sigma} : \xi^{\alpha} \mathbf{P}_{de}^{\alpha}) \dot{\lambda^{\alpha}} \\
&+ \sum_{\alpha=1}^{N_v} \left((\boldsymbol{\sigma} : \mathbf{P}_{tr}^{\alpha}) - \frac{\partial \psi_h}{\partial \gamma_{tr}^{\alpha}}\right) \dot{\gamma}_{tr}^{\alpha} \\
&+ \sum_{s=1}^{N_s} \left((\boldsymbol{\sigma} : \mathbf{T}^{s}) - \frac{\partial \psi_{vp}}{\partial \gamma_{vp}^{s}}\right) \dot{\gamma}_{vp}^{s} - \frac{\boldsymbol{q}.\boldsymbol{\nabla} T}{T} \geq 0
\end{aligned}
\tag{A.16}
$$

Substituting for the free energy terms from Eq. A.4:

$$
\begin{aligned}
&= \left(\boldsymbol{\sigma} - \frac{\partial \psi_e}{\partial \boldsymbol{\varepsilon}_e}\right) : \dot{\boldsymbol{\varepsilon}}_e - \left(\alpha(\boldsymbol{\sigma} : \mathbf{I}) + s + \frac{\partial \psi_e}{\partial T} + \frac{\partial \psi_{ch}}{\partial T}\right) \dot{T} - \frac{\boldsymbol{q}.\boldsymbol{\nabla} T}{T} \\
&+ \sum_{\alpha=1}^{N_v} \left(g^{tr} \left(\boldsymbol{\sigma} : \mathbf{P}_{tr}^{\alpha}\right) - \beta \left(T - T_0\right) + (\lambda^{\alpha} - \lambda_0^{\alpha}) (\boldsymbol{\sigma} : \mathbf{P}_{de}^{\alpha}) - \frac{1}{2} \boldsymbol{\varepsilon}_e : \Delta \mathbb{C} : \boldsymbol{\varepsilon}_e\right) \dot{\xi^{\alpha}} \\
&+ \sum_{\alpha=1}^{N_v} \xi^{\alpha} (\boldsymbol{\sigma} : \mathbf{P}_{de}^{\alpha}) \dot{\lambda^{\alpha}} \\
&+ \sum_{\alpha=1}^{N_v} \left((\boldsymbol{\sigma} : \mathbf{P}_{tr}^{\alpha}) - \tau_p\right) \dot{\gamma}_{tr}^{\alpha} \\
&+ \sum_{s=1}^{N_s} \left((\boldsymbol{\sigma} : \mathbf{T}^{s}) - x^{s} - r^{s}\right) \dot{\gamma}_{vp}^{s} \geq 0
\end{aligned}
\tag{A.17}
$$

Since there is no dissipation during an elastic deformation and the contribution to dissipation from the elastic and entropy terms is zero, which leads to each of them being zero:

$$
\left(\boldsymbol{\sigma} - \frac{\partial \psi_e}{\partial \boldsymbol{\varepsilon}^e}\right) = 0 \;\; and \;\; \left(\alpha(\boldsymbol{\sigma} : \mathbf{I}) + s + \frac{\partial \psi_e}{\partial T} + \frac{\partial \psi_{ch}}{\partial T}\right) = 0
$$

Whereas the dissipation term due the heat flux using Fourier's law, is always positive and can

be taken out as a known quantity from the Eq. (A.17):

$$-\frac{1}{T}\boldsymbol{q}.\boldsymbol{\nabla}T = -\frac{1}{T}(-k\boldsymbol{\nabla}T).\boldsymbol{\nabla}T = \frac{1}{T}(k\boldsymbol{\nabla}T).\boldsymbol{\nabla}T \geq 0 \tag{A.18}$$

Thermodynamic driving forces

Each dissipation term in Eq. A.17 can be written as a product of thermodynamic force and its conjugate variable, which evolves due to the force. The thermodynamic forces driving the transformation, detwinning, slip due to TRIP and viscoplasticity and their conjugate variables are as follows:

$$\begin{aligned}
\Phi^{\alpha}_{tr} &= g^{tr}(\boldsymbol{\sigma} : \mathbf{P}^{\alpha}_{tr}) + \underbrace{(\lambda^{\alpha} - \lambda^{\alpha}_{0})}_{g^{det}}(\boldsymbol{\sigma} : \mathbf{P}^{\alpha}_{de}) - \beta\,(T - T_0) - \frac{1}{2}\boldsymbol{\varepsilon_e} : \Delta\mathbb{C} : \boldsymbol{\varepsilon_e} \quad \text{and} \quad \dot{\xi}^{\alpha} \\
\Phi^{\alpha}_{de} &= \xi^{\alpha}(\boldsymbol{\sigma} : \mathbf{P}^{\alpha}_{de}) \quad \text{and} \quad \dot{\lambda}^{\alpha} \\
\Phi^{\alpha}_{TRIP} &= (\boldsymbol{\sigma} : \mathbf{P}^{\alpha}_{tr}) - \tau_p \quad \text{and} \quad \dot{\gamma}^{\alpha}_{tr} \\
\Phi^{s}_{vp} &= (\boldsymbol{\sigma} : \mathbf{T}^{s}) - x^{s} - r^{s} \quad \text{and} \quad \dot{\gamma}^{s}_{vp}
\end{aligned} \tag{A.19}$$

The stress tensor $\boldsymbol{\sigma}$ in all the above forces is the microscopic resolved stress $\boldsymbol{\sigma_g}$ in each grain, defined in Section 3.2.3.5.

APPENDIX B

MACRO-MICRO APPROACH

The constitutive equations for plasticity/viscoplasticity defined at the macroscale [131, 153] and microscale [130] can be related by following the macro-micro approach developed in the article by Poubanne and De Bussac [11]. The approach involves comparing the macro and micro scale equations and variables to determine (or tailor) scaling coefficients between the macro and microscale parameters, based on the family of slip system considered. Each considered family of slip system is further dependent on the crystal-lattice known through atomistic studies. In other words, the macro-micro approach forms a bridge between the nano, micro and macro scale, which offers a *unique multi-scale advantage*. The macro-micro approach also offers a secondary advantage: In case of a lack of experimental data on single crystals, the data from polycrystals, i.e., macroscale deformations can be used to calibrate microscale (or single crystal) deformations by following the macro-micro approach.

Determining the scaling coefficients involves, evaluating the Schmid factor (m), using a slip plane normal $\mathbf{n}^s$, slip direction $\mathbf{l}^s$, and a crystallographic direction (of a grain), which can be either [001], [011] or [111]. The crystallographic direction giving the largest Schmid factor (m) is selected, and the number of slip systems that are activated along that direction are counted, to give the total number of slip systems (N_s) active for that particular family. The evaluated *m* and N_s are then implemented into the relationships between the macro and micro scales denoted by the superscripts *M* and *s*, respectively. *Note:* These two relationships represent scalar forms of the stress and strain tensors.

1. Stress relationship

$$\sigma_g^M = \left(\frac{1}{m}\right)\tau^s \tag{B.1}$$

2. Strain relationship

$$\varepsilon_{vp}^{M} = (N_s.m)\gamma_{vp}^{s} \tag{B.2}$$

Next, the following constitutive equations at the macro and micro scales are compared to obtain the relations between the coefficients:

3. Plastic/viscoplastic strain law at:

$$\begin{aligned} Macroscale \ : \ \dot{\boldsymbol{\varepsilon}}_{vp}^{M} &= C_{visco}^{M} sinh \left\langle \frac{||\boldsymbol{\sigma}^{M} - \boldsymbol{X}^{M}|| - \boldsymbol{R}^{M}}{K^{M}} \right\rangle^{n^{M}} \\ Microscale \ : \ \dot{\gamma^{s}} &= C_{visco}^{s} sinh \left\langle \frac{|\tau^{s} - x^{s}| - r^{s}}{K^{s}} \right\rangle^{n^{s}} \end{aligned} \tag{B.3}$$

4. Yield curve (including isotropic hardening) at:

$$\begin{aligned} Macroscale \ : \ \boldsymbol{R}^{M} &= \boldsymbol{R}_{0}^{M} + Q_{1}^{M}\boldsymbol{\varepsilon}_{vp}^{M} + Q^{M}\sum_{i}\sum_{j} h_{ij}(1 - e^{-b^{M}\boldsymbol{\varepsilon}_{vp}^{M}}) \\ Microscale \ : \ r^{s} &= r_{0}^{s} + Q_{1}^{s}\gamma^{s} + Q^{s}\sum_{i}\sum_{j} h_{ij}(1 - e^{-b^{s}\gamma^{s}}) \end{aligned} \tag{B.4}$$

5. Kinematic hardening at:

$$\begin{aligned} Macroscale \ : \ \boldsymbol{X}^{M} &= \frac{C^{M}}{D^{M}}\left(1 - e^{-D^{M}\boldsymbol{\varepsilon}_{vp}^{M}}\right) \\ Microscale \ : \ x^{s} &= \frac{C^{s}}{D^{s}}\left(1 - e^{-D^{s}\gamma^{s}}\right) \end{aligned} \tag{B.5}$$

On substituting Eq. (B.4) and Eq. (B.5) into Eq. (B.3), they are rewritten at the macro and micro scales:

$$\dot{\boldsymbol{\varepsilon}}_{vp}^{M} = C_{visco}^{M} sinh \left[\frac{\left\langle ||\boldsymbol{\sigma}^{M} - \frac{C^{M}}{D^{M}} \left(1 - e^{-D^{M}\boldsymbol{\varepsilon}_{vp}^{M}}\right)|| - \boldsymbol{R}_{0}^{M} + Q_{1}^{M}\boldsymbol{\varepsilon}_{vp}^{M} + Q^{M} \sum\sum h_{ij}(1 - e^{-b^{M}\boldsymbol{\varepsilon}_{vp}^{M}}) \right\rangle}{K^{M}} \right]^{n^{M}}$$

$$\dot{\gamma}^{s} = C_{visco}^{s} sinh \left[\frac{\left\langle \left| \tau^{s} - \frac{C^{s}}{D^{s}} \left(1 - e^{-D^{s}\gamma^{s}}\right) \right| - r_{0}^{s} + Q_{1}^{s}\gamma^{s} + Q^{s} \sum\sum h_{ij}(1 - e^{-b^{s}\gamma^{s}}) \right\rangle}{K^{s}} \right]^{n^{s}} \tag{B.6}$$

To derive the relations between the coefficients for each phase and family of slip system, Eq. (B.1) & (B.2) are recalled with the values of m and N_s depending on the family, and implemented. In case of martensite:

1. For the $\{001\}\langle 010\rangle$ family, $m = \frac{1}{3}$ and $N_s = 6$:

$$\sigma^{M} = (3)\,\tau^{s}$$

$$\varepsilon_{vp}^{M} = (2)\,\gamma_{vp}^{s}$$

Implementing the above relations into Eq. (B.6) at the microscale:

$$2\dot{\gamma^s} = C^s_{visco} sinh \left[\frac{\left\langle \left| 3\tau^s - \frac{C^s}{D^s}\left(1 - e^{-D^s 2\gamma^s}\right) \right| - r^s_0 + Q^s_1 2\gamma^s + Q^s \sum\sum h_{ij}(1 - e^{-b^s 2\gamma^s}) \right\rangle}{K^s} \right]^{n^s}$$

Rearranging the coefficients:

$$\dot{\gamma^s} = \frac{1}{2} C^s_{visco} sinh \left[\frac{\left\langle \left| \tau^s - \frac{2C^s/3}{2D^s}\left(1 - e^{-2D^s\gamma^s}\right) \right| - \frac{r^s_0}{3} + \frac{2}{3}Q^s_1\gamma^s + \frac{Q^s}{3}\sum\sum h_{ij}(1 - e^{-2b^s\gamma^s}) \right\rangle}{\frac{K^s}{3}} \right]^{n^s}$$

Comparing the above equation with the macroscale equation (Eq. B.6), the scaling coefficients for the family are obtained as shown by the first column in Table 3.1.

In case of austenite:

1. For the $\{110\}\langle\bar{1}11\rangle$ family, $m = \frac{1}{\sqrt{6}}$ and $N_s = 8$:

$$\sigma^M = \left(\sqrt{6}\right)\tau^s$$
$$\varepsilon^M_{vp} = \left(\frac{8}{\sqrt{6}}\right)\gamma^s_{vp}$$

Implementing the above relations into Eq. (B.6) at the microscale:

$$\frac{\dot{\gamma}^s}{\frac{\sqrt{6}}{8}} = C^s_{visco} sinh \left[\frac{\left\langle \left| \sqrt{6}\tau^s - \frac{C^s}{D^s}\left(1 - e^{-D^s\left(\frac{8}{\sqrt{6}}\right)\gamma^s}\right) \right| - r^s_0 + Q^s_1\left(\frac{8}{\sqrt{6}}\right)\gamma^s + Q^s \sum\sum h_{ij}\left(1 - e^{-\left(\frac{8}{\sqrt{6}}\right)b^s\gamma^s}\right) \right\rangle}{K^s} \right]^{n^s}$$

Rearranging the numbers and coefficients:

$$\dot{\gamma}^s = \frac{\sqrt{6}}{8} C^s_{visco} sinh \left[\frac{\left\langle \left| \tau^s - \frac{4/3}{8/\sqrt{6}}\frac{C^s}{D^s}\left(1 - e^{-8D^s\gamma^s/\sqrt{6}}\right) \right| - \frac{r^s_0}{\sqrt{6}} + \frac{4}{3}Q^s_1\gamma^s + \frac{Q^s}{\sqrt{6}} \sum\sum h_{ij}\left(1 - e^{-\left(\frac{8}{\sqrt{6}}\right)b^s\gamma^s}\right) \right\rangle}{\frac{K^s}{\sqrt{6}}} \right]^{n^s}$$

Comparing the above equation with the macroscale equation (Eq. B.6), the scaling coefficients are obtained as shown by the second column in Table 3.1.

2. For the $\{110\}\langle 001\rangle$ family, $m = \dfrac{\sqrt{2}}{3}$ and $N_s = 3$:

$$\sigma^M = \left(\frac{3}{\sqrt{2}}\right)\tau^s$$
$$\varepsilon^M_{vp} = \sqrt{2}\gamma^s_{vp}$$

Implementing the above relations into Eq. (B.6) and on rearranging it the final equation derived is:

$$\dot{\gamma}^s = \frac{1}{\sqrt{2}} C^s_{visco} sinh \left[\frac{\left\langle \left| \tau^s - \frac{2/3}{\sqrt{2}} \frac{C^s}{D^s} \left(1 - e^{-\sqrt{2} D^s \gamma^s} \right) \right| - \frac{\sqrt{2}}{3} r^s_0 + \frac{2}{3} Q^s_1 \gamma^s + \frac{\sqrt{2}}{3} Q^s \sum \sum h_{ij} \left(1 - e^{-\sqrt{2} b^s \gamma^s} \right) \right\rangle}{\frac{\sqrt{2}}{3} K^s} \right]^{n^s}$$

APPENDIX C

CODE ALGORITHM

Data: Material parameters, crystallographic orientation, transformation systems, detwinning systems, slip systems

Initialize $\xi, \dot{\xi}^{\alpha}_{re}, \dot{\xi}^{\alpha}_{irr}, \dot{\lambda}^{\alpha}, \dot{\gamma}^{\alpha}_{tr}$
Initialize $\boldsymbol{\epsilon}_{tr}, \boldsymbol{\epsilon}_{TRIP}, \boldsymbol{\epsilon}_{de}$
Define M_s, M_f, A_s, A_f
for α = *1 to* N_v **do**
    Define $Y^{\alpha}_1, Y^{\alpha}_2, T_0$
    if $\Delta T < 0$ **then** `/* Forward transformation */`
        Define $\Phi^{\alpha}_{tr}, \Phi^{\alpha}_{TRIP}, \Phi^{\alpha}_{de}$
        if $\Phi^{\alpha}_{tr} \geq 0$ **then**
            Check If $(\xi > 1)$
            if $\xi < 1$ **then**
                if $\xi^{\alpha}_{re} < 1$ **then**
                    Define $\dot{\xi}^{\alpha}_{re}, \boldsymbol{\epsilon}^{\alpha}_{tr}$
                    if $\Phi^{\alpha}_{TRIP} > 0$ **then** `/* TRIP */`
                        Define $\dot{\gamma}^{\alpha}_{tr}, \boldsymbol{\epsilon}^{\alpha}_{TRIP}, \rho_{TRIP}$
                    end
                    Define $\dot{\xi}^{\alpha}_{irr}$ `/* Retained martensite */`
                    if $\Phi^{\alpha}_{de} > 0$ **then** `/* Detwinning */`
                        Define $\dot{\lambda}^{\alpha}$ **if** $\lambda^{\alpha} > 0.5$ **then**
                            Define $\boldsymbol{\epsilon}^{\alpha}_{de}$
                        end
                    end
                end
            end
        end
    Continued on next page
end

Algorithm 1: Presents the steps accounting for the phenomena of transformation, TRIP and detwinning.

```
Continued from previous page
for α = 1 to N_v do
    else if ΔT > 0 then                                  /* Reverse transformation */
        Define Φ^α_tr, Φ^α_TRIP, Φ^α_de
        if Φ^α_tr ≤ 0 then
            Check If (ξ < 0)
            if ξ > 0 then
                if ξ^α_re > 0 then
                    Define ξ̇^α_re, ε^α_tr
                    if Φ^α_TRIP > 0 then                                  /* TRIP */
                        Define γ̇^α, ε^α_TRIP, ρ_TRIP
                    end
                    Define ξ̇^α_irr                          /* Retained martensite */
                    Define ε^α_de, λ^α                                /* Detwinning */
                end
            end
        end
    end
end
```

Algorithm 1: Presents the steps accounting for the phenomena of transformation, TRIP and detwinning.

Continued ;**Sum up** $\xi^{\alpha}_{re}, \xi^{\alpha}_{irr}, \boldsymbol{\epsilon}^{\alpha}_{tr}, \boldsymbol{\epsilon}^{\alpha}_{TRIP}, \boldsymbol{\epsilon}^{\alpha}_{de}$ over N_v to get $\xi, \boldsymbol{\epsilon}_{tr}, \boldsymbol{\epsilon}_{TRIP}, \boldsymbol{\epsilon}_{de}$
Initialize $\dot{\gamma^s}_{vp}, \rho_{vp}, \dot{\alpha}^s$; **Initialize** $\boldsymbol{\epsilon}_{vp}$
if $\xi > 0.999$ **then** `/* Plasticity in martensite */`
  for i = *1 to 6* **do** `/* 6 x [001](010) slip systems */`
    Define q^i, ρ^i, τ^i, x^i
    for j = *1 to 6* **do**
      Define r_{sum}, X
    end
    Define r^s, Φ^s_{vp}
    if $\langle \tau^s - x^s \rangle > 0$ **then** `/* Plastic yielding */`
      Define $\dot{\gamma}^s_{vp}, \dot{\alpha}^s, \boldsymbol{\epsilon}^s_{vp}$
    end
    Define ρ_{vp}
  end
end
else if $\xi <= 0.001$ **then** `/* Viscoplasticity in austenite */`
  for i = *7 to 18* **do** `/* 12 x [110](-111) slip systems */`
    Define q^i, ρ^i, τ^i, x^i
    for j = *7 to 18* **do**
      Define r_{sum}, X
    end
    Define r^s, Φ^s_{vp}
    if $\langle \tau^s - x^s \rangle > 0$ **then** `/* Viscoplastic yielding */`
      Define $\dot{\gamma}^s_{vp}, \dot{\alpha}^s, \boldsymbol{\epsilon}^s_{vp}$
    end
    Define ρ_{vp}
  end
  for i = *19 to* N_s **do** `/* 6 x [110](001) slip systems */`
    Define q^i, ρ^i, τ^i, x^i
    for j = *19 to* N_s **do**
      Define r_{sum}, X
    end
    Define r^s, Φ^s_{vp}
    if $\langle \tau^s - x^s \rangle > 0$ **then** `/* Viscoplastic yielding */`
      Define $\dot{\gamma}^s_{vp}, \dot{\alpha}^s, \boldsymbol{\epsilon}^s_{vp}$
    end
    Define ρ_{vp}
  end
end
Sum up $\boldsymbol{\epsilon}^s_{vp}$ over N_s to get $\boldsymbol{\epsilon}_{vp}$

Algorithm 2: Steps for the plasticity in martensite and viscoplasticity in austenite based on the martensite volume fraction.

Continued
Define Y_{p1}, Y_{p2}, ξ_{ir} `/* Transformation-viscoplasticity coupling */`
Define $\epsilon^{el}_{cum}, \epsilon^{th}_{cum}, \epsilon^{tr}_{cum}, \epsilon^{TRIP}_{cum}, \epsilon^{vp}_{cum}, \epsilon^{de}_{cum}$ `/* Cumulative strains */`
Sum up ϵ^{tot}_{cum} `/* Total strain */`
Define H `/* Tangent matrix */`

Algorithm 3: Presents the coupling equations and ends the entire algorithm with accumulating each strain tensors into a scalar quantity and summing them up to give the total strain which is then used in evaluating the tangent matrix.